AD-761 208

Use of Electron Beam Gun for Hard Rock Excavation

Westinghouse Electric Corp.

prepared for

Bureau of Mines Advanced Research Projects Agency

DECEMBER 1972

Distributed By:

NTIS

National Technical Information Service
U. S. DEPARTMENT OF COMMERCE

DISCLAIMER NOTICE

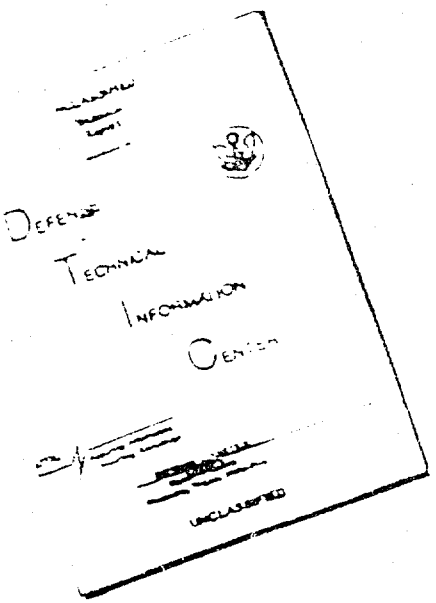

THIS DOCUMENT IS BEST QUALITY AVAILABLE. THE COPY FURNISHED TO DTIC CONTAINED A SIGNIFICANT NUMBER OF PAGES WHICH DO NOT REPRODUCE LEGIBLY.

REPRODUCED FROM
BEST AVAILABLE COPY

30 DECEMBER 1972

AD 761208

FINAL TECHNICAL REPORT
(1 JANUARY 1971–30 DECEMBER 1972)

USE OF ELECTRON BEAM GUN FOR HARD ROCK EXCAVATION

Submitted to

U.S. Department of the Interior
Bureau of Mines
Twin Cities Mining Research Center
Twin Cities, Minnesota

Contract No. H0110377

DDC
RECEIVED
JUN 11 1973
B

Sponsored by

Advanced Research Projects Agency
ARPA Order No. 1578
Program Code 0F010

Reproduced by
NATIONAL TECHNICAL
INFORMATION SERVICE
U S Department of Commerce
Springfield VA 22151

Westinghouse Electric Corporation

Missile Launching & Handling Dept.
Sunnyvale, California

Research Laboratories
Pittsburgh, Pennsylvania

The views and conclusions contained in this document are those of the authors and should not be interpreted as necessarily representing the official policies, either expressed or implied, of the Advanced Research Projects Agency or the U. S. Government.

Distribution of this document is unlimited.

UNCLASSIFIED
Security Classification

DOCUMENT CONTROL DATA - R & D

(Security classification of title, body of abstract and indexing annotation must be entered when the overall report is classified)

1. ORIGINATING ACTIVITY (Corporate author)
WESTINGHOUSE ELECTRIC CORPORATION
Missile Launching & Handling Dept.
Handy Avenue, Sunnyvale, CA
Research Laboratories
Pittsburgh, PA 15235

2a. REPORT SECURITY CLASSIFICATION
Unclassified

2b. GROUP
---

3. REPORT TITLE
USE OF ELECTRON BEAM GUN FOR HARD ROCK EXCAVATION
-Final Technical Report

4. DESCRIPTIVE NOTES (Type of report and inclusive dates)
Final Technical Report (1 January 1971 - 30 December 1972)

5. AUTHOR(S) (First name, middle initial, last name)
Dr. Berthold W. Schumacher/ R. G. Holdbrook

6. REPORT DATE
30 December 1972

7a. TOTAL NO. OF PAGES
~~283~~ 285

7b. NO. OF REFS
31

8a. CONTRACT OR GRANT NO.
H0110377

b. PROJECT NO. ARPA Order No. 1578

c. Program Code 0F10

d.

9a. ORIGINATOR'S REPORT NUMBER(S)
73-8C2-ROCUT-P1

9b. OTHER REPORT NO(S) (Any other numbers that may be assigned this report)

10. DISTRIBUTION STATEMENT
Distribution of this document is unlimited.

11. SUPPLEMENTARY NOTES

12. SPONSORING MILITARY ACTIVITY
Advanced Research Projects Agency
Washington, D.C. 20401

13. ABSTRACT

This is the Final Technical Report of Contract No. H0110377 U. S. Bureau of Mines. Original contract objectives, namely field tests of the electron beam rock cutting process on a semi-infinite rock face, were not met with the available funds. A mobile, field-worthy electron gun was checked out in a very limited series of outdoor tests on a 6 ft. cube of granite. Test results confirmed all expectations. It was proven that x-ray shielding posed no problems. A mathematical model of the electron beam piercing process and thermal stress cracking was devised which is in reasonable agreement with observations.

Since the collection of pertinent experimental data has not even been started the intended systems evaluation and economic projections beyond earlier estimates could obviously not yet be made.

DD FORM 1 NOV 65 1473

UNCLASSIFIED
Security Classification

14. KEY WORDS	LINK A ROLE	LINK A WT	LINK B ROLE	LINK B WT	LINK C ROLE	LINK C WT
Electron Beam						
Tunneling						
Mining						
Rocks						
Minerals						
Excavation						
Fracture Mechanics						
Evaporation						
Melting						
Thermal Stress						
Spalling						
Cutting						

Distribution of this document is unlimited.

72-8C2-ROCUT-P1 30 December 1972

Final Technical Report

USE OF ELECTRON BEAM GUN FOR HARD ROCK EXCAVATION

U.S. Bureau of Mines
Contract No. H0110377

ARPA Order No. 1578
Program Code 0F010

Effective Date of Contract:	11 December 1970
Contract Expiration Date:	30 December 1972
Amount of Contract:	$250,500 (CPFF)
Principal Investigator	R. G. Holdbrook (408) 735-2748 Sunnyvale, Cal.
Project Scientist:	Dr. B. W. Schumacher (412) 256-3522 Pittsburgh, Pa. 15235

Westinghouse Electric Corporation

Missile Launching & Handling Dept. **Research Laboratories**
Sunnyvale, California **Pittsburgh, Pennsylvania**

The views and conclusions contained in this document are those of the authors and should not be interpreted as necessarily representing the official policies, either expressed or implied, of the Advanced Research Projects Agency or the U. S. Government.

Distribution of this document is unlimited.

This research was supported by the Advanced Research Projects Agency of the Department of Defense and was monitored by the Bureau of Mines under Contract No. H0110377.

The views and conclusions contained in this document are those of the author and should not be interpreted as necessarily representing the official policies, either expressed or implied, of the Advanced Research Projects Agency or the U. S. Government.

ACKNOWLEDGMENTS

The work described in this document had many more contributors than those officially responsible for the report and those few already mentioned in the text.

The daily operations of the rock cutter gun were in the competent hands of Mr. A. Pranckevicius and Mr. C. R. Taylor. Without their devotion to this project, and their resourcefulness in the face of many obstacles the work would have not yet reached its present state.

The theoretical analysis of the e.b. piercing process and the stresses created thereby is essentially the work of Dr. R. C. Smith. In this connection we made use of computational methods developed by our Mechanics Department and are indebted to Dr. C. Visser and Mr. D. G. Thompson for help and advice. Dr. R. C. Smith also ran many of the laboratory and the later "field" tests.

In the course of the project, the physicists' and engineers' notions about rocks were steadily improved by the tutoring of Dr. Thelma Isaacs, Geochemist at the Westinghouse Research Laboratories, who always took a helpful and keen interest in our doings and results. In addition, she secured test specimens and provided us with their mineralogical analysis.

With respect to the promotional efforts which a project of this nature requires, internally and externally, the contributions and the steady encouragement of Mr. A. W. Possner of the Research Marketing Department were invaluable to the progress which we have made.

At Sunnyvale the arrangements for the field tests were in the hands of Mr. G. H. Frank. He and Mr. R. C. Barry made the x-ray surveys. The design of the carriage for the gun was exclusively in the

hands of Mr. R. E. Ryan. For many kinds of help before and during the tests at Sunnyvale we want to thank especially Mr. C. Caslander. We appreciated the lively interest shown by Mr. A. L. Paquette and Mr. R. Saunders, and last but not least the contribution of Mr. D. R. Nixon, who was initially the contract manager in the early phases of the contractual work.

Participating in the contractual work as consultants, in particular with respect to future mining and tunneling systems using the electron beam, was Hi-Z Mining Corporation, Albuquerque, N.M., especially Mr. D. I. Prickett.

The work under this contract was monitored by Dr. Kuppusamy Thirumalai, Project Officer, Twin Cities Mining Research Center, U. S. Bureau of Mines. We greatly appreciated his interest and numerous suggestions in connection with this work.

ABSTRACT

During the past four years, laboratory tests conducted by Westinghouse have shown that the electron beam gun is a promising tool for use in hard-rock excavation. However, because these tests were only conducted on small, unconstrained, laboratory test specimens weighing a few hundred pounds, their results are not appropriate for evaluating the use of the electron beam gun in large-scale tunneling and mining operations. Such an evaluation was the original, prime, objective of the U.S. Bureau of Mines contract (H0110377), of which this publication is the Final Technical Report. The contract was aimed at field tests to study the electron beam process on a semi-infinite, constrained rock mass, such as might be encountered in mining or tunneling. The objectives of the electron beam gun evaluation program were:

1. To obtain field operating data.

2. To determine the effectiveness and economic feasibility of the electron beam gun compared with conventional methods of hard rock excavation.

3. To determine practical optimums for equipment configuration and modes of operation.

In support of the foregoing effort, laboratory experiments and theoretical studies were also to be conducted to compute, and if possible to predict, the thermal stresses and the resultant rock fragmentation for various cutting strategies and electron beam parameters in different types or rock.

When part of the above program was completed it was found that the carriage for the electron gun and other field support equipment had cost more than anticipated, and with the remaining funds actual field test could not be performed. By way of a revision of the original

contract, and as an interim objective towards the overall objective, it was therefore decided to complete the construction and tests of a mobile, field-worthy electron gun for rock cutting, and to use it for a limited series of process studies and cutting tests on a large block of granite which, at least for some of the tests, represented a quasi-infinite rock face. It is clear, however, that a proper assessment of the e.b. method for large scale cracking of rock ledges, etc., could not be expected from such limited tests. Also excluded by the contract revision was the originally intended Systems Analysis Study, which was supposed to project the conclusions of the tests into reference with a productive, rapid, hard-rock excavation system; such a study can only be based on full-scale field tests.

Under the contract several tasks were accomplished. A carriage was designed and built for making an electron gun sufficiently mobile to use in a series of rock cutting tests on a semi-infinite rock face. (The gun and its auxiliaries were not built under contract but are Westinghouse property existing prior to this contract.)

The electron gun was tested in a limited number of tests on a 6 ft. cube of granite. These test[illegible]ade outdoors with the equipment configuration eventually [illegible] field tests. As such, a remotely controlled, "long [illegible] gun has been successfully demonstrated.

A mathematical model was developed to approximate the electron beam piercing process and the subsequent development of thermal stresses, up to the point of cracking. This program identified the several critical parameters of the process and predicted stress configurations which are in qualitative agreement with the cracking configurations found experimentally.

In conclusion, the original contract objectives, namely field tests of the electron beam rock cutting process on a semi-infinite rock face, were not met with the available funds. However, a mobile, field-worthy electron gun was checked out in a very limited series of outdoor tests on a 6 ft. cube of granite.

Test results confirmed all expectations. Some evidence was obtained of cumulative cracking effects from successive piercing shots and melt-cuts. Use of the electron beam for spalling was also successfully demonstrated.

It was shown, by radiation surveys, that the problem of shielding against x-rays is easily accomplished with straight forward techniques.

Nothing showed up in the tests which would preclude consideration of the electron beam rock cutting process for large-scale operations. It is clear, however, that the present, very limited test results do not contain sufficient information to serve as a basis for an analysis of an integrated electron-beam excavation system.

TABLE OF CONTENTS

		PAGE
	LEGAL NOTICES	i
	ACKNOWLEDGMENTS	ii
	ABSTRACT	iv
1.	OBJECTIVES	1-2
2.	REPORT SUMMARY	2-1
3.	INTRODUCTION	3-1
4.	ELECTRON BEAM ROCK CUTTING TESTS	4.1-1
	4.1 Earlier Laboratory Studies of the Electron Beam Piercing, Melting, Spalling, and Cracking Processes	4.1-1
	4.1.0 General Comments	4.1-1
	4.1.1 Simple Observations	4.1-2
	4.1.2 The Piercing Process	4.1-5
	4.1.3 Melt-Cut Depth vs. Speed	4.1-6
	4.1.4 Flow of the Molten Rock and Manipulation of this Flow	4.1-9
	4.1.5 Thermal Stresses and Stress Cracking-Observations	4.1-11
	4.2 Equipment and Set-Up for Field Tests	4.2-1
	4.3 First Large Scale Tests on Semi-Infinite Rock Face	4.3-1
	4.3.0 General Comments	4.3-1
	4.3.1 Granite Block Tests Specimen	4.3-2
	4.3.2 Reaction to Piercing	4.3-3

PAGE

(a) Sierra White Granite 4.3-1

(b) Other Types of Rock 4.3-17

(c) Discussion 4.3-23

4.3.3 Reaction of the Sierra White Granite to Melt-Cuts 4.3-33

4.3.4 Thermal Stress Cracking and Cumulative Effects 4.3-39

4.3.5 Spalling 4.3-77

4.3.6 Termination of the Tests 4.3-83

5. THEORETICAL STUDIES 5-1

5.1 Tests in Support of Theoretical Studies 5-1

5.2 Analysis of the Piercing Process 5-10

5.3 Development of Thermal Stresses with Time 5-23

5.3.0 General Comments 5-23

5.3.1 Volume and Shape of Piercing Cavity 5-24

5.3.2 Temperature Distribution as Function of Time 5-24

5.3.3 Thermal Stress Calculations 5-32

5.4 Interpretation of Stress Fields 5-39

5.5 Rock Failure 5-42

6. MACHINERY AND SYSTEMS TESTS 6-1

6.0 General Comments 6-1

6.1 Combining Electron Gun and Carriage 6-2

6.1.1 Problems with Pump Mounts and Vacuum Hoses 6-2

6.1.2 Operator's Observation System and Control of Movement 6-5

	PAGE
6.2 Shielded Beam Catcher for Alignment Work on the Electron Gun	6-7
6.3 X-Ray Safety	6-8
6.3.0 General Comments	6-8
6.3.1 California State Registration Law	6-11
6.3.2 X-Ray Generation Laws	6-11
6.3.3 Tolerance Levels and X-Ray Shielding	6-16
6.3.4 Measurements in the Primary X-Ray Beam	6-22
6.3.5 Shielding Under Field Test Condition	6-27
(a) Observations/Sky-Shine/Trap for Primary Beam	6-27
(b) Final Radiation Survey	6-27
(c) Measures to Assure Crew Safety	6-33
6.4 Performance Record of the Electron Gun	6-34

APPENDIX

APPENDIX A

Carriage for the Electron Gun A-1

APPENDIX B

Preparations for Field Tests B-1

APPENDIX C

Literature Reference C-1

1. OBJECTIVES

During the past four years, laboratory tests conducted by Westinghouse have shown that the electron beam gun may be a promising tool for use in hard-rock excavation (Refs. 3 and 4).* These tests have been conducted on small, unconstrained, laboratory test specimens weighing a few hundred pounds. The present contractual work is aimed at field tests to study the electron beam process on a semi-infinite, constrained rock mass, such as might be encountered in mining or tunneling operations.

The end-objectives of the electron beam gun evaluation program are:

1. To obtain field operating data.

2. To determine the effectiveness and economic feasibility of the electron beam gun compared with conventional methods of hard rock excavation.

3. To determine practical optimums for equipment configuration and modes of operation.

In support of the foregoing effort, laboratory experiments and theoretical studies were also to be conducted to compute, and if possible to predict, the thermal stresses and the resultant rock fragmentation for various cutting strategies and electron beam parameters in different types of rock.

When part of the above program was completed it was found that the carriage for the electron gun and other field support equipment had cost much more than anticipated, and with the remaining funds actual field test could not be performed. By way of a revision of the original

---

*See list of references in Appendix C.

contract, and as an interim objective towards the overall objective, it was therefore decided to complete the construction and tests on a mobile, field-worthy electron gun for rock cutting, and to use it for a limited series of process studies and cutting tests on a large block of granite which, at least for some of the tests, represented a quasi-infinite rock face.

It was clear, however, that a proper assessment of the e.b. method for large scale cracking of rock ledges, etc., could not yet be expected from such limited tests.

Also excluded by the contract revision was the originally intended Systems Analysis Study, which was supposed to project the conclusions of the tests into reference with a productive rapid hard rock excavation system; such a study can only be based on full-scale tests.

2. REPORT SUMMARY

A carriage was designed and built for making an electron gun sufficiently mobile to use it in a series of electron beam rock cutting tests on a semi-infinite rock face. (The gun and its auxiliaries were not built under contract but are Westinghouse property existing prior to this contract.) When the gun was to be attached to the carriage, difficulties were encountered which necessitated redesigns and modifications of the carriage; these were costly and time consuming. In the preparations for field tests unexpected expenses were encountered also. With the available funds it was therefore only possible to check out the electron gun in a limited number of tests on a 6 ft. cube of granite. These tests were made with the equipment to be used in the field tests, and were made outdoors.

The electron gun performed as expected. Some evidence was obtained of cumulative cracking effects from successive piercing shots and melt-cuts, although a 6 ft. specimen is too small for any demonstration of effects of the size one would expect when working on a larger rock face. Therefore the present, very limited test results cannot yet be used as a basis for excavation systems analysis, and no such analysis has been made. On the other hand nothing unfavorable has shown up in the outdoor tests which would affect earlier estimates of the efficiency of the electron beam rock cutting process in large scale operation. In fact, a remotely controlled, "long barrel" electron gun has been successfully demonstrated. It has also been shown, by careful x-ray surveys, that shielding against the x-rays poses no problems.

Another task under the contract called for the development of a mathematical model describing the electron beam piercing process and the subsequent development of thermal stresses, up to the point of

cracking. This was successfully accomplished and a model devised which shows the influence of various critical parameters on the process, and which agrees reasonably well with test results of a number of evaluative laboratory tests and the outdoor tests.

3. INTRODUCTION

The reasons why one may consider focused electron beams as tools for rock cutting lie in the unique properties of this tool which shall be briefly described here in order that the later discussion of the test results may be understood better. In the electron gun electric energy is converted into electron beam energy and, surprising as this may sound to many people, the conversion efficiency is better than 90%. Even if we consider the power needed by all auxiliary equipment of the machine the conversion efficiency is yet better than 75%. At the same time the total power in a single electron beam which is presently about 30 kW can readily be increased to 100 kW and more. Single-beam guns with over 1 MW of beam power have been built for steel furnaces.

The electrons are bullets, and their energy is carried as kinetic energy and not, as one might think, in the form of electrical energy. The energy flux that can be achieved is highly directional; we find for the radiance a value of more than 10^{10} W/cm^{2}sr in a 150 kV beam. This means, if we focus the beam so as to get a power density of 10^6 W/cm^2 the angular aperture of the beam will still be less than 1°. This directionality is disturbed and destroyed when the electrons are scattered in matter of high density; let it suffice here to say that hot gas (hot rock vapor) is not of such high density as to impede our process.

Dwg. 2953A96

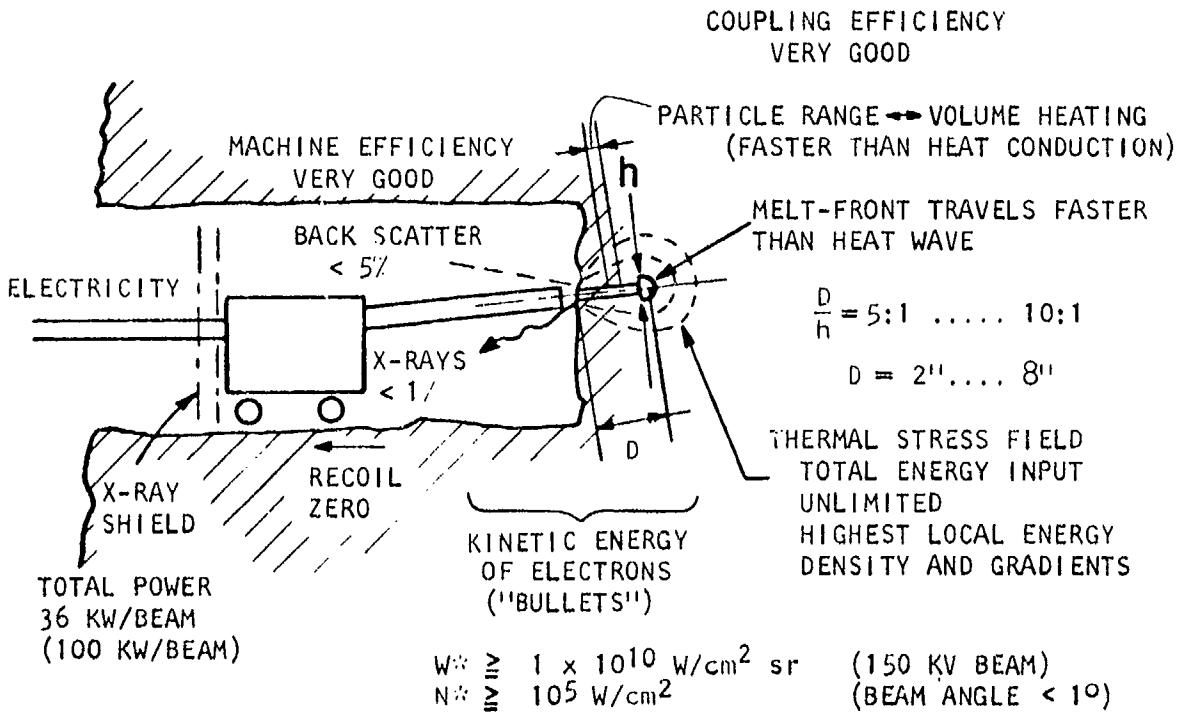

FIG. 3-1 Generalized Schematic of Rock Breaking Operation by Means of a Focused Electron Beam.

Where the focused electron beam impinges, the rock will melt and vaporize immediately. A simple calculation shows (see Section 5) the melt front will travel into the rock to a depth of 2 to 6 inches with a speed much faster than the heat wave, which obviously also emanates from the melt front. Stating the same facts

differently: we vaporize a deep and narrow hole into a rock within 10 to 60 seconds, and the heat does not spread very far in this period of time compared with the depth of the hole. We have, initially, a kind of drilling process. There is some back scatter of electrons, but it is less than 5%; in general, the coupling efficiency of the energy into the rock is very good.

The drilling process slows down when the depths of the cavity becomes so great that the power density is diminished by electron scattering; yet then we have already a depth-to-width ratio for the cavity between 5:1 and 10:1 with an actual depth of 2 to 8 inches. If we now simply keep the electron beam going, additional power is pumped into this cavity; moreover, it is mainly released at the deepest point. Hence, heat is flowing into the rock from a "source" which is, say, 6 inches below the surface. What we have accomplished by this process is to carry considerable amounts of energy quickly deep below the surface of the rock face. The expense which we incur because of the fact that we vaporize some rock is bearable, because the total volume of the melted and vaporized rock is small, because of the great depth-to-width ratio of the cavity. This is typical for electron beam processes, for instance for electron beam welding as well; the high depth-to-width ratio is something like a trademark for electron beam tools.

Now, as a first mode of usage we can obviously move the electron beam laterally along and make narrow and deep melt cuts in any kind of material. More about this aspect later. Neither hardness nor melting point matters.

The following is more important. Concurrently with the melting process there is heat flowing into the rock. Very steep thermal gradients and high thermal stresses are produced. It is important that these thermal stresses are <u>static</u> in nature and remain behind after the electron beam is moved or switched off. Stress fields, computed for certain temperature distributions, are shown and

discussed in Section 5. The stresses extend far into the cold region and further than the depth of the cavity. Fortunately, rocks are brittle and sooner or later every rock will break under these thermal stresses. If we use this aspect of our process intelligently, we can break much more rock than by simply making thin melt cuts. In other words, we have now two different processes available for the use of an electron beam of high power density, namely, (i) making melt cuts, or (ii) fracturing rock on account of the induced thermal stresses.

There is a third process to which the electron beam energy can be applied, although it works only in certain types of rock, namely: (iii) spalling of the rock surface. To keep a spalling process going the energy input density must be kept at just the right level; it will therefore be of no advantage that the electron beam can supply more. Nevertheless, the high coupling efficiency of the e.b. power input can be advantageous, and under certain conditions, this is a third mode of operation for the electron gun where it may be superior to the flame or radiant heating.

Sometimes it is only required to make a cut into a rock, rather than to break it up into pieces. The thinnest hairline crack will separate the parts and sever the coherence. This may be all that is needed if big blocks can be moved and removed in toto, as may be the case in certain tunneling operations, but not in mining.

The traditional tool for this job is the thin blade saw or abrasive disc. For rocks it must be a diamond saw or a wire saw. Neither is suited for large scale tunneling.

For tunneling much has been talked about kerf-cutting; the outline of the tunnel is cut in order to get a smooth wall, then the inner part may be removed even by drilling and blasting, the cracks will not jump the kerf and the outside wall will stay smooth and sound.

What matters in kerf-cutting is the energy needed per unit of length; the width of the kerf hardly matters as far as the purpose of the kerf is concerned, but it affects the energy which must be supplied.

As already mentioned the electron beam can make a narrow melt-cut. Since the energy flux density in the focused beam is in the order of 10^5 to 10^7 W/cm^2, the melt-front travels extremely fast, and the process is quasi-adiabatic (no heat loss by conduction). The melt-front speed is, in practice, limited not by power density but by fluid-flow processes. The melt must flow out of the beam path or it will be removed by vaporization. Ultimately, in the worst possible case, if all material has to be removed by vaporization, the cutting rate will be determined by the speed of the vapor-front. This is not as bad as it sounds, because the beam spot and vapor channel in which the beam travels is less than .3 cm wide. Hence, the higher specific energy requirement of vaporization is offset by the narrowness of the cut and the total energy per unit kerf length remains low; the electron beam represents a "thin sawblade".

With the electron beam we need <u>no</u> mechanical force to make a melt cut; there is not even physical contact between the machine and the rock. The energy coupling into the rock is between 70% and 90% efficient and the amount of energy deliverable to the rock is <u>not</u> limited by heat conduction of rock or tool as, for instance, in the case of flame or infra-red radiation!

The observed penetration rate of a focused 10 kW electron beam into rock is over 1 cm/sec. Higher power could be used to pierce even faster or to cut a longer slot. <u>This is certainly the fastest process known to sever the coherence of rock in a controlled way</u>. The task is to utilize it without running into the natural limitations of the process.

The natural limitation of the process is determined by electron scattering, which diminishes the power density, and causes the cut to become wider and the piercing rate to slow down with depth.

A maximum depth where the above piercing rate applies is between 5 and 10 cm (depending upon beam voltage and total power). But by cutting a double-kerf with a properly built electron gun the inherent process efficiency can yet be utilized for cutting kerfs as deep as 20 to 30 m, should this really be needed and make sense.

So far only a limited amount of experimentation and theoretical analysis has been done compared with these diversified aspects of the electron beam as a cutting tool. Theoretical studies under this contract are reported in Section 5, and tests made are reported in Section 4.

4. ELECTRON BEAM ROCK CUTTING TESTS

In the following Section 4.1 the experimental observations and results will be summarized which we had obtained in some earlier laboratory tests. Thus certain comparisons can be made with the recent contractual tests using the mobile field test equipment on a 16 ton block of granite which are reported in Section 4.3.

4.1 Earlier Laboratory Studies of the Electron Beam Piercing, Melting, Spalling, and Cracking Processes*

4.1.0 General Comments

The use of the electron beam for cutting rocks depends completely upon the availability of the non-vacuum electron gun with a focussed, high-power-density beam. This machine has, fortunately, seen a steady evolutionary development since the first model was built[9] in 1950. Higher power machines of this type were developed for welding, and only after they had become available, could one appraise (and take advantage of) the high power density features of the electron beam outside the vacuum, because certain aspects of the process depend upon total power, as well as on power density. For instance, beam scattering is lower the hotter the gases and vapors in the beam path; and with increased total power the work area becomes hotter, since heat conduction and convection losses become of less and less relative importance.

With the high-power, atmospheric, electron gun available at the Westinghouse Research Laboratories we began, in 1966, some studies

*Not on contract funds.

of how it could be applied to large scale rock cutting, with best advantage. The fact as such, namely, that small bodies of fragile materials could be shattered by bombardment with the non-vacuum focused electron beam had already been demonstrated with the above mentioned very first machine.

It was obvious that the electron gun could not simply be utilized as a substitute for other "heat-sources". Other people,[1] having only such a substitution in mind, and not being aware of the focused non-vacuum electron gun, have therefore ruled out the use of electron beams as "impractical". In addition, this erroneous conclusion was also based on a lack of knowledge about the real nature and the properties of electron beams, which we must use to our advantage, instead of being confounded by them.

The following sections give an account of the earlier observations. Part, but not all of the material presented in the following section has been published.

4.1.1 Simple Observations*

Placing various rocks under the 150 kV, 9 kW electron beam showed that the beam would melt a hole, or cut a slot when traversed over the rock. Vapor would also form. A stand-off distance between rock face and gun of 1/2 inch was safe; no damage to the gun would occur, even when at times the molten rock would rise and stick to the end plate of the gun. Sooner or later most of the specimens would crack up under the thermal stresses; only concrete blocks would not crack. (But later, with higher power, using larger blocks and longer

*See also References 3 and 4.

piercing times, we found that even concrete will crack). The melt of some rocks flowed like water, in other cases it was tacky like pitch; in some cases there was hardly any melt at all but only decomposition vapors and dust, e.g. in case of limestone. But always (even in limestone) a deep and narrow cavity or cut was formed. Some rocks showed spalling, even at 6 inch distances from the gun, notably those with a high quartz content. These same types would also crack very early when pierced, thus limiting the depth of the piercing cavity to about 2 inches before cracking occurred. (Of course, one could continue piercing and drill deeper, even after the cracks had formed.) This indicated that somewhere there were inherent scaling laws which must be watched. Placing some specimens under water, we could demonstrate,[5] as expected, that the process is little, if any, affected by the presence of water (the underlying reasons are discussed in Section 5.6). There was also a well-defined relationship between cutting speed and depth. The process speed increased proportional with increasing power.

It was always understood that at higher beam voltages the electrons are scattered less by gases and vapors and would therefore produce piercing holes or melt-cuts showing a yet greater depth-to-width ratio. We could, unfortunately, not yet make any tests at voltages above 160 kV, which is the limit of the presently available power supplies. There was no point in making tests at lower voltages.

Fig. 4.1-1
Various types of response to electron beam piercing.

4.1.2 The Piercing Process

As one would expect, an electron beam piercing hole gets deeper the longer the beam is applied, but one also has to expect a finite limit because of the scattering of the electrons. Early observations showed that the holes stayed narrow (1/2 to 3/4 inch diameter) over a considerable depth (2 to 4 inch). They were sometimes pointed at the bottom, sometimes round, as Fig. 4.1-1 shows. In a coarse granite, (a) in Fig. 4.1-1, a black glassy melt formed and dripped out. A sandstone (b) showed a point cavity with a glass-lined wall which split. Another sandstone (c) showed a rounded cavity with glass beads sticking to the wall. A grano-diorite formed a glass-lined chimney which broke away as a complete tube; this also happened in the limestone of picture (e), but not in all limestones; in the granite of picture (f) the cavity-tube remained stuck. Quartzite always showed the "glass-tube" as for instance in Fig. 4.1-6.

At a later time we also obtained, through the courtesy of the White Pine Copper Company, samples of a copper ore from Michigan, a siliceous shale. Typical piercing cavities can be seen in Fig. 4.1-7. They are glass-lined, and the glass tube splits in half when the rock cracks; most of the cavity material has flown out or been vaporized. The same is true for the black gabbro of Fig. 4.1-4(b) and Fig. 4.3-10. Two spectacular holes of 3.2" diameter and 8" depth developed in a block of norite, a nickel ore from Sudbury, Ontario, obtained through the courtesy of the International Nickel Company of Canada. Fig. 4.1-14 to 18 show this block and the piercing holes.

In an attempt to obtain a fuller understanding of the process, we analyzed the conditions necessary for obtaining a high depth-to-width ratio, and the factors limiting the ultimate depth of a cavity or melt cut. This analysis started from two different points of view. P. G. Klemens,[6] of the Westinghouse Research

Laboratories analyzed energy distribution aspects, showing a critical power density threshold must be exceeded before deep penetration could commence. The electron scattering and energy input to the wall of the cavity, and the continuous reduction in the central beam power density were studied by D. C. Schubert.[7,8] At the time, we did not take systematic measurements of piercing depth vs. time. Such measurements were made under the present contract, in support of the theoretical studies, and are reported in Section 5.1. As will be discussed in Section 4.3.2, the "Sierra White" granite differed in its response to piercing from what we had seen so far.

4.1.3 Melt-Cut Depth vs. Speed

Piercing depth as function of time, and melt-cut depth as function of speed are theoretically related,[6] but in practice the flow of the melt and similar factors dominate the process. Therefore, the depth of a melt-cut as function of speed and power must be experimentally determined. Not to be confused by the cracking of the specimens, we took a block of concrete to determine depth as function of speed for two power levels. Results are shown in Fig. 4.1-2 and 3. The slower the cut, the deeper the melt-zone as one would expect. However, the slower cut will also be wider, and more material is melted per unit length of the cut, then the increase in depth alone would indicate. A better measure for the efficiency is the cross-sectional area which the electron beam "knife" cuts out as a function of time or of energy expended. Obviously, this cross-section is given by the product of depth x speed, which is also shown in Fig. 4.1-3. It increases drastically with speed between 1 inch per minute and 10 inch per minute; even up to 30 inch per minute it will increase with speed although not as pronounced. Hence, it costs less energy to make a 3 inch deep cut in 3 runs at 14 IPM each (effective speed 4.6 IPM) than in 1 run at 2 IPM, as we would need to do (curve for

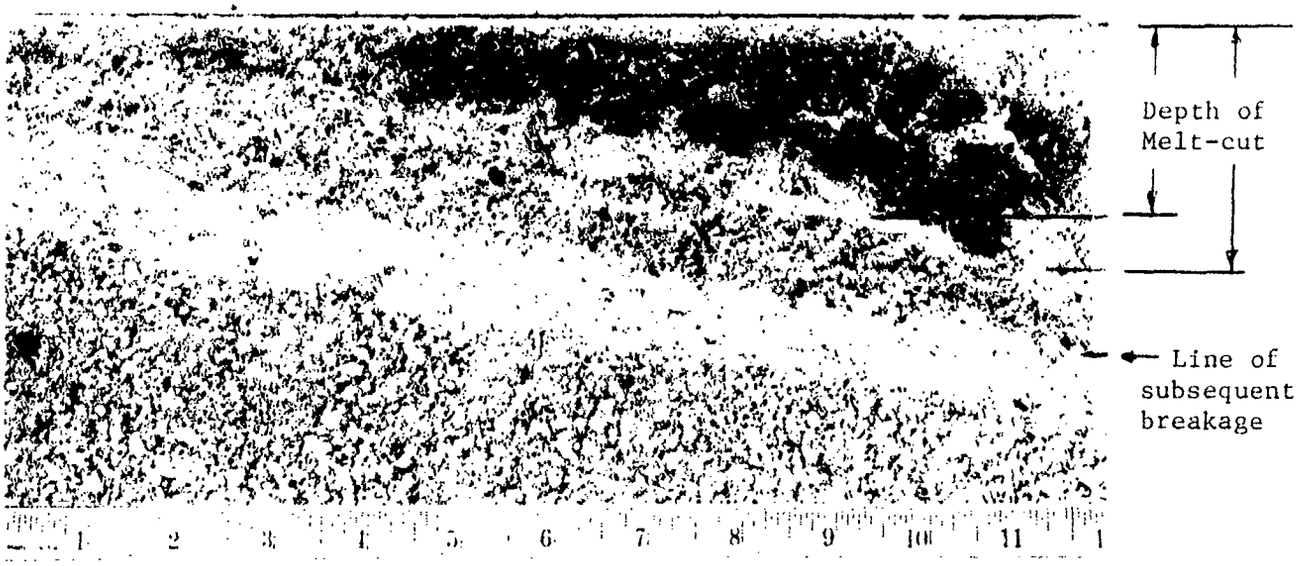

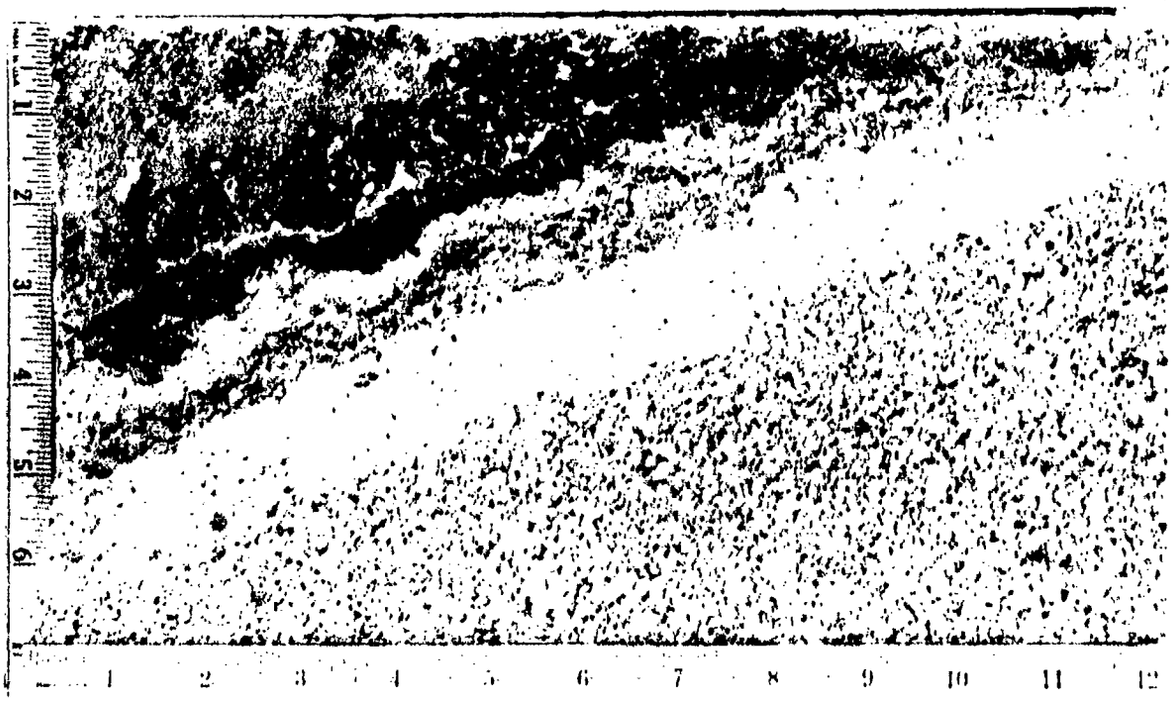

Fig. 4.1-2 Melt-cut depth vs. speed for 5 kW and 9 kW beam power in a concrete block.

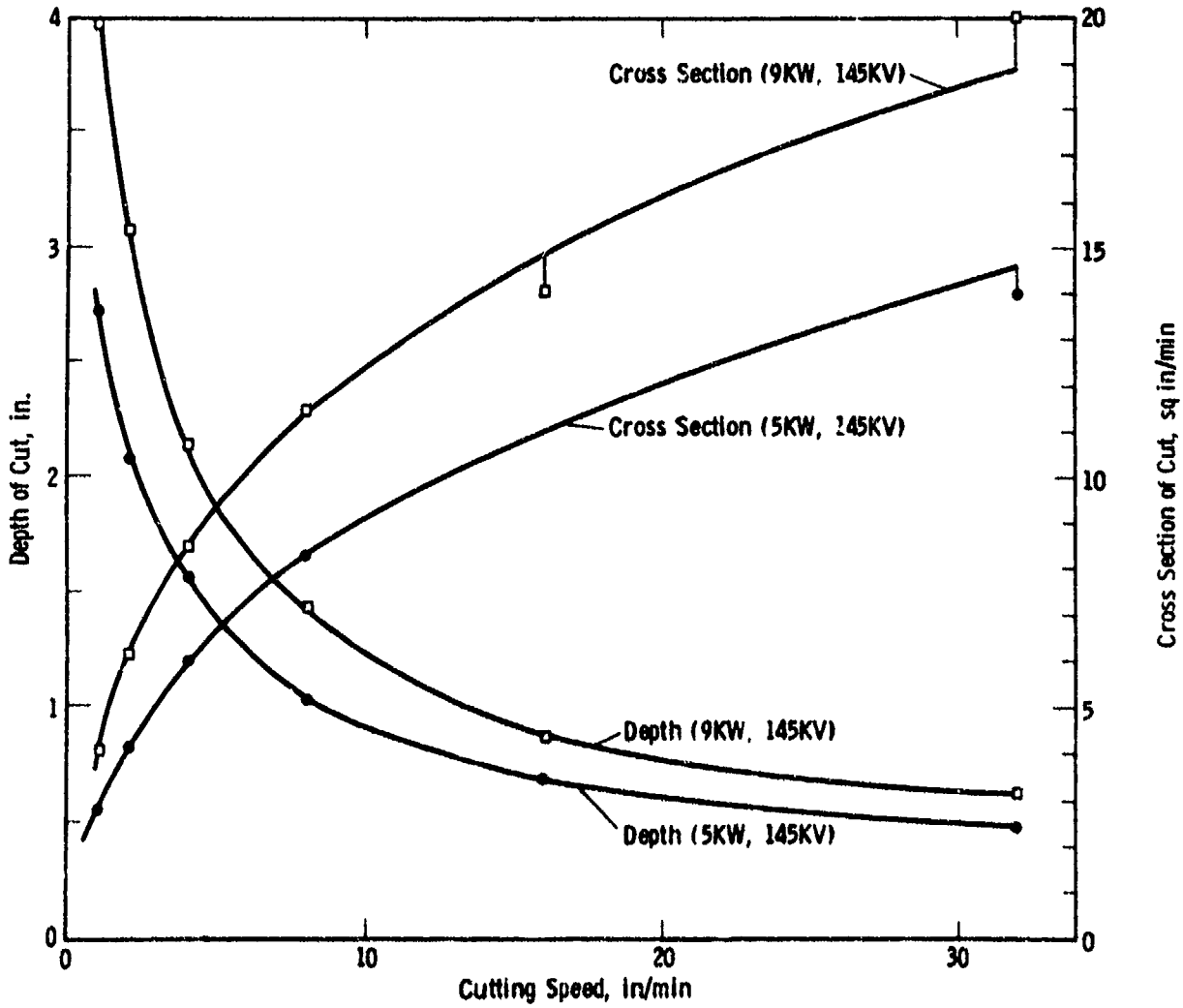

FIG. 4.1.-3 Relationship Between Power, Cutting Depth and Cutting Speed for Pure Melt-Cuts in Concrete. The Cross Section (Speed x Depth) is also Shown.

9 kW of Fig. 4.1-3). The only question is, are 3 successive runs strictly additive? This question is not fully answered as of today. The effect of multiple runs is certainly not additive if the debris after each run remains trapped in the cut. It also depends on the stand-off distance, and whether or not this can be or is adjusted after each run. We have not had an opportunity to make systematic tests; in Section 4.1.7 and 4.3.3 some relevant observations are reported.

Figure 4.1-3 also shows that with twice the power, one can cut equally deep at twice the speed. (At the same speed, one cannot cut twice as deep, for reasons explained above.)

In other types of rock, a cutting depth of 2" resulted rather consistently with a speed of 4 inch per minute and 9 kW of power. The heat of melting being not very different for different rocks, it does apparently not matter much whether the melt flows out or remains in the cut, as long as only the beam moves into fresh, solid rock and the debris does not flow into the beam, or block the beam in other ways. Figure 4.1-4 shows other examples of such melt-cuts. The associated breakage shall be discussed later.

4.1.4 Flow of the Molten Rock and Manipulation of This Flow

It was evident from the very first observations that the viscosity of the molten rock varied between wide limits, from a plastic tackiness to a watery flow. An example for the tacky type can be seen in Fig. 4.1-1(f) and 4.1-4(a) whereas the watery flow is evident from Fig. 4.1-4(b) and Fig. 4.1-5.

This is actually nothing new; people experimenting with flame-jet melting have observed this behavior of the different melts. The suggestion has been made by Margiloff[10] to add fluxes to the melt, like borax and soda in the form of a powder; this lowers the melting temperature and can also increase the fluidity of the melt.

(a)

(b)

(c)

Fig. 4.1-4 Typical melt-cuts in (a) granite, (b) black gabbro, (c) siltstone (copper ore).

For the cutting speeds which we are considering this would be too slow a process.

We tried, but not very systematically, blowing away the melt with an air jet. The jet-force must be considerable to overcome surface tension and inertial resistance; besides, it has a chilling effect on the melt making it more tacky. We have not yet tried water jets. They may, due to the quenching effect, break up the glass which forms, and thereby permit easier removal. A simple test with a water-overflow was made later and is recorded in Section 4.3.4.

Every such additional manipulation is a complication as far as the practical operation is concerned. We should therefore examine what is really needed. Actually, for effective cutting and piercing, the only region which should be kept free of the melt is the narrow path of the electron beam itself. This may be best accomplished by a gas jet concentric with the beam; no systematic tests have been made.

It is also evident that a melt-cut made vertically upwards will leave the melt below and will continuously expose new rock to the beam; not so in a cut made vertically downwards. On the other hand, we did, surprisingly, not find much difference in the effectiveness of downwards and horizontal piercing (see Section 4.1.7); but more systematic experiments would be desirable.

4.1.5 Thermal Stresses and Stress-Cracking--Observations

Differential thermal expansion due to temperature differences take place in all types of rock when pierced by the electron beam, and since all rocks are brittle, all will sooner or later break. In rocks containing quartz, an additional effect producing high stresses is the well-known phase transition which occurs at 573°C and which is associated with a 1% increase in volume. Hence, rocks containing quartz break particularly easily, as already our first observations

FIG. 4.1-5

Silt-Stone (White Pine Copper Ore) Being Pierced by a Horizontal Electron Beam Shows the Watery Flow of the Melt from the Piercing Hole.

showed. Figure 4.1-6 is a particularly striking example. All the specimens shown in Fig. 4.1-1 and 4.1-4 show cracking, except that the breakage in the granite of Fig. 4.1-4a is localized. But then, a second melt-cut made over the same track produced a crack splitting the whole block.

The fastest response we obtained when piercing the copper ore, shown in Fig. 4.1-4c and Fig. 4.1-7. Apart from having a silicous bond, this shale contains a large amount of water, which could be observed immediately after a crack had formed. The cracked surfaces showed large patches of moisture, for example, the black area on the right hand face in Fig. 4.1-7. Such spots dried up in

10 to 20 seconds. The water in some places was steaming. Obviously, the water vapor pressure aids to the cracking.

Two more of the early observations must be mentioned. In layered rock, the silt-stone for instance, a piercing shot perpendicular to the layers would lift-off, in a kind of ablative mode, layers as thick as the piercing cavity was deep, e.g., 2 to 4 inches. Figure 4.1-8 is an example. This mode should work in the same way even on a semi-infinite rock face, when the piercing holes are spaced 12 to 24 inches apart.

FIG. 4.1-6 Rose Quartzite Block Pierced and Cracked by a 9 kW Electron Beam in 9 Seconds.

Fig. 4.1-7 Copper ore block of 127 lbs pierced twice, first for 30 sec, then for 20 sec under a 15 kW beam.

Fig. 4.1-8 Siltstone pierced perpendicular to its natural layers.

The other observation concerns the breakage associated with a melt-cut; namely, the fact that it can be surprisingly smooth and straight. Figure 4.1-9 is an example; it shows the same block of black gabbro as Fig. 4.1-4b. This smooth breakage is obviously partly the result of the symmetry of the thermal stresses. Note also that the block of Fig. 4.1-7 broke along a surface containing both piercing cavities. But the collective effect of several piercing holes has not been studied further.

FIG. 4.1-9 Oklahoma Black Gabbro Cracked in a Single Passage with a 15 kW Beam Traveling 4"/Min.

4.2 Equipment and Set-Up for Field Tests

A description of the rock cutter electron gun, which was built on Westinghouse funds, has already been presented elsewhere.*

To understand what was done during the actual rock cutting tests, it is sufficient to describe here the equipment and setup "as it looks from the outside". This is indeed all the user or operator needs to know.

Figure 4.2-1 shows the electron gun prior to its assembly on the 5-axes carriage. The control cabinet can be seen in the background. Figure 4.2-2 is another view. As compared with the previous figure, a slight change will be noted insofar as beam position sensors have been added to the long nose gun column, making it 2" higher; Fig. 4.2-3 shows details of the control cabinet. A description of the 5-axes gun carriage can be found in Appendix A. Figure 4.2-4 shows the gun mounted on this carriage.

A general layout for any field test site is shown in Fig. 4.2-5, and Fig. 4.2-6 shows a scale drawing of the in-plant test site at Sunnyvale, where the tests described in Section 4.3 were made. This was an existing, radiation proof enclosure in the factory yard; it was previously used for gamma-ray radiography of heavy sections of machinery. A view of this facility from the outside is provided in Fig. 4.2-7. The entrance and operator's station is shown in Fig. 4.2-8 and 4.2-9.

---

*Mining Congress Journal, June 1972.

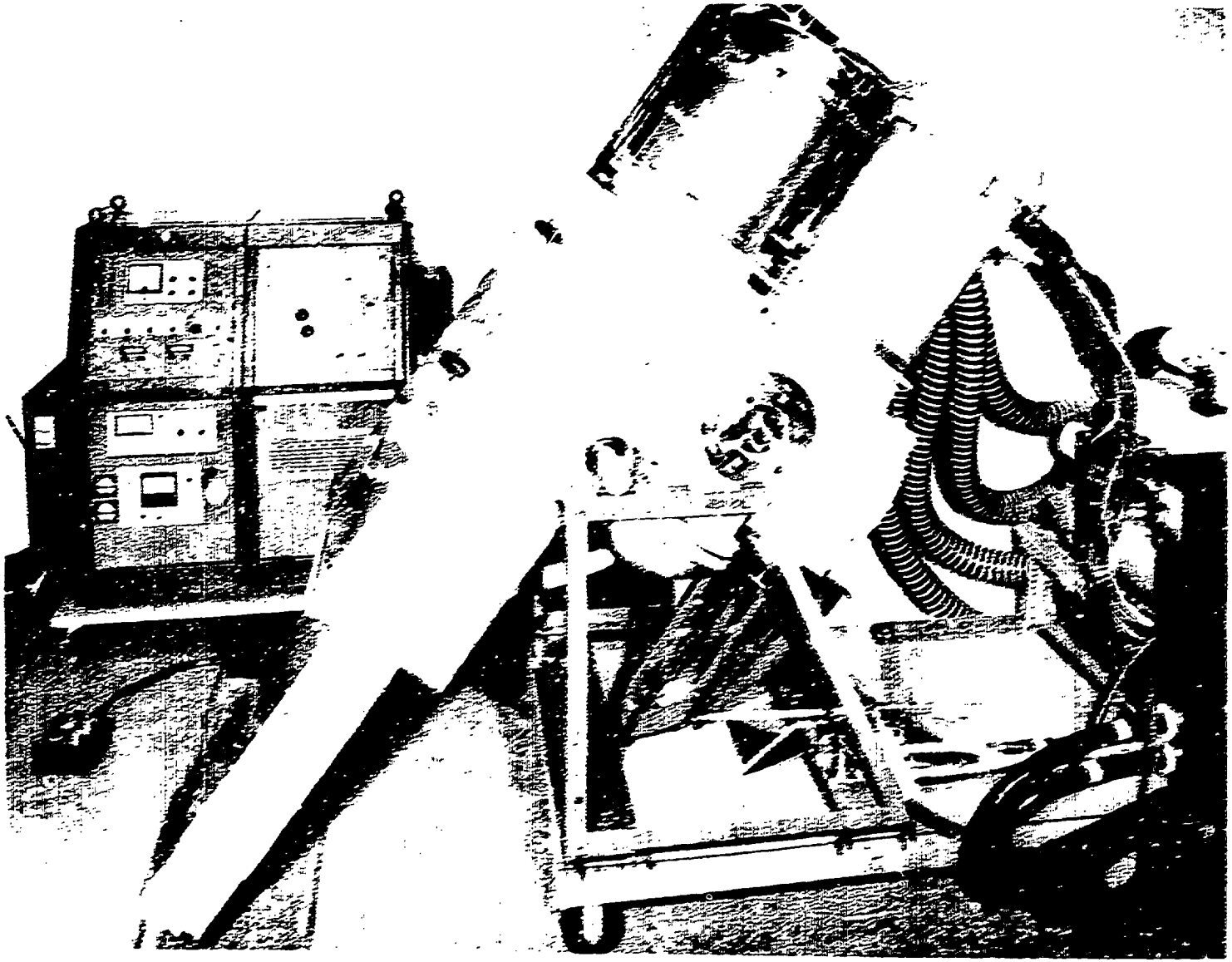

FIG. 4.2-1 Electron gun prior to assembly on the five-axes carriage; in the background the operator's console; the remote on/off button lies on the floor.

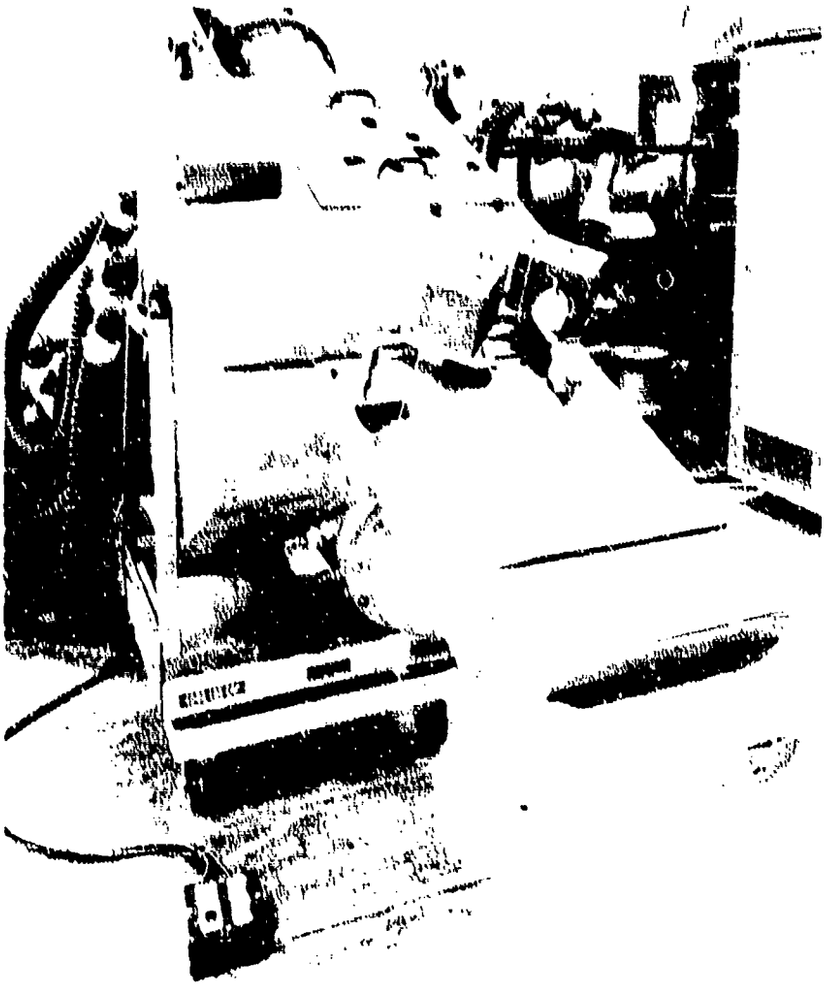

FIG. 4.2-2 View of the front end on the gun from above. The foremost section is a removable and replaceable copper sheet shroud with molybdenum face plate. The large rectangular box section is a lead shield on an angle iron frame which is sturdy enough to protect against falling rock, etc. The viewing optics for the beam position sensors are underneath the lead shroud, but the phototube sensors are located in the two cubical boxes on top, which have not yet been shrouded (missing in Figure 4.2-1)

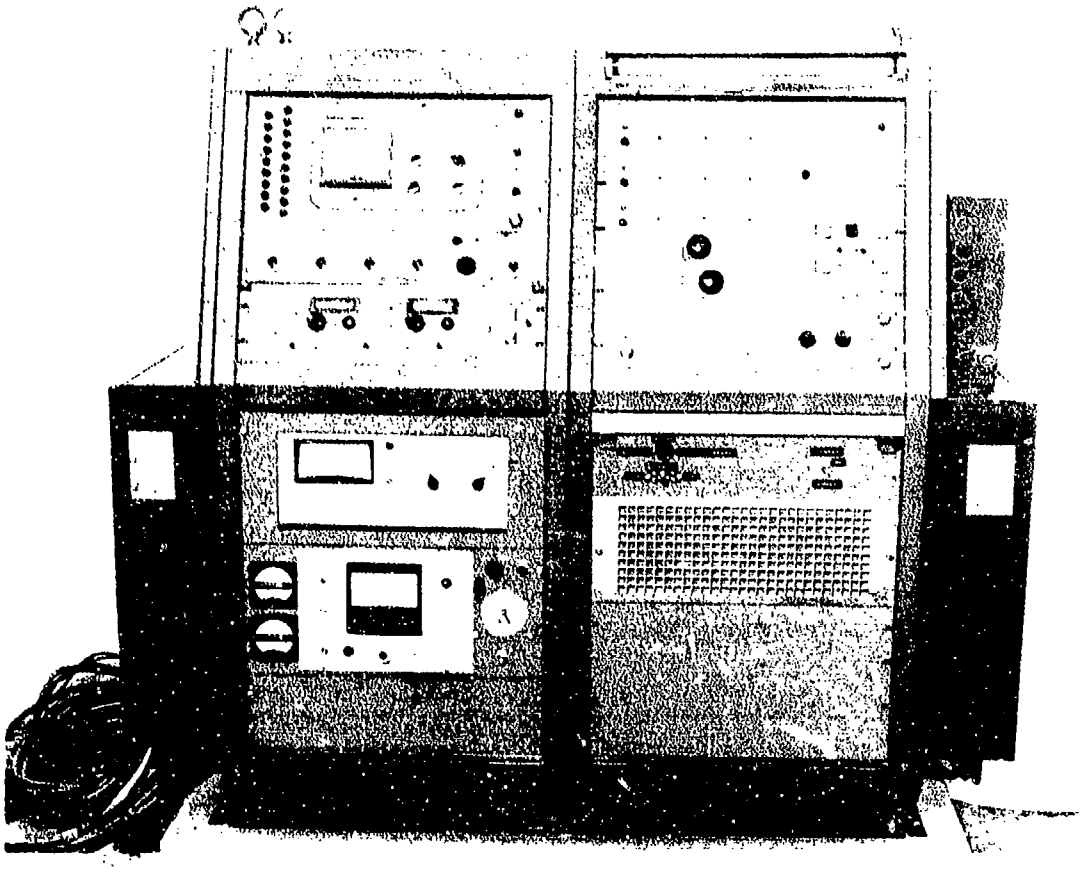

FIG. 4.2-3 Control cabinet for the electron gun. The left hand side holds: 3 vacuum gage read-outs, 3 timers, 5 temperature indicators and interlocks from the thermocouples attached to the gun nozzles, and the magnetic lens and deflection coil controls. On the right, the 9 identical meters show primary voltage and current into each of the three power supplies, and d.c. current drawn from each supply. The 3 large meters shown d.c. high voltage, cathode emission current, and transmitted current if the gun fires into a catcher; (if it fires into a rock, it runs "blind"). The two medium size meters show cathode input (heater) voltage and current.

Fig. 4.2 - 4 - Electron gun mounted on the 5-axes carriage of the field test installation. A granite block G is the test specimen. The lead panels S intercept the direct x-ray beam.

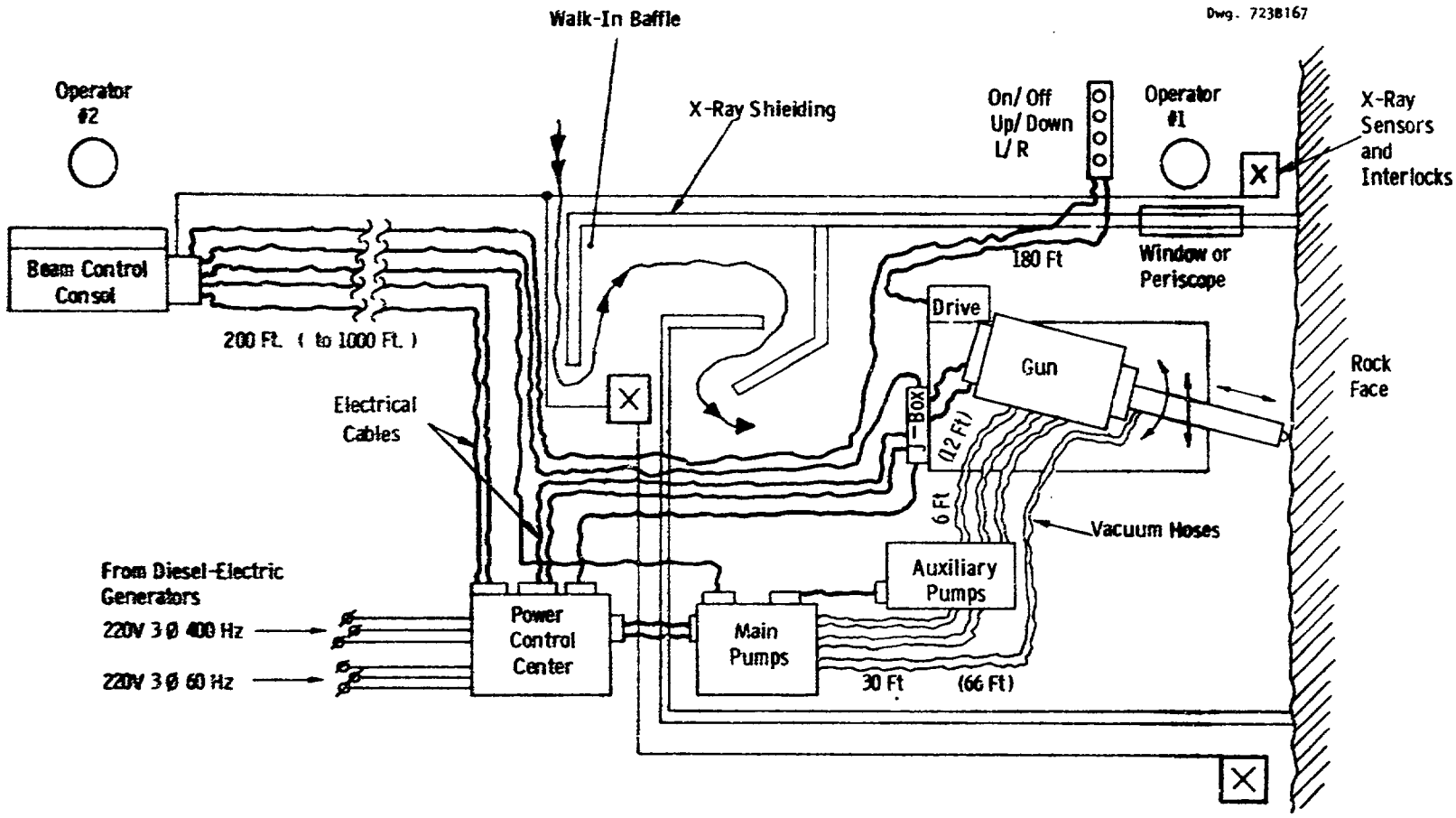

FIG. 4.2-5 Schematic of a complete electron gun and drive installation, including shielding and radiation monitors.

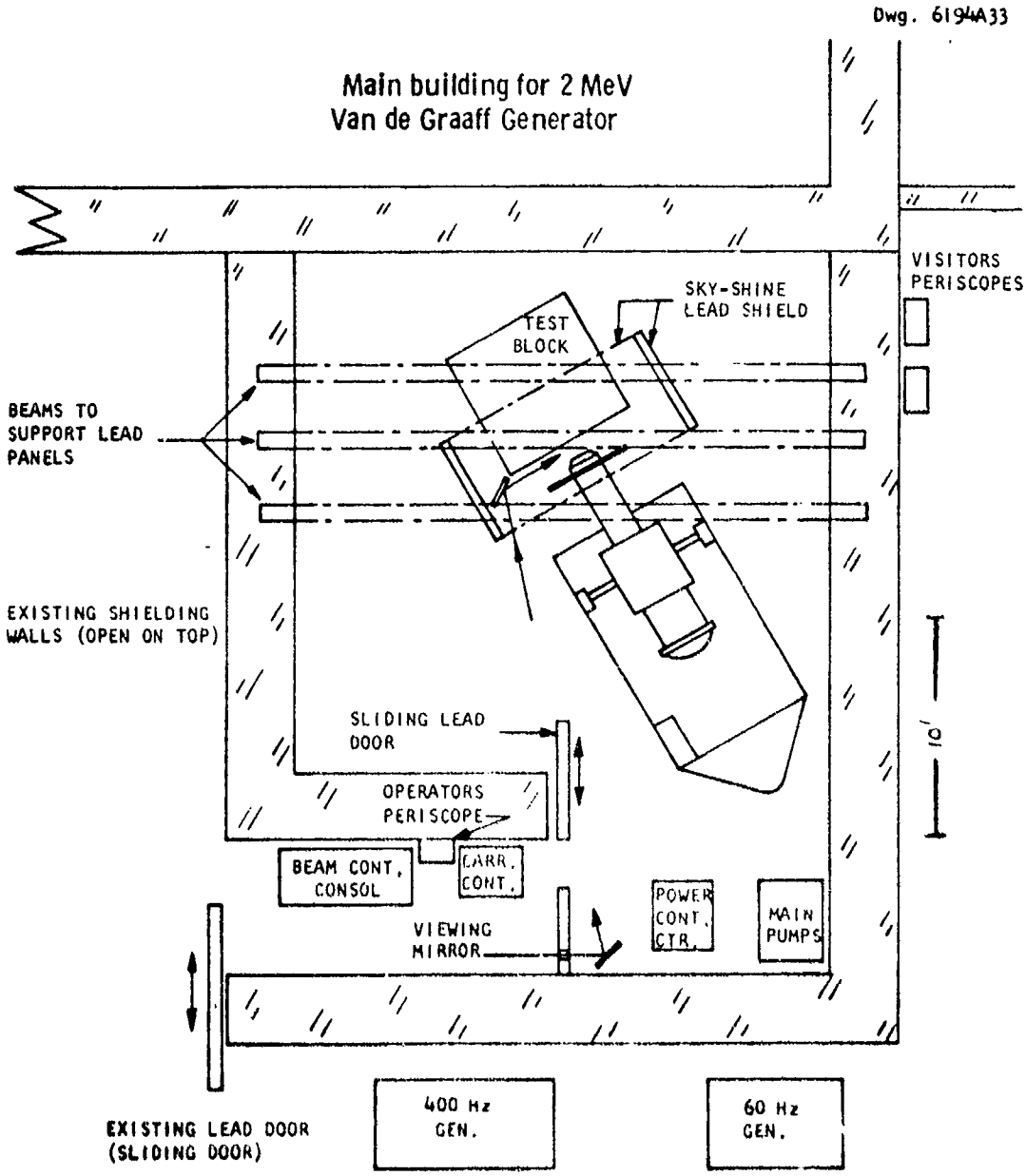

FIG. 4.2-6 In-plant test site at Sunnyvale; to scale.

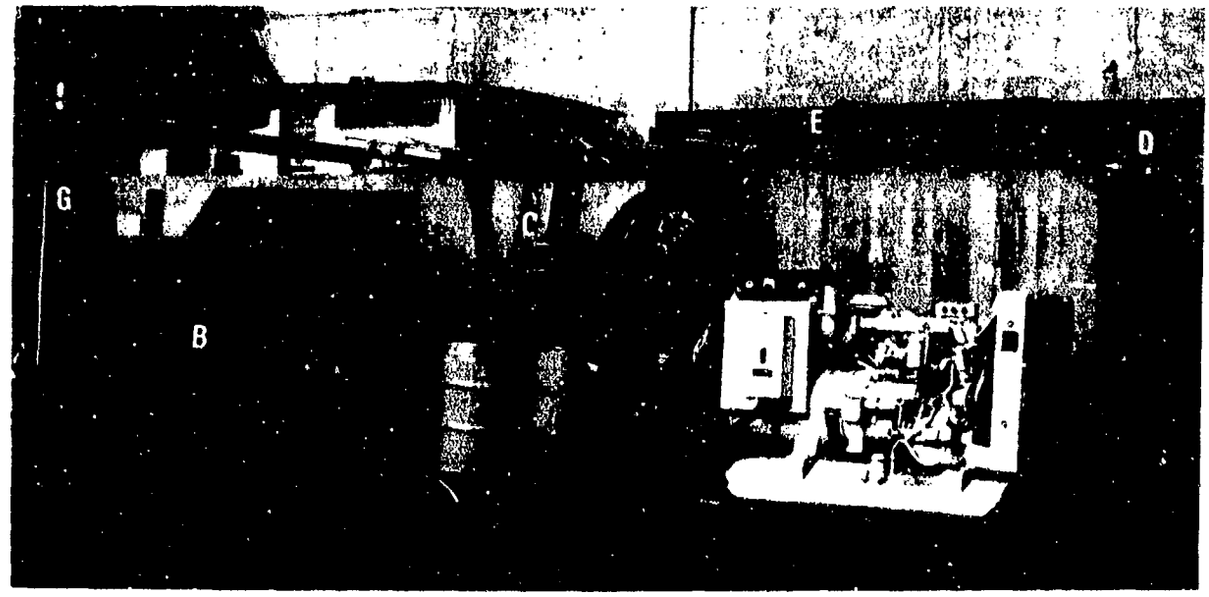

VIEW OF THE ELECTRON GUN INSTALLATION FROM OUTSIDE THE RADIATION ENCLOSURE. A and B are the diesel-electric generators for 220V 60 Hz and 440 Hz respectively; C are cables with 200 ft reserve length on the drums. D is a tarpaulin against sun and rain; E are support beams for the "sky-shine" radiation shield; I are periscopes to look over the wall into the radiation area and observe the cutting. The entrance is at G, through a sliding lead door.

FIG. 4.2-7

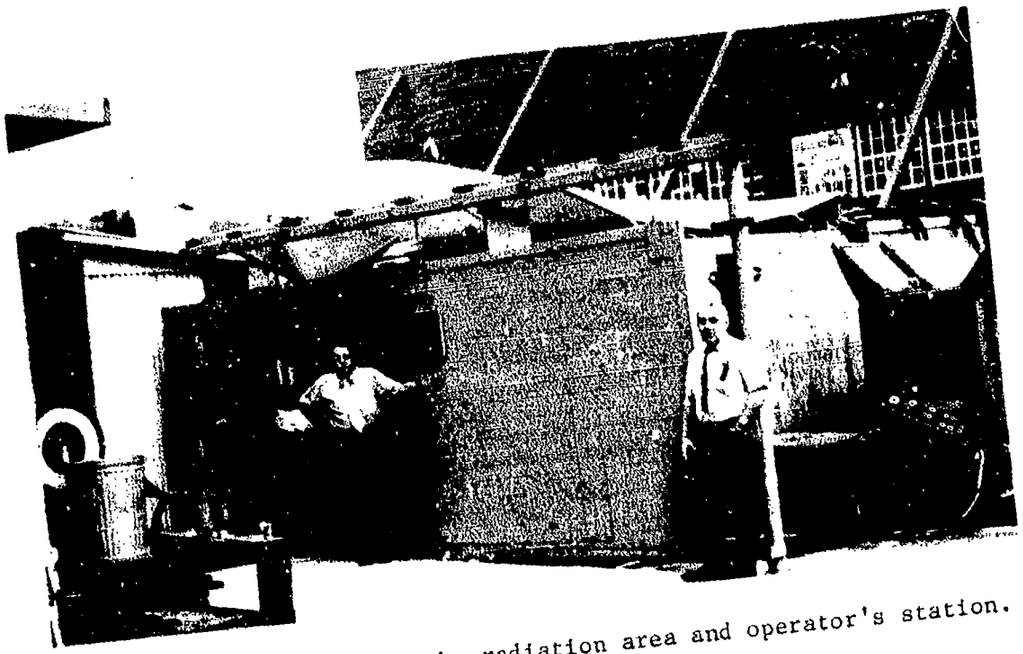

Fig. 4.2-8 Entrance to the radiation area and operator's station.

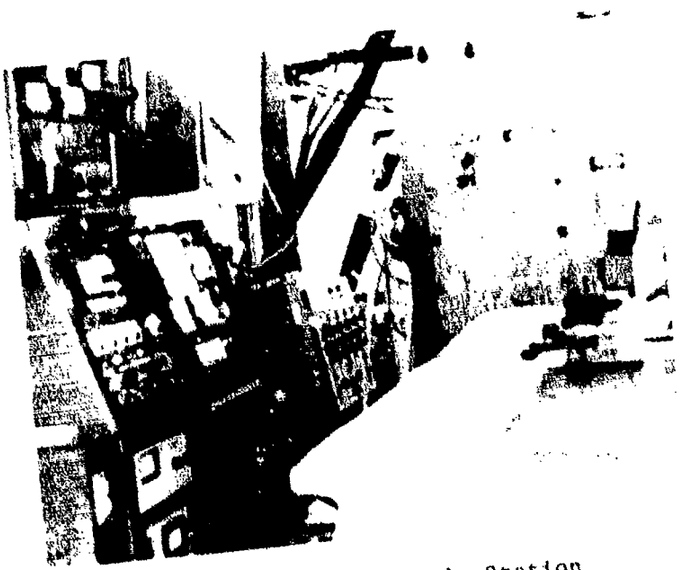

Fig. 4.2-9 Operator's Station

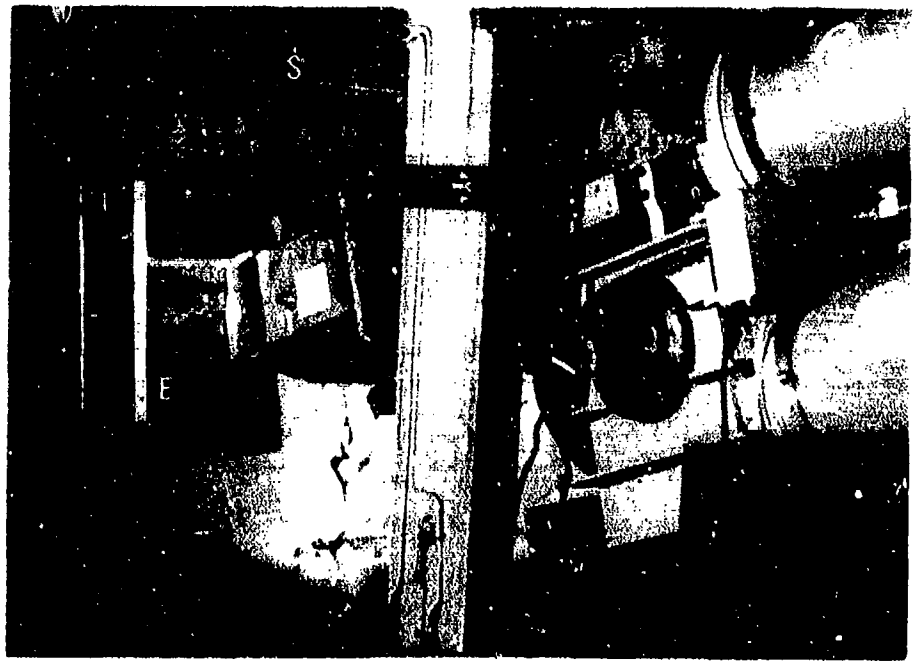

Fig. 4.2-10 Gun ready for action; the hinged lead panel E and the sky-shine-shields S intercept all primary x-rays coming from the cutting area.

In this situation, where the work area is open on top, it is necessary to block the direct x-rays from the target area by a lead panel which is hanging on the gun, as shown in Fig. 4.2-10, and by a sky-shine-shield consisting of an overhead lead panel and two side panels, all visible in Fig. 4.2-4 and 4.2-10. The suspension of the sky-shine-shield from overhead is shown in Fig. 4.2-11 whereas Fig. 4.2-12 shows how the test specimen, a 6 ft. cube of granite, can yet be turned by lifting it with an overhead crane. (Motorized crane driving up to the outside of the radiation enclosure).

To see the electron beam in action, it is necessary to have some simple mirror-periscopes to look over or around the x-ray shield. One such periscope is shown in Fig. 4.2-7. The very same type was provided at the operator's station. Fig. 4.2-13 shows what the operator can see through this device. Figure 4.2-14 shows the observation mirrors on the left of the x-ray shield.

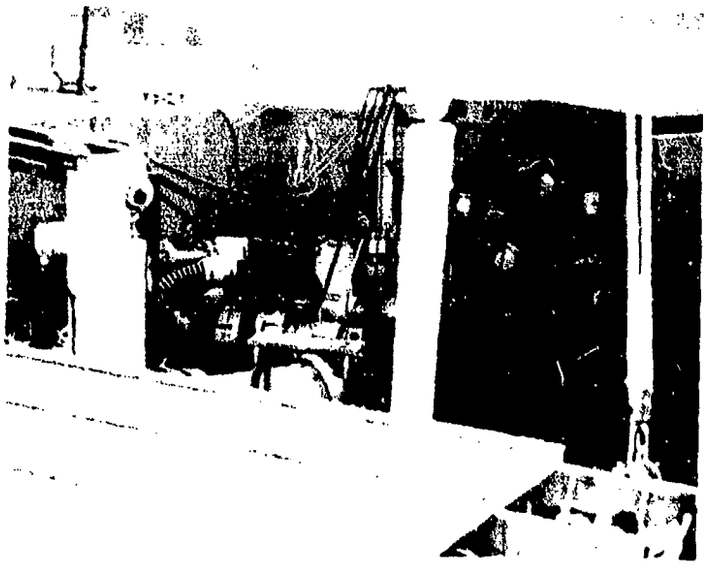

Fig. 4.2-11 Suspension of sky-shine-shield.

Fig. 4.2-12 The granite block is turned 90° to start working on the second face.

A telescope/periscope was projecting through a hole in the lead door, Fig. 4.2-15. It was not necessary to close this port with lead glass.

The 16 mm movie camera, used to record some of the tests, was housed in a lead box with a hole for the objective, and a mirror to bend the viewing direction by 90°. This was always sufficient to prevent x-ray exposure of the film. Figure 4.2-16 shows this camera.

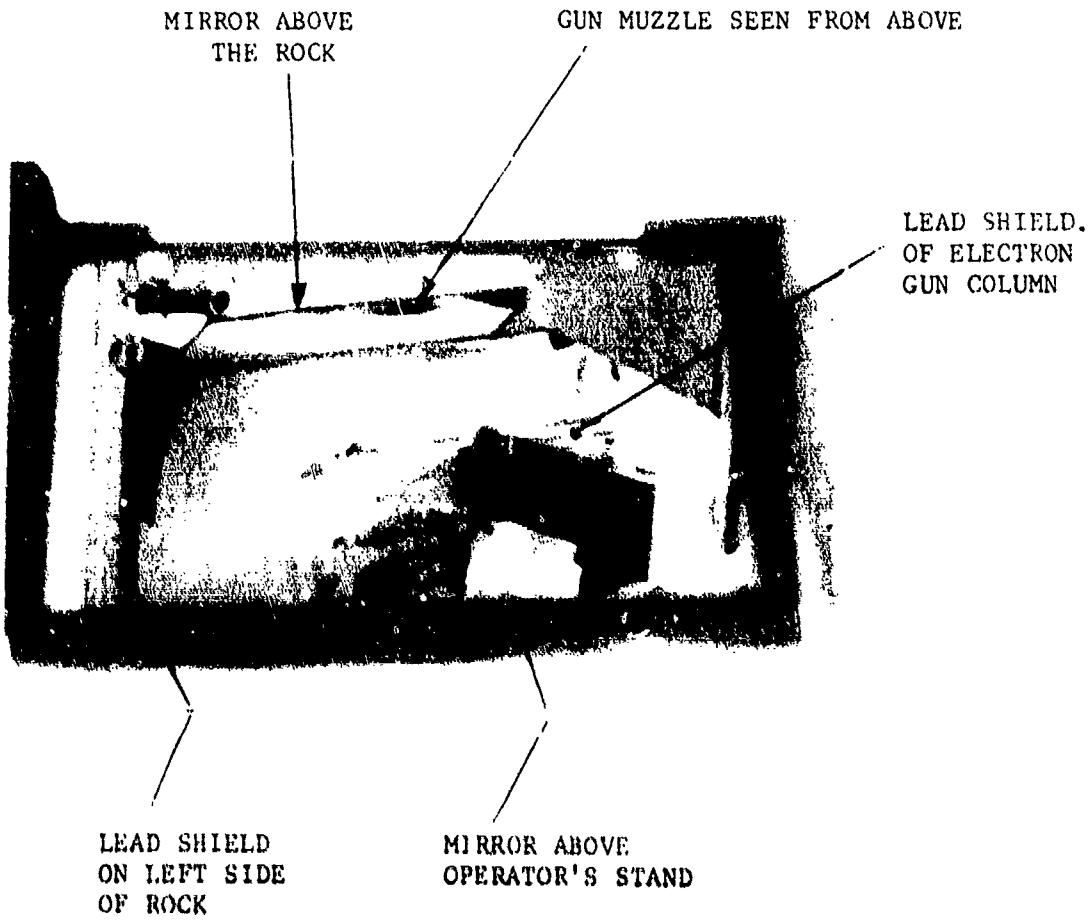

FIG. 4.2-13 Operator's view of gun and work area through overhead mirror periscope. The lead panel E of Figure 4.2-10 has been removed.

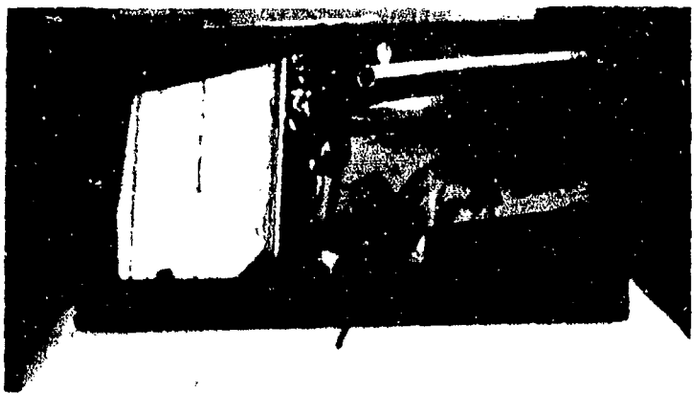

Cutting action as seen by operator through the overhead periscope and the mirror above the rock. This mirror was quickly covered by dust and became unusable.

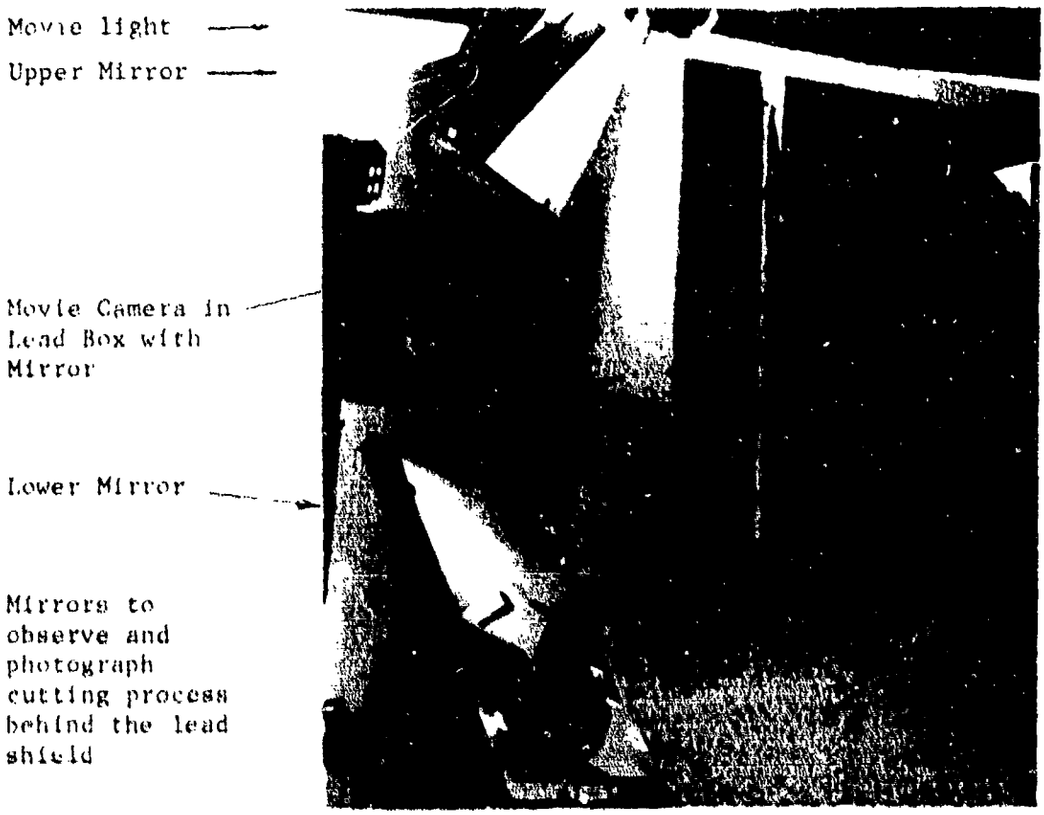

FIG. 4.2-14

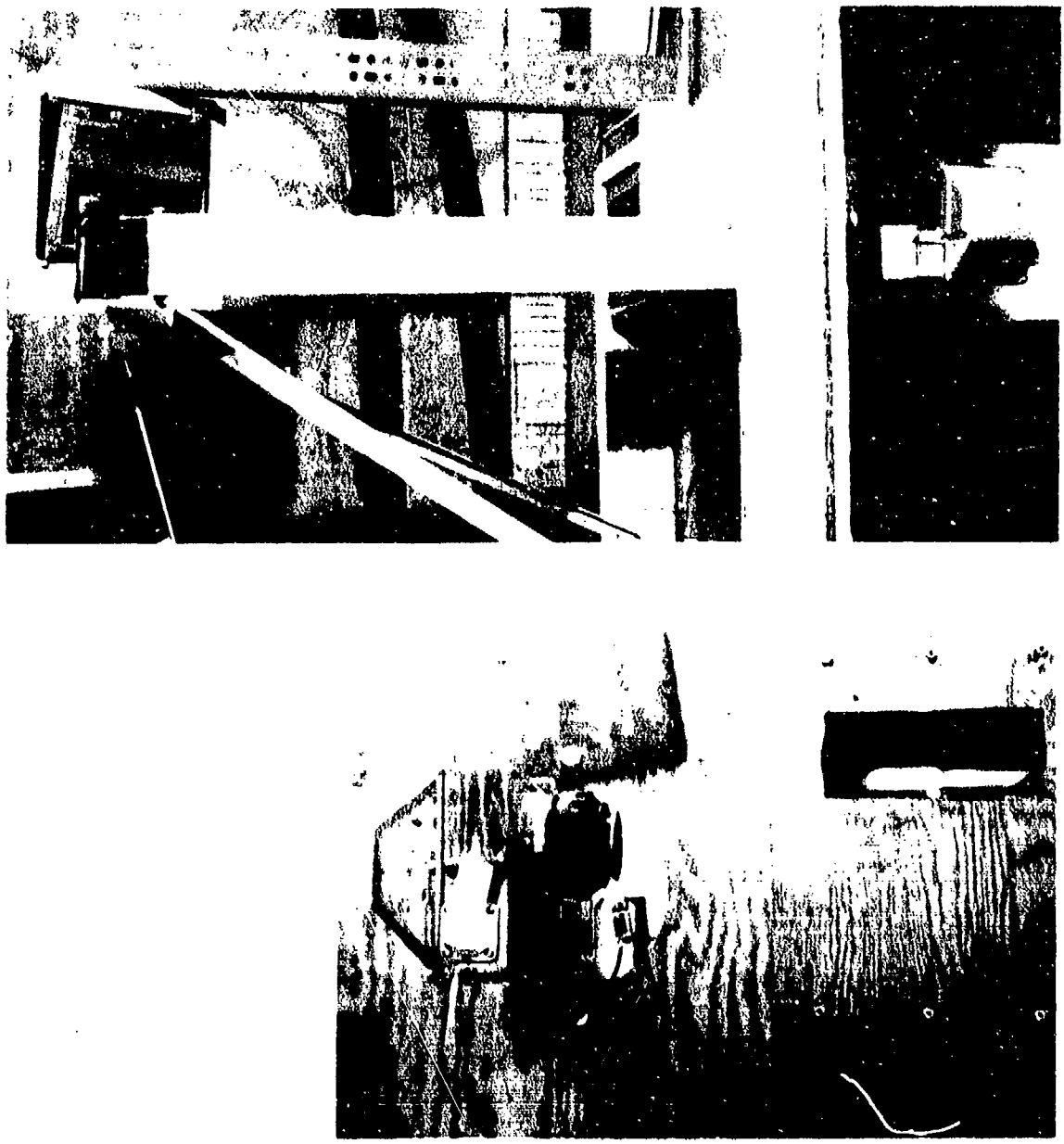

Fig. 4.2-15 Top: mirror with viewing port of the lead door, and telescopic periscope projecting through a hole in the lead door. Bottom: lead door from the outside.

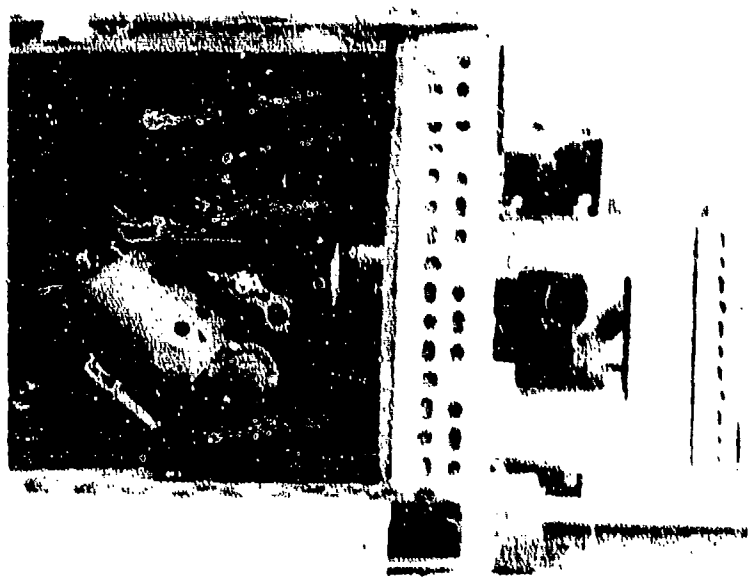

Fig. 4.2-16

Movie camera in its lead box (door open); on the right is the front surface mirror.

A SLR camera, frame size 18 x 36 mm, could be held against the eyepiece of the telescope/periscope shown in Fig. 4.2-15. It would record nearly the full field of view but not all details an observer could see, because of the limited quality of the mirrors which were used, and some vibration which was always present. The extreme brightness of the cutting area posed additional problems for the photography.

For future tests, a closed circuit TV-system should be acquired, which can be coupled to the moving gun.

Fig. 4.2-17 and 4.2-18 show what the operator could see through the telescope, which was, in fact, every detail of the cutting process. The photographs, for reasons already mentioned, did not always come out as well.

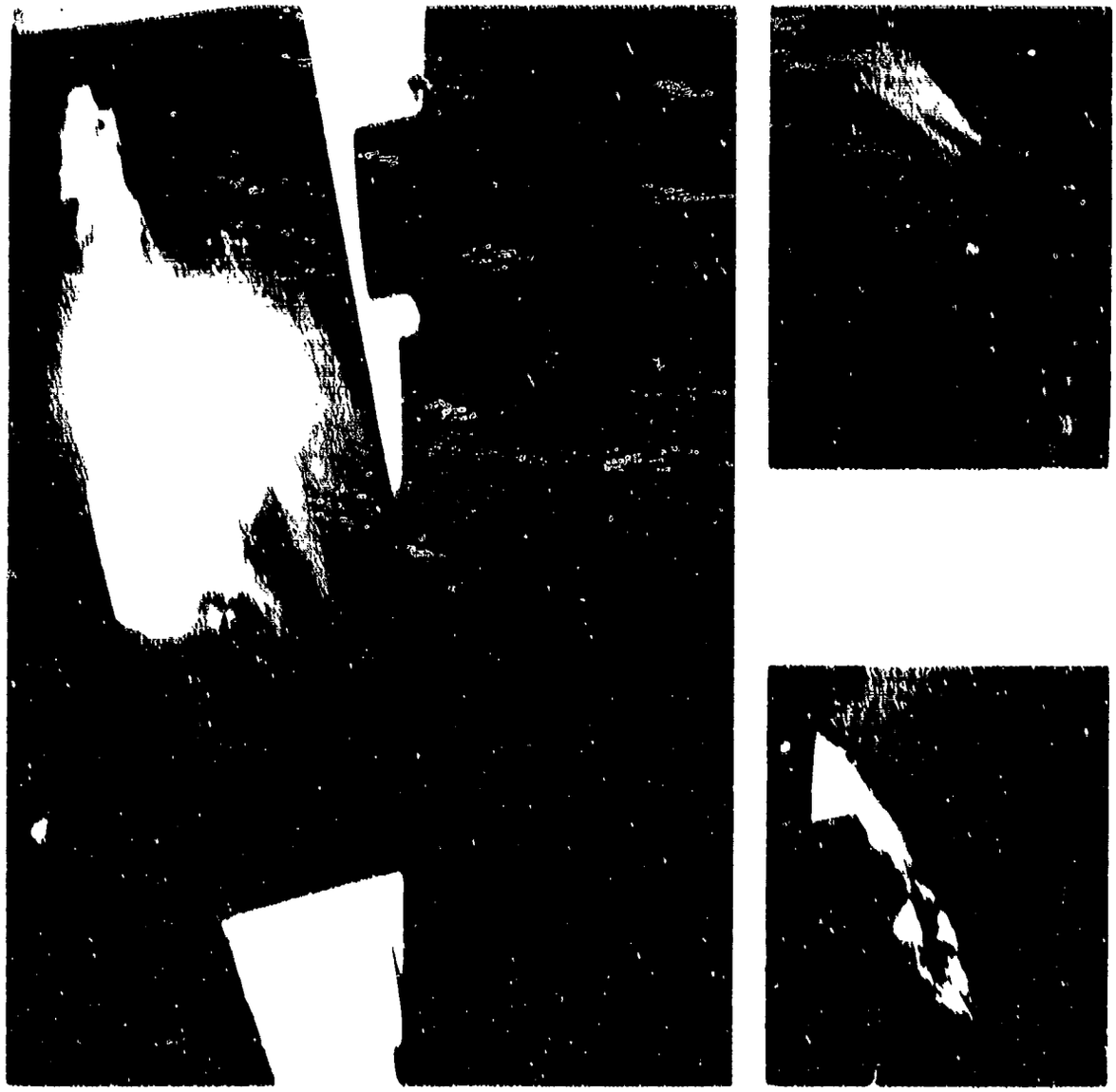

FIG. 4.2-17 View through the telescope-periscope in the lead door. On the left: cutting in progress; in the right hand corner a digital clock can be seen which identifies this picture. Top right: beam going into steel container. Lower right: another phase of the cutting process.

FIG. 4.2-18 A cut develops and is monitored through the telescope/periscope. The gun is moving away from the viewer. The digital clock shows 11:05:0, 11:06:0 and 11:07:0 as the time the pictures were taken (not readable in the reproduction). Vibrations and hot air schlieren limit quality of pictures. The gun is on the left and barely visible from this angle of view.

4.3 First Large Scale Tests on Semi-Infinite Rock Face

4.3.0 General Comments

The tests described in this section are not yet "field tests." Originally, they were meant to check out the machinery prior to going into the field. This was indeed accomplished and is reported in detail in Section 6.

The test specimen which was used in these tests was a 6 ft. cube of granite, larger than any test specimen which we had used before. In many respects it already represented a semi-infinite rock face to the beam, especially for the initial attack on such a face. We could even record collective effects, due to sequential piercing and cutting actions, clearly independent of specimen size. Yet such collective effects could not be tested on a large enough scale, because the limited size of the block precluded any cutting-out of ledges etc. of large enough size to take deliberate advantage of bulk effects and study the best strategy for large scale breakage. Some bulk effects were however, clearly demonstrated by large-scale cracking toward the edges of the 6 ft. cube.

It was unfortunate that this was the only big test specimen we had, because it was not a particular hard rock (only 20,000 psi), did not show particularly good stress propagation (it crumbled), and did not form a free flowing glassy melt. In short, it was not a type of rock which responded most favorably to the electron beam piercing and cracking process. It is all the more remarkable that the test proved the efficacy of the e.b. process under even those circumstances. There were indications that tests on a larger scale, on a larger rock mass, would have shown additional efficiency; in other words, the most favorable scaling relationships between, for instance, power input and breakage size have not yet been met in the present tests.

In the following the tests which we made are described not necessarily in chronological sequence, because initially we had to "get

the feel of things," before any more systematic experiments, could be planned. We also had to face the fact of very limited funds available for testing, and we wanted to do as many different tests as possible in a short time. In the following description everything about a particular kind of test is brought together in one sub-section, although the reported experiments were not necessarily done consecutively.

4.3.1 Granite Block Test Specimen

The granite block on which the following tests were made is called "Sierra White Granite", and it came from the same quarry at which later the field tests were to be made; details are discussed in Appendix B. Figure B-3 shows the site.

The following are data obtained from various sources which characterize this granite. The data of Tables 4.3-I and II were supplied by the Raymond Granite Co. The results of another set of tests, made by The Robbins Company are given in Table 4.3-III. There is a significant difference in the compressive strength measured by Raymond and by Robbins. The latter was aware of the data given by Raymond. The discrepancy may be due to a difference in the origin of the specimens or due to other factors. We did not ascertain which set of data more closely applies to the 6 ft. cube on which we made our tests.

Remarkable also is the considerable weakening of the compressive strength due to water, as revealed by the Raymond data. That this can occur is known, but apparently not fully understood.[29]

Another factor which may have much to do with the crumbling of the rock under heat (rather than melting) is the high content of CaO and K_2O in the analysis. Table 4.3-IV† shows some decomposition temperatures for $CaCO_3$ etc. which are of interest in this connection.

From thin sections we obtained the mineral analysis of the "Sierra White," and other samples which we used later, as shown in Table 4.3-V.

---

†Page 4.3-82.

The test block was an accurately sawed cube, fine grained, and uniform in the appearance of all its faces.

4.3.2 Reaction to Piercing

(a) Sierra White Granite

When the electron gun and the 6 ft. cube of granite were in position, and before any systematic test program could be formalized, we had to find out how this particular type of granite would behave under the electron beam, beginning with some piercing tests. The gun was positioned stationary in front of the fresh face of the granite block with .8" stand-off distance as shown in Fig. 4.3-1. A 16 kW beam was fired into the rock for a period of 6 minutes. As expected, the melt from this granite did not flow freely but accumulated between rock face and gun as shown. When the gun was removed, the melt and re-solidified material did not readily fall off but had to be broken out. The final hole which was left is shown in the same figure. The spontaneous breakage was minimal, only a surface layer of about 1/2" thickness lifted off on the base of that piercing hole. The piercing cavity as such was almost as wide as it was deep, namely, in each case about 3", which was thought quite unusual. Another peculiarity we noted was that the piercing cavity was hollow in an upward direction showing a cave or dome above the beam. The explanation for this we found only later.

We also noted that the walls of the piercing cavity were covered by a fine powdery dust, as we had found in laboratory experiments piercing limestone. (See Fig. 4.1-1e). Perhaps the rather high calcium content of this particular granite is responsible for it; but this is mere speculation. It was significant that the glassy melt, at least after it had resolidified, did not stick to and perhaps never had good contact with the walls of the cavity; and there were no fine local cracks in the wall of this cavity either. This was certainly different from what we have seen in other types of rock, even in some other types of granite.

INSPECTION

Lab. No.	70651
Mark	"Raymond"
Texture	Even
Grain	Fine
Color	Grayish White
Pyriten	Extremely small amount
Classification	Muscovite-biotite granite
Weathering	Probably very resistant

CHEMICAL ANALYSIS

Silica (SiO_2)	73.92%
Alumina (Al_2O_3)	14.90%
Ferric oxide (Fe_2O_3))	
Ferrous oxide (FeO))	1.95%
Titania (TiO_2)	0.14%
Manganese (MnO)	0.24%
Lime (CaO)	3.28%
Magnesia (MgO)	0.68%
Combined water (H_2O)	0.32%
Soda (Na_2O))	
Potash (K_2O))	4.51%

PHYSICAL PROPERTIES

Specific Gravity	2.64
Bulk Density (ASTM C97-47)	164.8 lb./ft.^{3}
Absorption (ASTM C97-74)	0.27%
Compressive Strength, Dry (ASTM C170-50)	34,800 psi
Compressive Strength, Wet (ASTM C170-50)	26,000 psi
Modulus of Rupture, Dry (ASTM C99-52)	2050 psi

Table 4.3-I: PROPERTIES OF SIERRA WHITE GRANITE

as determined by Raymond Granite Company, Raymond, California 93653

LABORATORY NO. 6-5351

IDENTIFICATION:	Sierra White		
BULK DENSITY: (ASTM C 97-47)			
Type of Specimens:	2" x 2" x 2" cubes		
Sample Number:	1	2	3
Bulk Specific Gravity:	2.64	2.65	2.64
Bulk Density (PCF):	164.6	165.2	164.6
Average Bulk Density (PCF)		164.8	
ABSORPTION: (ASTM 097-47)			
Type of Specimens:	2" x 2" x 2" cubes		
Sample Number:	1	2	3
Absorption (%):	0.27	0.27	0.26
Average Absorption (%):		0.27	
COMPRESSIVE STRENGTH: (ASTM 0170-50)			
Type of Specimens:	2" x 2" x 2" cubes		
Condition of Specimens:	Oven Dry		
Sample Number:	1	2	3
Compressive Strength (psi):	36,600	35,600	32,200
Average Compressive Strength (psi):		34,800	
COMPRESSIVE STRENGTH: (ASTM 0170-50)			
Type of Specimens:	2" x 2" x 2" cubes		
Condition at Test:	Immersed in water 48 hours		
Sample Number:	1	2	3
Compressive Strength (psi)	23,500	27,400	27,200
Average Compressive Strength (psi)		26,000	
MODULUS OF RUPTURE: (ASTM 099-52)			
Type of Specimens:	Approximate 4" x 8" x 2-1/4" prism		
Condition at Test:	Oven Dry		
Span Length:	7 inches		
Sample Number:	1	2	3
Modulus of Rupture (psi):	2060	2160	1920
Average Modulus of Rupture (psi):		2050	

Table 4.3-II: Details of tests by the Raymond Granite Company

Robbins Identification Number 671 DATE: Aug. 13, 1971

Location or Source of Rock United States, California, Raymond

Company Submitting Rock Westinghouse (Raymond Granite Company)

Rock Petrology Sierra White Granite / Muscovite-Biotite Granite

Specimen Identification	Bedding Orientation to Specimen Longitudinal Axis ▷	Specimen Dia. (in.)	Specimen Length (in.)	Ultimate Load (lbs.)	Ultimate Compression Strength (psi)
671 -1	15°	1.1	2.16	11,000	11,600
-2	10	1.1	2.16	18,000	19,000
-3	10	1.1	2.13	12,000	12,700
-4	15	1.1	2.24	16,500	17,400
-5	30	1.1	2.28	17,000	17,900
-6	30	1.1	2.18	15,000	15,800
-7	20	1.1	2.14	15,500	16,300
-8	20	1.1	2.23	21,500	22,600
-9	20	2.03	3.97	51.5	17,100

Abrasive Index: 3.7

Cutability/Wearability Index: Normal to Difficult/Moderate to High

Estimated Penetration Rate:

Comments: ▷ Principal Fracture Path

Table 4.3-III Properties as determined by The Robbins Company, 650 So. Orcas Street, Seattle, Washington 98108

Sierra White Granite	
Felspars (Soda and Potash)	55-60%
Quartz	30-35%
Micas (biotite and muscovite)	∿ 10%
Red Granite Sample	
Microcline felspar	∿ 60%
Quartz	∿ 33%
Biotite	∿ 5%
Dark opaque	∿ 2%
Black Diorite-Monzonite Sample	
Felspar (plagioclase ∿ 50% ortho-and microcline ∿ 20%) total	∿ 70%
	∿ 5%
Biotite and altered ferro-magnesia minerals	∿ 20%
Dark opaque	∿ 5%

Table 4.3-V: Mineral Composition of Test Samples (Estimates from thin sections, made at the Westinghouse Research Laboratories).

As mentioned before, to get any efficiency in this thermal stress cracking mode, one has to watch certain scaling parameters which depend upon the properties of the particular rock. We therefore increased the piercing time, firing the beam into a second spot about 6" away from the first piercing cavity but appearing still fresh and unaffected by the previous shot. Piercing time was 5 minutes. Immediatly after switching off the beam we pulled back the gun and the still molten and partly resolidified rock which stuck to the end plate of the electron gun was pulled out of the hole as shown in Fig. 4.3-2. The red hot rock, still being plastic, was partly pulled apart and the volume and size of the parts which were extracted appear larger than the cavity.

First piercing test on the "Sierra White" granite block. The melt shows extreme tackiness; with the cavity being wider at the bottom the re-solidified melt must be broken out by force. Only shallow stress cracks have developed.

Fig. 4.3-1

Melt can be withdrawn from the piercing cavity if the gun is pulled back before the melt has fully solidified; the interior is still white hot.

Fig. 4.3-2

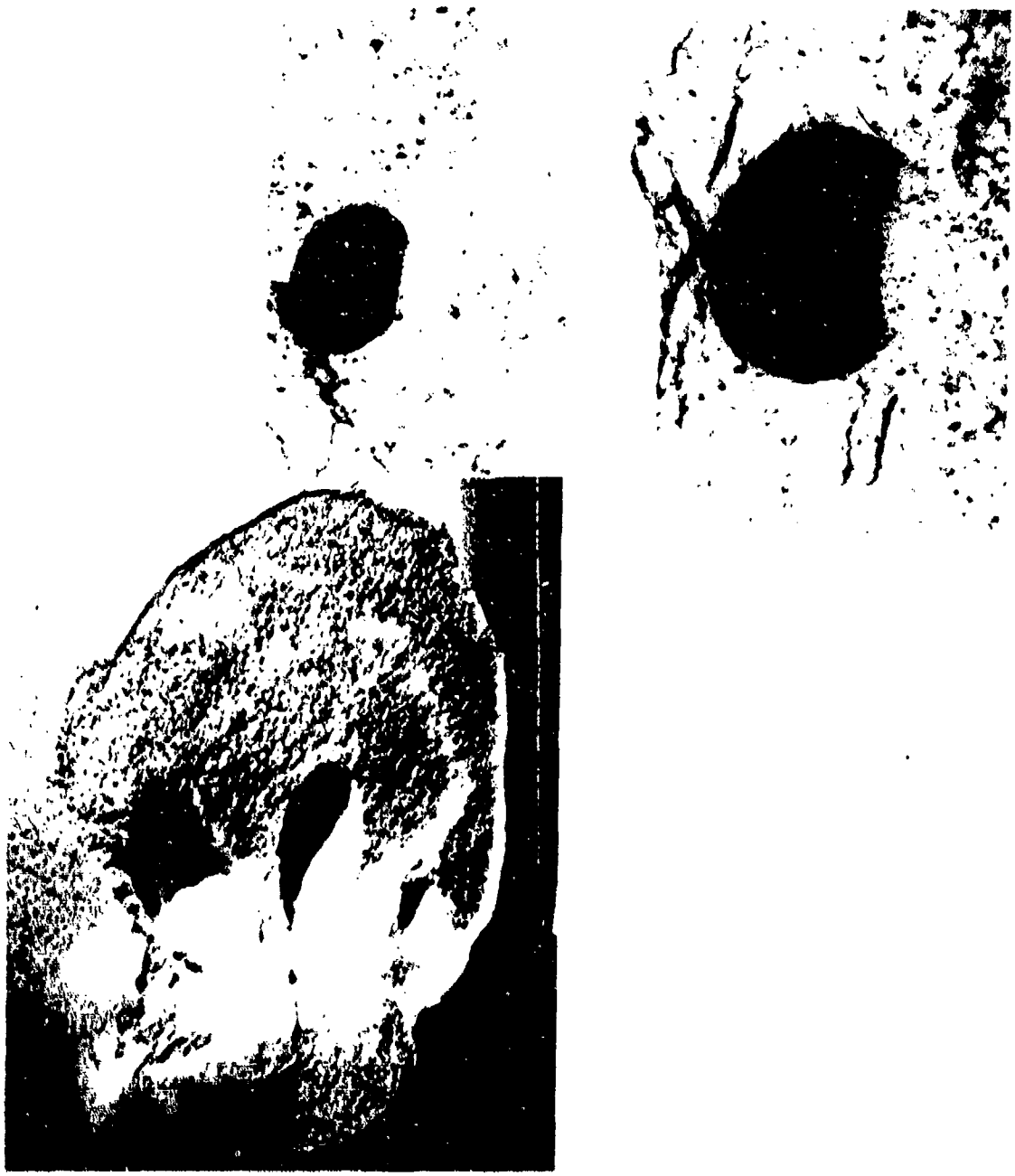

Several additional piercing shots prove that the nearly semi-spherical shape, somewhat higher on top, is typical for this granite. Shallow stress cracking over a one square foot area (lower picture) was first noticed because it sounded hollow when hit with a hammer, but it did not fall down spontaneously since it was held firmly along its perimeter.

Fig. 4.3-3

One can see from Figs. 4.3-2 that the hot melt has accumulated at the bottom and there is a hollow cavity above the plane of the beam. The cavity left in the rock again showed the hollow dome towards the top.

Because of the longer piercing time the cavity, as one would expect, was deeper namely, 5" at its deepest point. This was surprisingly shallow for the piercing time which we had applied here. In other rocks, like norite, we have produced cavities of 6.5" in depth and more, with this power input. It was also surprising, that although the two piercing cavities were close, there was no breakage in the wall which was left standing between them and which had a thickness of about 1-1/2".

A third cavity was pierced, once more 6" from the second one, but near the first one. After 4 1/2 minutes of piercing the debris was removed.

The depth obtained in this piercing shot was only 3.7" which was again surprisingly shallow. The dome on top of the actual beam axis was again very pronounced.

While surface breaking seemed minimal, we noticed by knocking at the rock face with a hammer, that a large hollow area existed. Prying loose whatever was hollow resulted in the breakage pattern shown in Fig. 4.3-3. Obviously the thermal stresses had lifted a slab of about 1-1/2 ft. in diameter, but only about 1/2" thick. There were scaling laws at work, but it was not obvious what the significant factors were. In some further piercing tests we found always the same behavior. When the melt was left in the cavity, to cool, and then pulled out, it had typically the appearance shown in Fig. 4.3-4, where the photograph on top represents a plan-view of the re-solidified melt, and the drawing below is a side-view cross section through the cavity. That part of the mass which is labeled "conglomerate" did not look as if it has been really melted, only the glassy top surface looked like a solidified melt. Insofar as the electron gun blocked the flow, the hot vapors which

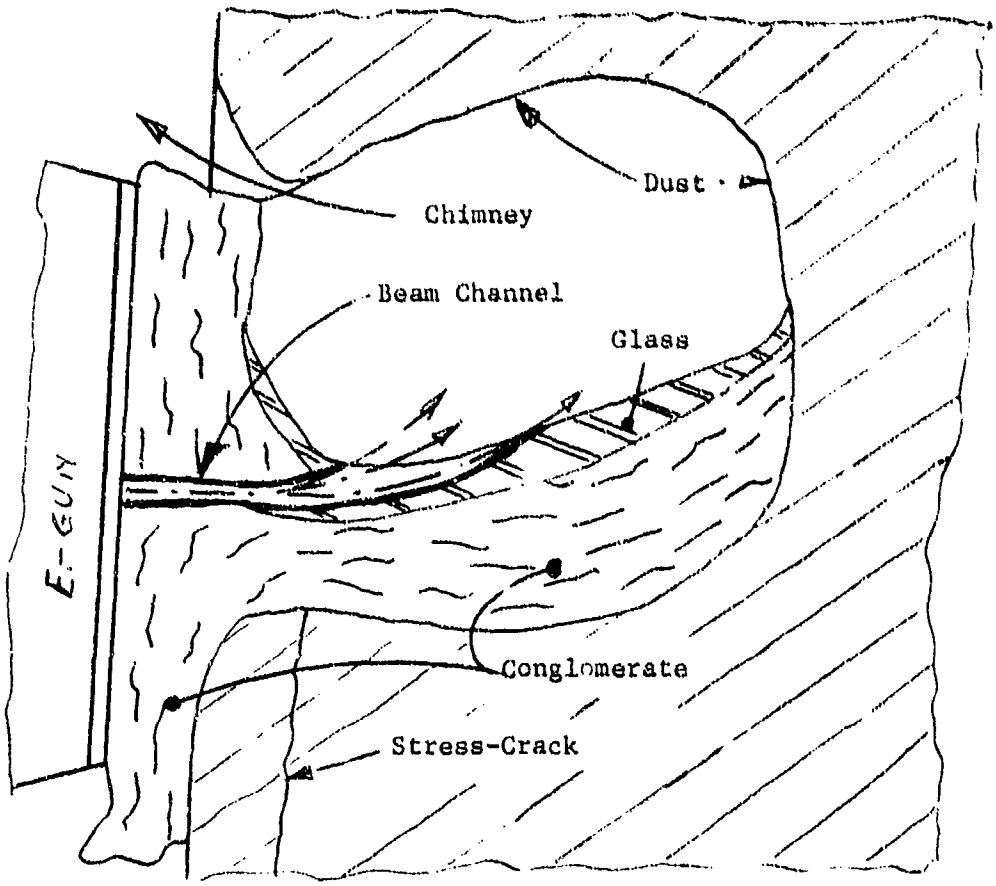

Re-solidified melt from a piercing cavity and typical cross section through the cavity.

Fig. 4.3-4

Fig. 4.3-5, left:

Piercing with a stationary beam. The melt is not flowing freely and is resolidifying between the front plate of the gun and the rock. The photograph was taken through the periscopic telescope while the piercing was in progress.

Below:

Look into the piercing cavity shortly after the gun was withdrawn. The cavity is hollow on top. On the bottom is a pool of viscous liquid rock, still bubbling, which will solidify into a glass.

were formed produced a "chimney" above the upper edge of the gun face; this is particularly evident from the later picture in Fig. 4.3-51. Also from a later test, but relevant to this discussion of piercing behavior, is Fig. 4.3-53; withdrawing the gun carefully one could look through the beam entrance hole into the cavity at the surface of the still liquid lava.

The explanation for the shape of the piercing hole, -- in particular its low depth-to-width ratio and the limited depth in spite of continued power input, -- was only found much later in connection with the spalling tests described in Section 4.3.5. What seems to happen is as follows: The beam penetrates to a depth of 3 to 4 inches by melting and vaporization in a yet rather narrow channel (1 to 1-1/2" diameter); but from then on scattered electrons and radiant heat reach the walls and especially the top of the channel, -- and now the peculiar nature of this rock comes into play, -- -- -- the rock begins to spall and the flakes fall down. Some spalling flakes cross the path of the electron beam and get melted; this scatters the beam even more toward the walls, and it absorbs energy which otherwise would have gone to the far face of the cavity. Other spalling flakes, which don't get melted but simply drop into the existing melt at the bottom of the cavity, form what was called the "conglomerate." We believe this successive spalling is the explanation for the formation of the "dome" of the cavity far above the plane of the beam itself.

The spalling and crumbling of this rock under the heat, and perhaps a chemical decomposition prior to melting, also explains why the piercing holes were never lined with glass, and why the re-solidified melt never stuck to the solid rock but that there was a powdery interface; the walls of all holes and cavities were always covered with a fine white dust (the later Fig. 4.3-52 shows this particularly well).

From the description of the piercing process it is obvious that there cannot be a particularly good flow of heat from the cavity into the solid rock. This would explain why we did not see the local

Top, left and right: A longer piercing shot has led to thermal stress cracking; bottom: the series of piercing holes after the breakage and debris has been removed.

Fig. 4.3-6

Piercing depth as function of time was determined in a series of shots. Except for the shortest times the holes were partly filled with debris, which could be withdrawn with the gun as long as it was still hot, as shown here.

Fig. 4.3-7

breakage which we had found for instance on the granite shown in Fig. 4.1-3a.

In order to make sure that what we had observed was due to the behavior of the rock and not to perhaps differences in the electron beam, i.e. difference in power density, we decided to make a quick series of short time piercing test in the Sierra White granite and in some other types of rock which had behaved differently in the past. Fig. 4.3-6 shows a series of piercing holes in the Sierra white made with increasing time. The depths of these holes as a function of time is given in the graph of Fig. 4.3-14. The initial piercing rate was nearly as good as expected. If early in the piercing the power input was stopped, and the gun withdrawn, one could withdraw a melt core which showed a fair depth-to-width ratio. An example is shown in Fig. 4.3-7. Widening of the cavity to nearly hemispherical shape or even higher than it was wide would begin only later. This raised the question of scaling laws once more. It was thought that one perhaps should keep the piercing short but apply multiple piercing shots in a closed spaced row. Such a row of holes is shown in Fig. 4.3-8 but they did not produce any collective kind of cracking.

(b) Other Types of Rock

To ascertain once more that the electron beam was not any different than in earlier tests, we included other types of rock in this present series, Fig. 4.3-9 shows a piercing hole in a quartzite plate. It is narrow and deep just as expected, hence showing that the behavior of the electron beam was not different from what we had seen before. Fig. 4.3-10 shows a series of piercing holes made in a black gabbro which we acquired from a local monument shop (origin unknown)*.

*Later analysis showed it to be rather a diorite/monzonite; see Table 4.3-V.

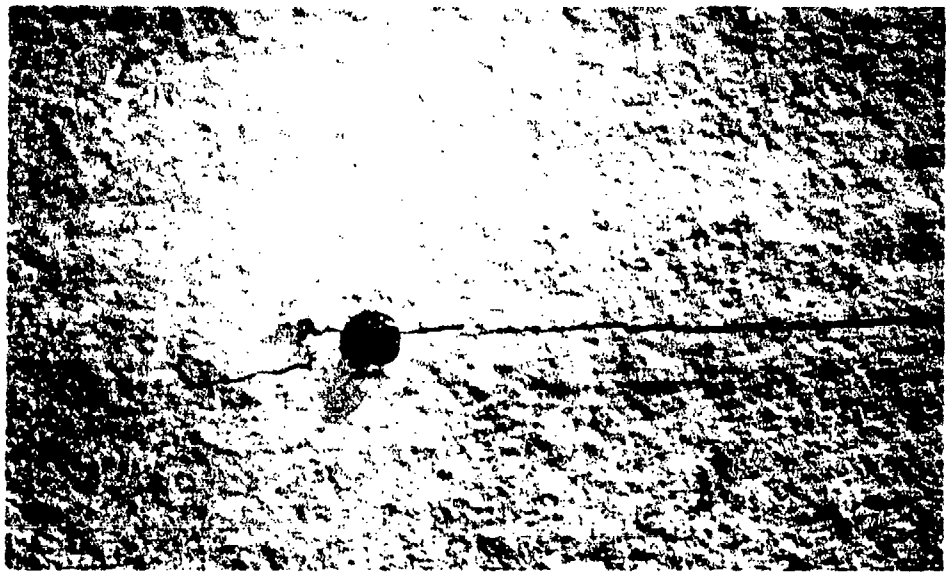

In a plate of quartzite, 1" thick, a short piercing shot produces a needle thin hole of .1" diameter, but nevertheless a crack as well. Note the lighter colored area above the hole; this is a white dust of silica on the otherwise yellowish plate.

Fig. 4.3-8

Row of piercing holes in the "Sierra White" granite does not produce any "collective" cracks.

Fig. 4.3-9

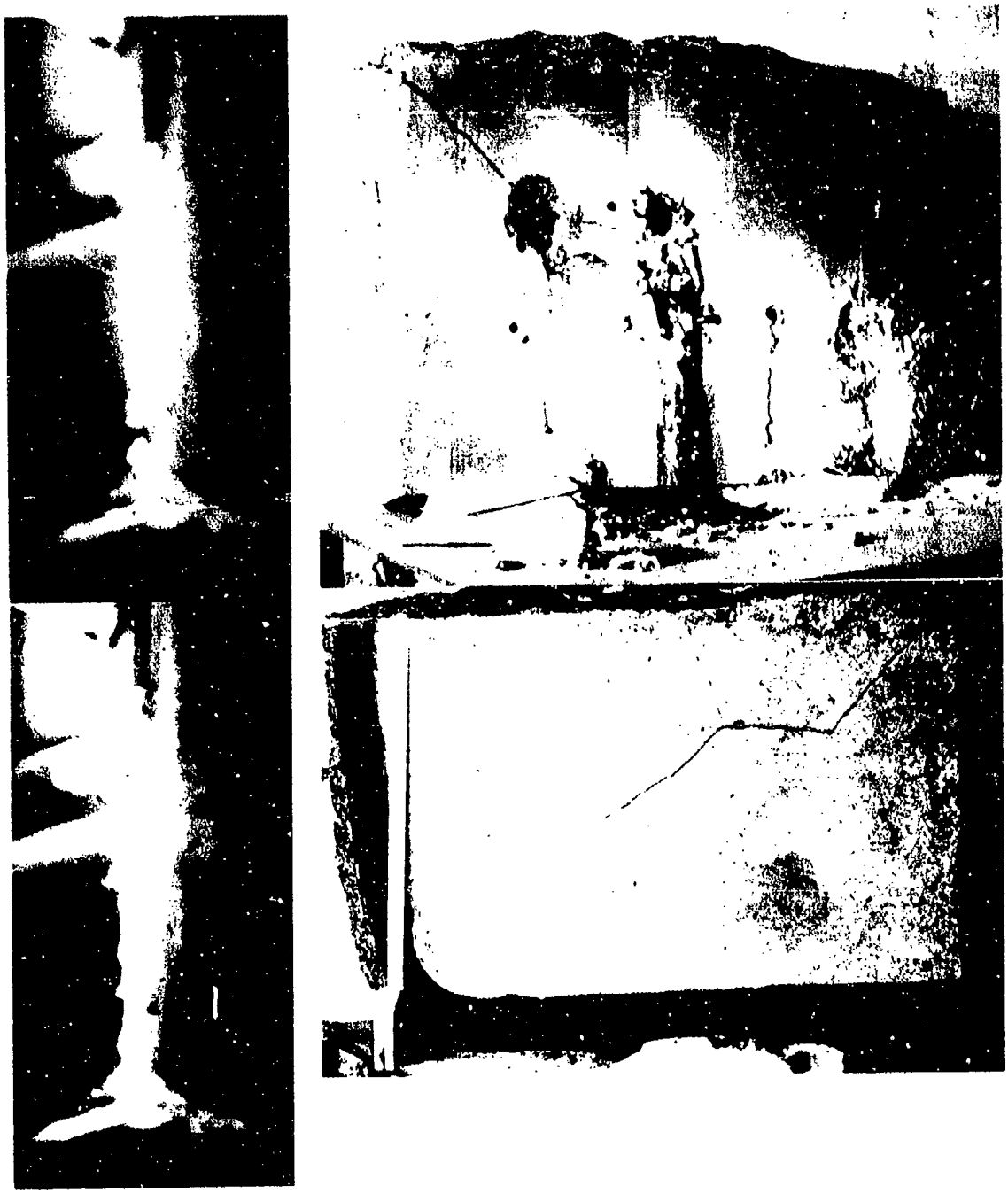

For comparison piercing tests were made in this block of black gabbro. On the left the easy flow of the watery melt. Top right, breakage due to the longer duration shots although they did not penetrate the 5.5 inch thick block, as the rear view (lower right) shows.

Fig. 4.3-10

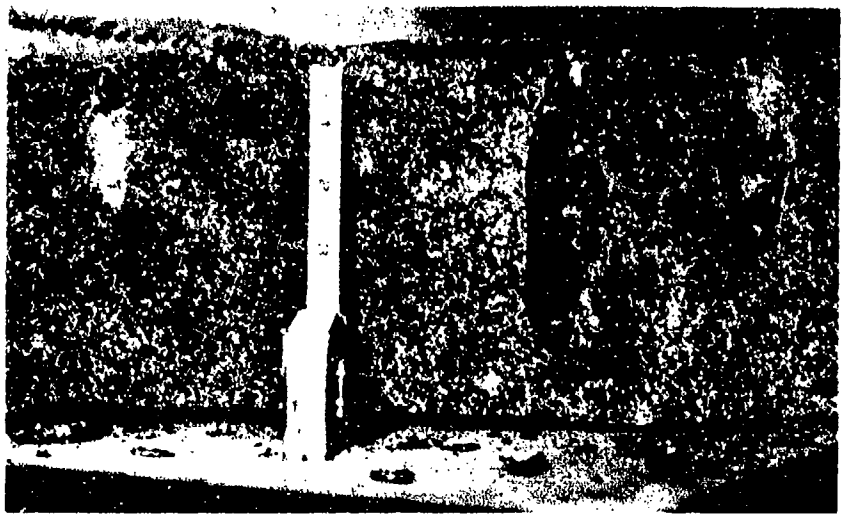

Shape of the piercing cavities in the black gabbro of the previous picture.

Fig.4.3-11

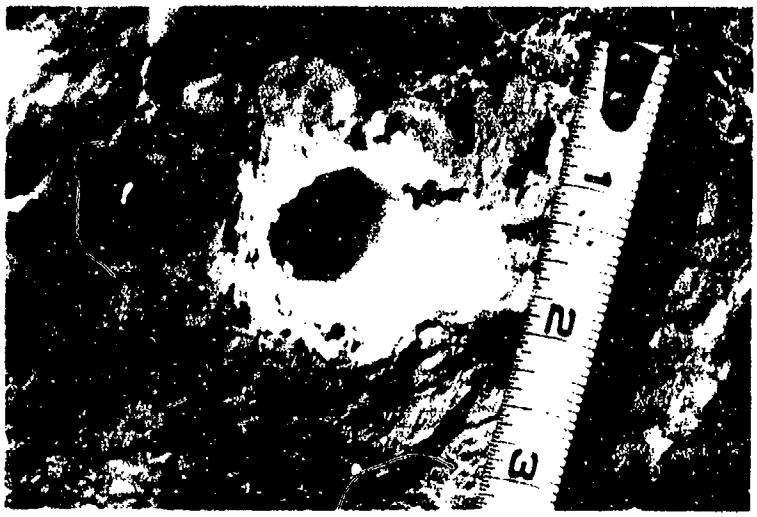

Glass-lined piercing hole in a boulder of quartz breccia.

Fig. 4.3-12

The melt flowed freely as we had observed before on this type of rock. The piercing holes were deep and narrow and led to stress cracking, as expected. Fig. 4.3-11 shows the shape of the holes and the fact that the glossy melt stuck to the wall and split when the block split.

The glass lined piercing hole which was obtained in a quartz-breccia is shown in Fig. 4.3-12. In Fig. 4.3-13 we show piercing holes made in a red granite which was also obtained locally. In this case the melt did not flow quite freely but stuck to the gun, as also shown in

Fig. 4.3-13

For comparison a slab of a red granite was pierced; on top: a short shot leaves a clean hole; below: longer piercing leads to cracking and debris will stick to the gun.

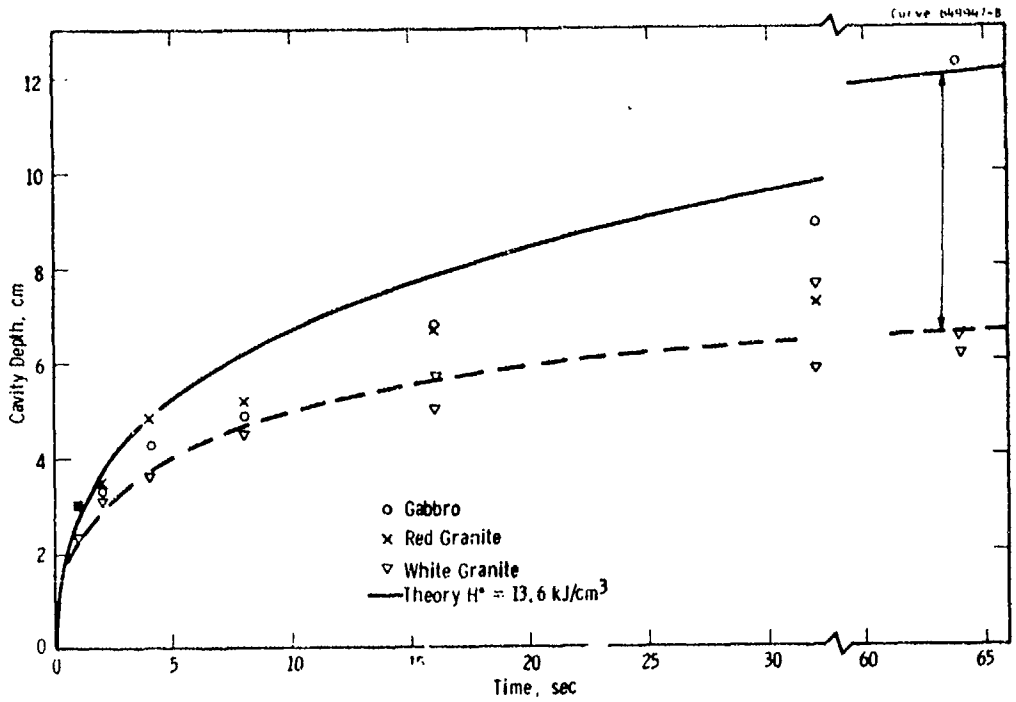

Fig. 4.3-14 Measured growth of cavity with time for several types of rock, from tests made with the horizontal beam of the electron beam rock cutter piercing into the body of the sample. (Beam power 15.9 kW @ 156 keV; standoff, 1/2 in.) The white Raymond granite falls consistently short of the theoretical curve (see Section 5) being a factor of 2 lower than predicted at 64 sec. The gabbro also tends to be somewhat below the curve but is still in agreement with the theory at the 64 sec point. The red granite performs as well as the gabbro for at least as long as 15 sec.

the photograph. Nevertheless piercing holes showed a large depth-to-width ratio and a glass lined wall.

A comparison of all these results with the theory which was previously developed is shown in the graph of Fig. 4.3-14. The behavior of th Sierra White granite shows similarities to the behavior of the calcaceous sandstone of Fig. 5-3.

(c) Discussion

Again the question of optimum strategy and scaling laws arises. One may think of somehow taking full advantage only of the initial rapid piercing rate. In the last analysis this would lead one to the spall-cut mode of cutting. Before rendering any judgment we should, however, look at the radically different approach of simply higher energy input either from much longer piercing times or from a higher power beam. Some remarkable results with longer piercing are discussed in Section 4.3.4. In connection with this approach of dumping more power into one spot one can argue that the details of the power input don't matter, if only enough power (on a large enough scale) is quickly enough poured into a volume of solid rock, so as to produce differential thermal expansions. If this heat source is located as a "cavity" eight inches below the surface and an energy flux of 16 kW or more can be maintained, we have very favorable conditions, whether the cavity is 4" or 8" in diameter does not matter as much, although the highest depth to width ratio is still something one should aim for. Going to higher beam power via higher voltage would be a first step in this direction, as Fig. 5-6 clearly suggests.

4.3.3 Reaction of the Sierra White Granite to Melt-Cuts

Again we want to stress that the experiments reported in this section were made to gain an initial understanding about the interaction of the electron beam with this particular rock, and not to get very accurate data about one or the other mode of interaction.

(a) The first horizontal melt cut which was made with the rather high speed of 48 IPM going from left to right is shown in Fig. 4.3-15. The standoff distance varied from 1" at the left to 3/8" at the right because the carriage for the electron gun and the face of the rock were not quite parallel. With a beam power of 15.4 kW, a melt depth of 1/2" was achieved. This is less than one might expect from extrapolation of the curve of Fig. 4.1-3. However, these curves refer to a smaller standoff of 1/2", and the density of the concrete was lower than the density of the present test specimen.

Some additional cuts at similar speeds were made adjacent to the first one, and also some multiple cuts going over the same trace several times. The results are shown in Fig. 4.3-16. As we found to our regret, the electron beam carriage did not traverse the gun smoothly enough so as to get a cutting action at these high speeds which would resemble those of some spall cuts once made in the laboratory. As a look at the figure shows, the cuts show a rather regular pattern of "stitching", which came about by oscillations of the electron gun and/or an irregular pull of the chain drive. The pitch of the "stitches" which one can see is identical to the pitch of the links of the chain drive. We decided to give up further attempts at high speed melt or spall-cutting.

(b) A slower cut with 2 IPM at a beam power of 16 kW and a standoff distance of .7" produced a 2" deep triangular trench which is shown in Fig. 4.3-17 after the debris had been removed. This figure also shows how the standoff distance was measured and is recorded here, namely from the rock face to the front plate of the gun, yet the beam exit nozzle is another .1" behind this front plate. The beam is also pointed 15° downward and does not penetrate the rock face perpendicularly. This was the result of limitations in the carriage movement which did not permit us to reach every one point on the test specimen and keep the beam perpendicular to the face at the same time.

(c) The first attempt at a slow but deep horizontal melt-cut is shown in Fig. 4.3-18. At a speed of 2 IPM, 16 kW beam power, and 3/4"

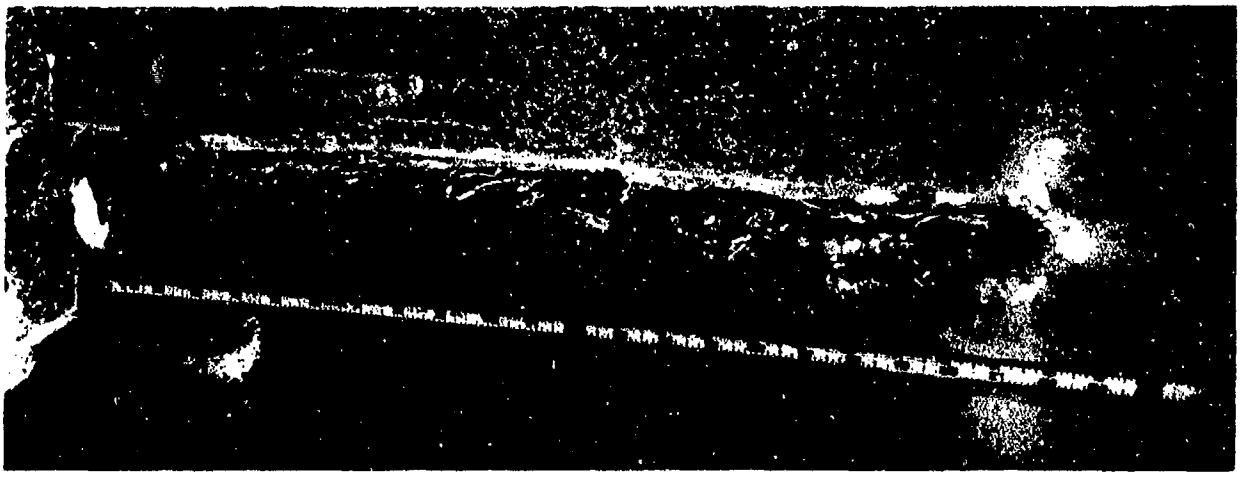

Fig. 4.3-15 Fast melt cut in the "Sierra White" granite with 15.4 kW, 1" standoff at left, 3/8" at right, speed 48 IPM left to right; melt-depth 1/2".

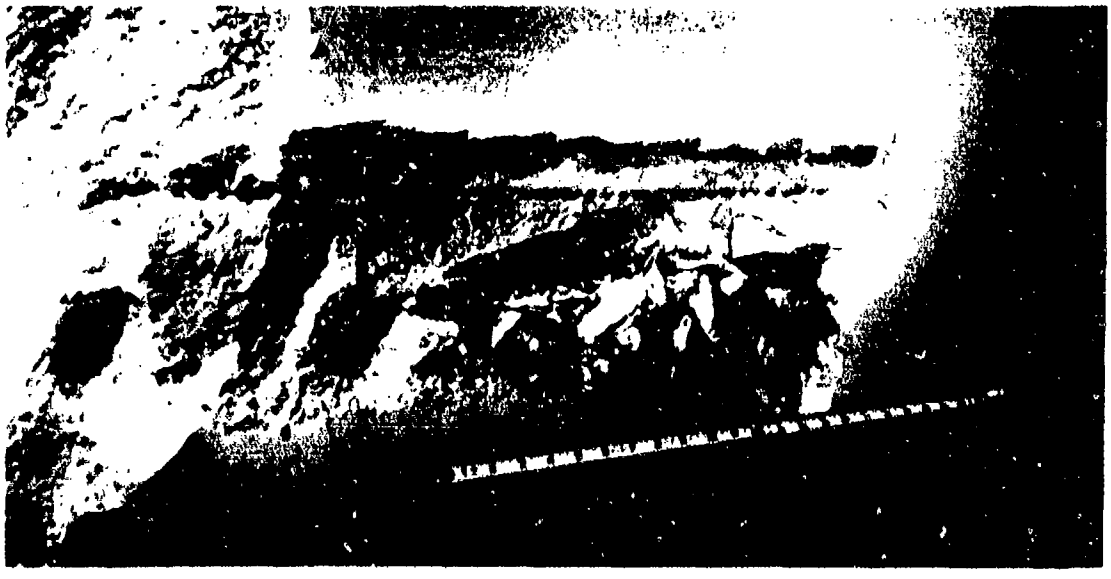

Fig. 4.3-16 Subsequent cuts at similar speeds as the first one; also multiple runs over the same path; top trace is the same as in the previous figure.

standoff distance the depth of 2" was reached; serious cracks appeared at both sides of the cut. Most remarkable was the way the debris behaved: already with the cutting in progress we could observe it to coil in a most bizarre fashion, as shown in Fig. 4.3-18 in the left photograph. The molten rock, and the spalling flakes which were imbedded in it formed a plastic mass and did not break off. The right photograph in Fig. 4.3-18 shows the coiled-up debris after the gun and the beam had been stopped, but the gun had not yet been withdrawn, giving some support to the debris. Note that the left picture in Fig. 4.3-18 is taken through a mirror, and is therefore the mirror image

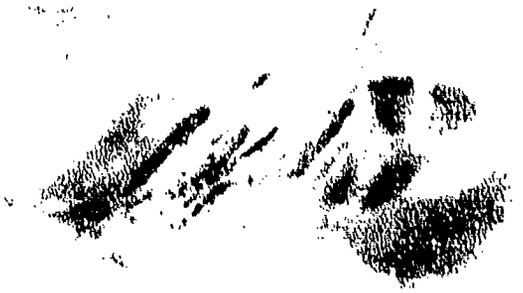

Fig. 4.3-17

Slow run at 10 kW - 1PM, at .7" standoff has produced 2" deep triangular trench (after melt was removed); second run over this trench increased depth to 3.2".

Note how standoff is measured; beam direction is pointed 15° downward.

of the picture on the right.

When the gun was withdrawn from the rock face, some of the debris broke off, but some still hung from the groove as shown in Fig. 4.3-19a. Photographs b and c show the subsequent removal of the parts loosened by thermal stress cracking.

Without changing the stand off distance of the gun from the original rock face, a second cut was made with the same speed and power over the cleaned up groove. The starting point was somewhat to the right of the beginning of the original groove; then, since the gun was left on for a predetermined time rather than for travelling a predetermined distance, the second run overshot the first groove by a few inches. This gave us the chance to compare the depth of a subsequent cut with that of the first cut, with identical beam parameters and travelling speed. The results are shown in Fig. 4.3-20. The additional melt-depth achieved in the second cut was 1.5". The depths of the overrun (single cut with 3/4" standoff) was again 2", as shown in Fig. 4.3-21.

Several additional runs under similar conditions did not produce any new results. We noticed, that just as in the case of piercing, if the gun was withdrawn at the right moment the melt would stick to it. Near the termination of the cut the debris would still be red hot; Fig. 4.3-22 shows a photograph which was taken through a red filter to enhance the red glow of the still incandescent melt. This molten rock does not damage the gun in any way. One can avoid the sticking of the melt to the gun and let it sit in the melt-trench as also shown in Fig. 4.3-22. Of course, the red hot debris may drop to the floor, and if something there can be ignited it may start a fire; some caution must be exercised.

(d) The appearance of the first face of the 6 ft. cube, after these initial tests is shown in Fig. 4.3-23. At this time we decided to make some of the systematic piercing tests which were already

Fig. 4.3-18 Slow horizontal melt cut at 2 IPM, 16 kW, 3/4" standoff. On the left the cutting is observed through the mirror periscope, the gun is moving away from the viewer. Below: the cut is completed, the gun is still in the cutting position, the semi-plastic debris has coiled up in a bizarre fashion but did not break.

(a)

(b)

(c)

Fig. 4.3-19 Removal of the debris from the melt-out shown in the previous figure. (a) Part of the coiled-up debris is still hanging from the groove. (b) Lower parts which cracked due to thermal stresses are partly removed. (c) Removal of upper parts cracked by thermal stresses; the crack-line is clearly visible in (b) above the yardstick.

(a)

(b)

(c)

Fig. 4.3-20 Second run over the groove from the previous figure. Starting point is not quite at the beginning (on the left) of the old groove, and termination lies beyond the old groove (on the right). The depth of this overrun is shown in the following figure.

reported in section 4.3.2. The location where these piercing shots were made is shown in Fig. 4.3-23 by the letters A and B. Thereafter we decided to make a melt cut with multiple passes, and to throw much more energy into the same linear trace than we had done before. The approximate location for this experiment is shown by the letters CC in Fig. 4.3-23. The beam was on for 12 minutes when a crack occurred breaking out a triangular prism which was later found to weigh 30 kg. This break and the removal of the debris is shown in Fig. 4.3-24.

The breakage associated with this melt-cut is of course not as informative as we would like it to be, since again the specimen size is obviously a factor influencing the breakage. On the other hand, we can see from the picture that the cracks did not run out to the right and left until they reached the end of the 6 ft. cube. Hence this breakage towards the top edge of the cube corresponds to a breakage which we could expect if we had previously cut a ledge into a larger rock face.

Fig. 4.3-21 This is the depth and profile of a single-pass melt-cut with 16 kW and 3/4" standoff (154 kV beam), at 2 inches per minute. It is actually the over-run section of the double pass shown in the previous figure.

Fig. 4.3-22 Top: Debris from a horizontal melt-cut sticks to the gun when the gun is carefully withdrawn at the right moment; the last section of the debris is still red-hot as shown here in the left photograph made through a red light filter. Bottom: Sticking of the debris to the gun was avoided and the red-hot lava is still hanging in the melt-cut slot.

Fig. 4.3--23 First face of the granite block after the initial trials about its response to various modes of attack with the electron beam. A and B show the location of subsequent piercing holes and C is the location of a subsequent melt-cut which led to the breakage of a large triangular prism.

We will discuss the breakage efficiency of this test and similar other ones in context, later.

(e) Next in this series of cursory investigations of the various modes of operation of the electron gun we run some vertical micro-cuts at high speed. The vertical mode has the advantage that the debris flows away from the beam impingement point, which is not the case in the horizontal mode; besides we found that the vertical drive of the electron gun had a more uniform speed. We also decided to mount a tangential air jet onto the front plate of the gun, to blow out the debris from the melt-cut to the extent this was possible. The location of this air jet nozzle can be seen in Fig. 4.3-25. The first cut which is shown in Fig. 4.3-26 was made with 40 IPM at a standoff distance of

Fig. 4.3-24 Breakage produced by a horizontal melt-cut with a 15.9 kW 156 kV beam, at 1.5" to 2" standoff distance, moving back and forth over a 21" long track for 12 minutes 45 sec at a speed of 38 IPM. Weight of debris 30 Kg. The black spot on the fresh rock face is moisture which must have come from within the rock.

1 inch; it is 8" long. The depth which was achieved was .44" below the original rock surface. Towards one side of the cut thermal stress cracks are visible. The air jet has obviously blown out some of the melt from the groove and it is hanging on the outside of the groove, in part looking and feeling like rock wool. The cross section of this slicing action, given by speed x depth, amounts to 17.6 sq.in./minute. If we compare this figure with what we might extrapolate from Fig. 4.1-3, we see that we have not achieved a particular good value. The difference is of course that Fig. 4.1-3 refers to concrete with a density of only 2.2 g/cm^3 whereas the present granite has a density of 2.6 g/cm^3. We also had to use 1" standoff distance here, whereas the graph of Fig. 4.1-3 refers to a standoff distance of 1/2".

We tried to run similar traces with a lesser standoff distance; but the carriage drive of the electron gun was so "soft" that the smallest build-up of debris between the rock face and the gun would stop the movement of the gun, at least for a moment until it could break free again; thus it would produce a very irregular cutting action. No real reason exists why the gun movement could not be forecful enough so as to push the debris, which accumulates, out of the way. The difficulty which we had in this respect is certainly not due to the electron gun per se, but to the response of the traversing mechanism which could not be improved at the time.

It was of interest to compare the depths which could be achieved by multiple cuts at high speed with the depths which could be achieved with a single cut at slower speed. Making four vertical runs at a speed of 20 IPM, a standoff distance of 1", which was kept constant, and without removing any debris from the prior cut, we achieved the following successive values for the depths: .51" in the first pass, .79 to .87" in the second pass, 1.1" in the third pass, and 1.4" in the fourth pass. The width after the completion of the four passes was 1", although it is difficult to decide what is melt-width and what is local thermal stress breakage. Fig. 4.3-27 shows the succesion of these four cuts.

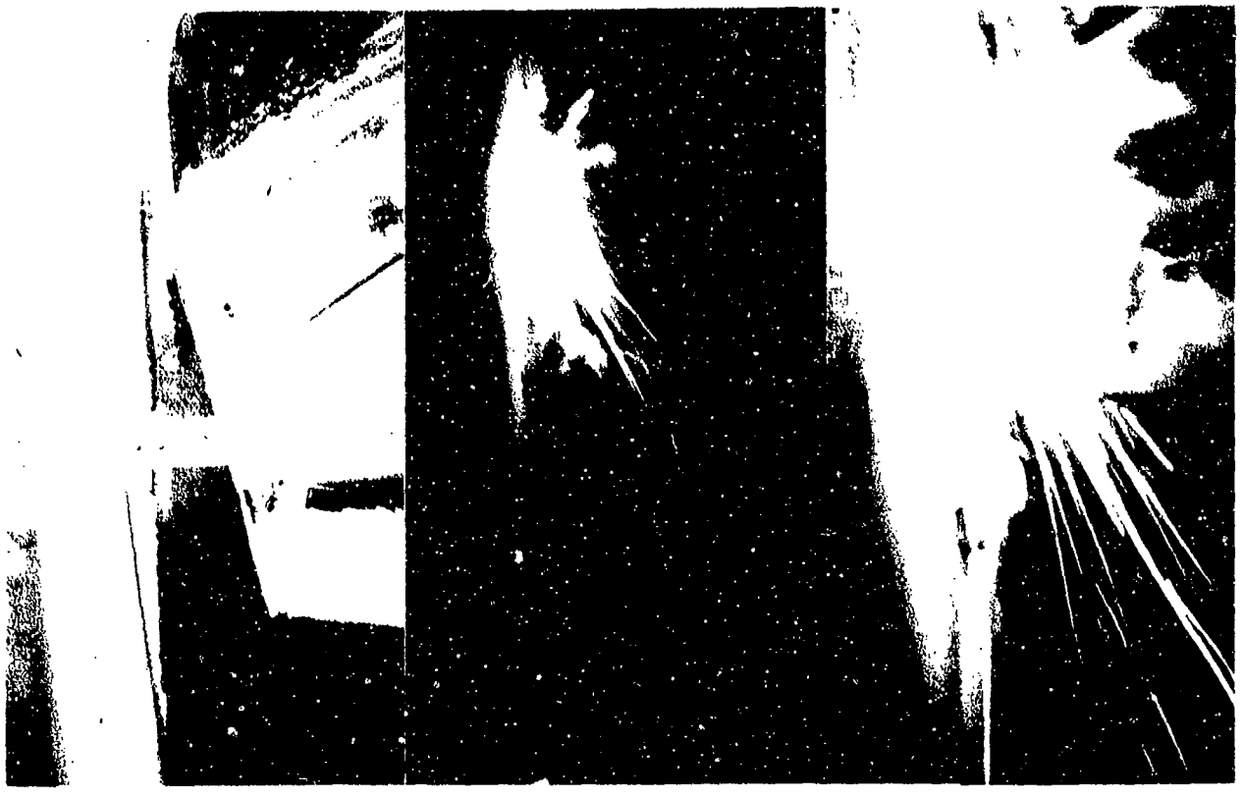

Fig. 4-25 (above):

High speed melt-cut with auxiliary air jet for blowing out the debris.

Fig. 4-26 (left):

Result of the above cut; speed was 40 IPM at 15.5 kW 155 kV; depth of melt-trace .44 inch below original rock surface.

Fig. 4.3-27 Four successive fast passes over the same trace gave an increase in the depth of the groove as follows: .51", .82", 1.1", 1.4". Speed was 20 IPM at 15.5 kW and 1" standoff. Thermal stress cracks have also developed.

For comparison a similar melt-cut was now made with 1/4 of the previous speed, namely 5 IPM, but with the same beam power, standoff distance, and air jet. The total beam time for the 8" long cut was therefore the same as the total for the four consecutive cuts made earlier, namely 1 min. 36 sec. The depth of this melt-trace was 1.25". Its width was of the same order, which means it was actually wider than the width of the multi-pass cut, and not as deep. The result of this experiment is shown in Fig. 4.3-28. Obviously multiple cutting at higher speeds has advantages, as expected. Unfortunately, the drive system of the gun, as it was, did not permit yet higher speed cuts at closer standoff, so as to achieve a pure spall-cut mode.

Fig. 4.3-28 Single-pass melt-cut with the same total power input as in the multi-pass cut of the previous figure; the depth here is less; the width of the breakage zone is larger. Cutting speed 5 IPM at 15.5 kW.

At this time we decided to terminate the various experiments which we had made on this first face of our granite specimen and to rotate the block through 90° in order to start a series of more systematic slow speed cutting tests on a fresh second face. Fig. 4.2-12 shows how the block was turned around with the help of an overhead crane.

4.3.4 Thermal Stress Cracking and Cumulative Effects

(a) The following tests were made on the second face of the granite block which had been turned by 90°. One of the objectives was to find out to what extent we would get cumulative effect from successive cuts of a reasonable depth and within a reasonable distance of one another. For a start we decided to cut a square, with sides approximately 18" long, by making 4 slow melt cuts, two going vertical up, two horizontal.

Cutting upwards the electron beam will always hit fresh solid rock, assuming the melt and the spalling products will fall down. The first vertical cut was made with the air jet nozzle installed and therefore with a relatively large standoff distance of 1.25". Cutting speed was set at 1 IPM; the beam power was 14.1 kW at 160 kV. The cut proceeded smoothly for 6-1/2 minutes but then so much debris had been accumulated between the rock face and the gun that the nozzle of the gun got hung up and did not move upwards anymore. As it turned out, the air jet had not been turned on and because of the very soft, non-rigid mounting of the gun the debris could not be pushed aside. Fig. 4.3-29 gives the operator's view of the cutting while in progress and shows the accumulation of the debris. The gun was withdrawn from the rock face and the melt and debris was broken out of the groove. The depths of the melt zone was found to be 4.8" and the width 2.5" which includes some thermal stress breakage. The appearance of this cut is shown in Fig. 4.3-30 labelled "First Section."

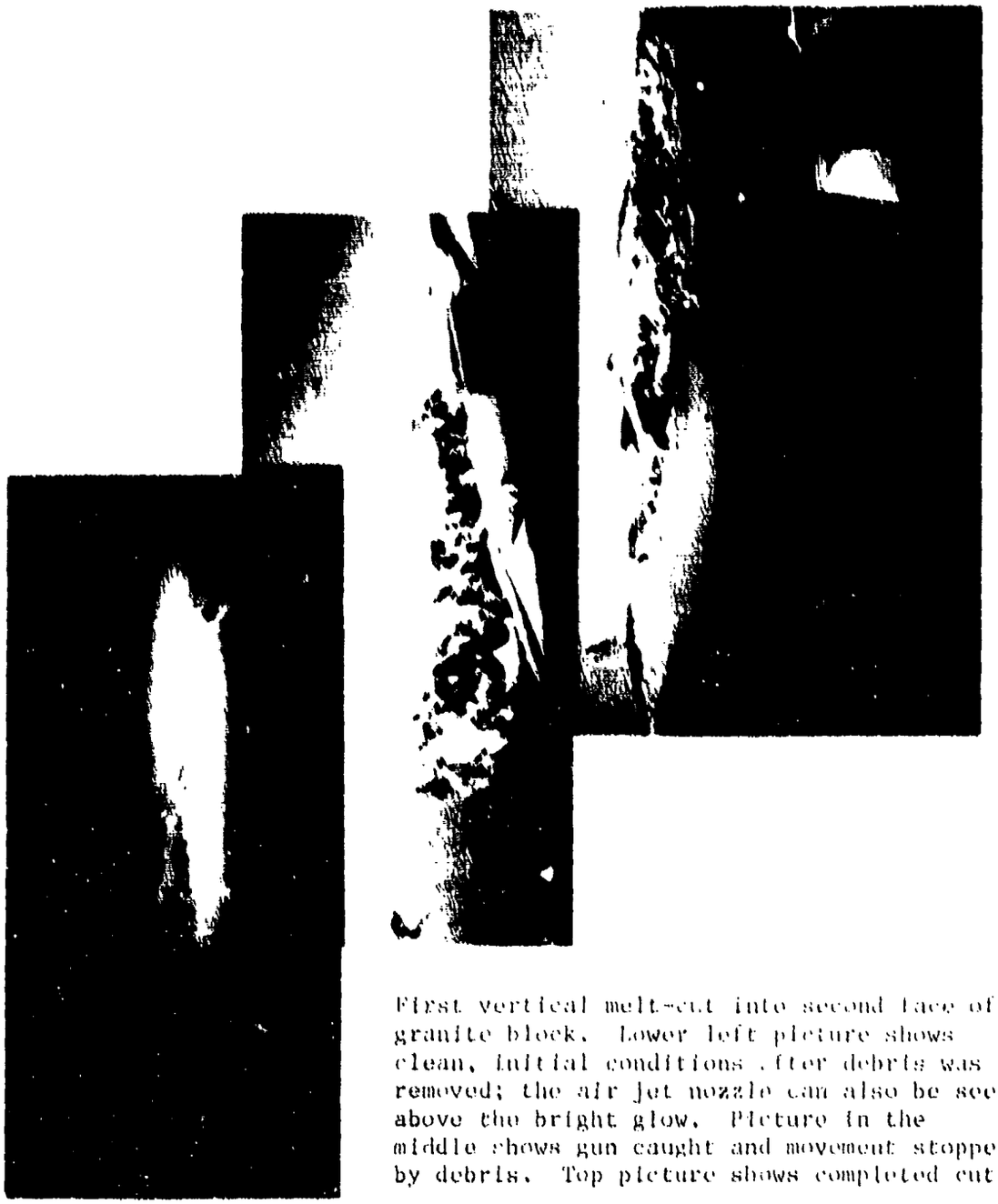

First vertical melt-cut into second face of granite block. Lower left picture shows clean, initial conditions after debris was removed; the air jet nozzle can also be seen above the bright glow. Picture in the middle shows gun caught and movement stopped by debris. Top picture shows completed cut.

Fig.4.3-29

3rd SECTION
Spalling trench from fast moving gun after it was pulled back from the face and swung upward inadvertantly

2nd SECTION
Resolidified melt cannot fall out because cut is wider in the depth than at the front face

1st SECTION
Melt core removed by force

First vertical melt-cut into the new, second face of the 6 ft-cube of granite. Starting at the bottom and traversing upward at a rate of 1 inch per minute at a stand-off distance of 1 inch the first section had to be stopped when debris blocked the further movement of the gun. When this occurred again, some time after the second section was in progress, the gun was pulled back, but the beam left on; the release from the blockage made the gun muzzle swing upward fast, which left a shallow spall-trace. To complete the third section the gun was repositioned.

Fig.4.3-30

The gun was repositioned at the same standoff distance of 1.25" with the beam fired 11° downwards, traversing speed and beam power the same as before. After 4 minutes 42 seconds we noticed that the gun nozzle would not move any more probably because it was again caught by the debris, and we decided to move the gun back slightly while the beam was going. This movement freed the gun nozzle from the debris, but because of the soft response of the drive system the nozzle swung upwards by a few inches the moment it was freed; this rapid movement did of course not produce the desired melt-cut but produced a spall-cut which can also be seen in Fig. 4.3-30 labelled "Third Section." We had to stop the gun and reposition it. We had also seen a warning light indicating a slight overheating of the gun nozzle. It proved necessary to resume the cutting at a slightly lower power of 13.6 kW. Cutting speed and standoff distance were kept the same and the third section of this vertical cut was completed in 7 minutes. Removing the external debris revealed the red hot core which was caught and held in the cutting groove as shown in Fig. 4.3-31a. The first part of this melt zone, the lowest part, was found to be 3.25" deep by 1" wide; higher up it became 3.5" deep and 1.5" wide; at the very top it was 2.6" deep. We believe these irregularities to be due to irregularities in the travelling speed of the gun. The layered structure of the "melt"-core is shown in Fig. 4.3-31b.

(b) After completing the first vertical cut we immediately proceeded to make a horizontal cut to the right, with the same cutting speed of 1 IPM, a standoff distance of 1.25", a beam pitch angle of 11° downwards, and a beam power of 13.1 kW at 160 kV. The result of this cut is shown in Fig. 4.3-32. The photograph at the top right of this figure shows that the melt zone is not very smooth; in fact the beam was going for a total of 30 minutes but traversed only 21". At times the gun muzzle was trapped and held stationary by the debris in which case we moved the gun back from the rock face without stopping the beam, just to free the gun muzzle and resume the movement. The width of the melt zone varied from 2" to 4"; the depths from 1.9" to 2.75".

Knocking off the external debris immediately after completion of a section of the vertical cut reveals the red-hot, re-solidified melt in the lower part of this section to where the molten rock seeped down. Width of the cut is about 1 inch depth 3.5 inch.

Fig. 4.3-31a (top) and b(left)

Appearance of the "melt." The layered structure is probably due to spalling chips falling into the melt without ever fully melting themselves.

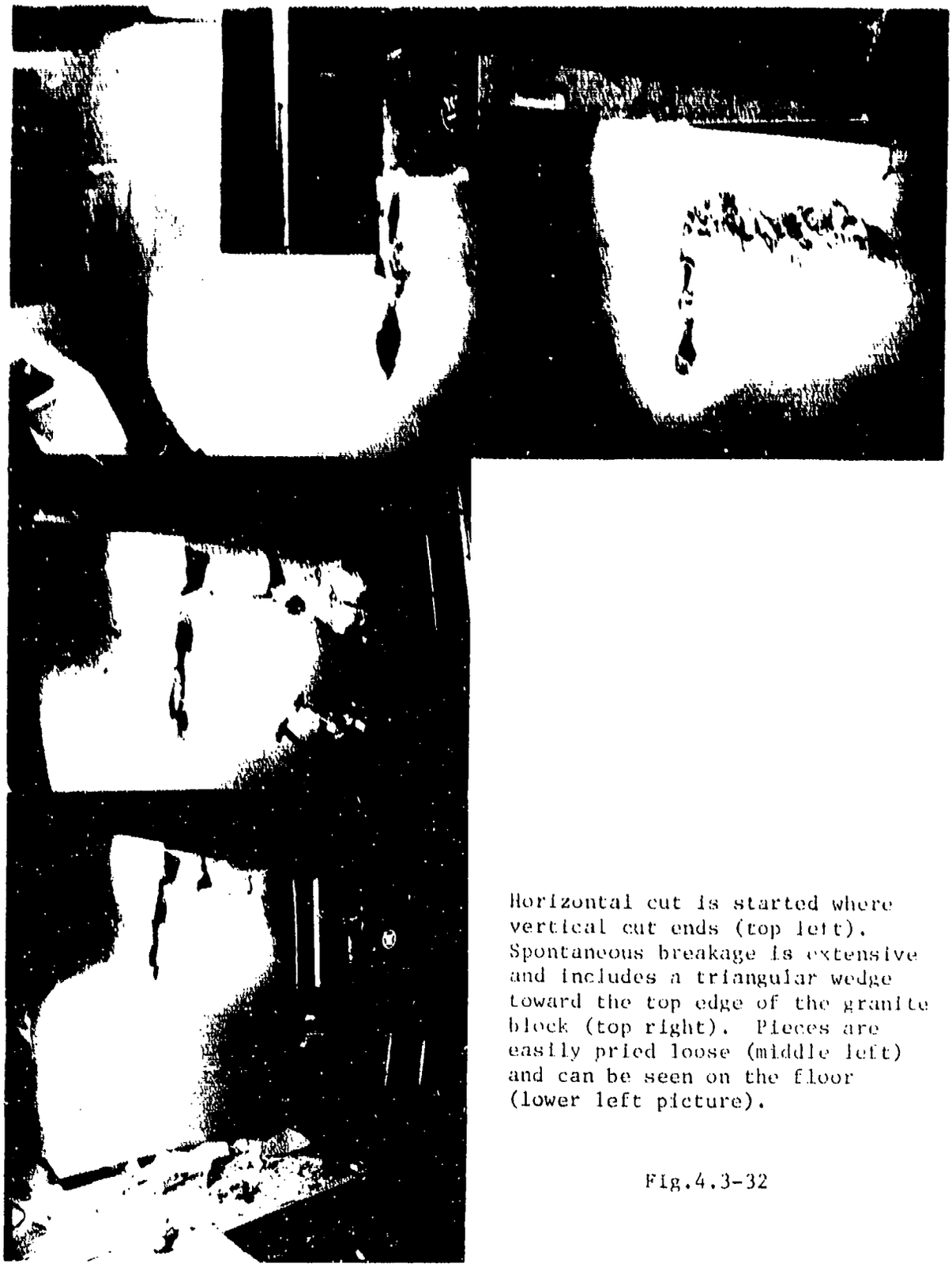

Horizontal cut is started where vertical cut ends (top left). Spontaneous breakage is extensive and includes a triangular wedge toward the top edge of the granite block (top right). Pieces are easily pried loose (middle left) and can be seen on the floor (lower left picture).

Fig.4.3-32

Although this horizontal cut was more than 12" from the upper edge of the granite block, the thermal stresses caused breakage of a triangular prism, as one can see in Fig. 4.3-32. It is not known when exactly the crack occurred during the 30 minutes of beam time.

(c) To join with the previous horizontal cut, we proceeded to make the second vertical cut starting again at the bottom and moving upward with a cutting speed of 1 IPM at a beam power of 13.1 kW, 160 kV. Standoff distance was again 1.25" but the beam was directed downwards by a pitch angle of 16.5". This was necessary to reach a low enough starting point. This time no air jet was used, and the air jet nozzle dismounted because it seemed to be a contributory cause for the blockage of the gun movement by the debris. The beam ran for 26 minutes and traversed a distance of 24 inches. The depth of the melt zone was found to vary between 4.0" and 2.75", the major portion being 3.6" deep. The widths varied between 1.75" and 2.3". This cut is shown in Fig. 4.3-33.

The total material removed in these three cuts amounted to 54.8 kg; with the power which was expended this amounts to a specific energy of 1100 J/g or 2980 J/cm^3.

(d) The second horizontal cut was made with the gun travelling from right to left at a beam power of 13.0 kW, 160 kV with a standoff distance of 1", a pitch angle of the beam of 14° downwards and at a cutting speed of 1.5 IPM; at least this was the initial speed setting. As it turned out, the gun travelled for 9:45 minutes over a distance of 19", at which time the end of the traverse of the carriage was reached, but then the beam was left on for another 5:15 minutes in a quasi-stationary piercing mode. The appearance of this cut before and after removal of the debris is shown in Fig. 4.3-34. The breakage was very irregular and minimal.

Knocking at the rock in the center of the square area, which had not broken out we noticed a hollow sound. But we could not find an open crack which would permit us to pry loose the hollow section.

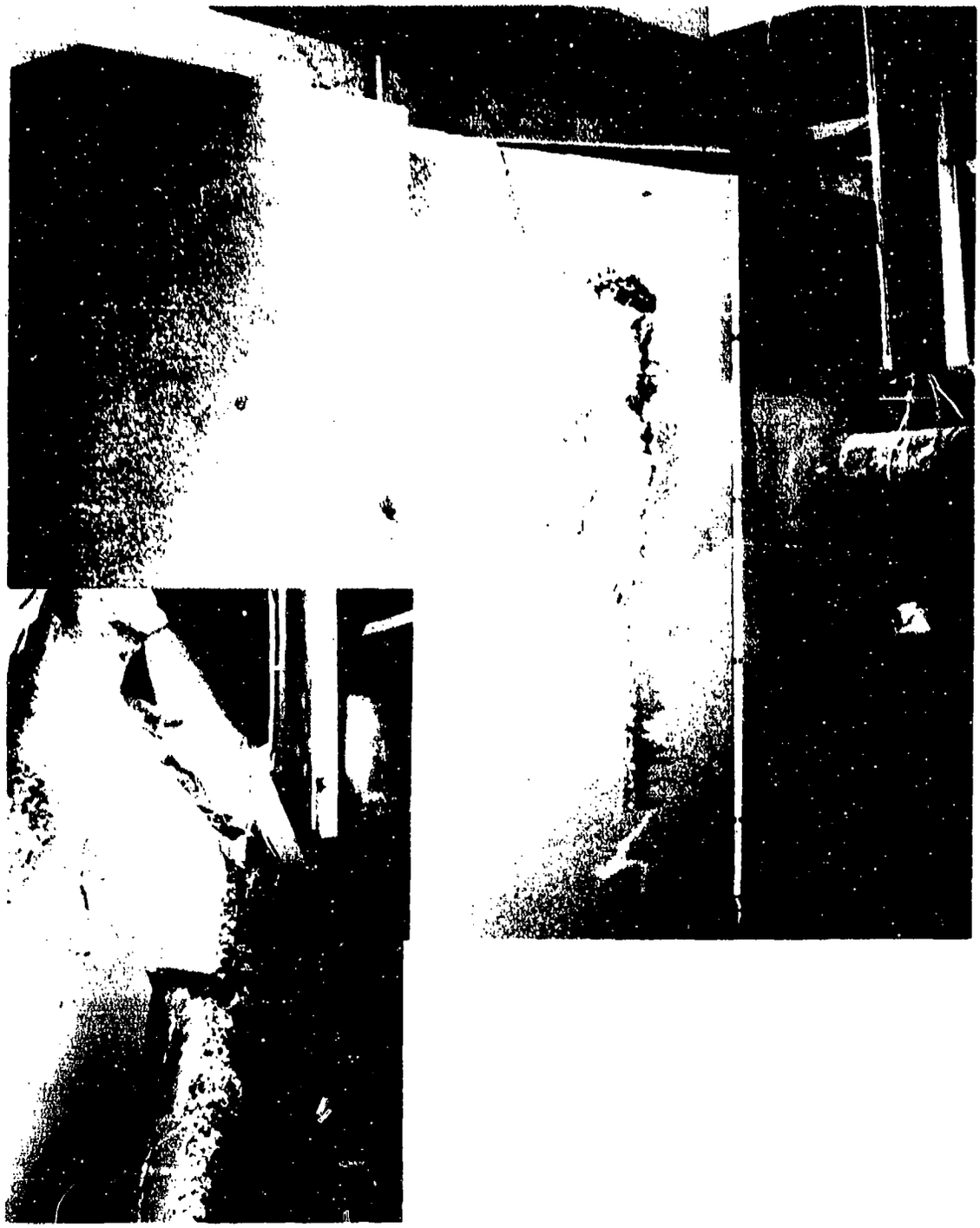

Fig. 4.3-33 Second vertical cut is completed.

Second horizontal cut, completing an 18" square pattern. Spontaneous breakage is minimal, traversing speed was very irregular.

Fig.4.3-34

Attempt to break the center section by stationary piercing. Some spontaneous breakage. Some cracks are visible which terminate without leading to breakage.

Fig.4.3-35

The breakage from this second horizontal melt-cut amounted to 8.6 kg, which means a specific energy of 1.36 kJ/g or 3.67 kJ/cm^3 had been expended. In this case there cannot be an argument as to the presence of size-effects because of the finite size of the test specimen, as we had seen it in the first horizontal cut. On the other hand, the figures do reflect earlier cracking which may have been produced by the prior vertical cuts.

(e) In order to break loose the already hollow-sounding center section we decided to pierce it at the highest point. Fig. 4.3-35 shows the result of 6 minutes of piercing with a 13 kW beam at a standoff distance of .75". A number of stress cracks can be seen in the photograph but the various slabs are still attached to the main rock body at the edges; they had to be pried loose with a screwdriver. A total of 9.1 kg of material was removed which amounts to a specific energy of 514 J/g or 1.4 kJ/cm^3. But there were still more hollow-sounding sections left which could not be pried loose. An additional piercing shot lasting 45 seconds led to the breakage of another 4.3 kg of material, which would amount to a specific energy of 317 J/g or 857 J/cm^3.

A third piercing shot lasting 1 minute led to the breakage of an additional 8.9 kg of material which would amount to a specific energy of 103 J/g or 279 J/cm^3.

Obviously these low and favorable efficiency figures are entirely due to the fact that we have taken advantage of hidden cracks from the previous melt cuts. This is a "cumulative" effect which we had hoped to see. Although it appeared here on a relatively small scale only, it justifies our expectations that on a large semi-infinite rock face it can be made to work in our favor on a larger scale.

The piercing shot shown in Fig. 4.3-35 produced a beautiful example of the formation of the cavity with a liquid melt pool at the bottom and a hollow dome on top. A close-up photograph of this cavity was already shown in Fig. 4.3-5.

(f) We had now, as a by-product of the foregoing tests produced some free faces on our previously homogeneous rock. Hence we could try and see what kind of effect they would have on subsequent cuts. Therefore a second vertical cut was started at a distance of 6" from the original first vertical cut. This is shown in Fig. 4.3-36. The left photograph shows the rock face prior to the cut; the photograph in the middle shows the rock face after some spontaneous breakage; and the righthand photograph shows the rock face after all the debris had been broken out of the actual melt cut region.

What actually happened during this run can be seen from Fig. 4.3-37. The beam power was 13.0 kW, the standoff distance 1", and the beam direction was 14° inclined downwards; the standoff distance was 1.75". After 6 minutes, and a travel of 5.8", a large piece of rock broke loose and fell against the gun. This did not cause any damage, but of course we stopped the beam. The depth of the actual melt cut, which can be seen in Fig. 4.3-38, was 4.2" at the top and 3" at the bottom of the 5.8" long section, the width was 2". The weight of the large pieces which had broken off was 19.6 kg, this would amount to a specific energy figure of 241 J/g or [illegible]

The appearance of this se[illegible] granite block after all these tests is shown in Fig. 4.3-39 [illegible] this photograph we had found that the area marked by the letter A could also be broken off by prying into an existing crack with a screwdriver; not much force was necessary. It is remarkable that the plane of section A is 4" below the level of the original rock surface, just as deep as the original melt cut. This is another proof that cracks are produced by these melt cuts which are not immediately evident. It can also be seen from Fig. 4.3-39 that area A does not extend to the edge of the test specimen; hence there is no size effect involved, and in case of a semi-infinite rock face we would have had the same results.

1st Cut

Location of 2nd Cut

Line of Subsequent Breakage

1st } Vertical
2nd } Cut

Debris on the floor.

2nd vertical cut at 6" distance from first cut. When the cut had reached 6" in height a 2 ft high column of granite weighing 14 Kg broke loose spontaneously and fell onto the gun. The pictures show subsequent stages of this process. The 2 ft column broke only on impact to the floor. Details of the action are shown in the next figure, as follows: top left: break detected through the telescope; top right and lower left: the whole pillar leans against the shield of the gun; lower right: gun is withdrawn and the rock pillar is falling down.

Fig. 4.3-36

Spontaneous long-range cracking
For explanations, see caption of previous figure

Fig. 4.3-37

Close-up of the end of the 6" melt-cut which led to the breakage shown in the previous figure. The melt cut is 4" deep (note the 6" ruler sticking out). Additional cracks can be seen where material has not yet fallen off.

Fig.4.3-38

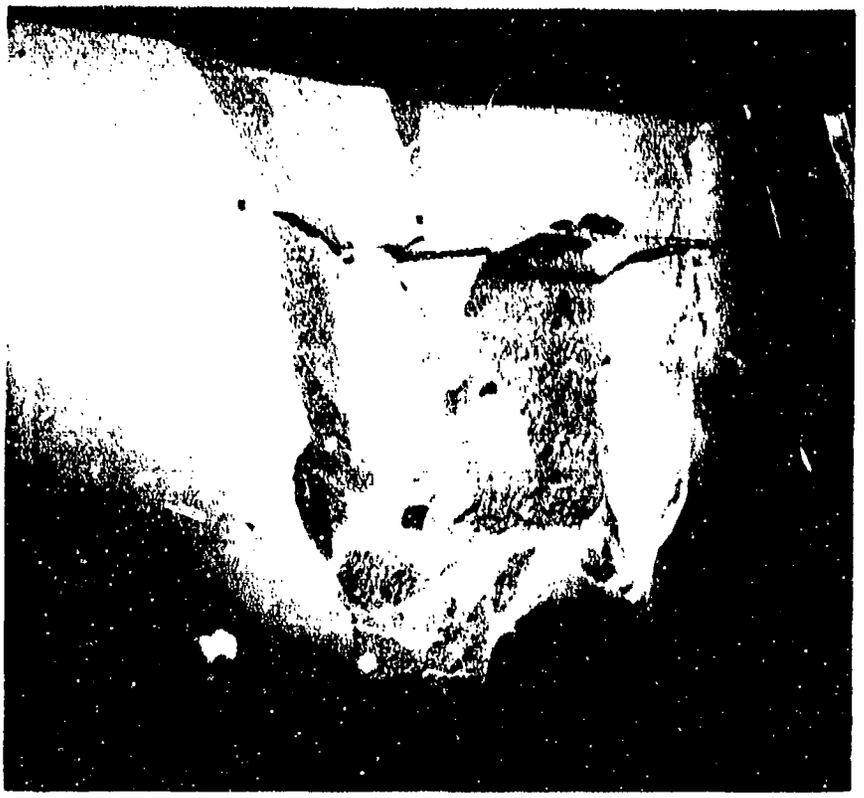

Final appearance of second face after all hollow sounding sections were pried loose. In area marked A plane of the crack is at the same level as the root of the melt-cut, namely 4" below the front surface of the block. The remaining ridge above area A rules out any possible influence of the edge of the finite size cube, although this edge was broken in an earlier cut.

Fig.4.3-39

(g) An additional vertical melt cut was made at a position 4" to the right of the one described in (c). The primary purpose was to determine if such a procedure would cause the removal of the resulting 4"-wide ridge between the two. As it turned out initially the ridge was broken to a depth only half that of the two parallel traverses. However, an indication of the existence of cumulative effects appeared subsequently when a single piercing shot, made some 20" to 30" away, caused the rest of the ridge to be broken off (see (i)). Most of the material cracked off by this vertical cut actually came from the right side, from a smooth, previously undamaged region of the original rock face. The cut was made with a 14 kW, 160 kV beam, at a speed of 1 IPM, and a standoff of 1.5". The gun was pitched downward by 18.5°. The total piercing time was 22 minutes during which the gun climbed 23". The melt produced in this cutting action again remained lodged in the groove. The removal of it appears in Figs. 4.3-40 to 44 which show frames from a 16 mm movie film. In Fig. 4.3-42h and i one can see particularly well that this debris consists of a mixture of melt and spalling flakes as has already been shown in Fig. 4.3-31b. With the material removed, the resulting trench was quite uniform in width (roughly 2"). The depth of the trench was typically 3.7". During the removal procedures shown in Figs. 4.3-40 to 44 there were 20 kg of material removed. If we attribute the energy expended in making the cut to this amount of debris, we find a specific energy of 0.9 kJ/g or 2.4 kJ/cm^3.

a) Vertical cut going at 1 inch per minute with a 160 kV 14 kW beam at a standoff distance of 1.5 inch is completed.

b) Fractured and loosely adhering pieces are knocked off.

c) The melt-core is loose within the groove but does not fall out readily.

Fig. 4.3-40

d) The melt-core is broken up.

e) More breakage

f) The same stuck melt-core, all along the groove

Fig. 4.3-41

g) More breakage

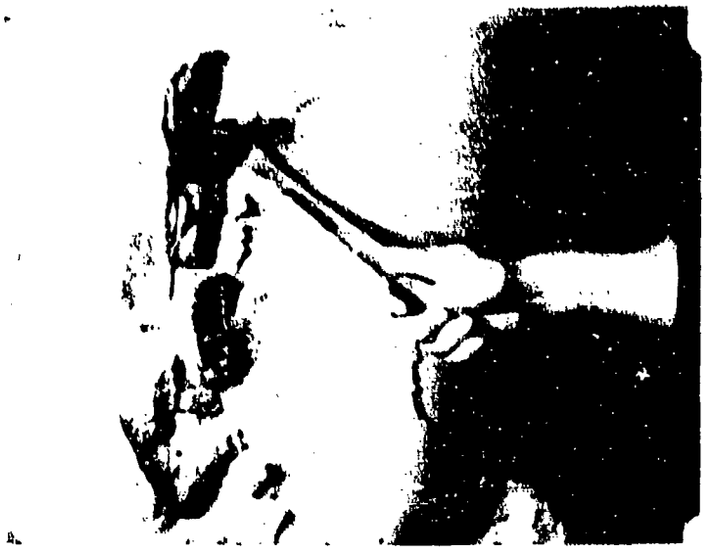

h) Part of the melt-core is free

i) Part of the melt-core is falling out. Here the great depth-to-width ratio of this melt-cut is very evident.

Fig. 4.3-42

j) Removing the lowest section of the melt-core makes also a slab of the adjacent rock fall down.

k) Obviously, previous spalling to the right of the cut now makes its influence felt. The flat conical impression is a spalling crack.

l) Breakage of the left side of the cut is only minor.

Fig. 4.3-43

m) Another slab was partly loose (see the crack in picture k) and can be pried off.

n) The black spot, where the previous slab has just fallen off, is water; it dries up very quickly as the next picture shows.

o) Everything cleaned out. The depth of the melt-cut is 4 inches below the original surface, its width is 2 inches.

Fig. 4.3-44

(h) In order to see what influence it would have if the cutting of this granite proceeded under water, we ran a flow of water down the vertical rock face where we started a new vertical melt cut. This was an area unaffected by the previous experiments. We did not use a water jet which had any force so that it would remove debris from the melt, rather the water just flowed over the surface. One effect one could expect from this arrangement was a chilling of the melt by the water which might cause it to crumble rather than to assemble in large solid blocks. However, even for this effect to become noticeable the amount of water was probably not enough. This test was recorded with the 16 mm movie camera and some frames from this film are shown in Figs. 4.3-45 and 46. The standoff distance was 1.5" and the beam was pitched downwards by 16.5°. Within 20.5 minutes a 24" long melt cut was produced, the depths varied from 2.75" to 3.6". The beam power for this cut was 13.8 kW at 160 kV. The first frames in Fig. 4.3-45 show the beam being turned on. The frame sequence is 24/second; it takes about .2 seconds until full beam power has been attained. The frames on the right show later phases in the cutting process, especially the dripping down of some droplets of liquified rock. In Fig. 4.3-46 this is once more shown in greater detail; the frames in this figure are not consecutive but show the development of the melt and the droplets within a time period of 5 to 25 seconds. There was never a buildup of a great amount of debris during this run; this can probably be attributed to the water flow; perhaps the cooling effect of the water prevented spalling of the surrounding area near the cut due to radiant heat. There was comparatively little stress cracking in the vicinity of this cut and the walls of the groove were smooth.

Consecutive frames from the movie film showing a vertical cut made with water flowing over the face of the rock; speed 24 frames per second. Beam 14 kW 160 kV traversing speed 1.1 IPM; stand-off 1.5".

Fig. 4.3-45

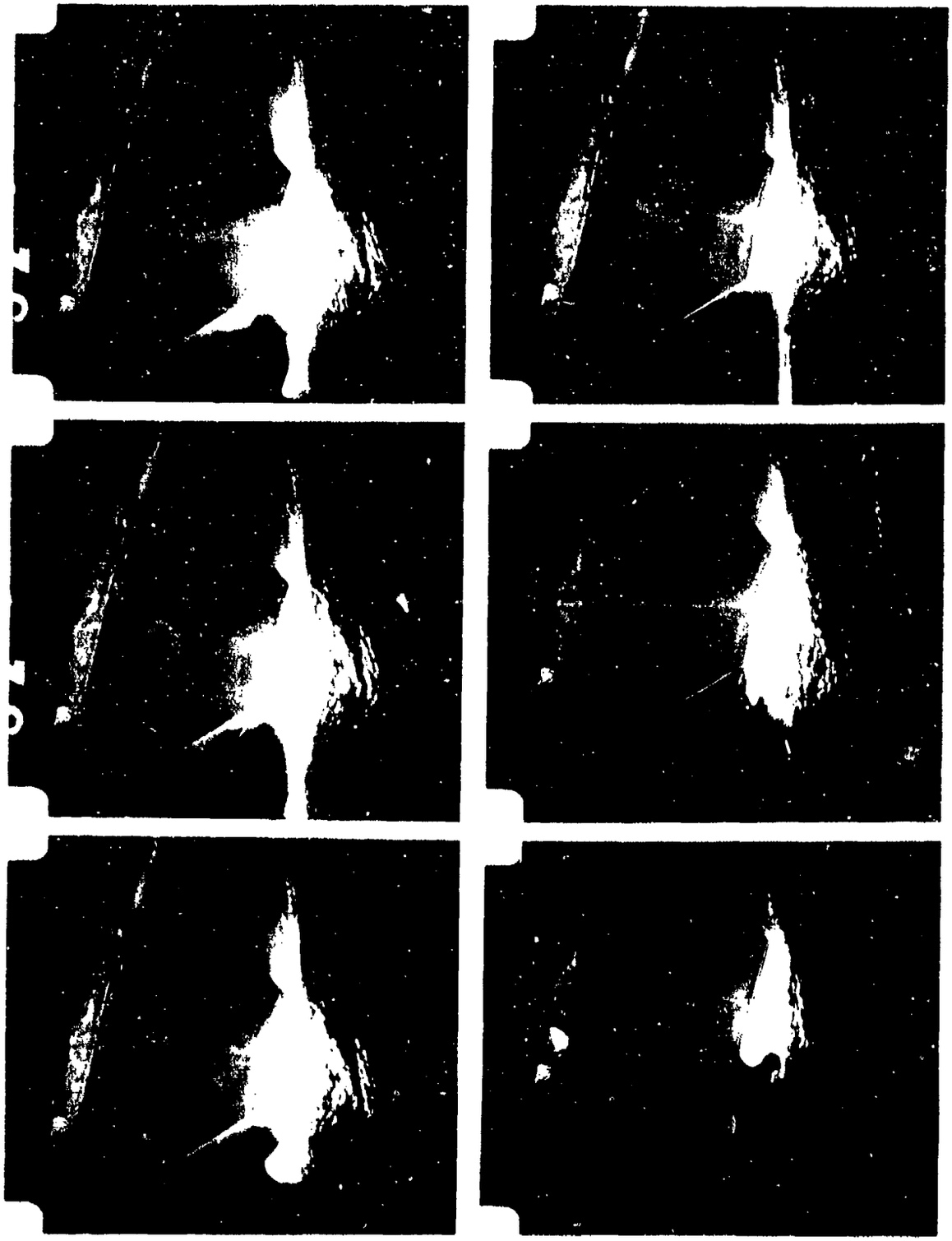

Selected frames from the movie film showing a vertical melt-cut with water flowing over the rock face. (See also previous figure.)

Fig. 4.3-46

(i) The next test was a single pierce lasting an extended period of time and causing a large amount of breakage. From the patterns of the breakage we determined that the effect of this pierce strongly depended on many of the previous tests made on this rock face. The beam power was 16 kW, at 160 kV. It was directed perpendicular to the rock face (i.e. horizontally) in a region whose surface was characterized by gentle undulations. The piercing position was within 3" of the center of the square outlined by the vertical and horizontal traverses described in (a) through (d). The standoff was 0.8". The total piercing time was 30 minutes, although a 65 kg piece was broken from the corner of the granite cube after the first 15 min. This piece is shown in the lefthand photograph of Fig. 4.3-47 as it looked at the end of 30 minutes.

The cavity caused by the beam was not typical of other piercing cavities in that a layer of glass roughly 1" thick lined the entire inner wall. We conjecture that the heat flow forced by this quite strong attachment was in part responsible for the large amount of resulting breakage. One reason for this lining was that practically no liquid was able to flow out of the cavity. The gun muzzle was in the way. It is still open to question, however, why the upper part of the cavity accumulated a liquid layer instead of spalling downward as we had observed on other occasions. With the remaining time of the testing period we were not able to reproduce this effect. When the solidified material had been removed, the cavity was measured to be 5" deep and 10" high, with the height extending 8" above where the beam entered. (See Figs. 4.3-47 to 4.3-49).

After this pierce 159 kg of material were easily dislodged, as can be seen in Figs. 4.3-49 and 4.3-50. These photographs were taken from a 16 mm movie sequence of the dismantling process. The bottom photograph of Fig. 4.3-49 shows a second large pierce being removed. Immediately to the right of that piece is material shown still in position but which was removed next. There are two interesting aspects to this latter piece. First, when it came off, so did the ridge between

the two parallel traverses described in (c) and (g) (in fact one can see in the photograph the vacuum left when the bottom half of this ridge dropped off spontaneously). Secondly, as this large piece was removed, it revealed a large amount of water covering the newly exposed surface. These two observations suggest that there were already deep cracks formed before the pierce was made. At least one of the cracks was caused by the two parallel traverses and piercings. The test immediately preceding this present one was the traverse made with water flowing across the top of the rock and then down the side being cut.

If we attributed all the breakage following this pierce to the energy extended in these 30 min., we would obtain specific energies of 180 J/g or 490 J/cm^3.

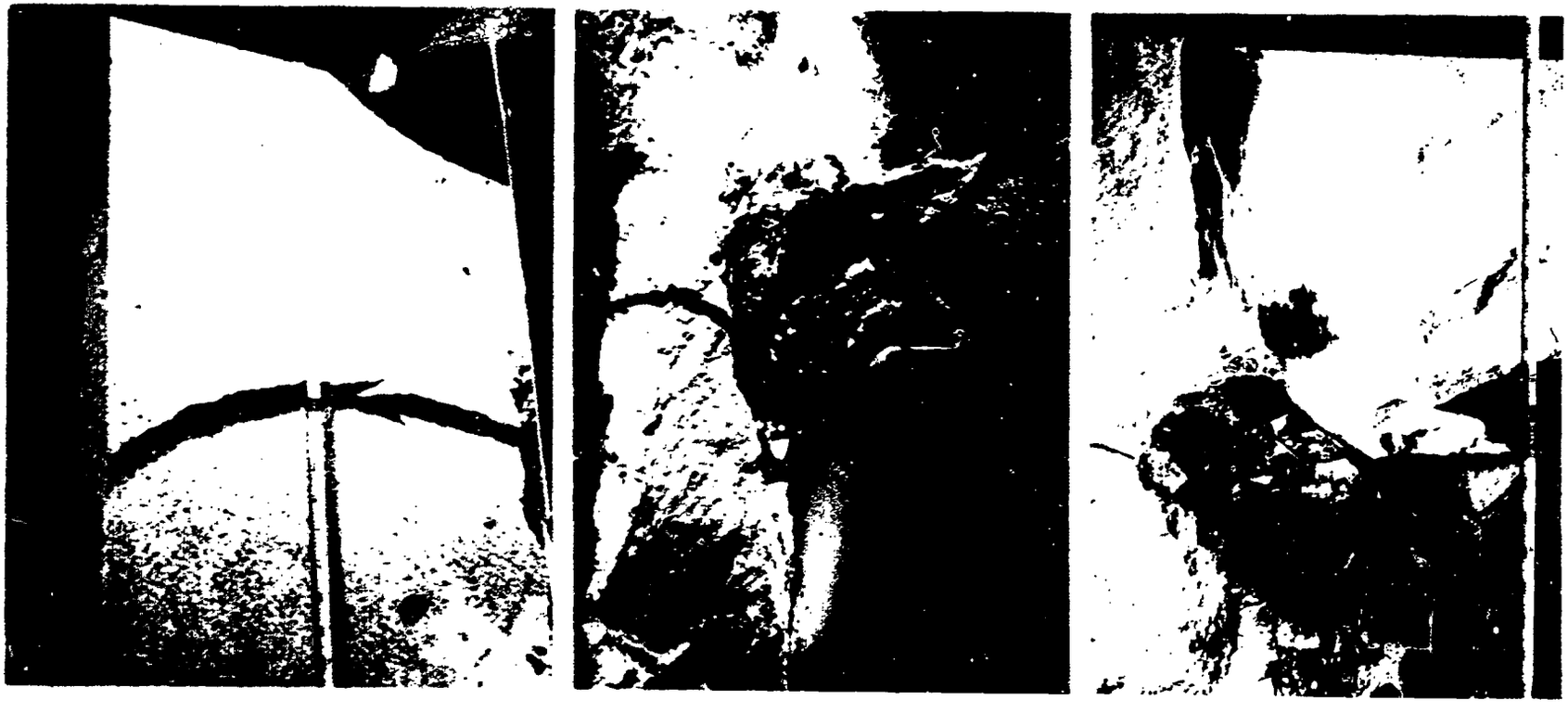

breakage after stationary piercing for a total of 30 minutes at 16 kW. The crack in the left picture showed already after 15 minutes. The center picture shows the gun trapping the melt in the cavity; a chimney has formed about 6 inches above the gun. The right picture shows the imprint of the face plate of the gun in the molten rock after the gun was pulled back. The chimney hole can also be seen, as well as cracks going to the right.

Fig. 4.3-47

After piercing for 15 minutes a large crack appears.

The cracks extend horizontally over 3 feet.

Knocking off some of the re-solidified melt.

Fig. 4.3-48

Crack extend to the right of the piercing spot.

A large corner block comes off.

More debris comes off and more cracks become visible.

Fig. 4.3-49

One of 3 pieces which formed the vertical slab between two earlier melt-cuts, which now becomes loose.

Part of the dust covered wall of the piercing hole

Inspecting the debris.

Fig.4.3-50

(j) The next pierce was also of long duration, 39 min. total. The first 9 min. were made at 16 kW, 160 kV (see Fig. 4.3-51). Subsequent power supply difficulties then caused a delay of about 15 min. before restarting the gun, after which time it ran at 10 kW, 150 kV. Only after 24 min. into the second stage of piercing did the original solidified glass begin to glow. The second piercing stage was stopped after 30 min.

The location of the pierce was 12" below and 4" to the right of the pierce described in (i). The standoff position was the same, 0.8", as was the pitch, 0 . Details of the cavity and stress cracks in the rock appear in Fig. 4.3-52. The appearance of the cavity and the debris after removal appear in Fig. 4.3-53.

In contrast to the previous pierce, the amount of breakage was more typical of what we had obtained from the traverses alone, i.e. 19 kg, which represents a specific energy of 1.5 kJ/g or 4.0 kJ/cm^3.

An additional pierce was made at the lower power, 11 kW at 150 kV, which showed quite poor energy coupling to the rock. The standoff distance was 1.25" and the gun was horizontal. Although the piercing lasted 45 min. the liquid rock failed to wet a major portion of the cavity wall. Material spalled from the top of the cavity and was either melted or vaporized by the beam. Only 6 kg of material could be removed, a value which represents specific energies of 4.8 kJ/g and 13.0 kJ/cm^3.

Stationary piercing with 16 kW, 160 kV after 9 minutes; stand-off distance 3/4 inch blocked-off by the melt; cavity has already extended upwards beyond the face plate of the gun and the molten rock M has formed a chimney for the hot gases G from the cavity to escape. Piercing at this position was continued for another 30 min. at 10 kW 150 kV; see the following figure.

Fig. 4.3-51

After completion of the 39 min. of piercing (previous figure) several thermal cracks can be readily seen, for instance at c and d, but others are not so evident. G is in the chimney hole of the cavity, the arrow B points to the beam hole which is shown in the close-up photograph on the right. The impression of the face plate of the gun in the molten rock can be seen clearly; the screws' heads appear dark since they have good thermal contact with the copper frame of the shroud whereas the molybdenum plate, and the rock in contact with it stays hotter and was still glowing when the picture was taken. Through the beam entrance hole (arrow) one can see the white-hot interior of the cavity.

Fig. 4.3-52

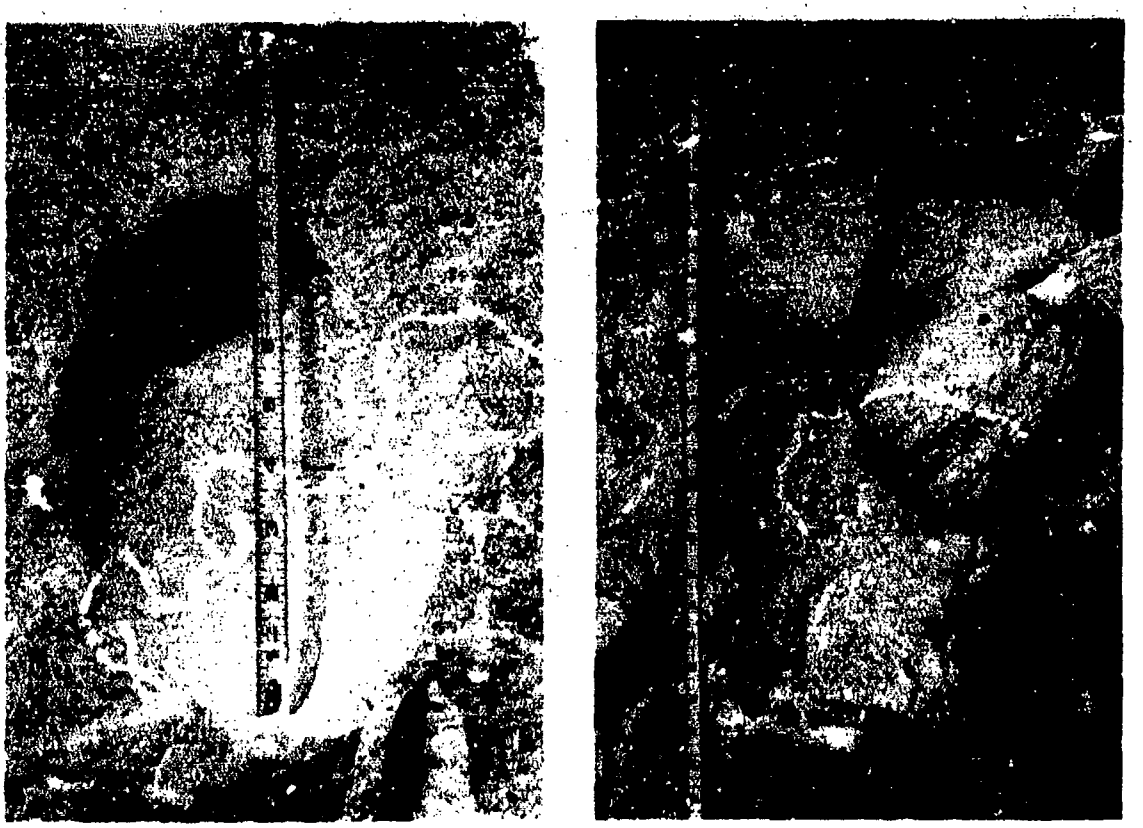

On the left: remaining cavity after all loose rock has been removed; the maximum depth measured from the original rock face is 3.6 in. Note the end of the ruler is buried in some of the remaining white dust which characteristically forms the solid-liquid interface in this rock. On the right: material broken out by this piercing shot, amounting to 18.5 kg.

Fig. 4.3-53

(k) At the lower power (10.7 kW at 153 kV) we performed an upward traverse to be compared with those made at higher power as described in (c), (g), and (e). The standoff distance was 1", the traversing speed was 1 IPM, and the downward pitch of the gun was 12°. The total beam time was 18 minutes which produced 4.5 kg of debris, thus yielding a specific energy of 2.5 kJ/g or 6.9 kJ/cm^3. Fig. 4.3-54 shows the results of the traverse before the melt and breakage were removed. Note the spall chips embedded in the true melt which give the material a flaky appearance. The major portion of the resolidified material could be removed in one piece as is shown in Fig. 4.3-55.

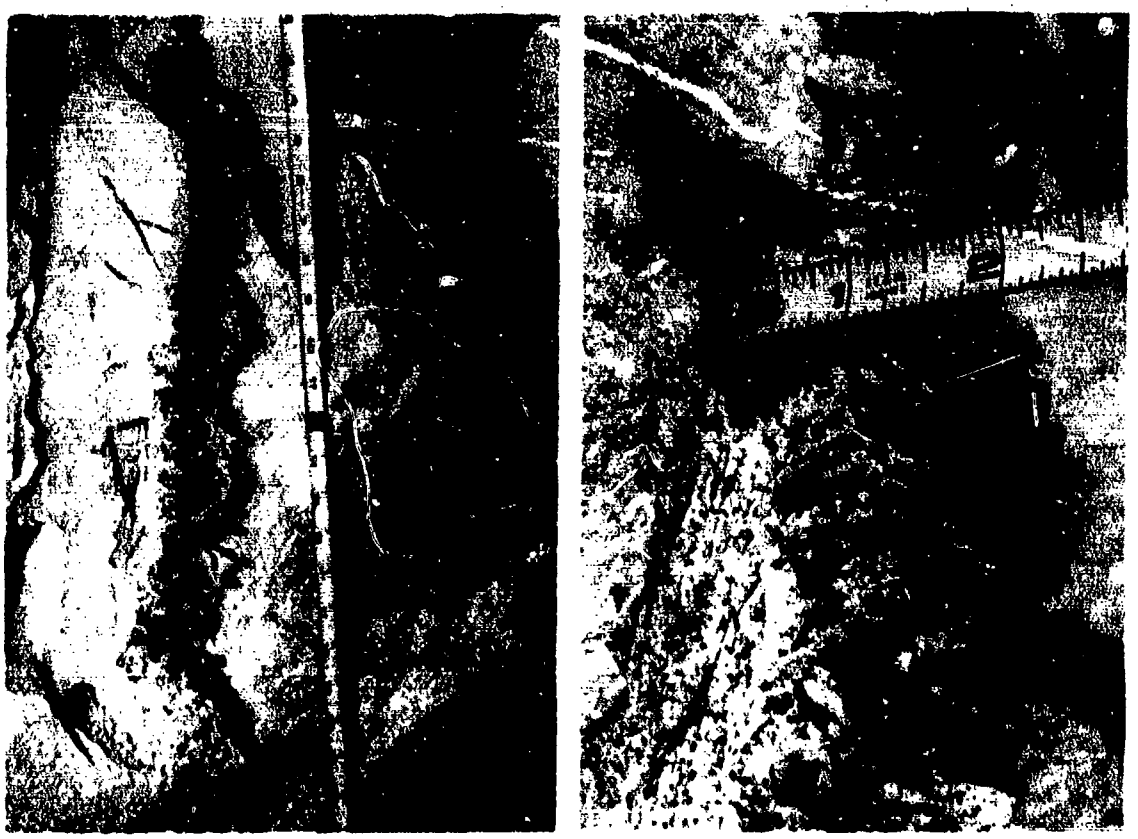

Vertical traverse with reduced power of 10.7 kW at 153 kV; 1 inch standoff; traversing speed 1 IPM upward. The re-solidified "melt" protrudes from the rock face by about .8 inch; the flaky character is due to spall-chips which get imbedded in the true melt. The trench depth was 2.6 inch at a width of 1.7 to 2.0 inch. The material removed weighed 4.5 kg. (See also the following figure.)

Fig.4.3-54

Measuring the characteristic depth of this melt cut was hampered by the undulating surface of the original rock face. Since the traverse was executed rather smoothly, we picked a location to measure where the standoff was indeed 1.0". The depth at this point was 2.5". The following table summarizes the results of the four vertical traverses, all made at 1 IPM.

The major portion of the resolidified material from the melt-cut of the previous picture could be removed in one piece and is shown here.

Fig.4.3-55

Traverse	Power (kW)	Voltage (kV)	Standoff (in.)	Trench Dimensions Depth (in.)	Trench Dimensions Width (in.)
(c)	13.1	160	1.25	3.7	2.0
(g)	13.6	160	1.0 tc 1.4	3.7	2.0
(e)	13.8	160	1.5	3.0	1.3
(k)	10.7	153	1.0	2.5	1.7

Studying this data one finds that <u>the depth tends to increase faster than proportionally with the power</u>, an effect found previously in laboratory piercing tests (see Section 5.1, especially Figs. 5-4 and 5-6)and expected from theory (see Section 5.2).

Case (e) appears to be an exception most likely because of its larger standoff, which causes additional degradation of the beam's power density before it reaches the rock face. The unusually narrow trench for (e) is possibly a result of quenching due to the flow of water used during that test.

(1) One test was performed on a small, 45 kg, rectangular block of white granite. This piece, although obtained locally, appeared very similar to the material of the 6' granite cube. The sample was 12-1/4" wide, 9" high, and 8-1/8" thick. We shot the beam horizontally into the center of a smooth vertical face. The beam power was 13.6 kW at 160 kV, and the standoff was 0.74".

The first of two piercings lasted 64 sec. and produced a cavity 2.4" deep, very similar to that found in the piercing tests on the large sample (see section 4.3.2 and Fig. 4.3-14). As was typical for this type of rock, this piercing depth was only slightly greater than half that expected from theory, i.e. 4.3". (See equation (5), Section 5.2 for which the present power level and standoff distance were used together with the constants given in Table 5-3.) Fig. 4.3-56a shows this cavity with the resulting solidified melt stuck to the e.b. gun. This piercing caused a hairline crack running vertically through the front face of the sample and bisecting the cavity. The crack extended about 2" into the rock face as determined from looking at the top face of the sample.

A second piercing was then made into the original cavity under the same conditions as the first. After 60 sec. of the second pierce, the original hair-line crack had propagated across the top of the rock. After 83 sec. the rock fell apart into two comparably sized pieces together with some smaller debris as can be seen in Fig. 4.3-56b. Taking <u>half</u> the original weight as the material broken away, we obtain a specific energy of 89 J/g or 240 J/cm^3.

(a)

(b)

Fig. 4.3-56 Small, 45 kg, 12-in.-long, rectangular, block of white granite similar in material to large test sample. (a) Cavity from a 64 sec piercing at 13.6 kW, 160 kV. Depth was roughly half that obtained in gabbro and predicted by theory. This result agrees with tests performed on the large test sample. (b) The block is split in half after 83 sec of additional piercing.

(m) From the preceding discussion of piercing and cutting the second face, we can obtain a very rough estimate of the specific energy needed for electron beam breakage of the large, 6', granite block. It is clear, however, that there exists a large number of variables which must be understood before the processes can be optimized. There were 16 different tests performed cutting or piercing this face, and debris was removed and weighed 10 times. The data collected during the tests was extremely useful in a descriptive sense, but the relatively small number of tests makes it impossible to untangle the correlations among the various operating parameters and cutting sequences. Substantially more data would be required to identify the optimum strategy and the associated specific energy.

At present, the best we can do is to present a total specific energy averaged over the experiments. The total energy delivered by the electron gun was 2.13×10^5 kJ. The resulting breakage was 314 kg. These values yield a specific energy of 679 J/g or 1830 J/cm^3. Theoretically with no heat losses, melting requires 2 to 3 times this energy, and vaporization requires 7 to 8 times as much. Experimentally, we find we needed to deliver 6 times this energy in spalling the same material (see Section 4.3.5).

4.3.5 Spalling

(a) Several spalling tests were made on the second face of the 6' granite cube. Of these, three were made without moving the gun along the face of the rock, but rather spalling away material to form cavities. Fig. 4.3-57 shows a sequence of photographs of one such test performed at 14 kW, 160 kV with an initial standoff of 6" and a pitch angle of 0°. The standoff was large enough to cause the beam to spread out thus reducing the power density, as can be seen in 4.3-57a. Distributing the beam power over a large area provides the extreme opposite to the quasi-adiabatic vaporization used in piercing and slicing. In principle, one would like the power density to be sufficiently low that none is wasted in melting and sufficiently high to cause a steep temperature gradient at the surface of the rock. Differential thermal expansion at the surface then causes small particles to shoot off. Some of these particles are visible as bright streaks in Fig. 4.3-57 as they are made incandescent by the electron beam. A photograph from an unrelated, short-duration test gives a view of a spall cavity stopped in the early stages of development (see the top of Fig. 4.3-58). It corresponds to a beam time of only 80 sec. The cavity diameter of 5" and its depth of 0.75" show the very low depth to width ratio to be expected when using a diffuse beam.

Returning our attention to Fig. 4.3-57, we see a white glowing mass collecting at the bottom of the cavity (see photographs b and c) and showing that a certain amount of material was in fact melted. Some of this melt probably came from the cavity walls and some from a collection of spalled fragments melted while traversing the beam.

This spall test lasted 30 min., during which time we advanced the gun toward the rock to keep the standoff distance more or less constant. The test resulted in the removal of 6.25 kg of material,

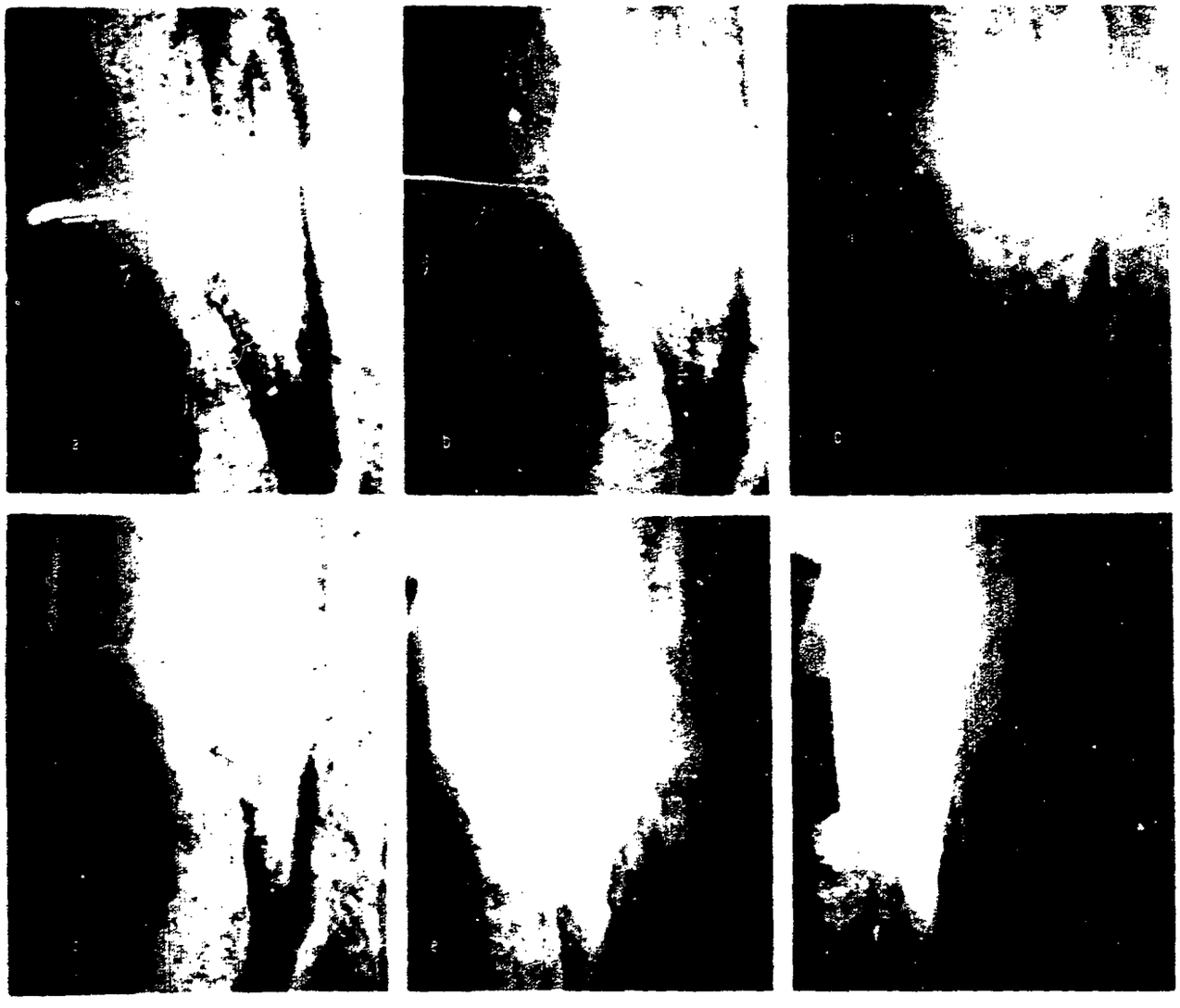

Fig. 4.3-57 Spalling hole in the "Sierra White" granite produced by a 160 kV 14 kW beam at initially 6 inch standoff (frame a), gradually adjusted to 2 inch (frame f) over a period of 30 minutes.

Spalling crater in the "Sierra White" granite (left), and the very fine, powdery debris which was produced (below)

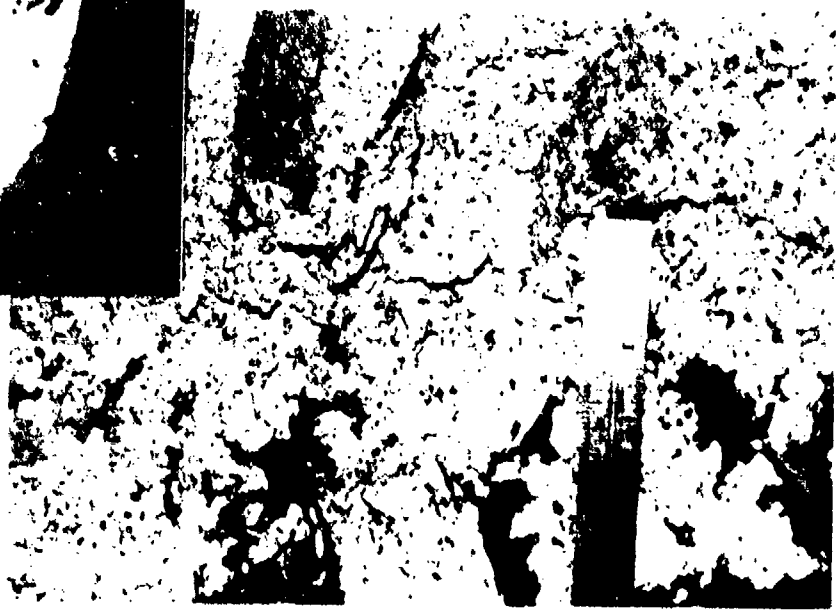

Fig.4.3-58

most of which was very fine and powdery, typical of that shown in the photograph of Fig. 4.3-58. This material corresponds to a specific energy of 4.15 kJ/g or 11.2 kJ/cm^3. It is interesting to note that there were no, immediately-apparent, stress cracks caused by this cavity.

(b) Rapid spalling traverses at small standoff could not be attempted in the granite because the carriage was too slow. However, one spalling traverse was attempted. We translated the beam vertically up and down over the same 23-inch long path 18 times in succession in an attempt to spall a trench of reasonable depth. The vertical direction was chosen to allow material melted inadvertently to fall out easily. The gun delivered 16 kW at 160 kV from a standoff distance of 5". A much closer standoff would have caused melting and vaporization. We used the maximum possible vertical traverse speed obtainable with the carriage, i.e. 37.5 IPM up, 20 IPM down. It was necessary to pitch the gun down (i.e. by 17°) in order to aim the gun at the rock while using the full range of the vertical motion of the carriage. Interrupting the process temporarily after 6-1/2 minutes (7 passes each up and down), we found that the spalled trench was already covered with a layer of solidified molten material. The trench was 3.5" wide and only 1.2" deep. After chipping out the solidified lining, we continued the process for an additional 20 min. In fact what we had generated was a wide, shallow trench which was lined with glowing, hot semimolten rock. It is interesting that the process did produce a substantial number of stress cracks in contrast to the stationary spall of (a) which produced none. Because of these stress cracks 44 kg of debris were removed. Of this, 26 kg were in a single piece from along the top free edge of the rock. When it was removed, water appeared on the newly exposed surface, presumably from the experiment using water (see Section 4.3.4(h)). Accordingly, that crack was pre-existing and as such is indicative of the cumulative nature of the process. Since most of the debris was caused by stress cracks, we cannot attribute the resulting specific energy to spalling. The value we get, similar to the average value obtained from all the piercing tests, is 0.58 kJ/g or 1.57 kJ/cm^3.

Appearance of the second face of the 6 ft. cube of "Sierra White" granite when tests were terminated.

Fig. 4.3-60

Table 4.3-IV Total Heat of Removal

Vaporization (prior to dissociation)			Dissociation (prior to vaporization)	
	SiO_2	Al_2O_3		$CaCO_3$
Average specific heat, Cp			Average specific heat, Cp	
Solid	1.17 J/g°C	1.04 J/g°C	CaO (solid)	0.84 J/g°C
Liquid	1.50	1.96	CO_2 (gas)	0.51
Temperature				
Melting	1710°C	2072°C	Temperature for which partial pressure of CO_2 reaches 1 atm	897°C
Vaporization	2227	2977		
Vapor pressure slope (at vaporization temperature)	4.22 torr/°C	5.05 torr/°C		
Latent heat				
Fusion	142 J/g	107 J/g	Heat of formation at 25°C, 1 atm	1827 J/g
Vaporization*	6395	5330		
Total heat of melting	2.11 kJ/g 5.62 kJ/cm^3	2.24 kJ/g 8.89 kJ/cm^3		
Total heat of vaporization	9.30 kJ/g 24.8 kJ/cm^3	9.25 kJ/g 36.7 kJ/cm^3	Total heat of dissociation	3.00 kJ/g 8.13 kJ/cm^3

*From Clausius-Clapeyron equation

4.3.6 Termination of the Tests

A chronological list of test runs made on the 6 ft. granite block is presented in Table 4.3-VI. Fig. 4.3-61 and 62 identify the various test locations. As mentioned, we first had to get a feeling for what would happen if the electron beam pierced this type of rock, and how the mobile gun could be manipulated. These first tests are therefore exploratory, each one different from the previous one. There is an additional reason for the differences in subsequent tests, namely after the first melt-cut there can be changes to a wider area than is readily apparent, and the next test takes place on an already altered rock. We have shown clear evidence for such cumulative effects which are, indeed, favorable for our purposes. Such cumulative effects, however, do not yield neat academic-type test series. On the other hand, because of our limited funds, we could not run enough tests for a statistical evaluation of the data.

It was also not possible to get data on large-scale cumulative effects from a block of only 6 ft. on a side. Accordingly, these tests, and their results, cannot and should not be taken as a substitute for field tests. What we can say at this time is that the electron gun as well as the cutting, piercing, and stress cracking processes as observed have met all our expectations. In addition, as expected, we have obtained evidence for cumulative effects.

Fig. 4.3-39 shows the first face and Fig. 4.3-60 shows the second face of the 6 ft. cube at the termination of the tests. It is perhaps indicated to reiterate that the damage to these rock faces was done by an energy beam from a distance (however small it was), without physical contact, and without physical force exerted from the outside, utilizing internally induced stresses.

Table 4.3-VI

DATA SUMMARY OF E.B. TESTS ON SIX FOOT BLOCK OF SIERRA WHITE GRANITE

(Listed chronologically to preserve sequence information. Test numbers are keyed to locations represented in Figure 4.3-61 and 4.3-62)

Date (1972)	Test Number	E. B. Output Power (kW)	E. B. Output Current (mA)	E. B. Voltage (kV)	Standoff Distance (in)†	Pitch Angle Below Horiz. (°)	Travel Direction of Gun Muzzle††	Travel Speed (in/min)	Beam-On Time (min:sec)	Trench Length or Cavity Height (in)	Trench or Cavity Width (in)	Trench or Cavity Depth (in) (Solidified liquid removed)	Energy Expended (kJ)	Material Removed (kg)	Energy per Mass Removed (kJ/g)	Energy per Volume Removed (kJ/cm³)	Figure Number	Text Page Number	Comments
9/15	1	13.5	90	150	.75	0	S	0.0	6:00	–	–	3.0	4860	0.795	6.11	16.5	4.3-1	4.3-3	a
9/18	2	15.6	102	153	1.0	0	S	0.0	12:00	4.5	4.0	5.0	11200	8.721	1.77	4.78	4.3-2	4.3-7	
9/18	3	15.6	102	153	1.0	0	S	0.0	4:30	3.0	2.5	3.7	4210				4.3-3	4.3-11	
9/19	4	15.6	102	153	.75	0	S	0.0	4:00	7.0	4.2	7.0	3744	0.17	22.0	59.5	–	–	b
9/19	5	15.4	100	154	1.0 .38	0	L	48.0	0:35	42.0	–	0.5	539	2.7	.485	1.31	4.3-15	4.3-24	
9/19	6	15.4	100	154	3.2 2.9	–	L	48.0	0:50	42.0	–	–	770				4.3-16	4.3-24	c,d
9/19	7	15.4	100	154	1.0 .38	–	L	48.0	0:50	42.0	–	0.75	770				4.3-16	4.3-24	c,e
9/19	8	15.4	100	154	1.0	–	L	0.8	1:34	13.0	–	–	1450	–	–	–	–	–	c
9/19	9	15.4	100	154	0.5 1.3	–	S	0.0	1:15	–	–	–	925	0.0	–	–	–	–	c,f
9/21	10	15.8	100	158	.75	15	R	2.0	9:00	18.0	8.5	2.0	8530	6.78	1.26	3.40	4.3-17	4.3-24	c,g
9/21	11	15.8	100	158	.75	15	R	2.0	9:00	18.0	–	3.5	8530	–	–	–	4.3-18 to 4.3-21	4.3-24 to 4.3-27	c,h
9/21	12	15.8	100	158	–	7.5	L	–	–	–	–	–	–	–	–	–	–	–	c

Table 4.3-VI Continued

Date (1972)	Test Number	E. B. Output Power (kW)	E. B. Output Current (mA)	E. B. Voltage (kV)	Standoff Distance (in)†	Pitch Angle Below Horiz. (°)	Travel Direction of Gun Muzzle††	Travel Speed (in/min)	Beam-On Time (min:sec)	Trench Length or Cavity Height (in)	Trench or Cavity Width (in)	Trench or Cavity Depth (in) (Solidified liquid removed)	Energy Expended (kJ)	Material Removed (kg)	Energy per Mass Removed (kJ/g)	Energy per Volume Removed (kJ/cm³)	Figure Number	Text Page Number	Comments
10/3	13	13.9	93	150	2.3 1.4	24	R	37.6	0:57	5.0	-	-	792	-	-	-	-	-	c,i
10/3	14	13.9	93	150	2.3	24	R	37.6	1:00	5.0	-	-	834	-	-	-	-	-	c,i
10/3	15	13.9	93	150	2.3 1.4	24	R U L	37.6 24.0 29.0	3:00 Total	31.0 18.0 15.0	- - -	0.5	2500	-	-	-	-	-	c
10/3	16	13.9	93	150	2.3 1.4	24	R U L	37.6 24.0 29.0	2:10 Total	31.0 18.0 15.0	- - -		1810	-	-	-	-	-	c,j
10/9	17	15.9	102	156	0.5	0	S	0.0	2:07 Total	See Comments			2020	0.0	-	-	4.3-6 4.3-7 4.3-14 4.3-23	4.3-17	k
10/9	18	15.9	102	156	0.5	0	S	0.0	1:55 Total	See Comments			1780	0.0	-	-	4.3-6 4.3-14	-	l
10/9	19	15.9	102	156	1.0	0	S	0.0	2:07 Total	See Comments			2020	0.0	-	-	-	-	m
10/9	20	15.9	102	156	2.0 1.5	0	RL	38.0	12:45	21.0	-	1.6	12160	30.7	0.34	1.07	4.3-24	4.3-31	
10/9	21	15.9	102	156	1.5	18	U	1.0	18:37	11.5 8.8	1.25 2.5	-	17760	10.0	2.74	7.40	-	-	n
10/10	22	15.5	100	155	1.0	-	U	40.0	0:12	8.0	0.5	0.44	186				4.3-25 4.3-26	4.3-33	o
10/10	23	15.5	100	155	1.0	-	U	22.0	1:36	8.0	0.9	1.4	1490				4.3-27	4.3-25	o,p
10/10	24	15.5	100	155	1.0	-	U	5.0	1:36	8.0	1.4	1.25	1490				4.3-28	4.3-38	o
10/10	25	15.5	100	155	1.0	0	S	0.0	7:15	3.5	-	4.0	6740				-	-	c,o

Table 4.3-VI Continued

Date (1972)	Test Number	E. B. Output Power (kW)	E. B. Output Current (mA)	E. B. Voltage (kV)	Standoff Distance (in)†	Pitch Angle Below Horiz. (°)	Travel Direction of Gun Muzzle††	Travel Speed (in/min)	Beam-On Time (min:sec)	Trench Length or Cavity Height (in)	Trench or Cavity Width (in)	Trench or Cavity Depth (in) (Solidified liquid removed)	Energy Expended (kJ)	Material Removed (kg)	Energy per Mass Removed (kJ/g)	Energy per Volume Removed (kJ/cm³)	Figure Number	Text Page Number	Comments
10/17	26	14.1	88	160	1.3	11	U	1.0	6:38	6.5	2.5	4.8	5610				4.3-29 4.3-30	4.3-39	q
10/17	27	14.1	88	160	1.3	15	U	1.0	4:42	5.0	1.0 -1.5	2.9 -3.1	3980				4.3-30	4.3-42	o,r
10/17	28	13.6	85	160	1.3	11	U	1.0	7:00	8.5	1.0 -1.5	2.6 -3.5	5710	54.8	1.10	2.98	4.3-31	4.3-42	o,s
10/17	29	13.1	82	160	1.3	11	R	1.0	30:00	21.0	2.0 -4.0	1.9 -2.8	23600				4.3-32	4.3-42	o,t
10/17	30	13.1	82	160	1.3	16	U	1.0	26:00	24.0	1.7 -2.3	2.8 -4.0	20400				4.3-33	4.3-45	
10/17	31*	13.1	82	160	6.0	16	S	0.0	1:20	5.0	5.0	0.75	1050	0.195	5.39	14.5	4.3-58	4.3-77	
10/17	32*	13.1	82	160	6.0	16	S	0.0	2:00	3.5	3.5	1.4	1570	0.295	5.33	14.4	-	-	u
10/18	33	13.0	81	160	1.0	14	L	1.5	15:00	19.0	-	-	11790	8.6	1.36	3.67	4.3-34	4.3-45	v
10/18	34	13.0	81	160	0.8	14	S	0.0	6:00	-	-	3.4	4680	9.1	.514	1.39	4.3-5 4.3-35	4.3-48	
10/18	35	13.0	81	160	0.8	14	S	0.0	1:45	-	-	2.0in 0:45	1360	13.2	.103	.279	-	4.3-48	
10/18	36	13.0	81	160	1.7	14	U	1.0	6:03	5.8	2.0	3.0 -4.2	4720	19.6	.241	.650	4.3-36 4.3-37 4.3-38	4.3-49	

Table 4.3-VI Continued

Date (1972)	Test Number	E. B. Output Power (kW)	E. B. Output Current (mA)	E. B. Voltage (kV)	Standoff Distance (in)†	Pitch Angle Below Horiz. (°)	Travel Direction of Gun Muzzle††	Travel Speed (in/min)	Beam-On Time (min:sec)	Trench Length or Cavity Height (in)	Trench or Cavity Width (in)	Trench or Cavity Depth (in) (Solidified liquid removed)	Energy Expended (kJ)	Material Removed (kg)	Energy per Mass Removed (kJ/g)	Energy per Volume Removed (kJ/cm³)	Figure Number	Text Page Number	Comments
10/19	37	13.6	85	160	1.0 1.4	18	U	1.0	22:00	23.5	2.0	3.7	17950	20.5	.875	2.36	4.3-40 to 4.3-44	4.3-53	
10/20	38*	14.4	90	160	6.0	0	S	0.0	30:00	6.0 -7.0	6.0	5.5	25920	6.2	4.15	11.2	4.3-57 4.3-58	4.3-77	
10/24	39	13.8	86	160	1.5	16	U	1.1	20:30	24.0	1.1 -1.5	2.7 -3.5	16970	-	-	-	4.3-45 4.3-46	4.3-59	w
10/24	40	16.0	100	160	0.8	0	S	0.0	30:00	9.0	-	5.0	28800	159.2	.180	.487	4.3-47	4.3-62	
10/25	41*	16.0	100	160	4-5	17	UD	20 -37	6:30	22.5	3.5	1.25	6240	43.8	.581	1.57	-	4.3-80	x
10/25	42*	16.0	100	160	4-5	17	UD	20 -37	20:00	22.5	-	1.5 -2.0	19200				-	4.3-81	x
10/25	43	16.0	100	160	0.8	12	S	0.0	9:20	8.5	5.5	3.6	8960	18.5	1.48	4.00	4.3-51	4.3-68	
10/25	44	10.2	80	150	0.8	12	S	0.0	30:00				18360				4.3-52 4.3-52	4.3-68	y
10/25	45	10.7	70	153	1.0	12	U	0.95	17:50	16.7	1.75 -2.0	2.6	11450	4.5	2.54	6.87	4.3-54 4.3-55	4.3-71	
10/26	46	10.7	70	153	1.3	-	S	0.0	45:00	8.5	5.1	3.0 -3.6	28890	6.0	4.81	13.0	-	-	

Table 4.3-VI Continued

Notes:

† Two values are given for some horizontal traverses. The first is the value at the left end; the second is the value at the right end.

†† S: stationary; U: upward; D: downward; L: left; R: right

* Spalling attempts

Comments:

a. First indication that cavities grow upward at expense of depth.

b. Pierced into pre-existing hole #1.

c. Does not appear on location chart.

d. Pierce for 25 sec.; then begin translation.

e. Made one pass, chipped out glass, and made second pass; material broke off between #5 and #7.

f. Sequence of 15 sec. piercings (5 of them) spaced 4 1/4 in. apart. Produced no cracks.

g. Width is of triangular cross section which broke off as result of cut.

h. A second, identical pass increased the depth by 1.5 in.

i. Traverse stopped by x-ray interlock.

j. This was a second pass made over #15.

k. A series of seven separate piercings. Cavity widths at rock face and depths were as follows:

Piercing Time (sec.)	Width (in.)	Depth (in.)
1	0.19	0.91
2	0.25	1.22
4	0.33	1.42
8	0.33	1.77
16	0.33	1.97
32	0.87	2.99
64	1.45	2.56

Table 4.3-VI Continued

l. Separate piercings repeating the last three of #17.

Piercing Time (sec.)	Depth (in.)
16	2.25
32	2.28
64	2.40

m. Repeat of #17 but with a 1.0-in. standoff.

Piercing Time (sec.)	Width (in.)	Depth (in.)
1	0.39	0.90
2	0.51	0.90
4	0.67	1.22
8	0.79	1.57
16	0.91	2.12
32	1.04	2.68
64	1.26	2.76

n. The trench was in two sections because of a skip resulting from the gun's jamming against the rock face.

o. Use air jet.

p. Four successive traverses at the same position.

Pass #	Depth (in.)	Width (in.)
1	0.51	0.5
2	0.79-0.87	-
3	1.1	-
4	1.4	0.9-1.0

q. Gun jammed against rock making traverse speed uncertain.

r. Gun movement stopped because of debris stuck to muzzle.

s. Deepest penetration was at beginning where beam was held stationary for 25 sec.

t. Gun periodically withdrawn slightly to free it from being held by debris or jamming against rock face due to lack of parallelism between direction of motion and rock face.

u. Spall test performed without moving gun from position of #31. Cavity width is listed as smaller than that of #31 since this second cavity appeared in the center of the previous one.

Table 4.3-VI Continued

v. Traverse lasted for only the first 9 min. 45 sec.

w. Flow water over rock surface during traverse.

x. Up and down in rapid succession, 37 ipm up, 20 ipm down.

y. This is a continuation of #43 after a 15 min. cooldown.

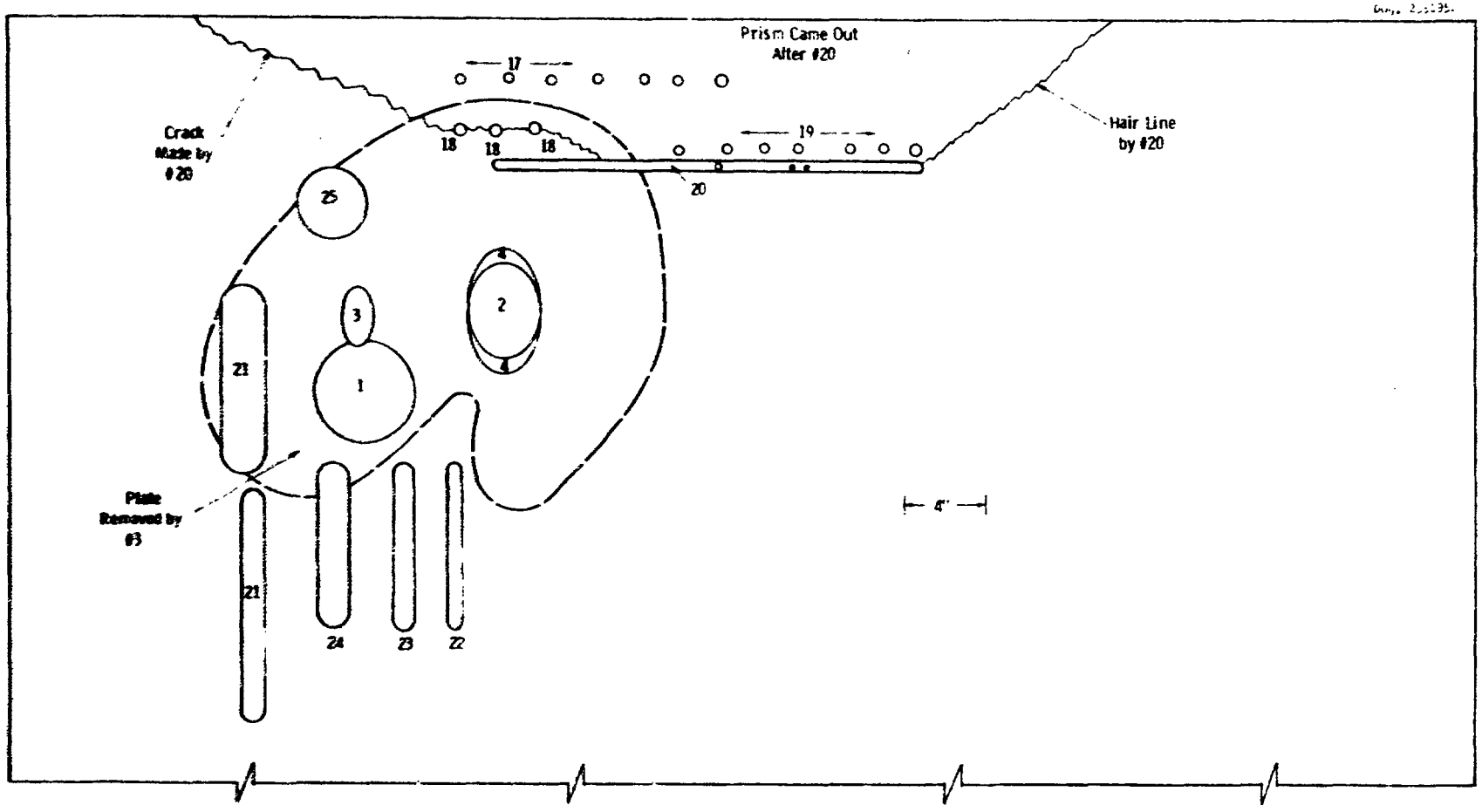

Fig. 4.3-61 Schematic view of first face of 6-foot cube of Sierra White Granite. Numbers are keyed to the data summary of Table 4.3-VI.

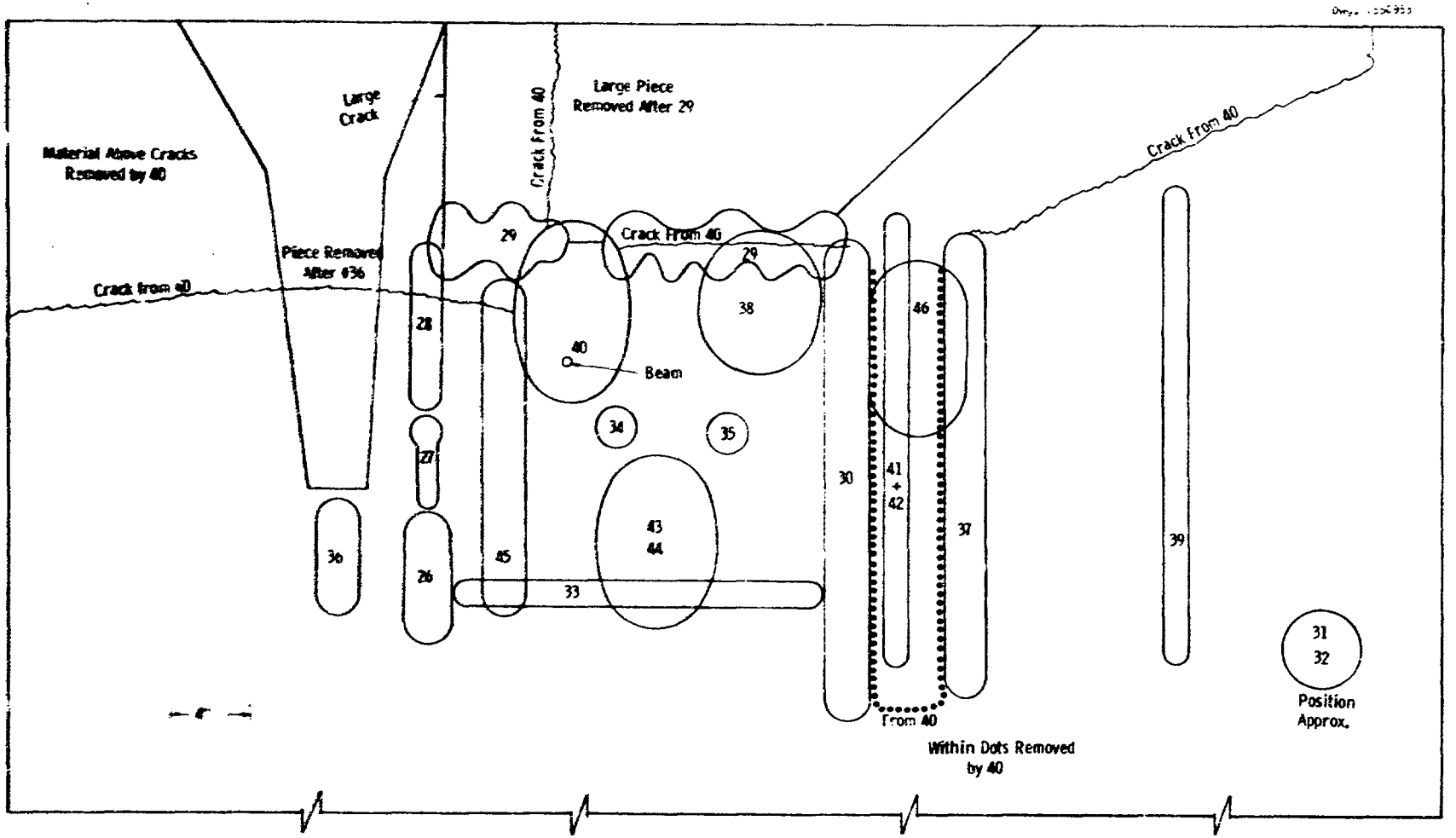

Fig. 4.3-62 Schematic view of second face of 6-foot cube of Sierra White Granite. Numbers are keyed to the data summary of Table 4.3-VI.

5. THEORETICAL STUDIES

5.1 Tests In Support of the Theoretical Studies

To check the penetration rates predicted by equation (5), of Section 5.2, a few laboratory tests were made with our low-power 9 kW electron gun shooting a beam vertically downwards.. In one series of tests, the beam was fired into the top face of a larger piece of rock, as we have done in the past. This has the disadvantage that liquified rock may accumulate at the bottom of the cavity; this factor is not included in our theoretical analysis. Therefore, another set of tests was made in which the beam drilled the cavity very close to a vertical face of the rock. In this case, the cavity breaks through and the liquified rock can flow downwards and out. This corresponds more closely to our theoretical assumptions, and would closely resemble the conditions that we find drilling a cavity with a horizontal beam. Besides, the test is not involuntarily interrupted by the fracture of the rock. Figure 5-1 shows such "cavities" drilled along the smooth face of a block of black gabbro from Oklahoma. The beam, running parallel to the face, hit the top of the sample roughly 0.025 inch from the edge of the rock. Figure 5-2 summarizes the penetration as a function of time as measured in both types of tests.

For the penetration observed along the rock face, the theoretical curve follows the experimental points closely. However, penetration into the body initially proceeds faster, which can be explained by the fact that the vapor temperature is higher in the closed cavity. Therefore, the beam scattering is lower, and the power density remains higher than is assumed in the theory. On the other hand, the penetration into the body levels off after 6 to 7 seconds, most likely because liquid rock has accumulated at the bottom of the cavity. These differences have not been investigated further.

Beam "ON" Time (secs)	32.0	17.9	8.0	4.0	2.1	1.1

Fig. 5-1 Cavities drilled along the smooth face of a sample of Oklahoma gabbro. The beam, running parallel to the face, hit the top of the sample roughly 0.025" from the edge of the rock. 9 kW beam power, 150 kV; standoff distance 1/2 in. Beam "on" time, from left to right, 12.0/17.9/8.0/4.0/2.1/1.1 seconds.

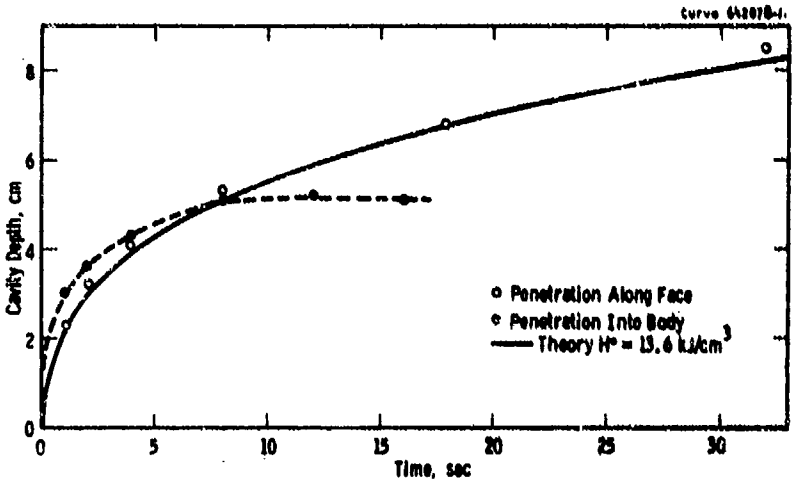

Fig. 5-2 Measured growth of cavity with time for Oklahoma gabbro. The beam, aimed vertically downward into the body, is stopped at 5 cm by the continual accumulation of liquid flowing from the cavity walls. Penetration along the face simulates the action of a horizontal beam, in that the liquid does not collect at the cavity bottom. The solid curve represents the theoretical prediction derived in Section 5-2 which agrees well with the experimental data shown here. (Beam power, 9 kW @ 150 kV; standoff, 1/2 in.)

Figure 5-3 shows how our general theory agrees with what we find in different kinds of rock. Cavities were drilled, again along the face of the rock, in copper ore, in a calcareous sandstone, in so-called Sioux quartzite, and in the Oklahoma gabbro. If anything may be concluded from these few tests, then we can say that the initial penetration is perhaps faster than predicted by the theory based on heat of evaporation of $H^* = 14$ kJ. The later penetration is not as deep as predicted, especially for the sandstone. In quartzite, the cavity is not produced by melting but rather by spallation and the explosive expulsion of small particles; in other words; less energy H^* is needed than for vaporization. The experimental points fall roughly on a curve computed with a value of $H^* = 2.6$ kJ. In this case, the whole experiment was also self-terminating after five seconds when the small block burst into pieces.

Figure 5-3 also shows theoretical curves computed for $H^* = 2.6$ kJ, 7.5 kJ, 13.6 kJ, and 21.3 kJ. The different behavior of the sandstone can perhaps be explained on the basis that, initially, it spalls ($H^* = 7.5$ kJ) and later spalling is inhibited by a layer of molten rock. Alternatively, liquid that keeps flowing into the beam region may inhibit cavity growth. It could also be that heat conduction is greater in the sandstone than in the other rocks and the assumption of an adiabatic process is no longer true.

Obviously, there are many details yet to be investigated but, in general, we feel that our simple theory represents very well the initial piercing rates at least for the first 30 seconds, and it can be used as a basis for the temperature and stress computations.

Another test seemed of particular interest, namely, to determine the penetration efficiency as a function of beam power. Figure 5-4 shows how cavity depth increases with beam power when the total <u>energy input</u> is held <u>constant</u>. The more quickly a given amount of energy is delivered, the deeper is the cavity, since the adiabatic conditions are more closely approached. When adiabatic conditions are fully

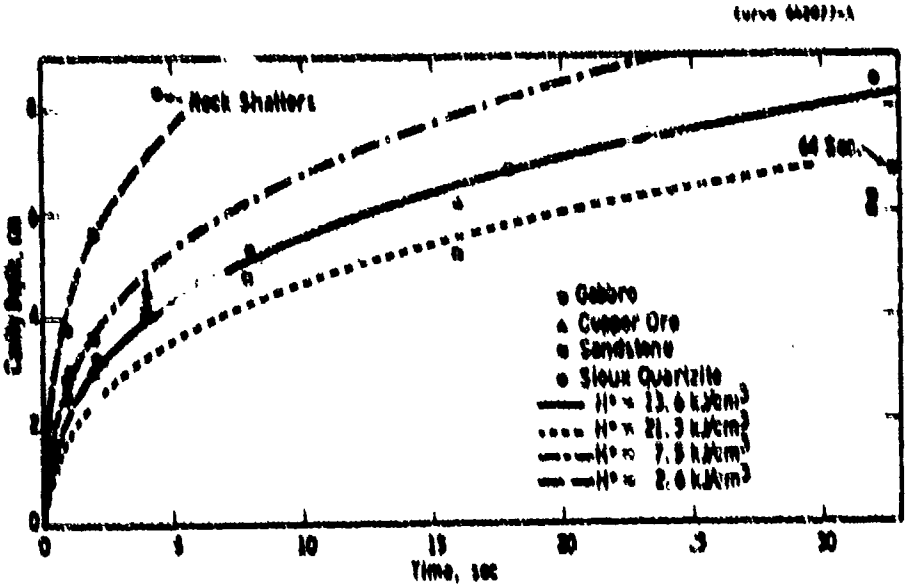

Fig. 5-3 Measured growth of cavity with time for several types of rock. Gabbro and copper ore siltstone agree with the original theoretical curve ($H^* = 13.6$ kJ/cm^3), Sioux quartzite exhibits a lower heat of removal ($H^* = 2.6$ kJ/cm^3) because the material spalled out of the cavity in the form of a fine sand. The sandstone does not agree well with the theory, following the $H^* = 7.5$ kJ/cm^3 for the first few seconds and then dropping below the $H^* = 21.3$ kJ/cm^3 line near 15 sec. This discrepancy may have the same cause as the drop in the depth-to-width ratio for sandstone as shown in Fig. 5-8.

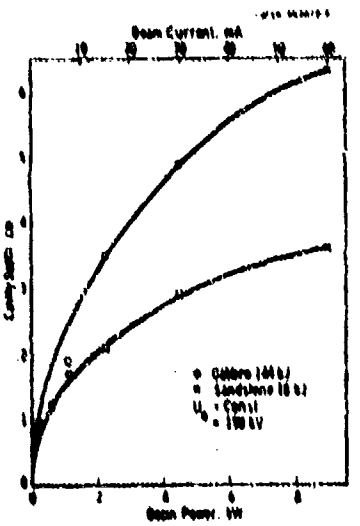

Fig. 5-4 Influence of the beam power on the achieved piercing depth for constant energy input (variable piercing time). The higher power beam is obviously more efficient. This is one of the power dependent effects mentioned in Section 3.2.2. Standoff distance, 1/2".

obtained, then the cavity depth should no longer depend on beam power. For the gabbro and the 9 kW beam, this is not yet quite the case. Hence, with the higher beam power that we will have for the field tests, the piercing rate should increase faster than proportionally with power. Figure 5-4 illustrates rather drastically the importance of the adiabatic conditions and, therefore, the fact that with a low power beam, say 2 kW, one simply cannot get representative experiments that provide a valid basis for extrapolation to higher power levels. Obviously tests at higher power and higher voltages, say at 200 kV, 60 kW, would be extremely interesting.

As mentioned earlier, the beam width is not entirely determined by beam scattering but also by beam optics, mainly the angular aperture of the beam as it is focused by the magnetic lens. The angular aperture as well as the position of the so-called crossover can be moved by changing the current through the lens. As discussed elsewhere the product of angular aperture α_o and diameter of the beam at the focus spot, $\bar{d}_o$, is constant or, in other words, the so-called radiance of the beam is an invariant. If we reduce the angular aperture, we will automatically increase the diameter of the beam at the focus and reduce the power density N*. As to which factor is of the greater importance if we aim for maximum penetration, it depends on the circumstances. For instance, if the power density is already so high that adiabatic conditions prevail, then it is not necessary to increase it further. With our present machine, we can vary the position of the crossover only within narrow limits. But to see whether the focus position is of any importance under our present conditions we made the comparative test with the results listed in Table 5-1. A reduced focus current means the crossover is further away from the orifice of the gun and closer to the top surface of the rock. A small change in focus position will produce an increase in the depth of the cavity of 10 percent in the case of the sandstone and of 17 percent, for the gabbro.

A spinning disc beam analyzer was used to measure beam power profiles. Figure 5-5 shows an example corresponding closely to the

Focus Current 1.28 A

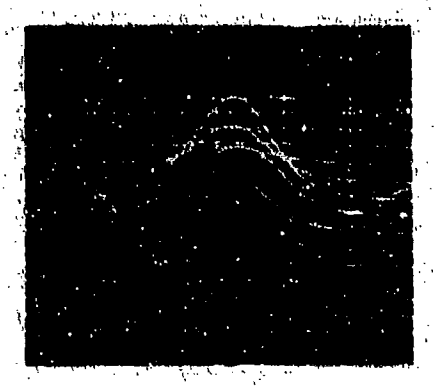

Focus Current 1.14 A

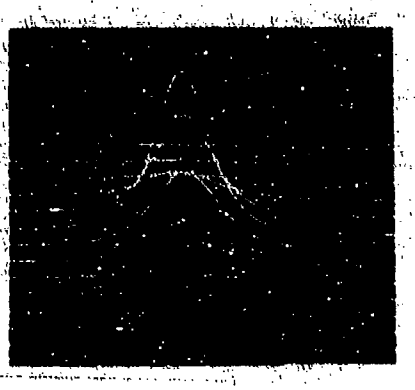

Fig. 5-5 Measured beam power density as a function of focus current.

Table 5-1
Influence of Focus Position on the Depth of Penetration

Rock	Beam Current	Elapsed Time	Focus Current	Cavity Depth	Increase in Cavity Depth
Sandstone	15 mA	8.0 sec	1.30A	2.1 cm	-
"	15	8.0	1.18	2.3	10%
Gabbro	30	8.0	1.30	2.8	-
"	30	8.0	1.24	3.3	17%

(The extent to which the focus could be changed was limited by certain design parameters of this gun.)

conditions of Table 5-1. Total beam current was 60 mA and 150 kV and the plane of measurement, 1/2 inch below the gun exit orifice. At 1.28 A focus current, optimum beam transmission efficiency was obtained, but at 1.14 A, the beam spot in the plane of measurement is noticeably narrower. The beam angle is also smaller because of the longer focusing distance. The gun was adjusted to keep the beam current the same for both cases. Each trace in Figure 5-5 represents a scan through the beam at various distances from the center axis. The horizontal scale is 1 major division = 0.085 cm; scan lines are separated by 0.04 cm. The vertical scale is arbitrary. Detailed evaluations have not been made at this time.

Our field test gun will have a greater latitude in the position of beam focus than was available for the test of Table 5-1.

Just to collect all the information that is contained in the above tests, and without any attempt at completeness of the analysis, we have replotted in Figure 5-6 the observed depth vs. beam power (as already shown in Figure 5-4) in logarithmic coordinates. Going to higher beam powers, yet keeping the expended energy constant, clearly has advantages. Furthermore, Figure 5-7 shows the depth-to-width ratio obtained from <u>constant energy input</u> but with <u>various</u> beam <u>powers</u>; there is a marked difference between sandstone and gabbro. If, however, we plot depth-to-width as a function of depth for a power of 9 kW, as in Figure 5-8, we get initially (for small depths in the order of 1 inch) large differences for different rocks. Yet these disappear when we reach 2 to 4 inches depth. There, the depth-to-width ratio approaches a common value of about 4.25. Because of the limited number of observations, we do not want to speculate on the reasons for this behavior.

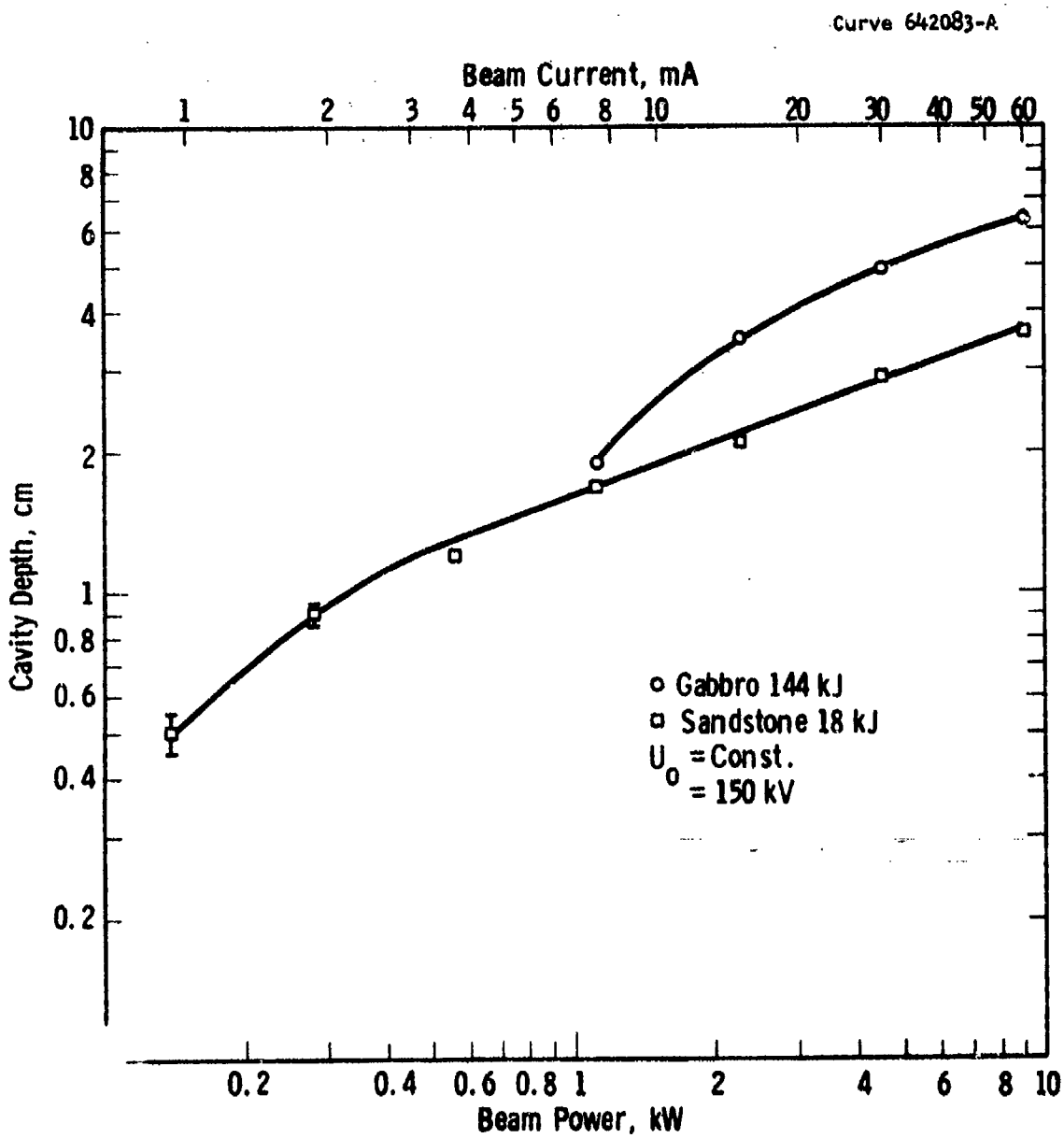

Fig. 5-6 Increase in efficiency with beam power. Same data as Fig. 5-4, but on a log scale. There is no indication of any levelling off at 10 kW.

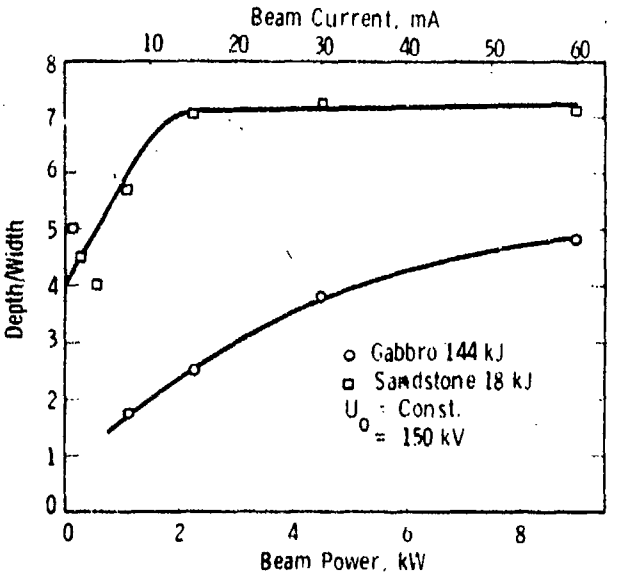

Fig. 5-7 Depth-to-width ratio as observed vs. beam power for constant energy input. The beam power obviously may or may not be of importance, depending on the type of rock and on the power level itself. Standoff distance 1/2".

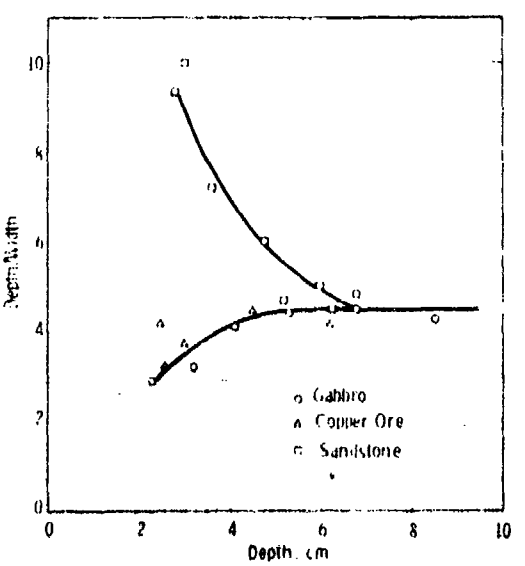

Fig. 5-8 Depth-to-width ratio as a function of final depth; the exceptional behavior of sandstone may be due to initial spalling, but it was not further investigated (see also Fig. 5-3). Beam power 9 kW, 150 kV; standoff distance 1/2".

Long after the here discussed tests were completed, the piercing tests reported in Section 4.3.2 were made, of which Fig. 4.3-14 gives a summary. These tests were limited in scope for various reasons, as mentioned. Obviously one would want to see the curve of Fig. 5-6 extended to (a) higher power and (b) to include the Sierra White granite. Similarly one would like to know where in Fig. 5-8 the points for the Sierra White granite would fall. We had to leave these question open, to be answered by later investigations.

5.2 Analysis of the Piercing Process

High-powered electron beams, when sharply focussed, can quickly vaporize deep, narrow cavities in rock, the three major factors in the process being the high power of the beam, the high power density at its center, and the low thermal diffusivity typical of rock. The piercing occurs because of intense thermal energy generated by the kinetic energy of electrons as they bombard the rock. Furthermore, this energy is delivered so quickly and in such small areas that only a small portion of it can diffuse into the rock by heat conduction (a quasi-adiabatic condition made possible by the low thermal diffusivity).[27] Accordingly, the major portion of the energy causes extreme local heating which melts and vaporizes material off the cavity bottom and thus extends the cavity's depth.

Initially, the penetration speed is very high (typically 2.5 in/sec at 9 kW) but decreases with increasing depth because the power density of the beam suffers increasing degradation as the beam travels the ever increasing distance to the bottom of the cavity. Note that the electron gun is many times wider than the cavity and therefore cannot follow the receding rock face. The degradation of the beam's power density is due primarily to multiple scattering of the electrons by molecules of air and vaporized rock in the cavity. Although this

scattering process absorbs only a small fraction of the electron energy, it nevertheless broadens the diameter of the beam, thereby diminishing the density of its power while preserving nearly all of the initial total power. Consequently, as the cavity grows deeper and the power per unit area hitting the bottom decreases, the growth rate of the cavity also decreases.

Although the diameter of the cavity grows with time, it does so more slowly than the depth. At the widest point, usually about half way into the cavity, the diameter is typically only 1/4 the depth. Its slow growth rate is a result of the relatively small amount of power striking the walls as compared to that hitting the cavity bottom. The power to the walls comes from the relatively few electrons which are scattered out of the main beam and from the transfer of thermal energy from the jet of hot gas vaporized off the cavity bottom. The energy is deposited sufficiently slowly that a substantial fraction is carried away by heat conduction into the rock, and the quasi-adiabatic condition is therefore not satisfied. As a result, only a portion of the power to the walls is available for vaporizing away material, i.e. available for expanding the cavity diameter. In fact, one finds the walls covered with a layer of (often viscous) molten rock through which heat flows into the solid material. It is this heat flow, in fact, which sets up the steep temperature gradients that produce the thermal stresses on which the rock-cracking process ultimately depends.

Previous experience has shown that a beam of, say, 9 kW and 150 kV will pierce a 2 in. deep hole within 15 to 30 seconds, by which time failure from thermal stress will usually have ocurred in laboratory rock samples (typically blocks 6 to 10 in. on a side). In larger blocks it is necessary to pierce for longer periods (2 to 5 minutes) during which time the cavity will grow further to a depth of 4 to 6 in. For considerably longer piercing times, the depth of the cavity will grow so slowly that its speed is no longer comparable to the speed of the thermal conduction. Under such conditions the quasi-adiabatic approximation no longer applies, and calculating the dependence of depth on time becomes quite complicated.

With a view towards understanding the effects of electron beams on rock, we have developed a mathematical model that predicts rate of penetration as a function of time. In calculating the penetration rate, recognizing the high total beam power as well as the high power density at the center of the beam, we use the quasi-adiabatic approximation which greatly simplifies writing down heat balance relationships. This condition holds true at the bottom of the cavity for nearly all piercing times of interest and consequently allows us to calculate the rate of material removal (through vaporization) and thus the depth to which the cavity will grown in a given time. Conversely, it is difficult to predict the shape of the cavity because the quasi-adiabatic condition is violated on the walls. Since the complicated boundary conditions make it too costly and time consuming to calculate the expected cavity shape at this time, we use a simple illustrative model in the subsequent phases of the theoretical program where we estimate the time dependence of the temperature profile and stress distributions within the rock.

Besides, the quasi-adiabatic removal of material the piercing rate is dominated by a decrease with distance of the power density at the center of the beam, which is caused mainly by the multiple, small-angle scattering of the electrons. Other effects do exist which also tend to degrade the beam, but are quite small for the power levels and distances involved. For example, because of the low gas density in the cavity, energy lost from the beam through ionization of the gas causes a loss of only about 3% in the energy of the average individual electron before it reaches the bottom of a 5 in. deep cavity. Another factor is the broadening of the beam and consequent reduction in power density due to an initial angular divergence of the beam at the exit nozzle of the gun as caused by the electron optics system. This effect is also small; for an initial beam envelope half angle of as much as 3° it accounts for only 6 percent of the beam diameter at a typical stand off distance of 1/2 in. This contribution continues to drop with distance from the gun to only 3% at the bottom of a 5 in. deep cavity. That the initial beam divergence has such a small effect is a consequence

of the random-walk process of the multiple scattering. For relatively small initial beam divergence angles, it is appropriate to combine the effects of divergence and scattering by adding the two contributions in quadrature. Consequently, the effect of scattering almost entirely masks the effect of the initial beam angel. As a result, as long as the beam's initial angular divergence is sufficiently small, its actual value has negligible influence on the beam divergence outside the gun. Another energy loss mechanism which turns out to be small is bremsstrahlung (energy loss to x-rays produced in the electromagnetic field of the atomic nucleus). It becomes important only at electron energies greater than about 7000 keV, i.e. much greater than the 150 keV of the electron beam rock cutter. In fact, measurements show that only about 1/4% of the total incident beam power is lost to x-rays. However, at the point where the electrons hit the dense molten rock or the solid rock of the walls or of the bottom of the cavity, energy loss through ionization is the dominant effect. It is through this mechanism that the electrons give up nearly all of their kinetic energy to the material and thus produce the intense heat needed for piercing. In losing its energy, an individual electron characteristically penetrates 80 to 100 μm into the molten or solid material, and although it is possible for it to back-scatter out of the material, only about 5% of the incident power is reflected in this fashion.

As mentioned above, under the quasi-adiabatic approximation, the peak power density of the beam, i.e. the power per unit area, N*, at the beam center, determines the growth rate of the cavity depth. Knowing this power density makes it possible to evaluate the power transferred as thermal energy to a small area at the bottom of the cavity. Then knowing the energy required to remove a unit volume of rock through, for example, vaporization and making the assumption that no heat is conducted away, one can calculate the thickness of the layer of material removed in a given time and thus obtains the penetration speed (See Fig. 5-9). To determine the peak power density N*, one first considers the current density of the beam at various distances

from the electron beam gun. According to multiple scattering theory,[17] valid for particles which lose only a small portion of their energy when passing through a thickness of material, an electron beam, initially

Dwg. 2958A28

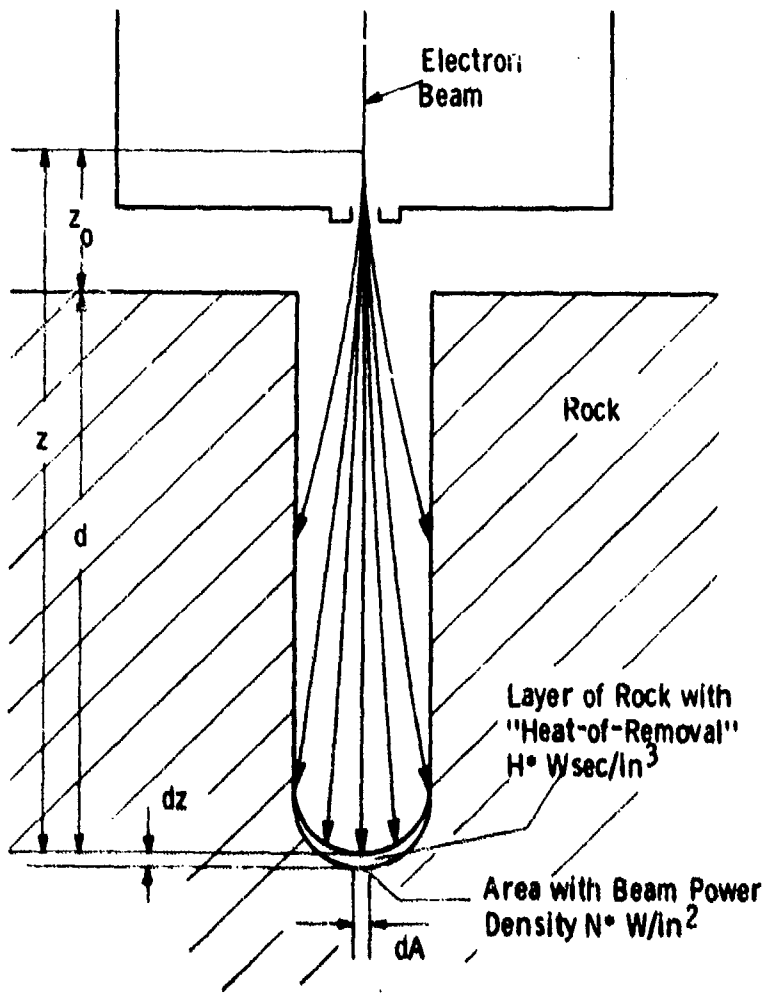

Growth rate of cavity (under adiabatic conditions, i.e. no energy loss due to heat conduction)

$$\frac{dz}{dt} = N^*/H^* \text{ In/sec}$$

Fig. 5-9 Schematic diagram with definitions for cavity growth rate calculations.

of negligible diameter, flowing in the +z direction through the gas and starting at z = 0 has a current density distribution whose z-component at a distance z can be approximated by a Gaussian in the x-y plane of the form:

$$J_z(x,y,z) = \frac{I_o}{2\pi\alpha z^3} \exp\left\{ - \frac{x^2 + y^2}{2\alpha z^3} \right\} \quad \mathrm{Acm}^{-2} \qquad (1)$$

where I_o is the total beam current and where the parameter α is given by:

$$\alpha = \frac{2\pi}{3} n \left(\frac{2Ze^2}{pv} \right)^2 \ln\left(\frac{192}{Z^{1/3}} \frac{p}{mc} \right)^{1/2} \quad \mathrm{cm}^{-1} \qquad (2)$$

Here n is the number of atoms in the vapor or gas per unit volume, Z is a weighted average of the atomic numbers of the elements in the gas, e is the electronic charge, p is the relativistic momentum of each individual electron, v is the electron velocity, m is the mass of the electron, and c is the speed of light. For such a beam, the characteristic (rms) radius is

$$r_o = (\alpha z^3)^{1/2}$$

which, it will be noted, increases faster than proportionally with distance, i.e. with the 3/2 power of z. The peak power density, N^*, found at the center of the beam, is obtained by setting x and y to zero in equation (1) and multiplying the resulting peak current density by the electron gun acceleration potential V_o, which even at the cavity bottom is very nearly equal (numerically) to the individual electron energy measured in eV.

$$N^* = J_z(0,0,z)V_o = \frac{I_o V_o}{2\pi\alpha z^3} = \frac{W_o}{2\pi\alpha z^3} \quad \mathrm{Wcm}^{-2} \qquad (3)$$

W_o is the total beam power $I_o V_o$.

The following argument gives the penetration rate. If H^* represents the total heat of removal per unit volume, then it is necessary to supply the energy H^* dAdz (see Fig. 5.1) to remove an infinitesimal volume of rock from the bottom of the cavity. However, the energy entering this volume during the time interval is given by N^* dAdt, which when set equal to the removal energy, gives the equation

$$H^* \, dAdz = N^* \, dAdt$$

from which we obtain:

$$\frac{dz}{dt} = \frac{N^*}{H^*}$$

Combining this result with Equation (3) gives the penetration rate as a function of z.

$$\frac{dz}{dt} = \frac{W_o}{2\pi H^* \alpha z^3} \tag{4}$$

Integrating equation (4) gives the cavity depth $d(= z-z_o)$ as a function of time (again refer to Fig. 5-9).

$$d = \left\{ \frac{2W_o}{\pi H^* \alpha} t + z_o^4 \right\}^{1/4} - z_o \tag{5}$$

Here z_o is the distance the beam goes from the point where it first begins to scatter to the point where it first hits the unpierced rock face.

The quantity α, which characterizes the scattering process and which is an important parameter in the speed and depth of penetration, depends directly on n, the atomic density of the gas in the cavity (see Equation (2)). This density, which varies inversely as the gas temperature,

is difficult to predict theoretically and inconvenient to measure experimentally. Consequently, as a value for α, we use $\alpha = 1.10 \times 10^{-3}$ cm^{-1} (or 2.78×10^{-3} $in.^{-1}$) which was experimentally determined from previous beam profile measurements made at our customary beam voltage (150 kV).[18] The theoretical expression for α as shown in equation (2) is useful, however, for indicating the expected dependence of the beam divergence on electron energy and rock material. Figure 5-10, for example, for which the above value of α was used, shows the severe drop in peak beam power density with cavity depth as calculated using equation (3). The figure contrasts the sharp loss of power density with the nearly constant energy of the individual electrons which make up the beam.

Several remarks can be made concerning the influence on the cavity growth of the beam current I_o and the accelerating voltage V_o. For example, the quantity α varies almost inversely as the square of the voltage since (a) pv in equation (2) is nearly proportional to the individual electron energy for voltages up to $\sim$ 250 keV and (b) the logarithm term in equation (2) is only a slowly varying function of electron momentum. Accordingly, since the total power is given by $W_o = I_o V_o$, the piercing speed is directly proportional to the beam current and is <u>roughly proportional to the cube of the voltage</u>, i.e.

$$\frac{dz}{dt} \sim I_o V_o^{\,3}$$

This relationship shows that the piercing performance of future higher-power electron beam guns depends strongly on whether the power increase results from raising the current or from raising the voltage the latter being made more desirable. Figure 5-11 compares the piercing speeds obtained by raising the power through current increase vs. raising the power through voltage increase. Both curves are calculated using equation (3), for which the dependence of α on electron momentum is calculated using equation (2). It should be noted, however, that at high voltages and small depths, the voltage-increase curve is too

optimistic, for the multiple scattering will eventually be reduced to such an extent that the loss of peak power density will become dominated by the initial beam divergence angle. Conversely, the current increase curve is too pessimistic, for the penetration rates at higher power will increase more than is indicated as a result of the increased heating of

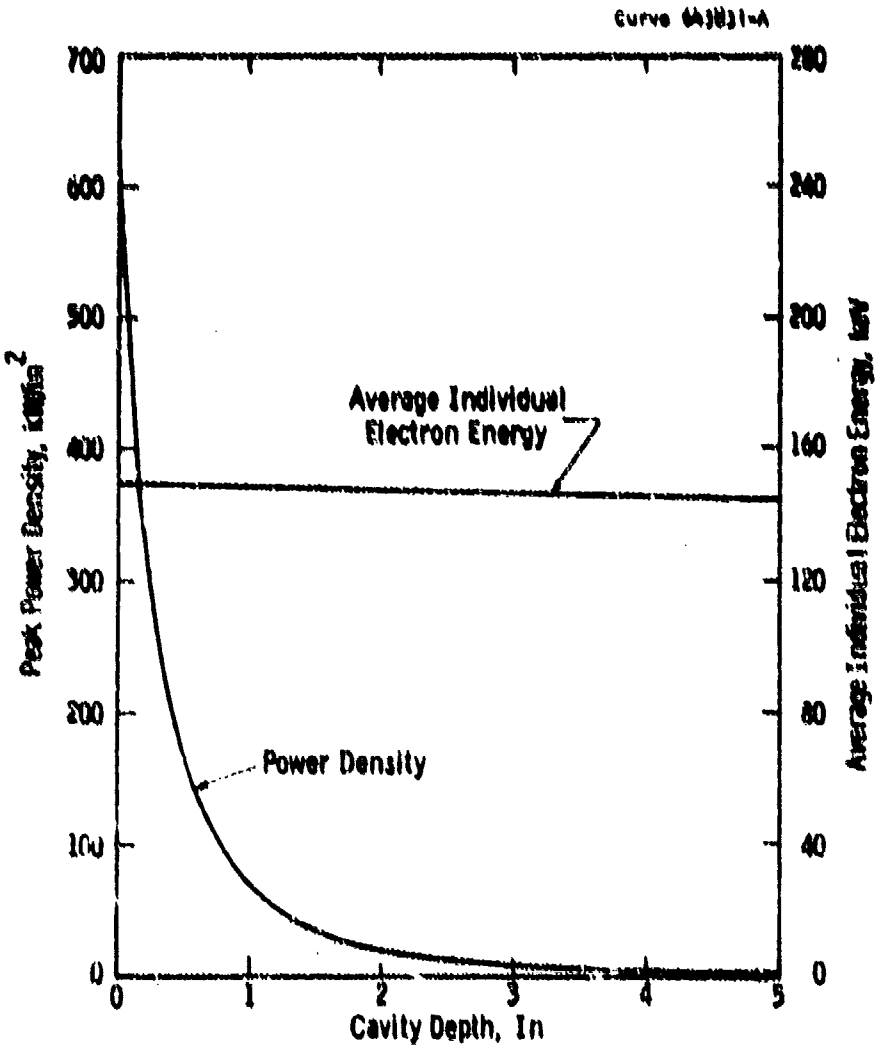

Fig. 5-10 Peak electron-beam power density as a function of cavity depth into rock for a 9 kW, 150 kV electron beam gun, standoff, 1/2 in. Also shown in the average energy vs. depth of a single electron passing through the vapor in the cavity.

the gas in the cavity. With increased gas temperature, the gas density n will decrease, the quantity α will therefore decrease, and the penetration rate will then increase.

The piercing speed also depends on the types of target material. Rocks with higher values of total heat of vaporization H^* will be pierced more slowly. In addition, the quantity α depends on the material type through the square of the average atomic number Z (See equation (2);

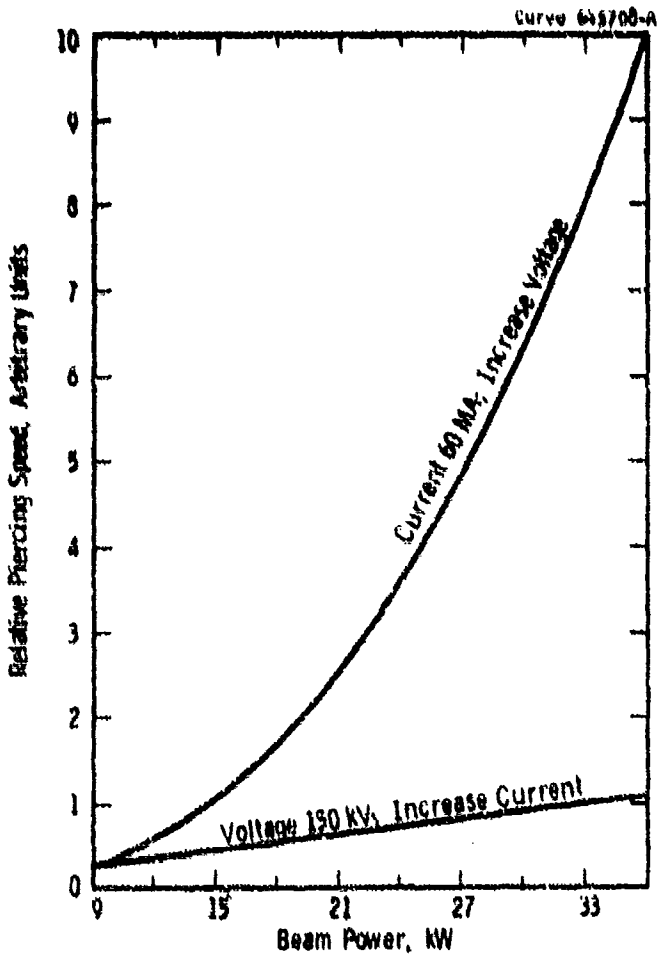

Relative piercing speed of electron beam into rock versus electron beam power

Fig. 5-11 The dependence on beam power of the theoretical piercing speed of an electron beam into rock. The two curves contrast the effects of raising power by increasing either voltage or current.

again the logarithm term is slowly varying. Since the gas in the cavity is mainly vaporized rock, the piercing rate according to equation (4) for a given value of H^* will tend to drop as the square of the weighted average atomic number of the rock's constituent materials. In addition, the gas density n, to which the piercing rate (through α) is inversely proportional, depends on the gas temperature, which, in turn, depends on the vaporization temperature of the rock and super heating by the beam.

The theoretical time development of the cavity depth, as given in equation (5), often agrees remarkably well with which our experimental data as can be seen by the comparison of the theoretical curve (solid line) with the experimental points from laboratory tests made with a 9 kW beam, (see Figures 5-2 and 5-3). We get similar agreement with data taken at 15.9 kW (see Fig. 4.3-14). In each case we get best agreement with the gabbro, for which molten material from the walls readily runs out and allows the beam free access to the bottom of the cavity. In making these theoretical calculations, we use a value of $H^* = 13.6$ kJ/cm^3 for the heat of removal since it fits the gabbro quite well over a large range. As a contrast note the substantially higher value for SiO_2 in Table 5-2. The parameters used in the calculations appear in Table 5-3.

From small values of time (much less than 1 sec at 9 kW) equation (5) indicates that the depth is directly proportional to time. For large times, the depth is roughly proportional to the 1/4 power of the time. Our experimental data are mostly from the intermediate region between these two cases, where the depth appears to vary roughly as the 1/3 power of time.

Remarkable are the absolute values of the initial piercing rate, as well as the first 5 sec. and 10 sec. average, which one can obtain from equation (5) or from Fig. 5-3 and which are listed in Table 5-4.

Three effects have not been considered in formulating the theoretical model for piercing: 1) the spatial variation of temperature, and therefore of gas density, in the cavity as a result of non-uniform heating by the beam; 2) the motion of the molten rock within

Table 5-2
Calculation of the total heat of vaporization of SiO_2
(Quantities from Ref. 19 and Am. Inst. of Phys. Handbook)

Quantity	Value
Specific Heat	
Solid	∿ 0.28 cal/g°C
Liquid	∿ 0.36 cal/g°C
Temperature of	
Melting	1710°C
Vaporization	2227°C (2141°C at 400 torr)
Latent Heat of	
Fusion	34 cal/g
Vaporization*	1530 cal/g
Total Heat of Vaporization	2.22 k cal/g 24.8 kJ/cm^3**

* from Clausius-Clapeyron equation.
** similar to the dotted curve of Fig. 5-3

Table 5-3
Parameter values for depth vs. time function used to compare theory with experiment.

Parameter	Value
W_o	9.0 kW, 15.8 kW
H^*	13.6 kJ/cm^3 = 223 kJ/in.^{3}
α	1.10×10^{-3} cm^{-1} = 2.78×10^{-3} in.$^{-1}$
z_o	2.4 cm = .94 in.

Table 5-4
Initial piercing rates in various rocks (from Fig. 5-3)

Rock Type	1st sec ave.	5 sec ave.	10 sec ave.
Sandstone, H^* = 21.3 kJ	1.7 cm/sec	.72 cm/sec	.46 cm/sec
Gabbro , H^* = 13.6 kJ	2.1	.86	.56
Sandstone, H^* = 7.5 kJ	2.8	1.1	.67
Quartzite, H^* = 2.6 kJ	4.3	1.5	.9
9 kW 150 kV beam			

the cavity as a result of boiling and the force of gravity; and 3) the variation in beam power density caused by macroscopic electromagnetic fields in the beam path caused by the beam's interaction (e.g. ionization) with the material. With regard to the temperature variation effect, the assumed Gaussian beam profile, on which the calculation depends, itself depends on the gas density being constant. However, the gas at the center of the beam is heated much faster than that near the edges and to the first approximation is therefore less dense; thus the assumption of uniform density is violated. On the other hand, there do exist strong convection currents in the cavity together with jets of vaporized rock. These will tend to break up any steep temperature gradients which form within the confines of the cavity and may thus tend to maintain the gas density more or less constant. As for the effect of molten rock, the thickness of the liquid layer is only a small fraction of the cavity diameter in most cases. It is true, however, that for vertical cavities drilled downwards, liquid from the cavity walls does flow to the bottom where it must be continuously removed by the beam. Experimental confirmation of this effect appeared during laboratory tests, where the depth of vertical cavities reached a maximum limit in violation of the prediction of equation (5) (See Fig. 5-2). Note also that for rocks with large concentration of high alkali feldspar the molten material is very viscous, a fact that prevents it from draining quickly off the walls and allows the cavity to become clogged and the piercing to be impeded. Accordingly our calculations are most appropriate for rock with high ferro-magnesium content, for which the molten rock flows easily (e.g. gabbro). Finally, we have found no indication of any macroscopic electromagnetic effects causing equation (5) to be contradicted by our experimental data. Discussion of the laboratory tests and the degree to which they support the theoretical calculations also appear in Section 4.3.2.

5.3 Development of Thermal Stresses with Time

5.3.0 General Comments

Experimental and theoretical experience gained prior to and during the first three months of the project concerning the rate at which electron beams penetrate rock (Section 5.1 and 5.2) has been applied to the theoretical calculation of the resulting thermal stresses. These stresses, in turn, cause the rock to crack. To allow for correlation of the results with experimental data from a then existing 9 kW gun, the calculations were made for the case of an EBG that delivers 9 kW at 150 kV and is 1/2 in. (= 1.3 cm) from the rock face. The size of the rock used in the calculation is typical of a laboratory sample. It is a cylinder, 10 inches in radius and 10 inches high. We assume the beam pierces the center of one of the circular faces so as to give the calculations azimuthal symmetry. Consequently we can apply boundary conditions that are convenient for existing axisymmetric, thermal-stress, computer programs.

Because of the diversity in material parameters among various rock types, extensively detailed results are of only limited use. Our interest lies rather in obtaining a semi-quantitative description to serve as a guide for electron beam excavation. For these reasons we have chosen to make calculations for a single, fictitious, yet typical, type of rock. The cavity growth under an electron beam is therefore assuemd to be similar to that of Oklahoma gabbro because of our success in predicting the piercing rate with this rock. The elastic parameters and thermal diffusity have been chosen similar to those of Dresser basalt since they seem to be smoothly varying with temperature and have been rather well measured.[20] The melting temperature is chosen as that of silica i.e. 1700°C.[19]

To provide the desired information on the time development of the thermal stresses, six separate stress calculations were made. In each case all conditions were kept the same except that each successive calculation was made for a longer piercing time. The six elapsed times were 5, 10, 20, 40, 80, and 300 seconds.

5.3.1 Volume and Shape of Piercing Cavity

If adiabatic conditions prevailed along the walls of the cavity as they do at the bottom, the volume of the cavity would be expected to grow in proportion to the total energy input, and it would be possible, with knowledge of the spatial distribution of energy flow in the beam, to calculate the shape of the cavity in addition to its depth. It has been pointed out, however, that much of the heat to the walls is actually conducted away and carried away by flowing molten material, thus making energy balance calculations too costly and time-consuming to be practical for the present investigation.

From experience we know that cavities tend to be substantially narrower than deep, a tendency illustrated by experimentally determined depth to width ratios shown in Fig. 5-8.

To arrive at a cavity shape to be used in calculations of the temperature distribution and subsequent calculations of the thermal stress distributions, we choose a simple model designed to be reasonable yet tractable. The assumed shape is a cylindrical cavity with a hemispherical bottom. The cavity diameter is taken to be 1/4.2 times the depth, a typical value according to the data in Fig. 5-8. The total depth as a function of time is given by equation (5). Table 5-3 gives the values of the parameters used in the calculations, chosen to represent a 9 kW, 150 kV gun with a 1/2 in. stand-off distance.

5.3.2 Temperature Distribution As Function of Time

To avoid lengthy and costly computations required to solve the time-dependent heat flow equation with complicated boundary conditions, the following simplifying assumptions are made for temperature-distribution calculations:

1. For calculating the heat flow into the rock (and therefore the temperature), the walls of the cavity are considered as a moving isotherm held at the melting temperature T_m of the rock. This isotherm represents the solid-liquid interface, the layer of liquid being thin compared with the cavity diameter.

2. Of this isotherm, chosen to be a cylinder with a hemispherical base, we let only the base move forward in the direction of the beam and assume it has a constant diameter equal to that which the cavity will have at the end of the piercing time under consideration. In this model the depth grows with time, but the diameter does not.

3. The thermal diffusivity is independent of temperature. The value chosen as typical for rock is 5×10^{-3} cm^2/sec.[21]

With these assumptions, it is possible to determine an approximation to the temperature distributed within the rock by a simplified calculation. Since the piercing speed is considerably faster than a representative speed of heat flow into the rock, the heated regions of the solid material tend to be close to the cavity. As seen from much of the heated region, therefore, the cavity appears roughly similar to an infinitely long cylinder. Accordingly, for the basis of our approximated temperature distribution we use a standard solution to the time-dependent heat equation for the case of an infinitely long cylinder imbedded in an infinite medium of constant thermal diffusivity. In particular, the solution corresponds to the case where the cylinder is initially at temperature T_m and the surrounding medium is initially at temperature T_o. Then at time t=0 heat is allowed to flow into the medium while the cylinder is continuously maintained at T_m. The temperature $T_c(r,t)$ in the surrounding medium at time t and radius r is then given by:

$$T_c(r,t) = (T_m - T_o)\left\{1 - \frac{2}{\pi}\int_o^\infty e^{-\tau u}\frac{2[J_o(u)Y_o(Ru) - Y_o(u)J_o(Ru)]du}{u[J_o^2(u) + Y_o^2(u)]}\right\} + T_o \quad (6)$$

$$\tau \equiv \frac{at}{b^2}$$

$$R \equiv \frac{r}{b}$$

where b is the radius of the cylinder; a, the thermal diffusivity; and J_o and Y_o, the first-order Bessel function of the first- and second-kind respectively.[22]

In order to approximate the effect of a growing cavity, rather than one of infinite length, we next make the following further approximation. In a plane at each depth below the rock surface, the temperature is taken to be given by T_c (r,t) where the value of the time used in the solution depends on the depth. Planes at greater depths are then heated for shorter tiems than those near the outer surface of the rock. Since, by and large, the cavity bottom advances into the rock faster than the temperature can propagate, the time appropriate for a given depth is taken to be the elapsed time from when the cavity passes through that depth to when the beam is turned off. Thus, this procedure gives a temperature distribution that is wide near the outer surface of the rock and decreases in width with depth until it becomes zero at the cavity bottom. By keeping the cylinder radius constant in time, the calculation procedure is simplified, as it avoids the complication of a moving cylindrical boundary advancing into the heated rock. Specifically, the heating time is taken to be the difference between the piercing time needed to reach the full depth d, at which the beam is shut off, and the piercing time needed to reach the depth z of the point of evaluation. Using equation (5) we obtain

$$t_{heating}(z) = \frac{\pi \alpha H^*}{2W_o} \left\{ (d+z_o)^4 - (z+z_o)^4 \right\} \qquad (7)$$

The cylinder radius used in the solution T_c (r,t) at the given depth is given by the radius of the full-grown cavity at that depth. In most cases, therefore, the appropriate radius is simply the radius of the cylindrical portion of the cavity. However, at values of z approaching the depth of the cavity, the radius becomes that of the circle cut by a plane perpendicular to the beam and passing through the spherical bottom of the cavity.

Fig. 5-12 shows the heating time calculated from (7) for various depths z in the case of a cavity which has reached a depth of 4 in. (In this and the following figures the beam direction points upward to allow compatibility with the existing thermal-stress computer programs.)

Curve 643124-A

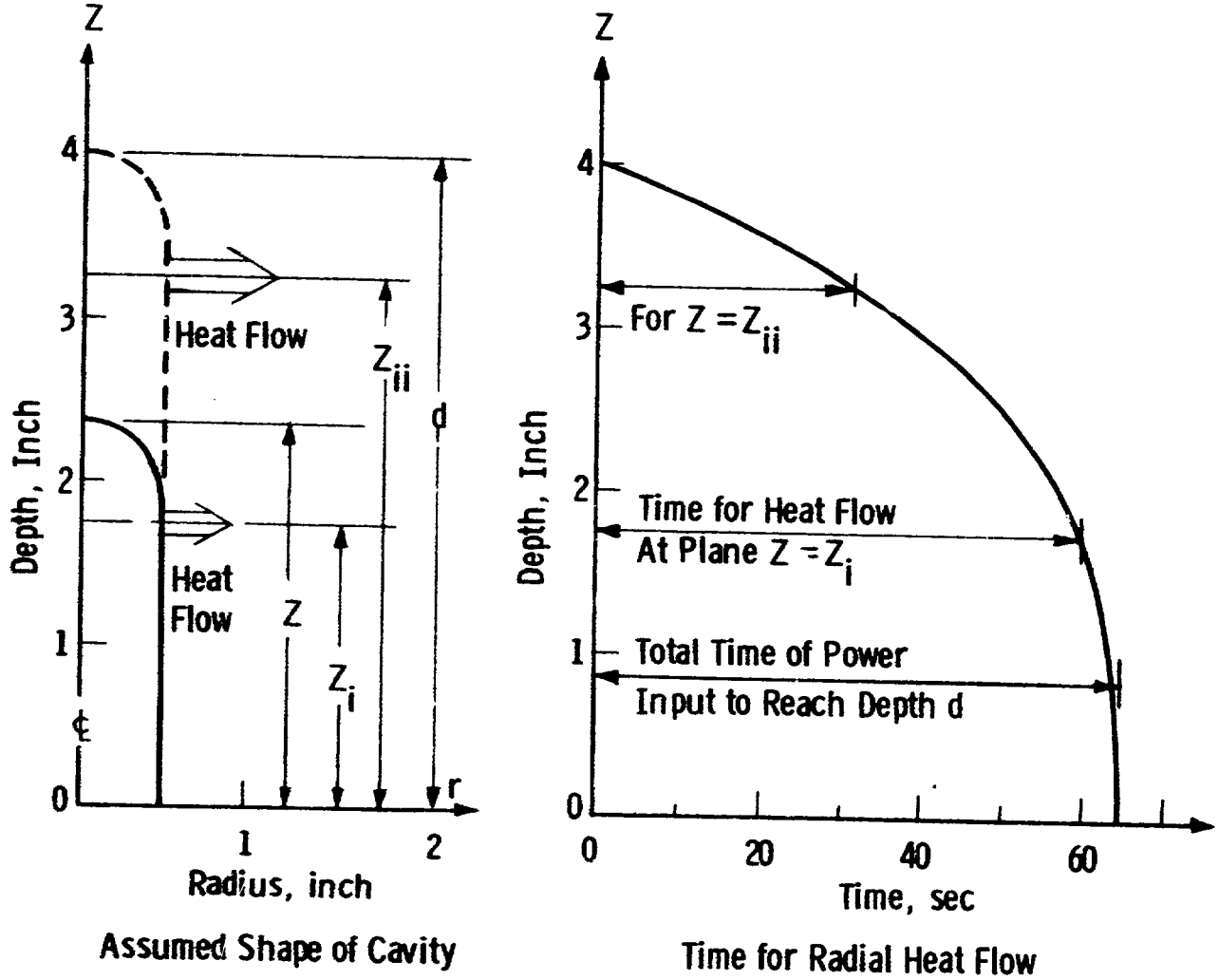

Fig. 5-12 Time for which heat flow takes place in a plane perpendicular to the z-axis.

Figs. 5-13a through 5-13f show the resulting isotherms plotted using the above model. The cavity boundary is assumed to remain at 1700°C; the isotherms are shown in increments of 100°C. Each figure represents one of the six piercing times considered in the study. Notice that the isotherms converge to a point at the bottom of the hole. In this way, the model approximates the very steep temperature gradient at that point which results from the advancing motion of the melt front. The extent to which the cavity depth increases much faster than the heat can diffuse into the rock can be estimated by assuming for the moment that the speed of penetration is constant. With this simplification and by use of a one-dimensional approximation, an upper limit can be calculated for the small distance that heat will penetrate into the rock at the bottom of the hole. The temperature rise at a distance Δz below the bottom of the hole will be given by:[23]

$$T = T_m \exp\left[- \frac{V \Delta z}{a} \right] \tag{8}$$

where V is the speed at which the melt front is advancing (assumed here to be constant), and a is the thermal diffusivity. For V, equation (4) is used to obtain

$$V = \frac{W_o}{H^* \, 2 \, \pi \, \alpha \, (d+z_o)^3} \tag{9}$$

which gives the penetration speed of the electron beam for a given depth d. Combining equations (7), (8), and (9) gives the resulting temperature penetration depth:

$$\Delta z = \frac{H^* 2 \, \pi \, \alpha}{W_o} \left\{ \frac{2W_o}{\pi \, \alpha \, H^*} \, t + z_o^{\,4} \right\}^{3/4} \quad a \ln \frac{T_m}{T} \tag{10}$$

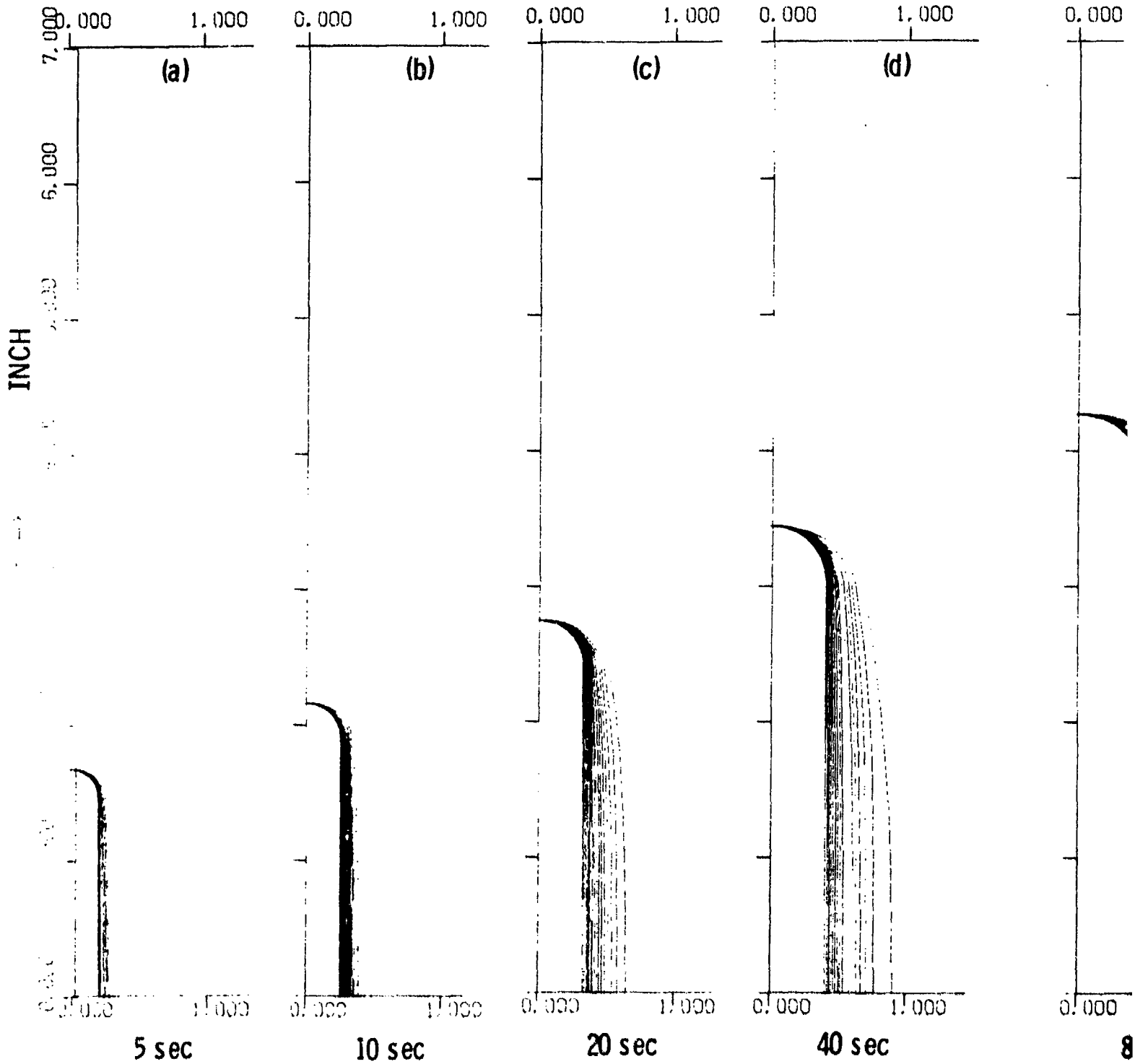

Fig. 5-13 Isotherms as calculated with the simple model. Cavity boundary is assumed to remain at 1700°C. Isotherms as shown are 100°C apart.

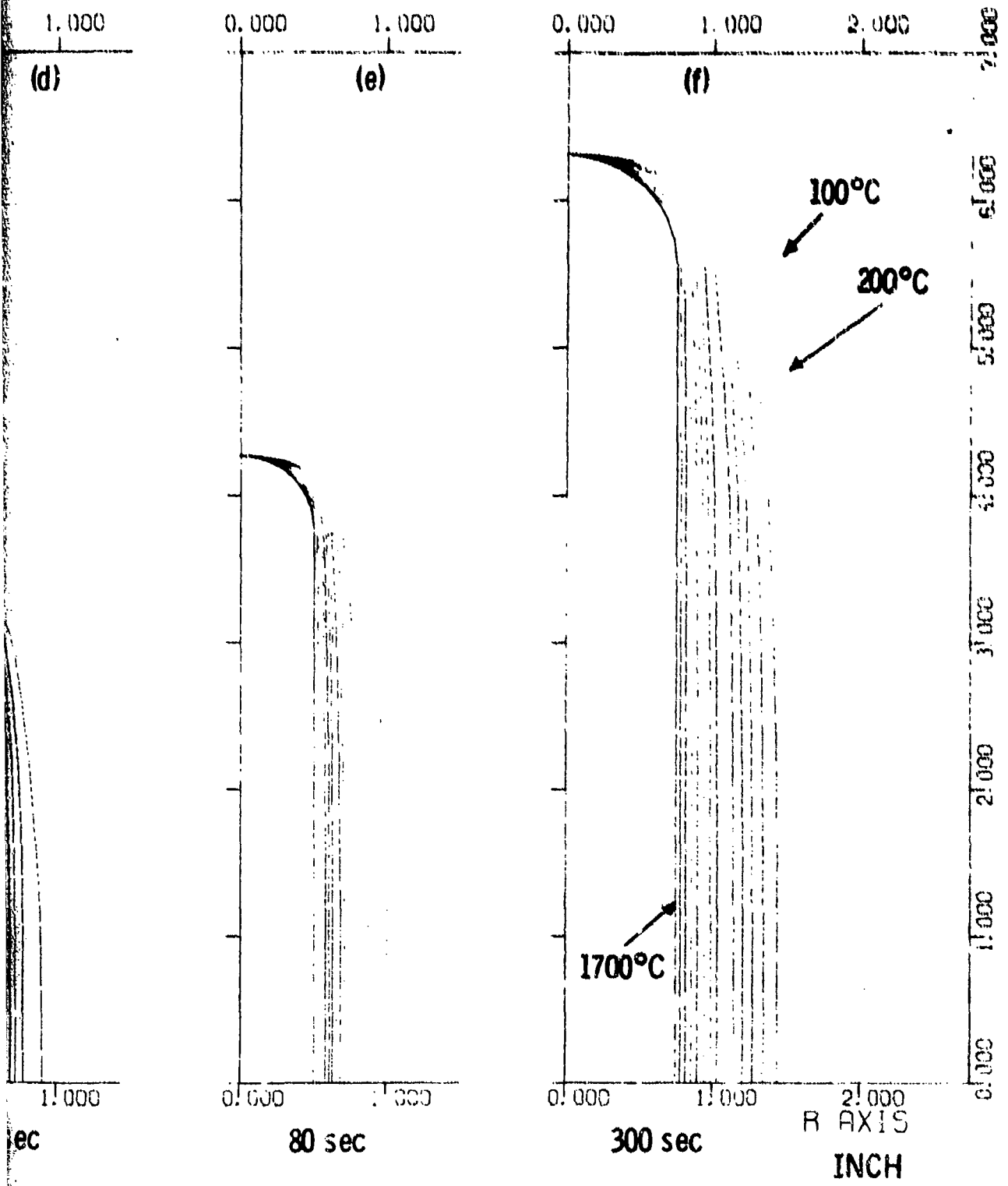
1.000
(d)
1.000
ec
0.000
1.000
(e)
0.000
80 sec
0.000
1.000
2.000
(f)
100°C
200°C
1700°C
0.000
1.000
2.000
300 sec
R AXIS
INCH

5-29

Fig. 5-14 shows plots of equation (10) giving this estimate of the distance of penetration of thermal energy into rock below the end of the cavity as a function of piercing time for several values of temperature under the conditions listed in Table 5.2 for 9.0 kW with $a=5 \times 10^{-3}$ cm^2/sec and T_m = 1700°C. The arrows in the figure designate the piercing times chosen for the stress calculations that we subsequently consider. As one would expect, penetration of the heat into the solid rock increases with time

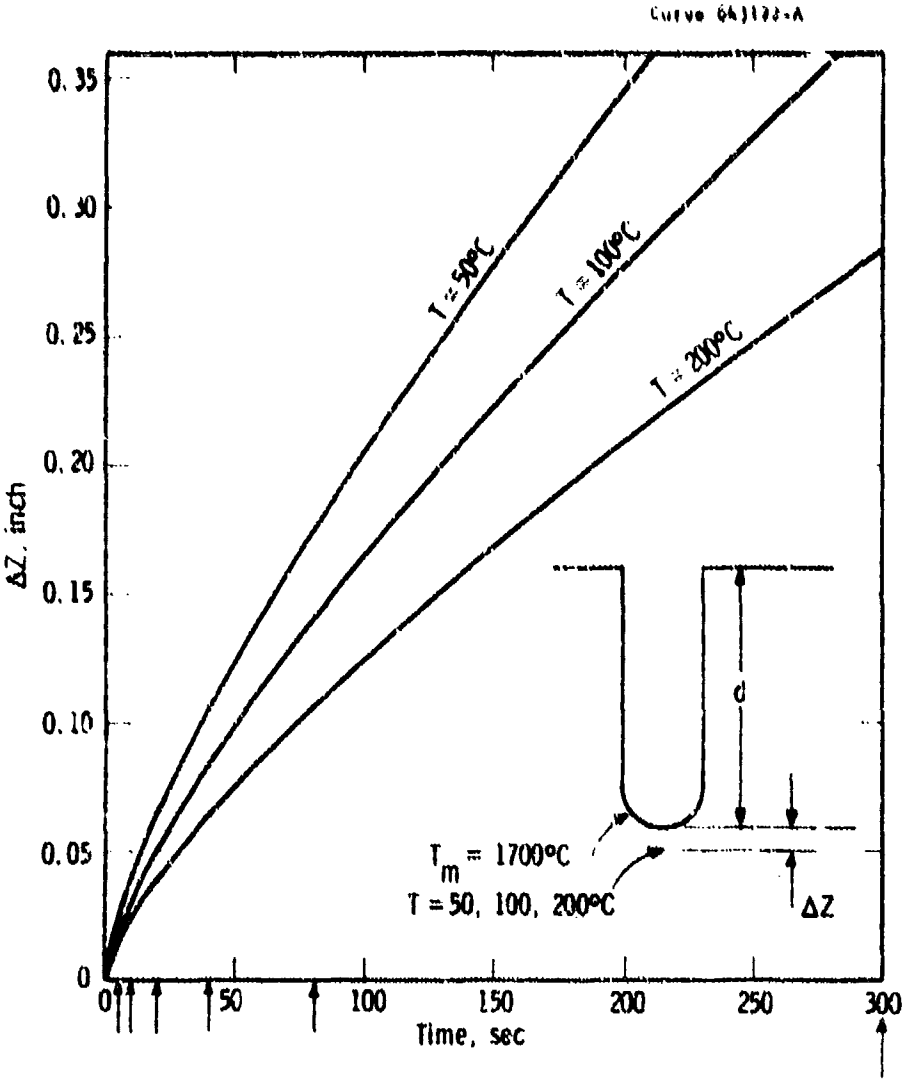

Fig. 5-14 Distance of temperature penetration into rock below end of cavity as a function of piercing time.

and is large for lower temperature isotherms. Contrary to the simplifying assumption made in the above calculation, the speed V is not a constant but is, in fact, a decreasing function of time. Accordingly, the actual heat penetration rates at the base of the cavity will be even slower than those given by equation (10).

It should be pointed out that these temperature calculations overestimate the distance into the rock to which the heat actually penetrates. First, the radius of a real cavity does, in fact, expand with time and at a speed comparable to the speed of much of the heat conduction, in contrast to that of our model which has a constant radius. Therefore, by the time the radius of an actual cavity reaches its full size, it overtakes much of the thermal energy that has already diffused into the rock. In our model, however, we have assumed that the heat begins diffusing from a point located at the maximum radius of the cavity and that none of the heat is overtaken and thus have overestimated the extent to which the rock is heated. Second, the thermal diffusivity does not remain constant with temperature as we have assumed but, for example, can decrease by a factor of 5 as the temperature goes from 20°C to 600°C.[21] The value of diffusivity chosen corresponds to 200°C for Dresser basalt or 280°C for Charcoal granite. Yet, for example, with these two rocks, the thermal diffusivity drops at elevated temperatures (i.e., greater than 600°C) to half the value used. Such a drop will inhibit heat flow from the hot cavity and will therefore also restrict the distance the heat propagates.

It is certainly possible to improve the model for calculating the temperature distribution. For example, one could numerically solve the axi-symmetric, time-dependent, differential equation for heat conduction for the case of a cavity growing in diameter as well as in depth and for a thermal diffusivity that changes as a function of temperature. The time development in cavity shape would have to be taken from experimental data, since an energy balance calculation would be prohibitively complicated, governed as it would be by such processes as turbulence in both the hot gasses and molten rock, the energy deposition distribution,

vaporization, etc. To be complete, the calculation should also include the additional complication of the insulating effect of small cracks, which are, in turn, caused by the same thermal stresses we are trying to estimate. Such calculations are beyond the scope of the present investigation.

5.3.3 Thermal Stress Calculations

Thermal stresses in the rock were calculated using a package of finite-element computer programs whose details are proprietary. Another program, TEMPMAT, was used to prepare the additional input data temperature field, etc. for the stress calculations.

Meshes for two of the runs, for 5 seconds (the shortest time) and for 300 seconds (the longest time) are shown in Figure 5-15. Note that the nodal points are spaced closely together in the general direction of the temperature gradient and are kept rather close together in the region of greatest interest, i.e., just outside the heated region where the highest tensile stresses are expected. Instead of starting at the walls of the cavity, the mesh begins on the 700° C isotherm, which is taken as the temperature at which the rock becomes plastic.

The program TEMPMAT calculates the temperature for each mesh nodal point and punches out the values, which are then used as inputs for the stress calculation programs. In addition, to approximate the variations with temperature of the elastic and thermal properties of the rock, TEMPMAT makes use of a material type-specification in the stress calculation programs and assigns to each element a value for each of the elastic and thermal parameters according to the average temperature of the element (see Table 5-5).

Figures 5-15 through 5-19 show the results of the stress calculations. Four different stresses are shown: (1) azimuthal tension (θ stress), (2) maximum (tensile) principal stress in the r-z plane, (3) azimuthal compression, and (4) minimum (compressive) principal stress in the r-z plane.

Table 5-5

ELASTIC AND THERMAL PARAMETERS ASSIGNED TO EACH ELEMENT ACCORDING TO ITS TEMPERATURE

Temperature (°C)	Coefficient of Thermal Expansion	Young's Modulus (psi)	Poisson Ratio
0-100	2.6×10^{-6}	145×10^{5}	0.24
100-225	6.0	141	0.23
225-350	8.2	135	0.21
350-475	10.2	126	0.19
475-600	11.2	107	0.145
600-620	11.7	83	0.105
620-640	11.8	64	0.09
640-660	11.9	46	0.07
660-680	12.0	28	0.05
680-700	12.0	9	0.02

Note: These data are similar to that for Dresser basalt in Table 4-4, page 18 of Ref. 20.

In each of the four cases there are six plots representing the six piercing times 5, 10, 20, 40, 80, and 300 seconds. For the plots of tensile stress, the contours represent 500 to 10,000 psi in 500 psi increments. For the azimuthal compressive stress, the contours represent 0 (dashed line) to -80,000 psi in -5000 psi increments. And for the compressive principal stress, the contours represent 0 (dashed line) to -76,000 psi in -4000 psi increments. The directions of the principal stresses in the r-z plane are more or less parallel to the isostress contours.

Fig. 5-15 Finite element triangular meshes: (a) piercing time 5 seconds, (b) piercing time 300 seconds.

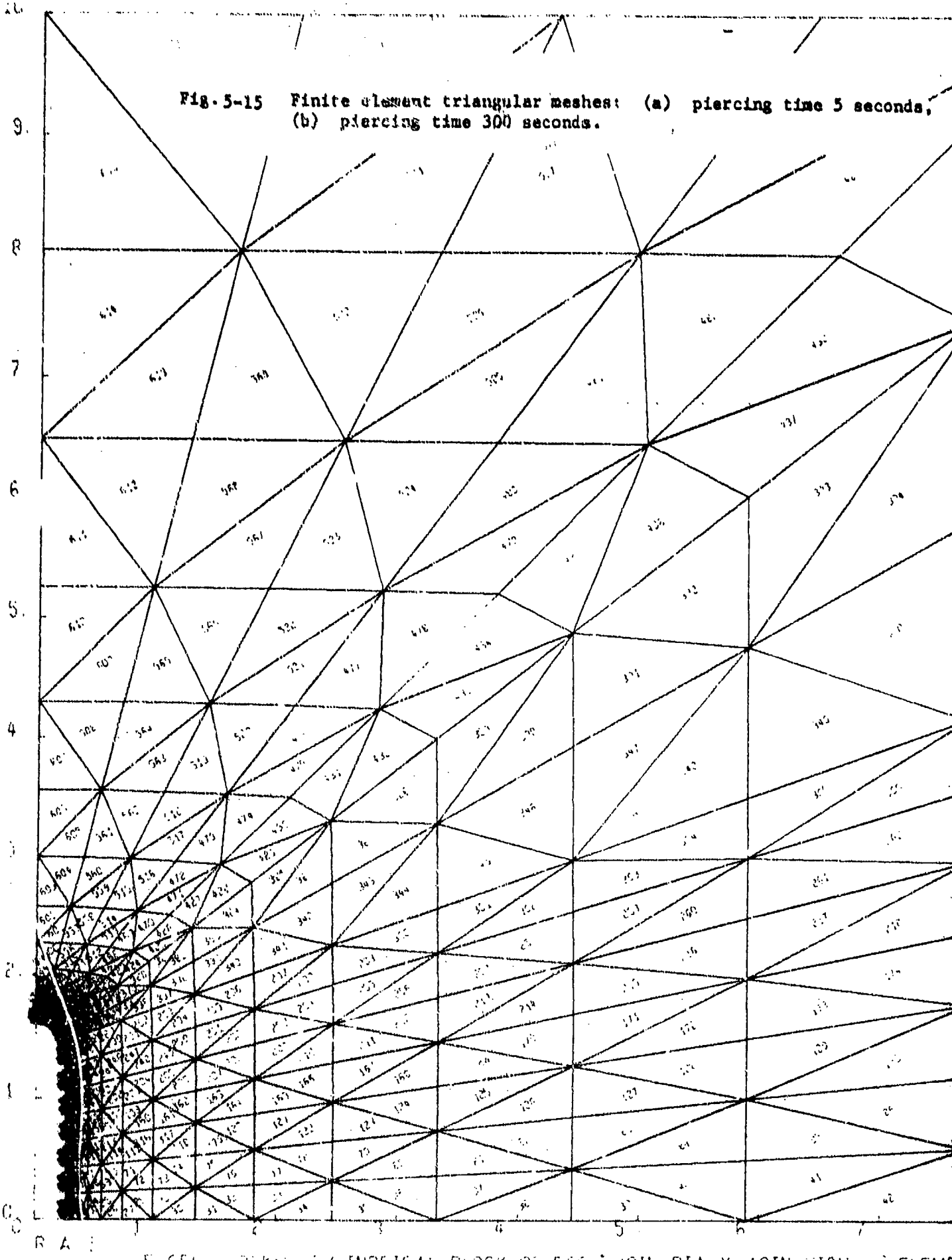

(a)

gular meshes: (a) piercing time 5 seconds,
00 seconds.

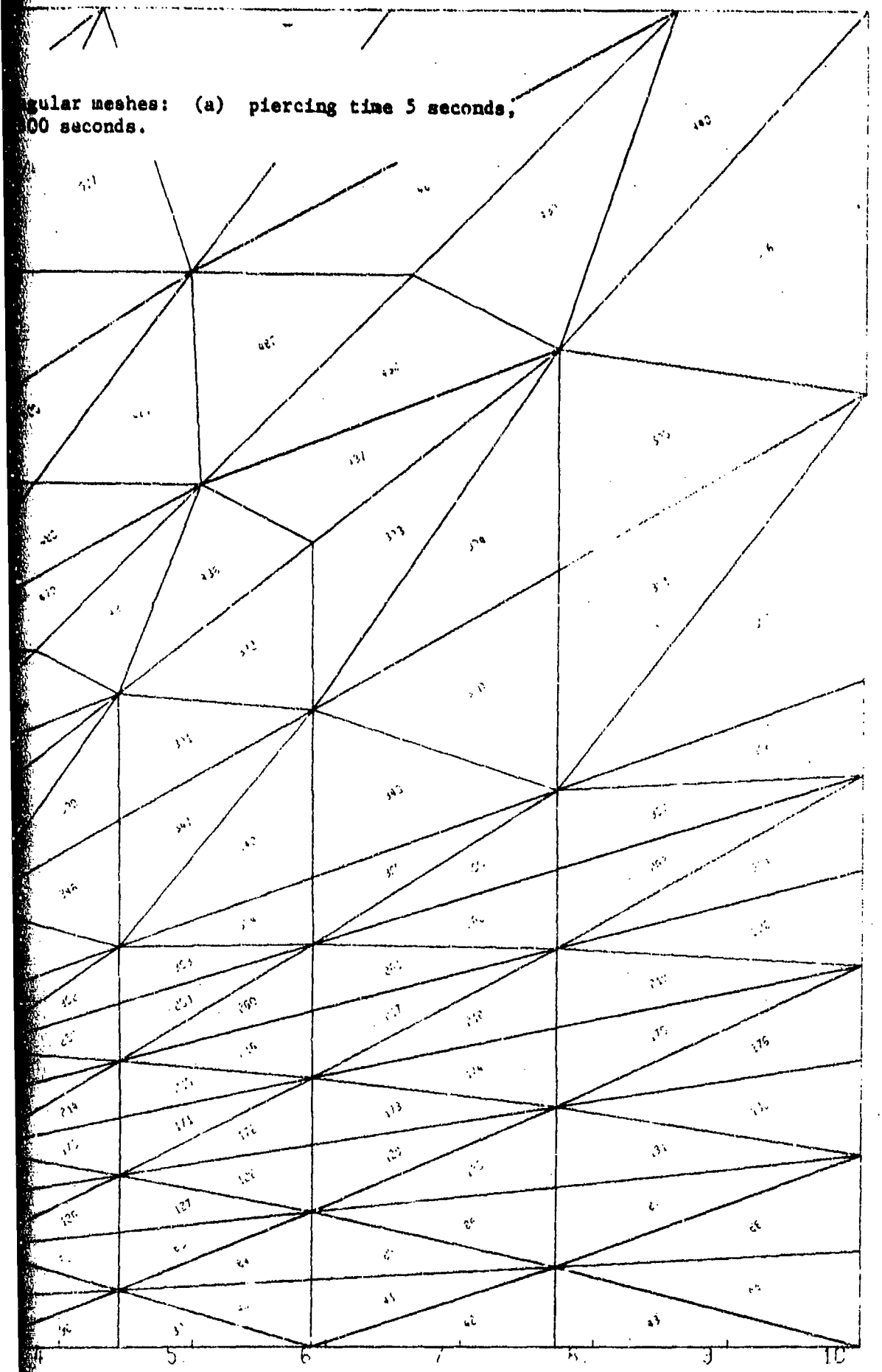

K OF ROCK 20IN DIA X 10IN HIGH ELEMENT GEOMETRY

(a)

5-33-9

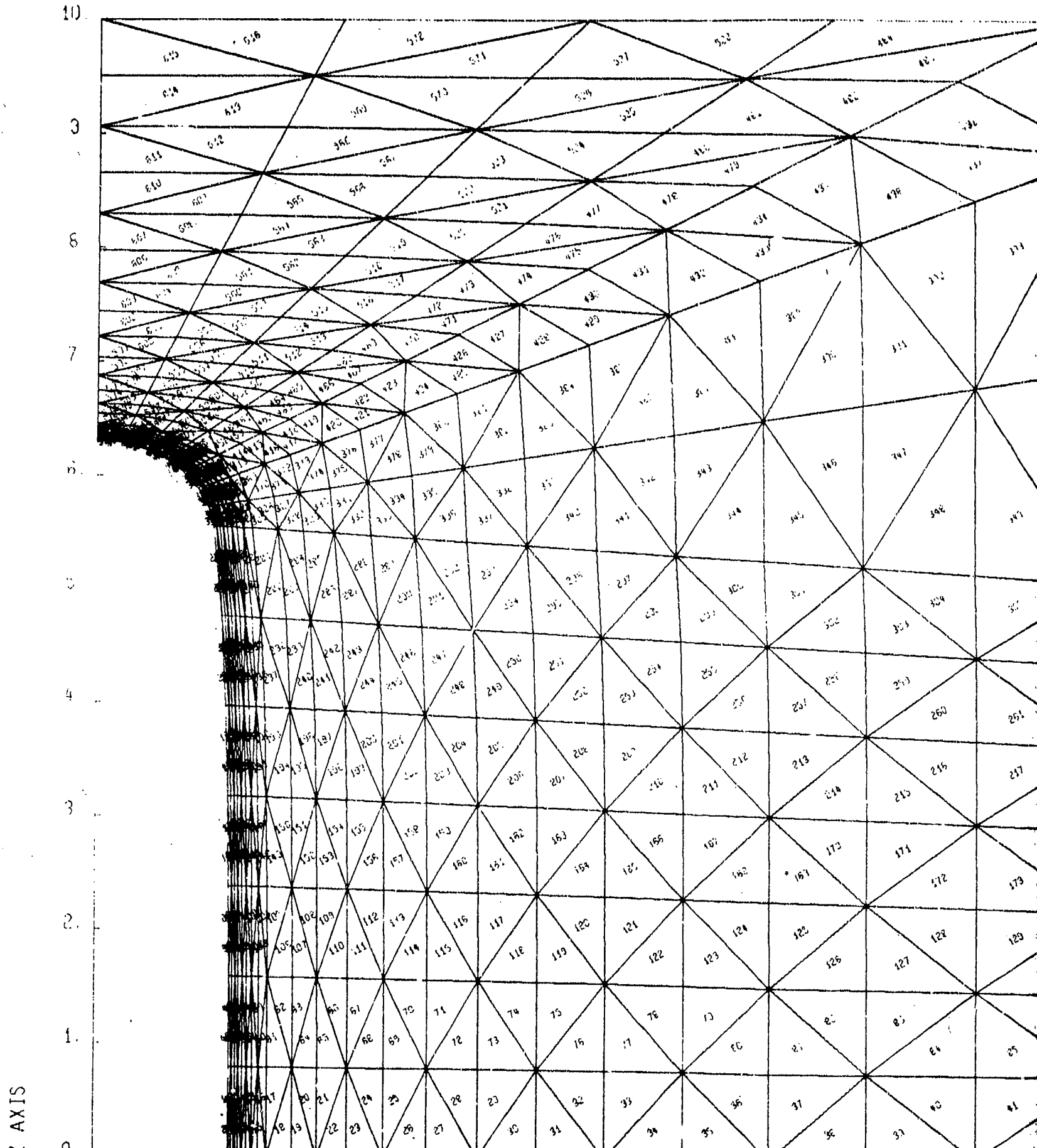
Z AXIS
R AXIS
300 SEC 9 KW CYLINDRICAL BLOCK OF ROCK 20IN DIA X 10IN HIGH ELEMENT GEO

(b)

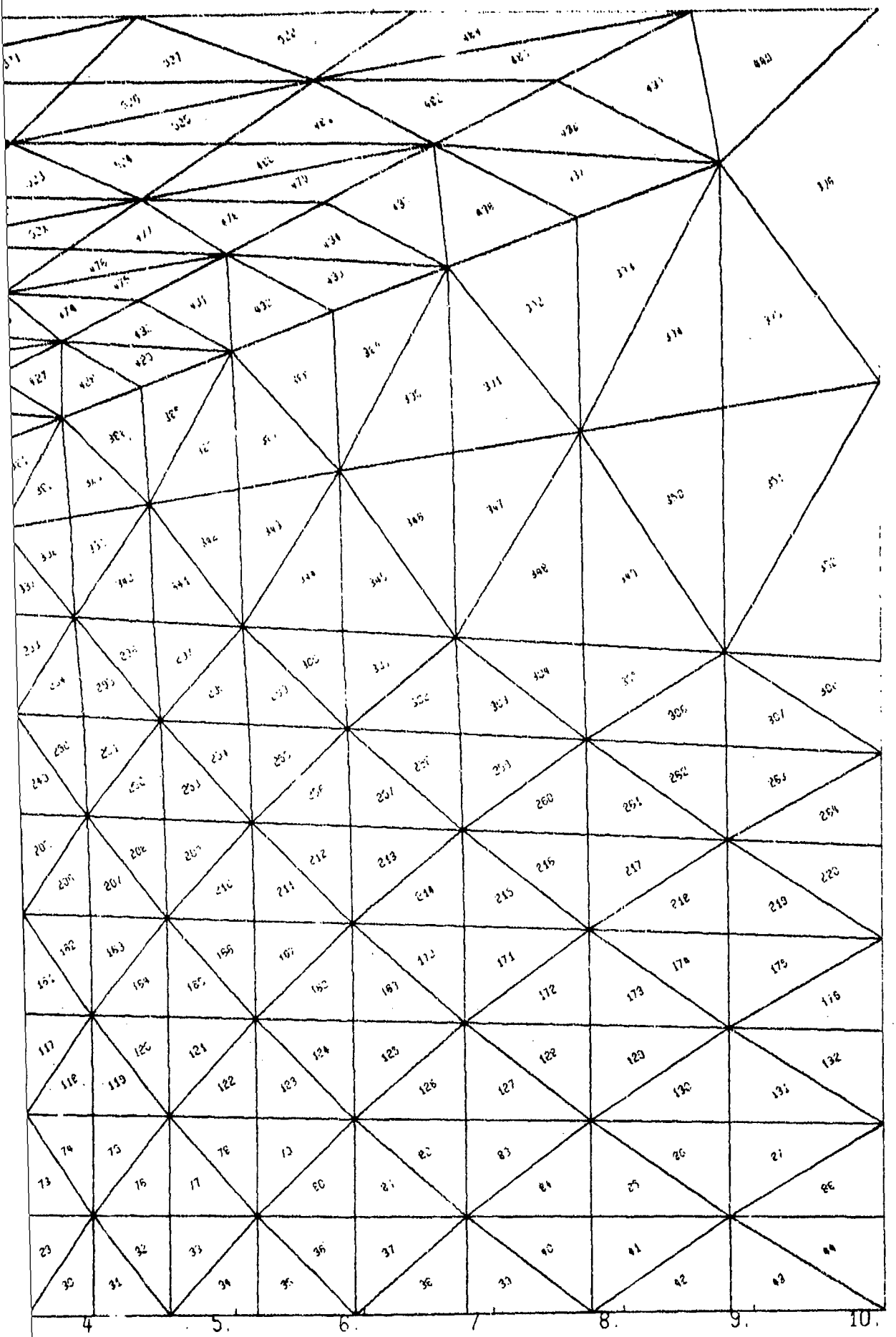

BLOCK OF ROCK 20IN DIA X 10IN HIGH ELEMENT GEOMETRY

(b)

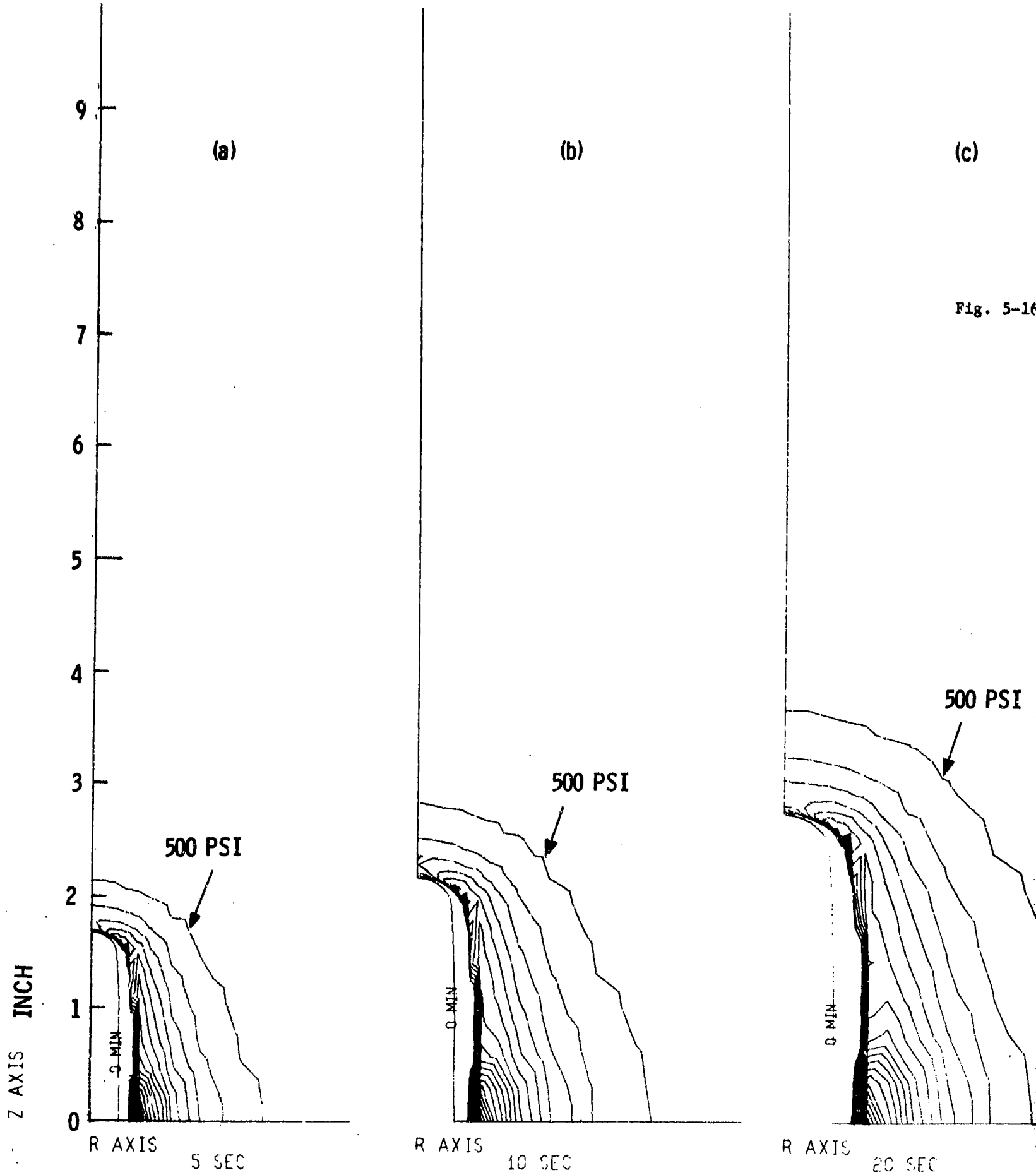
(a)
(b)
(c)
500 PSI
500 PSI
500 PSI
Q MIN
Q MIN
Q MIN
Z AXIS INCH
0
1
2
3
4
5
6
7
8
9
R AXIS
R AXIS
R AXIS
5 SEC
10 SEC
20 SEC

Fig. 5-16

(c)

(d)

Fig. 5-16 Calculated azimuthal tension (θ stress) for piercing times of 5, 10, 20, 40, 80, and 300 seconds.

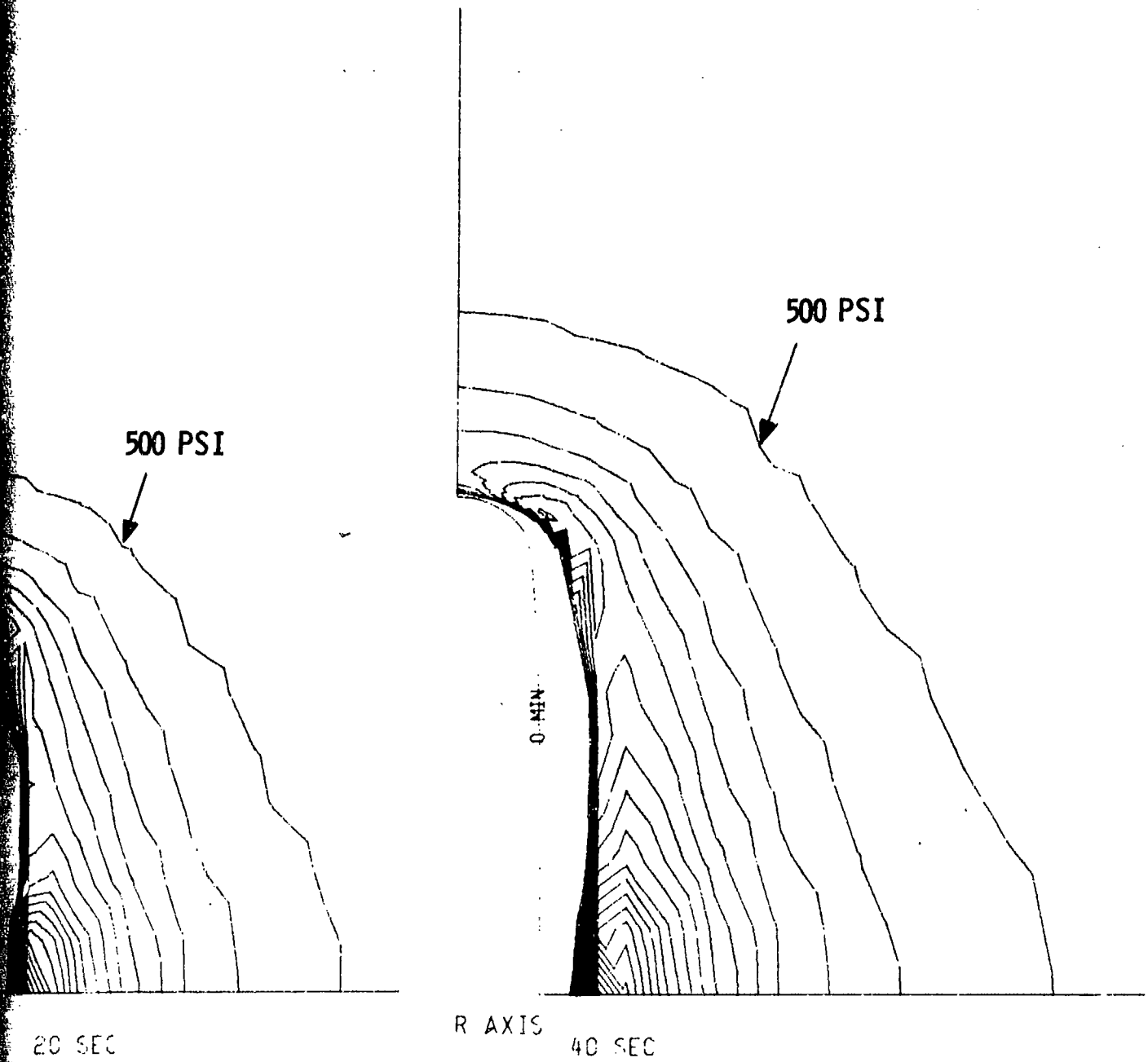

(e)

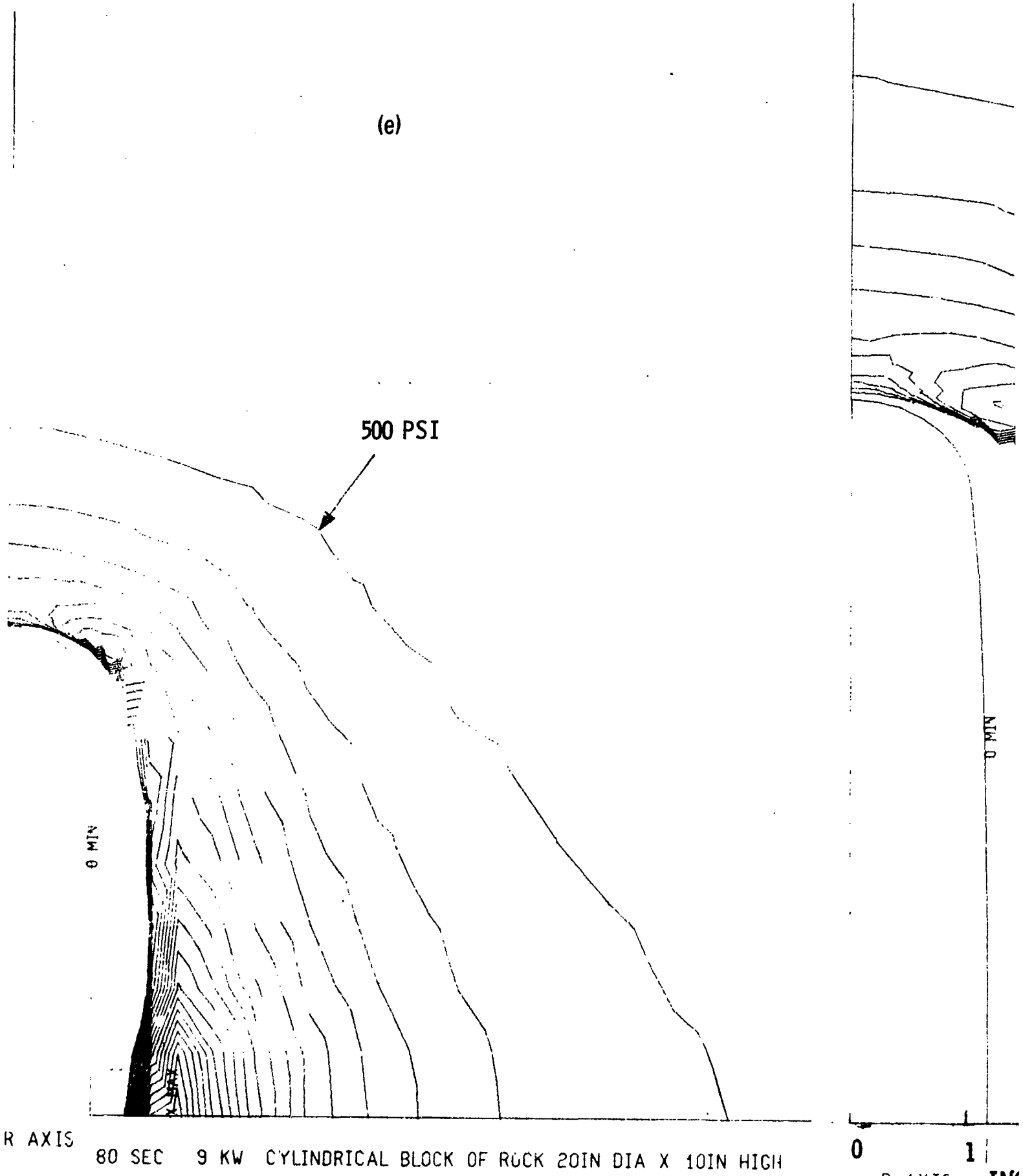
500 PSI
0 MIN
R AXIS
80 SEC 9 KW CYLINDRICAL BLOCK OF ROCK 20IN DIA X 10IN HIGH
0 MIN
0
1
R AXIS
IN(
300 S

(f)

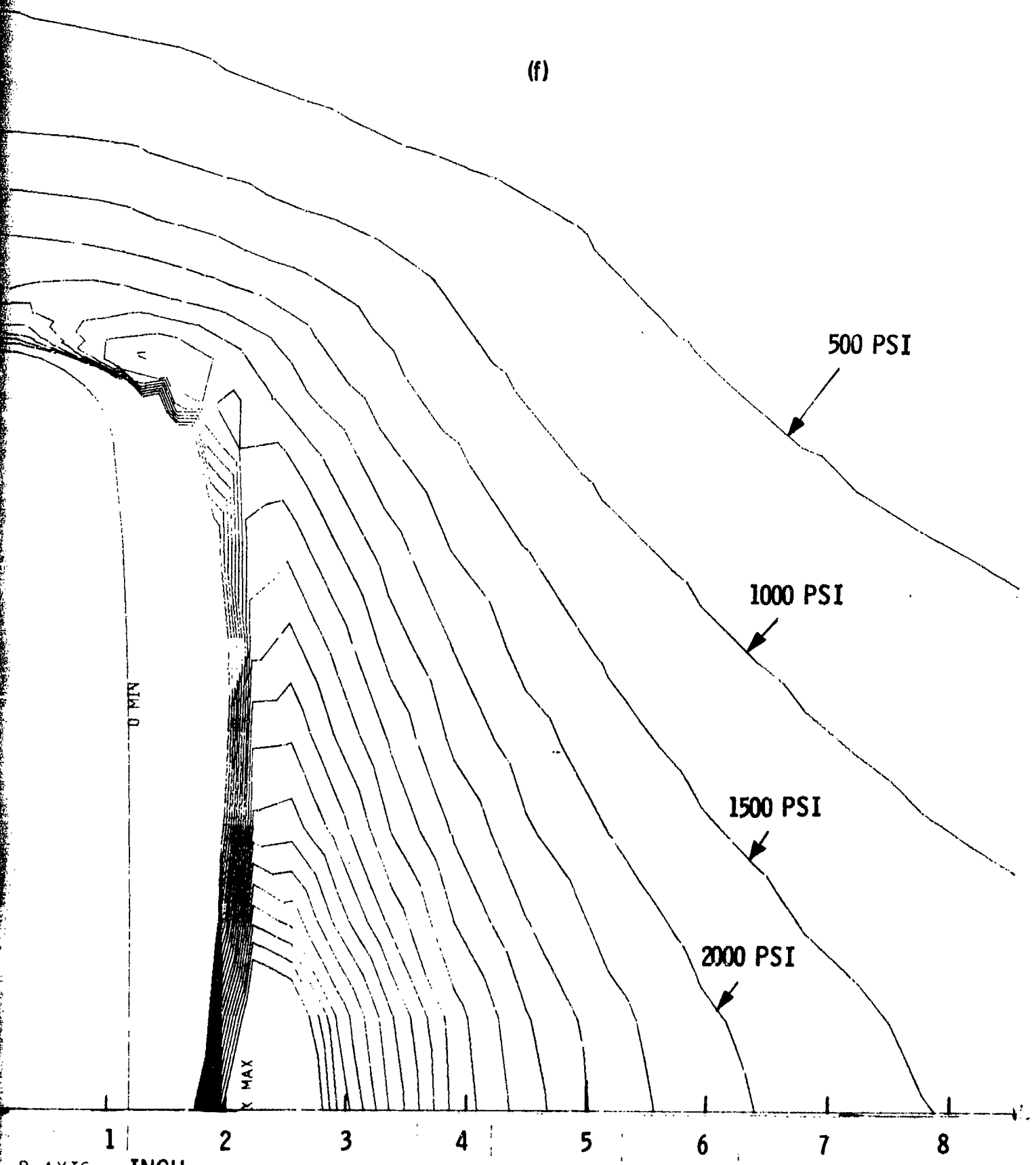
500 PSI
1000 PSI
1500 PSI
2000 PSI
0 MIN
X MAX
1
2
3
4
5
6
7
8
R AXIS INCH
300 SEC 9 KW CYLINDRICAL BLOCK OF ROCK 20IN DIA X 10IN HIGH θ STRESS

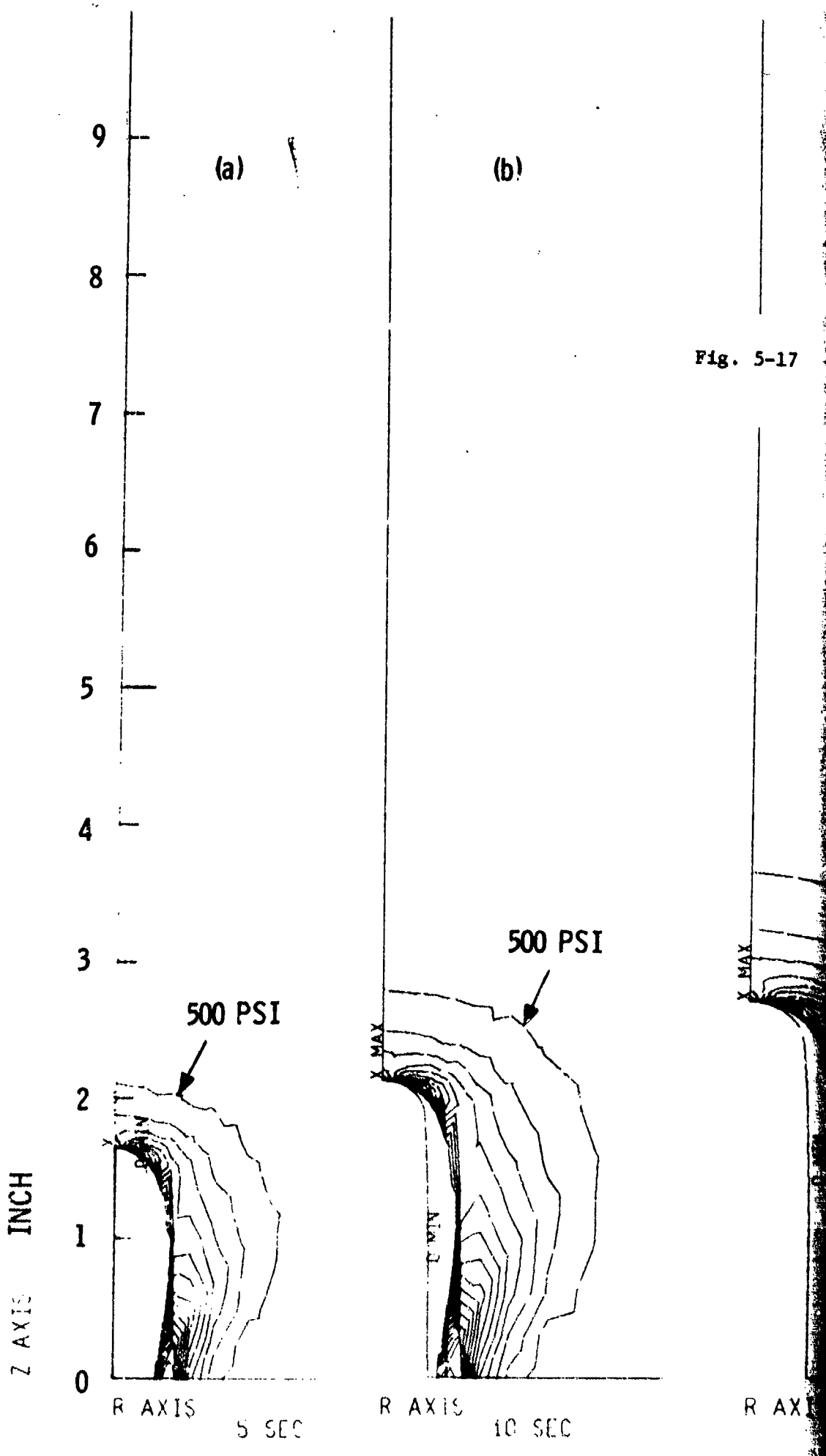
(a)
(b)
9
8
7
6
5
4
3
2
1
0
INCH
Z AXIS
500 PSI
500 PSI
X MAX
X MAX
R AXIS
R AXIS
R AXI
5 SEC
10 SEC

Fig. 5-17

(c)

(d)

Fig. 5-17 Calculated tension in r-z plane (maximum principal stress) for piercing times of 5, 10, 20, 40, 80, and 300 seconds.

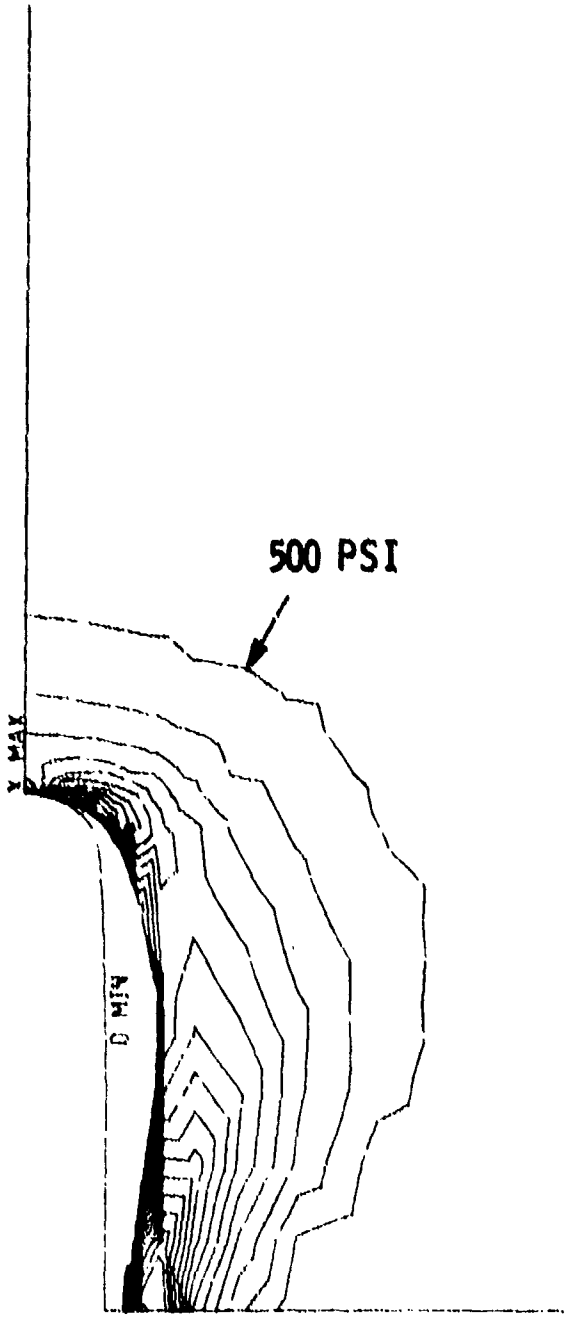

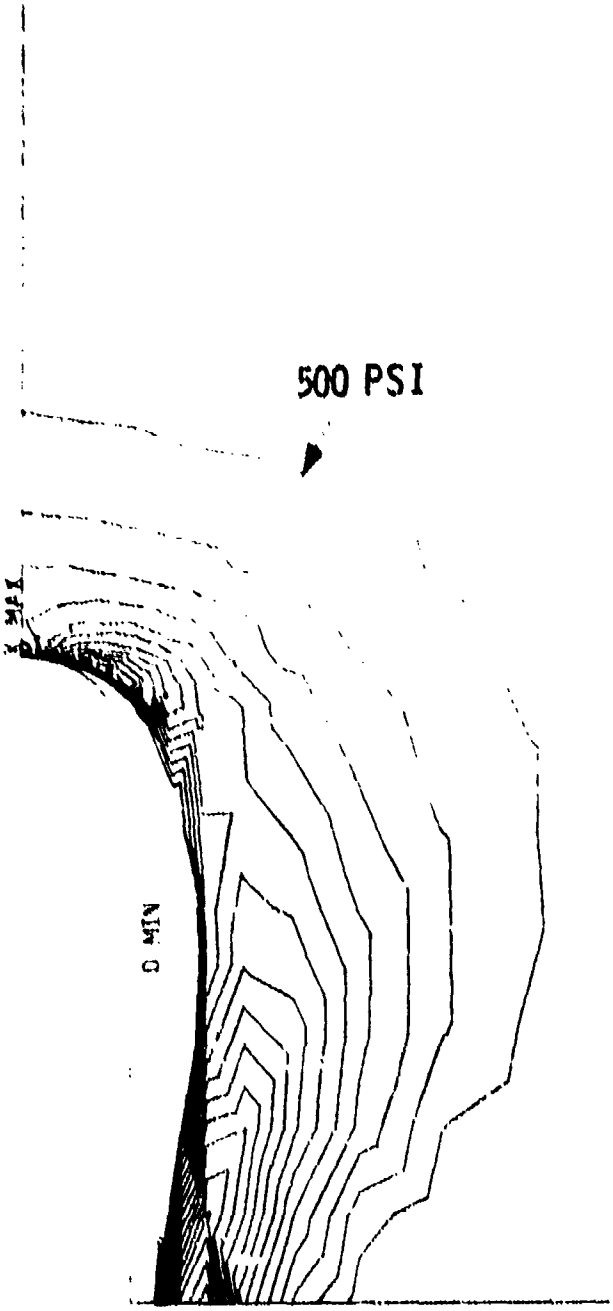

5-33 E

(e)

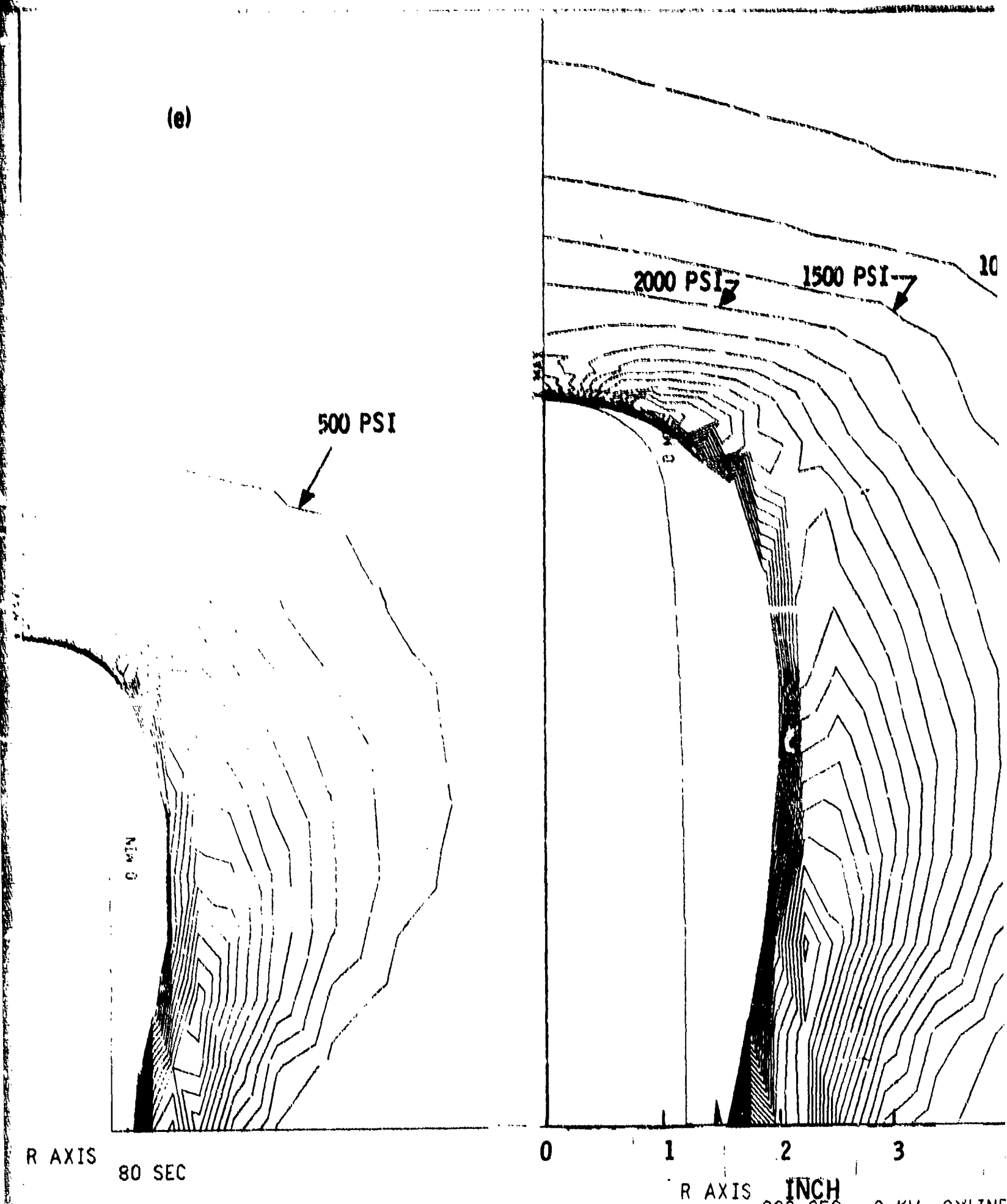
500 PSI
2000 PSI
1500 PSI
10
0 MIN
R AXIS
80 SEC
0
1
2
3
R AXIS
INCH
300 SEC
9 KW CYLIND

(f)

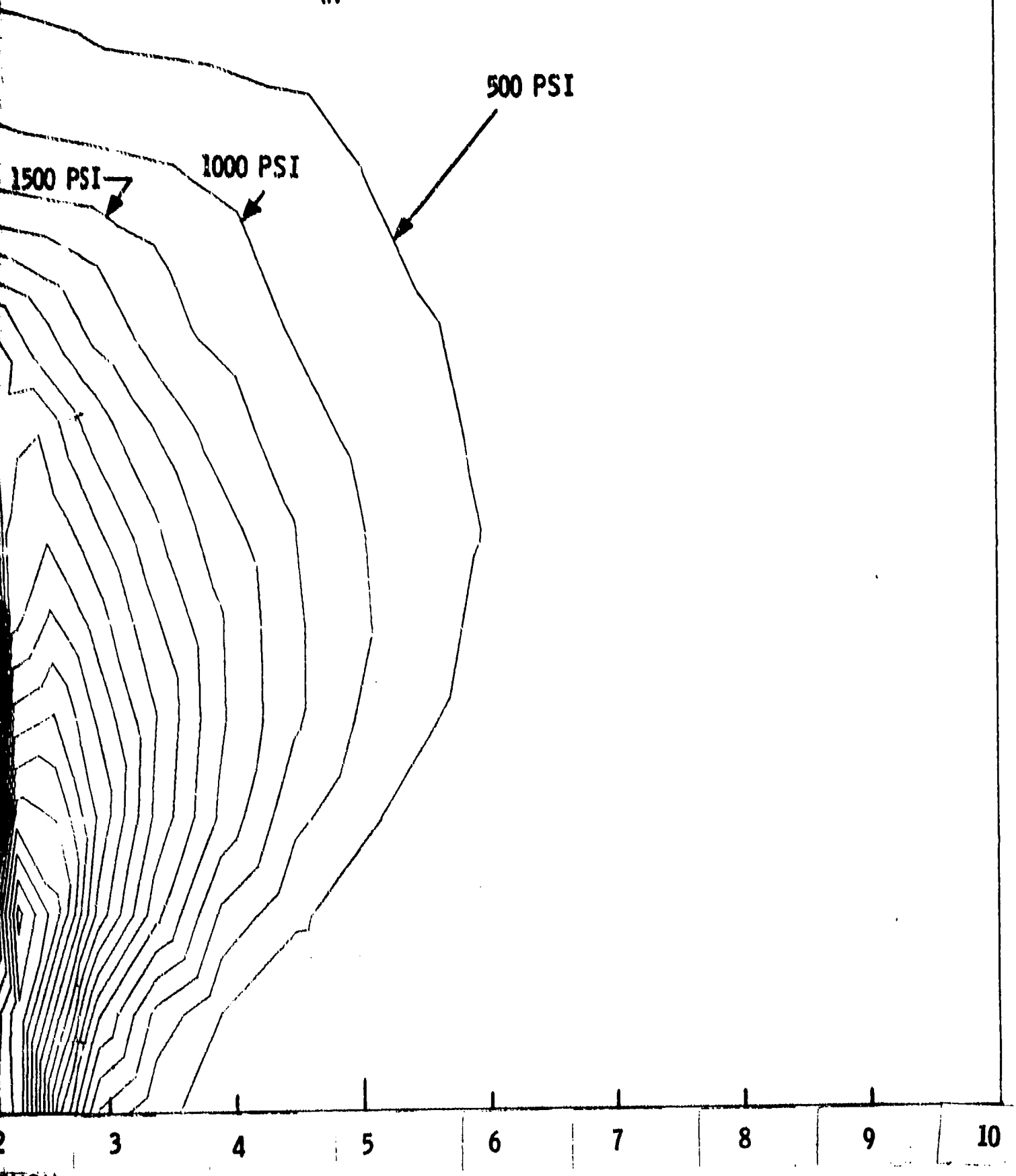

0 SEC 9 KW CYLINDRICAL BLOCK OF ROCK 20IN DIA X 10IN HIGH MAXIMUM STRESS

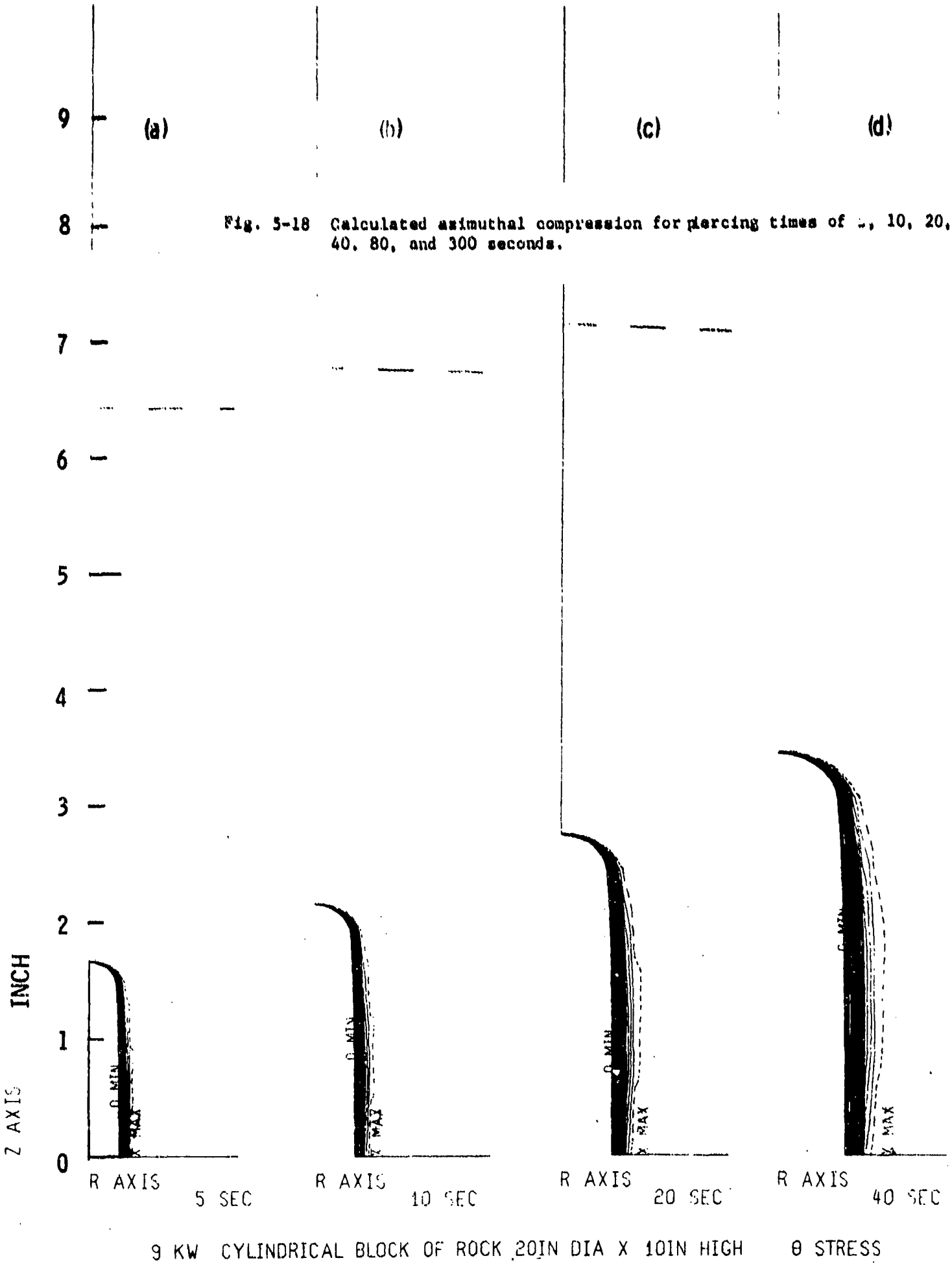

Fig. 5-18 Calculated azimuthal compression for piercing times of ., 10, 20, 40, 80, and 300 seconds.

(d) (e) (f)

5, 10, 20,

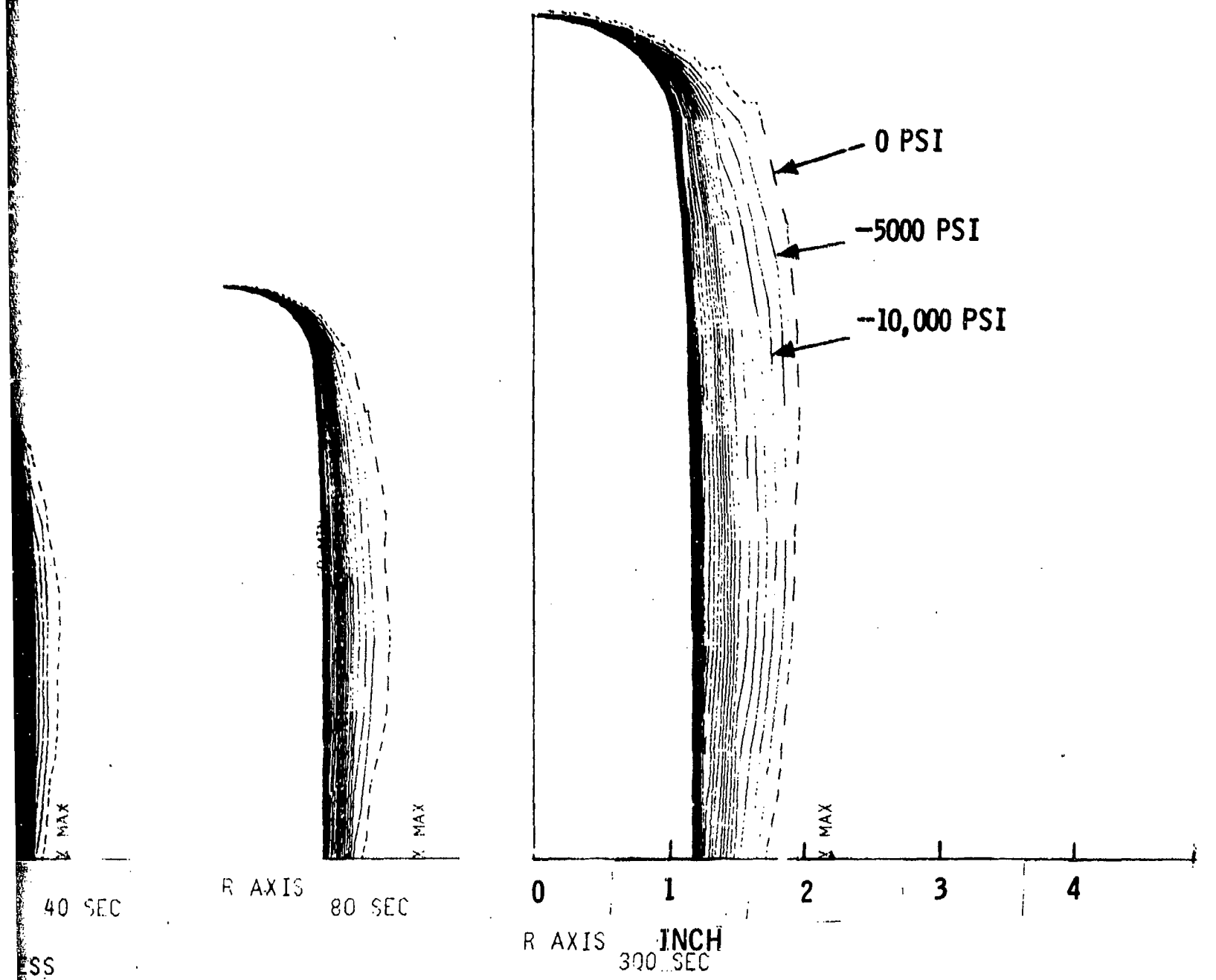
0 PSI
-5000 PSI
-10,000 PSI
MAX
MAX
MAX
40 SEC
R AXIS
80 SEC
0
1
2
3
4
R AXIS
INCH
300 SEC
SS

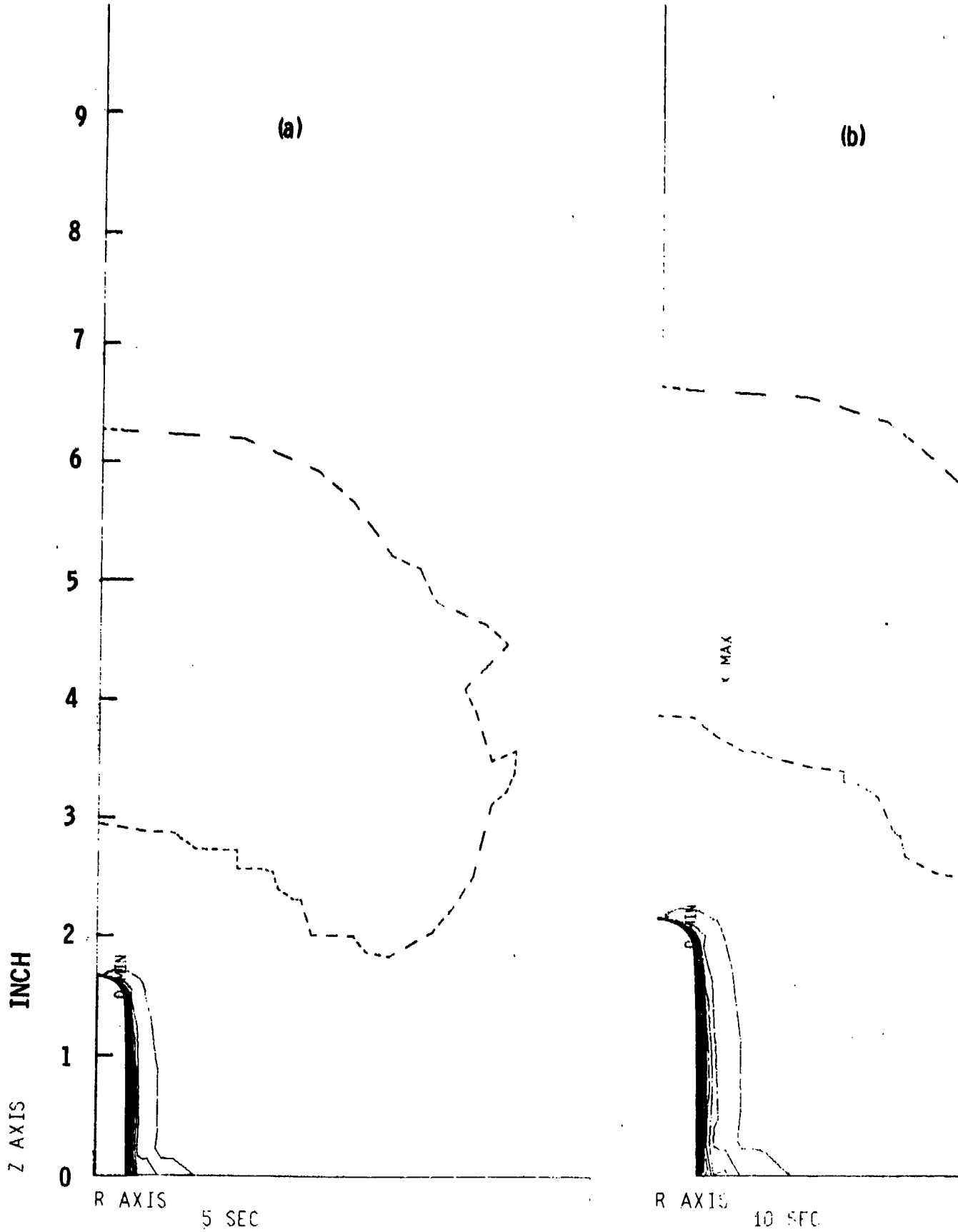

5-33.H

(c)

Fig. 5-19 Calculated compression in r-z plane (minimum principal stress) for piercing times of 5, 10, 20, 40, 80, and 300 seconds.

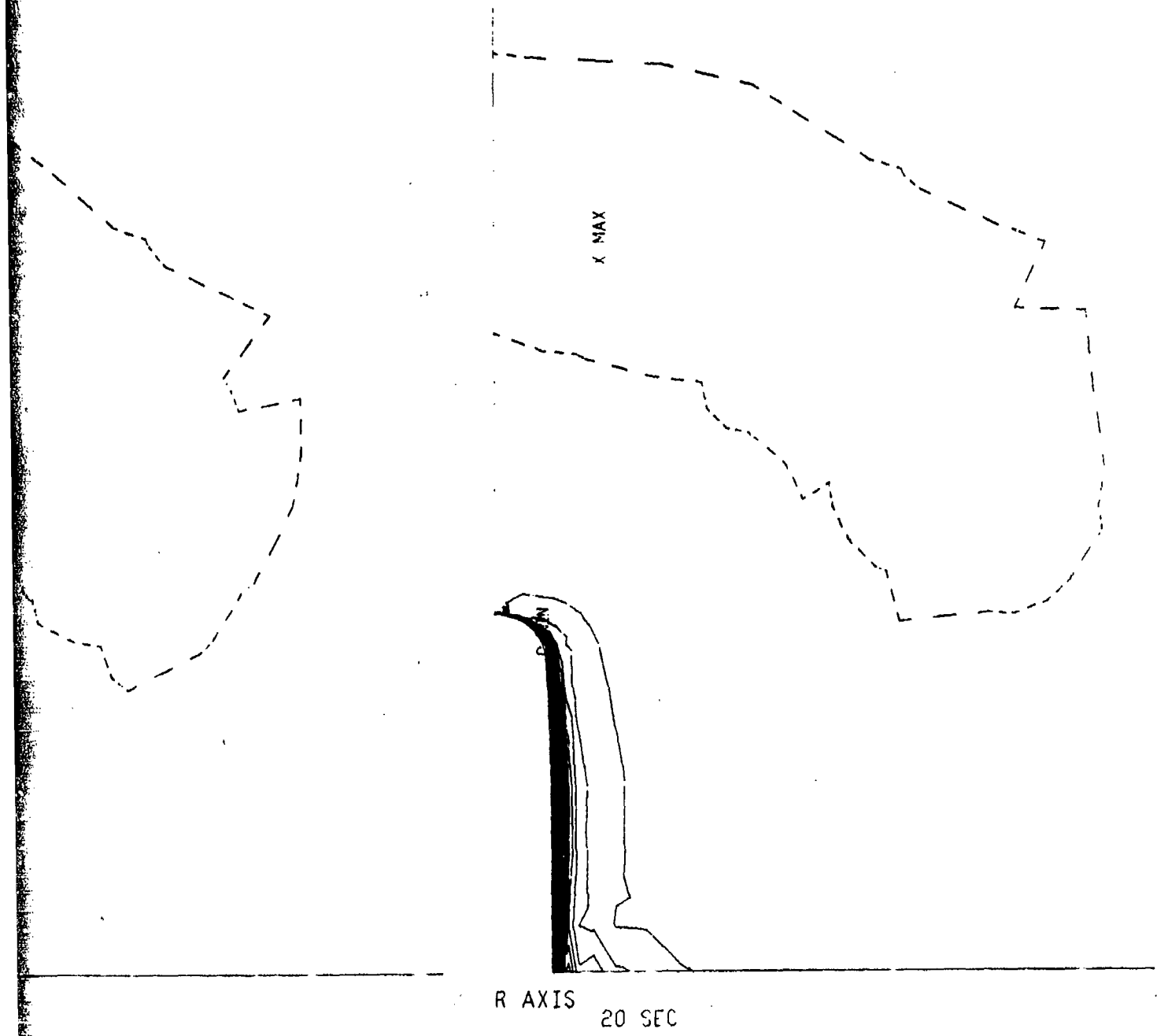

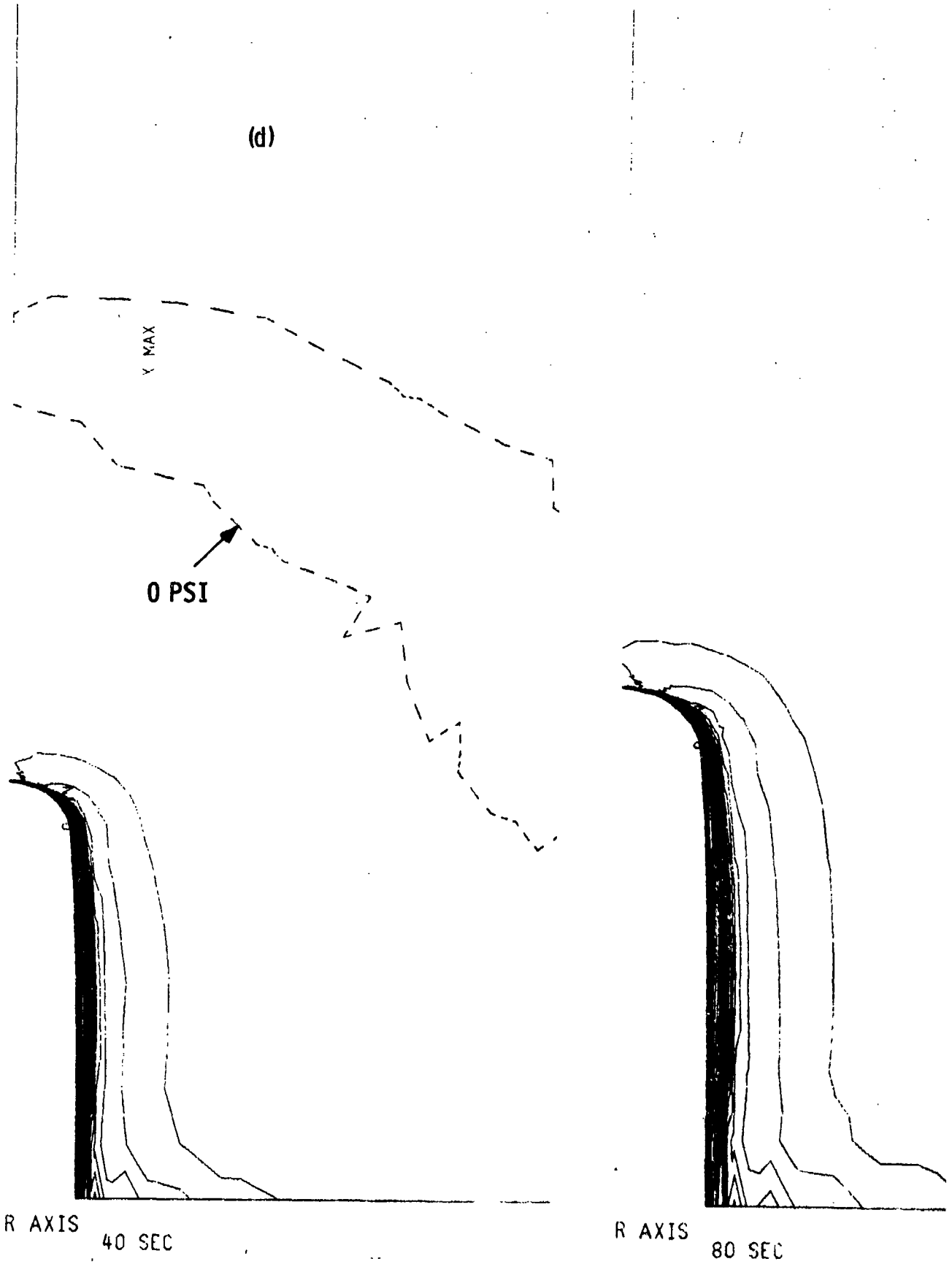

9 KW CYLINDRICAL BLOCK OF ROCK 20IN DIA X 10IN HIGH MINIMUM S

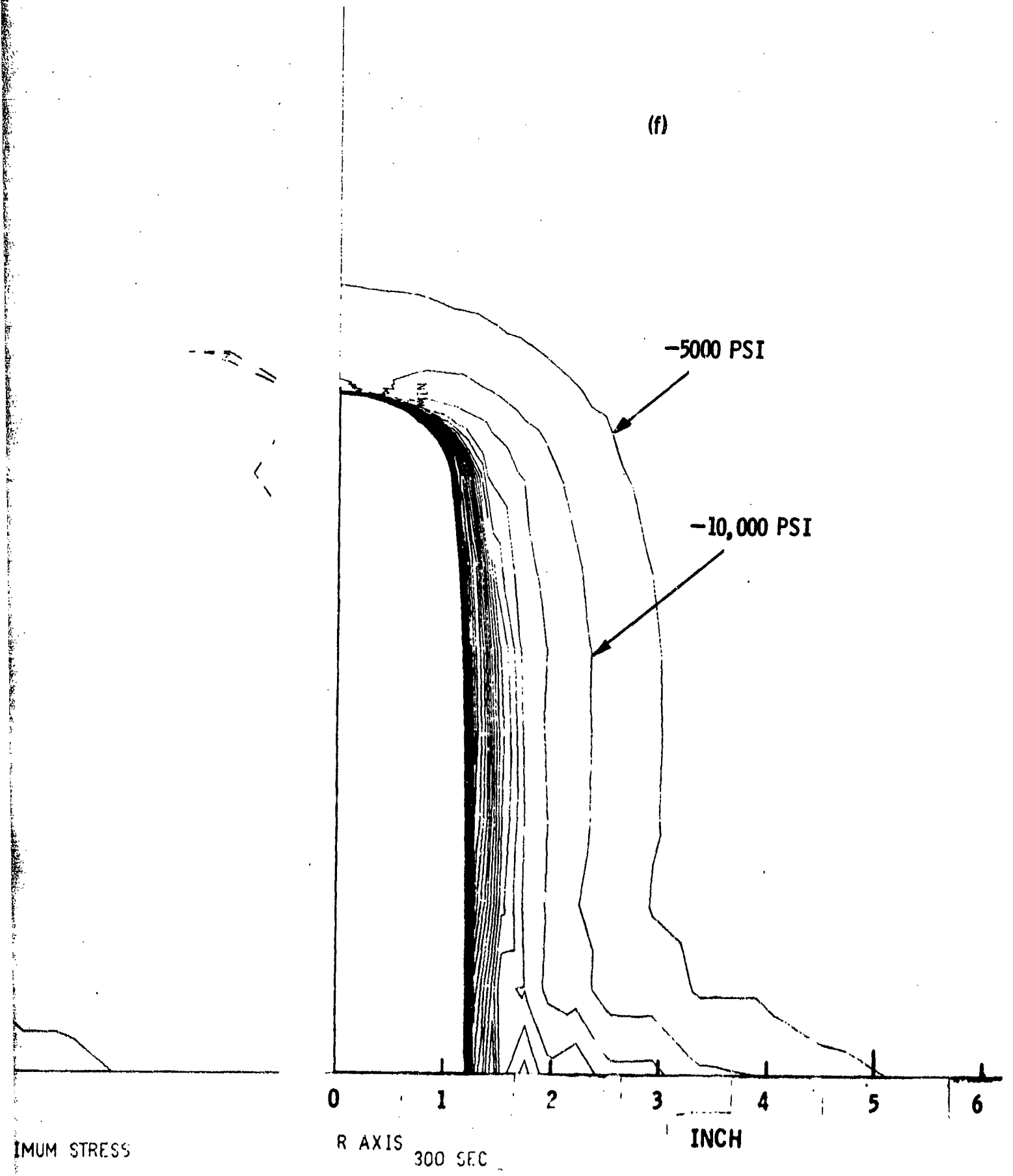

5.33.I

5.4 Interpretation of Stress Fields

There are several interesting qualitative features of the stress plots in Figure 5-16 through 5-19.

1. Compressive stresses and stress gradients are many times larger than tensile stresses and stress gradients, i.e., typically by one order of magnitude. (However, there is an even wider disparity between compressive strength and tensile strength; hence, the predominant failure mechanism is failure under tension.)

2. In the neighborhood of the cavity, the stresses are compressive wherever rock is heated. This compression is caused by the presence of the surrounding cold region, which restrains the thermal expansion of the hot region.

3. Outside the heated region, the rock is under tension.

   a. The expansion of the hot region along the axis of the cavity tends to stretch the cold region in the z direction. This stress will tend to cause cracks in a plane perpendicular to the axis of the cavity.

   b. The radial growth of the heated region causes tension in the azimuthal direction. This stress will tend to cause cracks in planes that are parallel to and contain the axis of the cavity.

4. Azimuthal tension is greater than tension in the r-z plane at depths down to those comparable to the depth of the cavity. <u>At depths similar to that of the cavity and below</u>, tension in the r-z plane begins to exceed azimuthal tension. Such stresses can produce failure configurations similar to those observed in laboratory experiments, namely, <u>a combination</u> of a vertical crack (caused by the azimuthal tension) in a plane containing the cavity axis together with a horizontal crack (caused by the r-z tension), which cuts through the bottom of the cavity.

Figure 5-20 (also Fig. 4.1-6) shows the best example available of this theory. The cavity in this block of pink Jasper quartzide is only 2 inches deep (one half the height of the block), whereas in other cases the cavity nearly penetrated blocks of this size before splitting. In these latter cases, the horizontal cracks, clearly visible in Figure 5-20, could not develop. Moreover, this quartzite is very fine grain, homogenous, and isotropic. Note also the fine cracks and the lifting of the material near the top edge of the cavity.

5. The region over which the stresses act expands with time, as one would expect. The depth of the stress field exceeds the depth of the cavity, particularly for longer piercing times.

6. For each piercing time, the calculations show nontrivial values <u>in the cold region</u> where the tensile stress is <u>many times greater than a typical tensile strength of rock</u> ($\sim 10^3$ psi).

Because of the uncertainty in the temperature calculation, it was deemed instructive to look at the effect that a drastic change in the assumed rate of heat propagation has on the calculated thermal stresses in the rock. Accordingly, stress calculations were made for piercing times of 5, 20, and 300 seconds for which the thermal diffusivity was assumed to be $5 \times 10^{-3} cm^2/sec$ i.e., just half the value used in the original calculations. The procedures followed were identical to those used with the original diffusivity. The results were similar to those of the original calculation for corresponding piercing times. The isostress plots had nearly the same shape in both cases, although halving the thermal diffusivity reduced the width of the stressed region by 15 to 20 percent. However, there was on the average no siginificant decrease in maximum value of tensile stress calculated for the three piercing times.

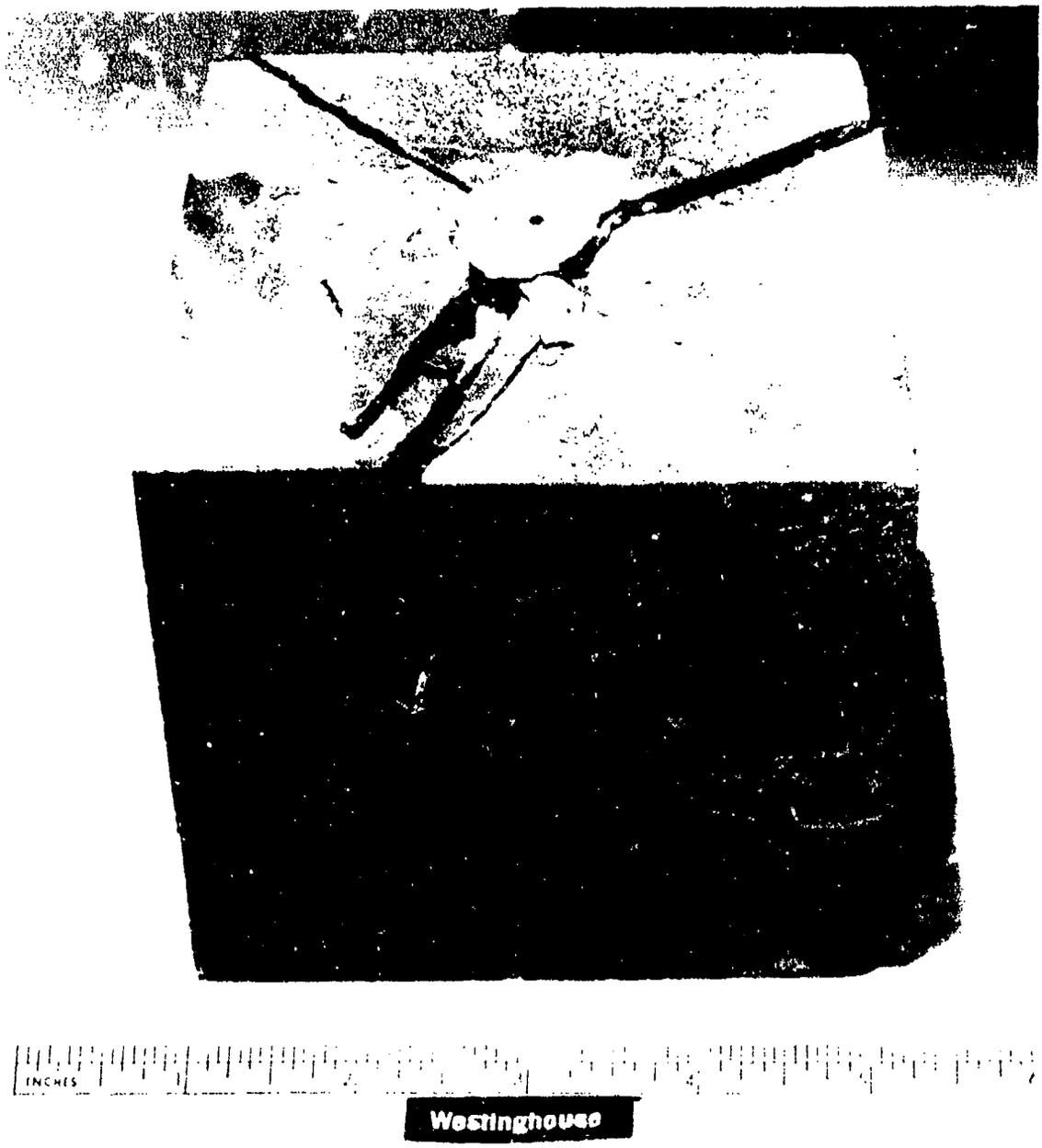

Fig. 5-20 Pink jasper quartzite cracked after 9 seconds of piercing with 9 kW, 150 kV beam (from Ref. 4).

5.5 Rock Failure

Although the rock is expected to fail under tension, it is difficult to predict the time, location, and configuration of the fracture surface. In fact, there is actually no unique tensile strength for a given type of rock. As pointed out by Jaeger and Cook (Ref. 24 p. 140), "the tensile strength of rock is more variable and more influenced by specimen size than any other mechanical property of rock."

A promising line of reasoning is based on the proposition that the variation in tensile strength with sample size depends on statistics. The larger the volume under tension, the higher the probability of initiating a failure somewhere in the volume. A situation of this type can be described by a version of the so-called weakest link theory. Jaeger and Cook (Ref. 24 p. 186) discuss such a formulation by Weibull,[25] which is the basis for the following argument. If one calls ΔP the probability that a failure occurs within a small volume of rock ΔV, then a probability density dP/dV can be defined as a function of position and stress such that, for small volumes, the failure probability is

$$\Delta P = \frac{dP}{dV} \Delta V$$

The probability S that the whole rock survives with no failure is given by the product of the survival probabilities $1 - \Delta P$ of all the volume elements making up the entire volume of the rock.

$$S = \prod_{i=1}^{n} \left(1 - \frac{dP}{dV} \Delta V_i\right)$$

Taking the logarithm of both sides converts the product into a sum, which for the condition $(dP/dV)\Delta V_i << 1$, becomes

$$\ln S \approx - \sum_{i=1}^{n} \frac{dP}{dV} \Delta V_i$$

Letting n go to infinity as ΔV_i goes to zero converts the sum to an integral, and the failure probability $P = 1 - S$ becomes

$$P = 1 - \exp\left[1 - \int_V \frac{dP}{dV}\, dV\right]$$

This expression gives the probability that a failure will occur somewhere within the rock. For simplicity Weibull assumes a power law for dP/dV given in the notation of Hudson by[26]

$$\frac{dP}{dV} = \left(\frac{s}{s_o}\right)^m$$

such that

$$P = 1 - \exp\left[-\int_V \left(\frac{s}{s_o}\right)^m dV\right]$$

where m and s_o are constants depending on the type of rock, and s, a function of position, is the maximum principal tensile stress (in psi). Although Hudson found s_o and m to vary somewhat with volume, it is instructive to use some typical values that he obtained from measurements on red granite, i.e., $s_o \approx 2000$, and $m = 6$. These values together with the calculated stresses as a function of position and time (from section 5.3) result in plots of probability density shown in Figure 5-21.

The quantity plotted in Figure 5-21 is actually dP/dA, i.e., the probability of failure per unit area rather than per unit volume and is more appropriate for a case with cylindrical symmetry than is dP/dV. The quantity (dP/dA) ΔA represents the probability that a crack will occur somewhere in a ring of small cross-sectional area $\Delta A = \Delta r \Delta z$ located at radius r; dP/dA is given by

$$\frac{dP}{dA} = 2\pi\, r\, \frac{dP}{dV}$$

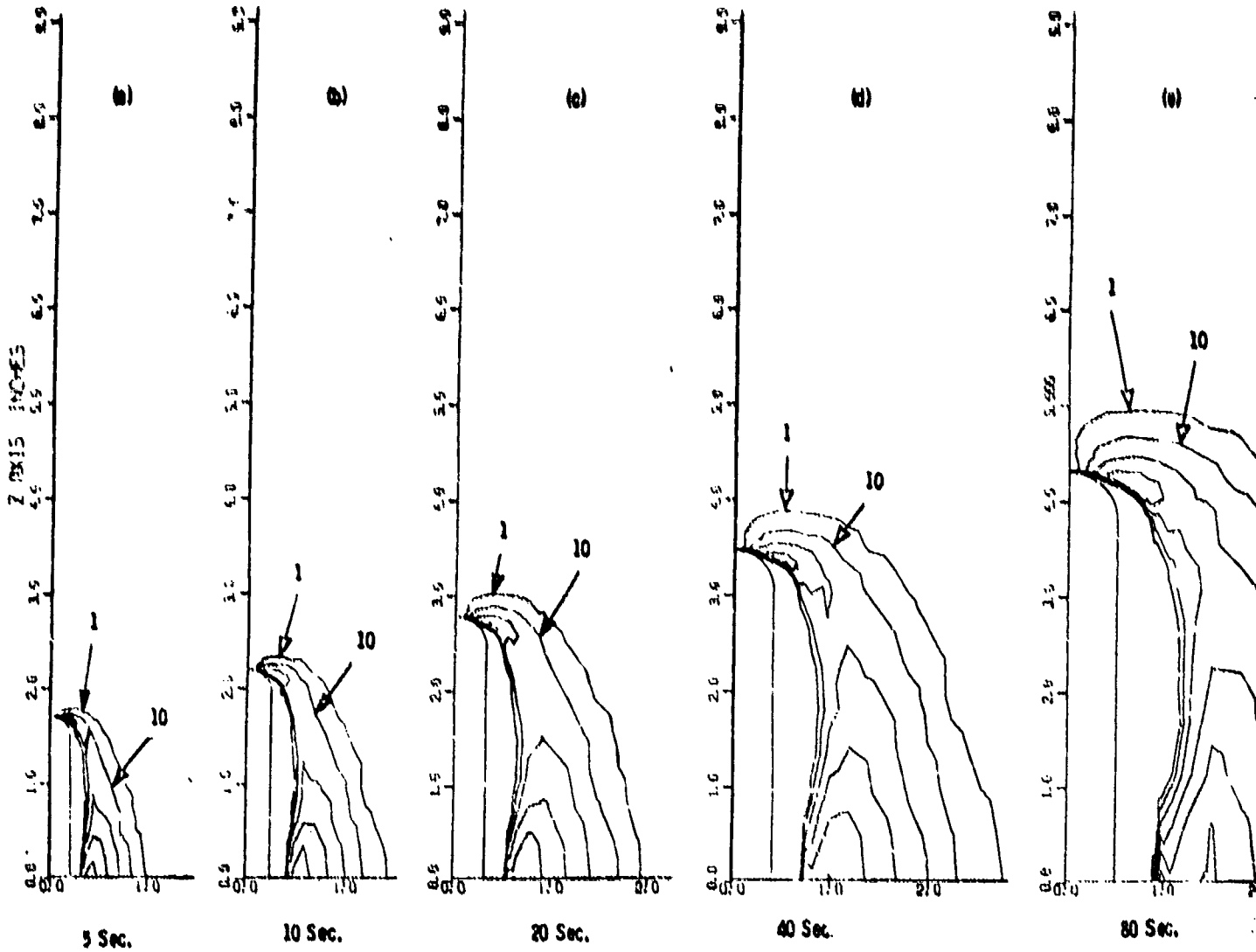
(a)
(b)
(c)
(d)
(e)
1
10
5 Sec.
10 Sec.
20 Sec.
40 Sec.
80 Sec.

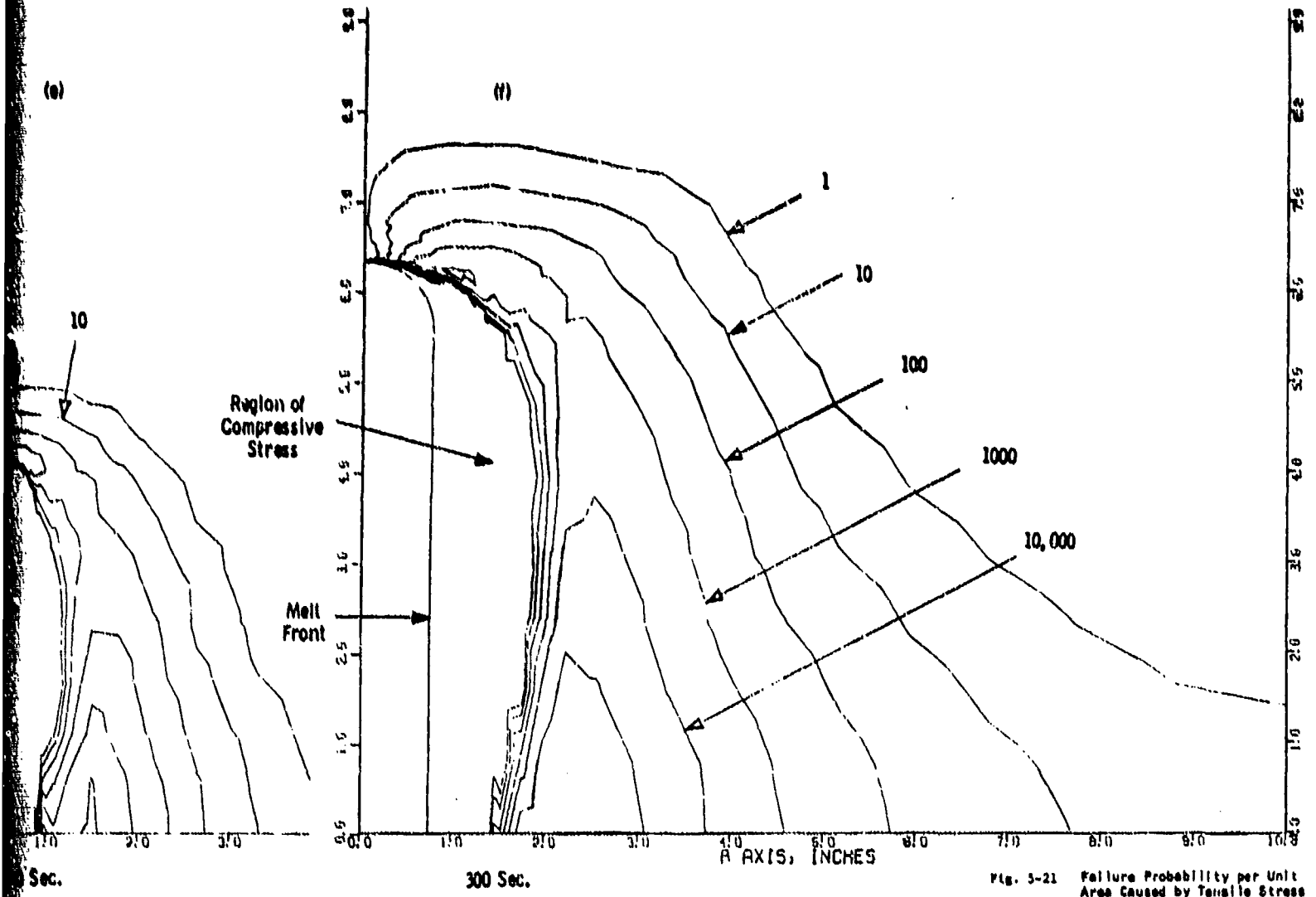

Fig. 5-21 Failure Probability per Unit Area Caused by Tensile Stress

5-43.

The contours plotted in Figure 5-21 are for dP/dA = 1, 10, 100, 1000, 10,000, and 100,000. Panels (a) through (f) represent piercing times of 5, 10, 20, 40, 80, and 300 seconds, respectively. These results are for a 9-kW, 150-kV beam, with a 1/2 inch standoff distance. The probability P that the rock will crack somewhere turns out to be essentially unity for each of the piercing times considered. The contours in Figure 5-21, however, show graphically the points at which the cracks are most likely to start.

It is apparent from the figure that cracking commences as soon as piercing begins and continues with increasing vigor, presumably until the number and/or size of the cracks alter the geometry of the rock so much that the stress relief invalidates the model used for the calculation. By that time, of course, the rock has suffered large-scale failure, which is the objective of the process. However, the details of how and when the large cracks begin to propagate are not yet understood. The degree to which small cracks formed early relieve the stress is unknown as is the effect of these small cracks being overtaken by the advancing front of molten rock. Further study of this subject will be necessary to determine the extent to which such a complicated sequence of events does occur. One would also like to know to what extent such a process would alter the temperature field, and at what point the cracks cease to be localized and propogate far from the cavity.

It is pure conjecture at this time, but the occurrence of macrocracks may have nothing to do with the microfracturing near the melt-front and is only determined by the heat flow and stress in the deeper layers of the solid rock. Such a situation would be in agreement with our observations and the stress field data from our idealized calculations.

6. MACHINERY AND SYSTEMS TESTS

6.0 General Comments

To prevent possible misunderstandings, let us repeat here that the present contract did not call for the development of an electron gun. The only part of the contract calling for the construction of hardware concerned a carriage for the electron gun to make it sufficiently mobile that it could be manipulated in front of a rock face in the field. Construction of the gun itself was started at the Westinghouse Research Laboratories already prior to the inception of the contract, using existing components from experimental electron beam welder systems to the maximum extent possible, and using for the auxiliaries, like for instance the vacuum pumps, items which happened to be available at the time. The additional developmental effort on the gun was directed at packaging the components in such a fashion that a mobile gun would result, which could also stand the rigor of outdoor use. One more very essential feature which was developed and incorporated, and which is not present in the electron beam welders, is a long beam transfer column which brings the beam exit forward to the end of a long arm or long "gun barrel". It was felt that this feature was essential for a rock cutting machine, because there is no room for bulky equipment near the work face of a tunneling or mining operation; whatever room there is, is needed for the mucking equipment to remove the debris. In fact, statements have been made that an electron gun as such is too big and bulky to be combined with, for instance, a mechanical mole or an auger which would sweep up the debris which the electron beam produces. Our machine proves that this is not so. We have a functionable, reliable, rugged electron gun with a long beam transfer column of relatively small cross sections. On the other hand, neither under the present contract nor under our in-house development program have we attempted to build the ultimate model

of an electron beam rock cutter.

A description of how the present machinery looks "from the outside" has already been given in Section 4.2 as introduction to the description of the tests in Section 4.3. The following subsections will describe (a) our experiences in combining the present electron gun with the mobility equipment, (b) the operational aspects of gun and mobility system, (c) the safety precautions that have to be taken in view of the x-rays which are produced, and (d) summary of the experiences with respect to the performance of the present electron gun in these first tests made out of doors.

6.1 Combining Electron Gun and Carriage

6.1.1 Problems with pump mounts and vacuum hoses

The electron gun was shipped to the Sunnyvale site in April of 1972 to be mounted on the carriage which has been described in Appendix A. As mentioned there, certain shortcomings of the carriage drive system were recognized but not corrected at the time; it was unfortunately assumed they would not seriously interfere with the intended tests. The electron gun, which had to be mounted on this carriage, was shown in Figure 4.2-1. Also visible in this figure are the four vacuum hoses from the gun to a small set of pumps. For reasons of pumping efficiency it is necessary to keep the length of these hoses to less than eight feet. The pumps must, therefore, be placed close to the gun. Mounting space for this set of pumps had been provided on the carriage; but the actual mounting frame for the pumps became only available in August 1972. When finally the pumps were mounted on this frame, the movement of these hoses was found to be restricted by some members of the frame itself; additional clearances could not be provided because of the restricted space on the carriage.

After some modification to the mounting frame, mainly cutting it down so that the hoses could swing freely and unimpeded by the structure of the frame itself, we ended up with the system shown in Figure 6-1. This is actually a view of the gun and carriage from the other side than the one shown in Figure 4.2-4. It is evident that the clearance between the rear of the gun and the stand for the vacuum pumps is marginal, and that the hoses are flexed to their limit; furthermore, the yaw movement of the gun is also limited by the hoses. Actually, the pump stand

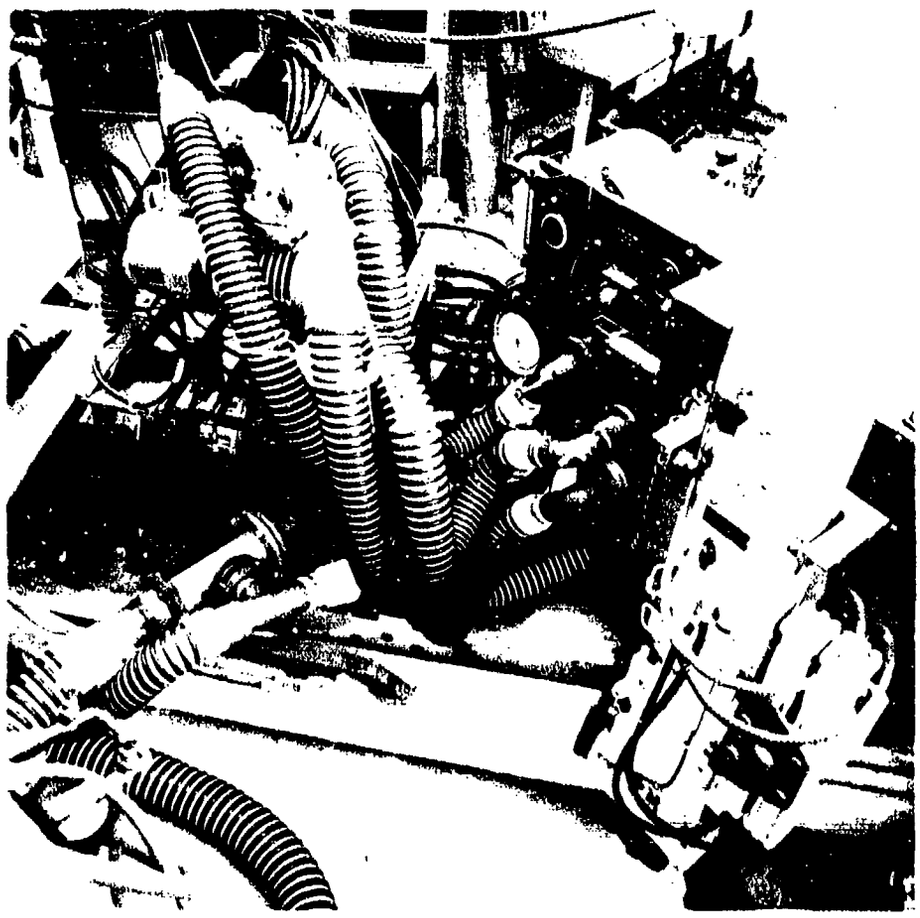

Fig. 6-1 Vacuum hoses between gun and auxiliary pump stand. It had been better if the auxiliary pump stand would follow the yaw movement of the gun; as it is, the flexibility of the hoses limits the yaw angle. The four thin hoses near the upper edge of the picture are hydraulic lines; in the lower right corner the hydraulic piston motor for the pitch drive can be seen.

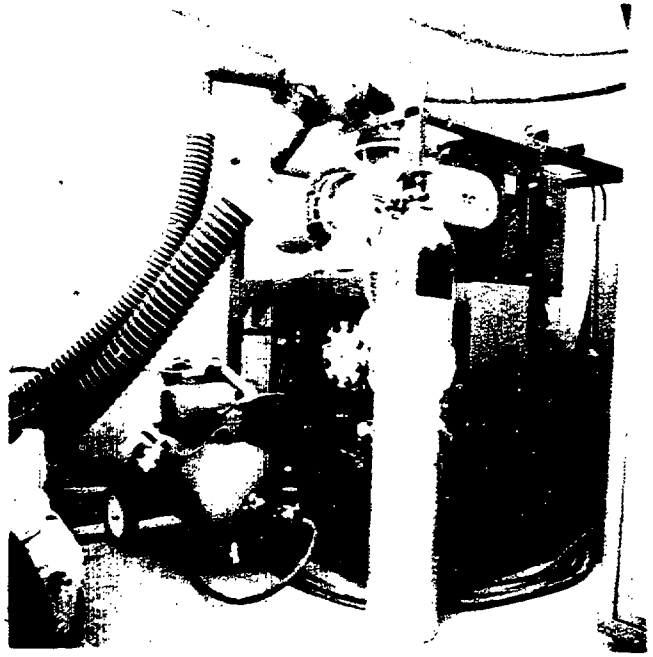

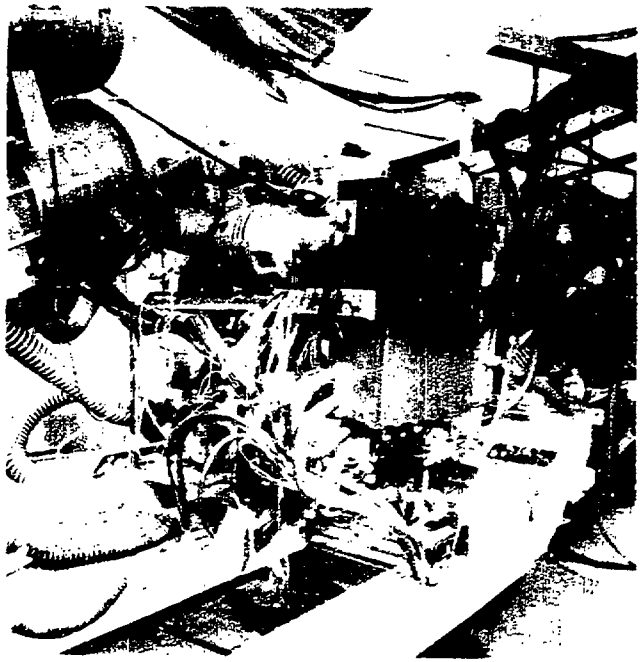

Fig. 6-2 (left): Main pump stand and small air compressor for the over-pressure chamber of the gun; the gas bottle contains SF_6 to refill power supplies, if need arises.

F8g. 6-3 (right): View of small pump stand and junction box (riding on the gun carriage) with main pumps in the background.

should have been mounted on the turntable for the yaw movement, so that the flexibility of the hoses was only needed to accommodate the pitch movement of the gun.

In the lower left of Figure 6-1, a 4" diameter and a 3" diameter hose connected in parallel lead to the back-up pumps, which are shown in Fig. 6-2. Here these two hose lines can also be seen.

Figure 6-3 is another view of gun, auxiliary pumps, and main pumps.

In spite of the somewhat abusive handling of the flexible vacuum hoses*, they remained tight and caused no problems whatsoever.

6.1.2 Operator's Observation System and Control of Gun Movements

In order to use the gun intelligently, the operator must be able to see what it does. Since a direct view at the working area is blocked by the necessary x-ray shields, a periscopic mirror system must be used to look around and behind this shield at the work area. How these mirrors were placed was already shown in Fig. 4.2-7 to 4.2-18. One of the overhead mirror periscopes was located immediately behind the control panel (Fig. A-9) for the electron gun carriage. But the distance to the electron beam work area was large; therefore, the picture which the operator saw was too small to be very useful as Fig. 4.2-13 shows. We also found that the overhead mirror on top of the cutting area became covered with fine rock dust very quickly and ther by lost its usefulness. The mirror located on the side and below the actual cutting area as shown in Figure 4.2-14 proved to be the most useful one. Remarkably, it never suffered any damage. This mirror could either be used with overhead periscope on the operator's stand or in conjunction with the telescopic periscope in the lead door which is shown in Figure 4.2-15. To see what was really going on in the cutting zone, this telescope was absolutely necessary. An example was already given in Figure 4.2-17.

---

*2", 3" and 4" hoses from PLASTIFLEX Corp., Elk Grove Village, Illinois, 60007.

It proved not possible to control the gun position and movement entirely from the operator's stand. For setting the standoff distance, for instance, prior to any cutting, another man had to go close to the gun and direct the operator by hand signals to move it forth or back. The various positions of the gun carriage could not be read out on any dial setting or counters etc. This would have been very useful.

We also found that the carriage once set to a certain position, would not remain there but because of pressure changed in the hydraulic system would move slowly forward in the X-direction; the yaw angle would also change, partly in response to the pull exerted by the flexible vacuum hoses, and because the hydraulic actuator system did not permit the settings to be locked. This had to be done on a makeshift basis.

It has already been mentioned in Appendix A that the speed setting required the fine adjustment of a hydraulic valve. Resetting these valves for a predetermined speed proved time consuming. On the other hand, these settings had to be changed often, for instance, if after a cut at slow speed the gun was to be moved to another position quickly.

It was not possible to obtain a smooth horizontal traverse. The chain drive introduced some irregularities with a pitch equal to the length of a link of the chain. Besides, the horizontal movement excited vibrations in the yaw movement; the latter had a particularly soft response and the suspension system of the gun did not go through the center of gravity so that every horizontal push also produced a moment around the yaw-axis. The faster horizontal traverses which we made, and which are described in Section 4.3, therefore give the appearance as if they had been made by a sewing machine. As a consequence, in none of our tests could we attempt to make a real spall-cuts where it is very essential that the correct speed and power setting are closely maintained, as explained elsewhere.

If the gun is set at any one yaw or pitch angle other than zero, then the Z-axis and the gun axis are no longer parallel. It is

then no longer possible to move the gun in and out parallel to the axis of the beam. From a purely practical point of view, a small movement of the gun in the direction of the beam axis, whether it is tilted in the yaw mode or in the pitch mode, would have been very useful.

Within the narrow confines of the shielding walls it was not readily possible to move the main carriage for the electron gun, although it has three wheels and was sitting on a concrete floor; a small tractor or similar vehicle for pushing the carriage could not be brought into the confines of these walls. However, since the X-movement of the gun was limited to 3 feet, it would have been advantageous to quickly relocate the main carraige by a few feet.

The wheels of the main carriage had no breaks. Therefore, when a Z-movement of the gun was started, for instance to retract it from the rock face after too much debris had built up, the main carriage started to rock and longitudinal vibrations were induced in the drive system. Once more, it was not possible from the operator's station alone to reset the gun to the proper distance.

The above mentioned shortcomings of the drive system and the operator's control must be corrected before the system is taken to the field for further tests.

For any further tests, a closed-circuit television system should also be installed which shows on a screen above the operator's console what is going on in the cutting region.

6.2 Shielded beam catcher for alignment work on the electron gun

If the electron gun has been shipped to a new test site, for instance from Pittsburgh to Sunnyvale, or if for any one reason the transfer column has been dismantled and reassembled, certain alignments have to be made to the gun and its magnetic focusing lenses, which are not critical but nevertheless, necessary. For these alignments we have not installed any remote control devices; at present they consist of several knobs and set-screws on the gun column.

Since these settings must be made under power, the gun column must be shielded against x-rays, as indeed it is. Furthermore, we need a beam target which is coupled to the gun column in such a way that a continuous x-ray shield is achieved. A simple lead box with a water-cooled beam catcher of copper is actually all that is needed. The photographs of Figure 6-4. show the gun coupled to such a lead box. It is now possible to stand directly beside the gun column when the beam is fired into the shielded catcher, and make the necessary alignments. A close-up view of the front end of the gun facing the shielded catcher, is shown in Figure 6-5. A description of the kinds of alignment which must be made will be found in Section 8.3.

We needed to make these alignments only once, when the gun was fired up the first time after shipment to Sunnyvale. Throughout all the tests at Sunnyvale the beam transfer column was never opened, and the gun itself only opened once for an exchange of cathodes, hence no realignment was ever necessary.

6.3 X-Ray Safety

6.3.0 General Comments

Where fast electrons are stopped (whether the beam goes into air or whether it hits a target like rock) x-rays are produced. X-ray shielding is well understood and easily accomplished. Very sensitive and reliable, yet inexpensive alarm devices are available to warn operating personnel of the continuous or occasional presence of x-rays. They can be interlocked with a beam-off switch. When the electron beam is off, there are no x-rays and no residual radiation of any kind. This fact emphasizes an important difference between radioactivity (and the associated long-term internal accumulation of radioisotopes by biological systems) and x-ray production, which represents only a temporary (external) condition, against which one can guard oneself.

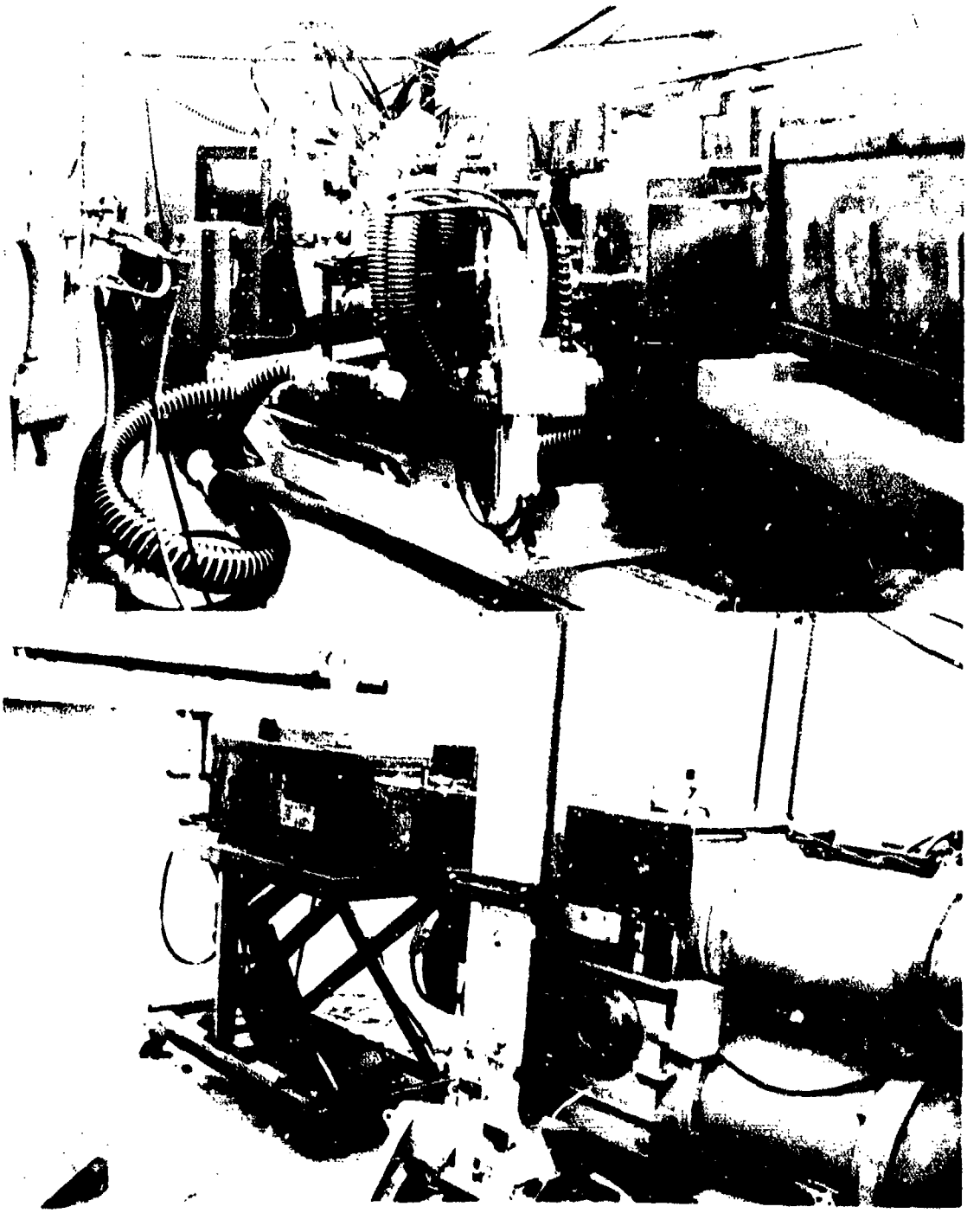

Fig. 6-4 Top: View along the right side of the gun and carriage; in the foreground the lead box for the shielded beam catcher; in the background the main pumps.
Bottom: Gun coupled to the shielded beam catcher in its lead box.

RM-55479

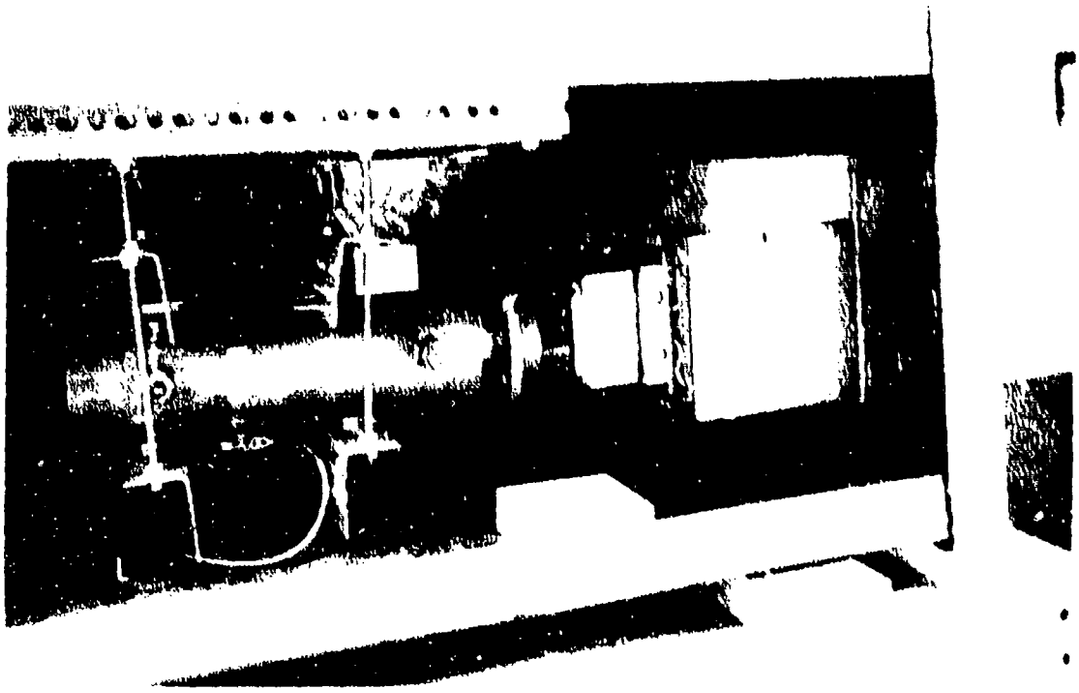

Fig. 6-5

Gun facing water cooled beam catcher F inside of lead box L. When box is closed the operator can stand beside the gun running at full power and, through lead glass windows, observe beam shape and alignment; the gun proper is completely self-shielding. M is the lead shroud which stays on the gun. A lead-room is not required to assemble and test the electron gun. In this picture the copper/molybdenum shroud has been removed from the front end of the gun to make the small round viewing window accessible, which permits seeing the beam inside the steel chamber S.

Although x-rays are the major disadvantage of an electron-beam system, handled with proper understanding they are more an inconvenience than a danger. The following sections present a summary of the major considerations in x-ray safety and an account of our activities in this connection.

6.3.1 California State Registration

As defined by the California Radiation Control Regulations,* the electron beam gun falls into the category of "radiation producing machines" and, therefore, must be registered with the State Department of Public Health. Public Health Department authorities have been contacted regarding registration requirements. State regulations also govern such items as radiation protection, warning sign markings, personnel monitoring, etc. Compliance with these regulations posed no difficulties.**

Some of the radiation surveys which we later performed (Section 6.3.4 and 5) were conducted in conjunction with personnel from the California State Dept. of Public Health.

6.3.2 X-Ray Generation Laws

Much has been written on x-ray shielding, and unfortunately much of it is very confusing. It seems justified therefore to give here a concise summary of x-ray facts, because the user of the electron guns has to live with and understand these facts. Fig. 6-6a shows the spectrum (wavelength or hardness distribution) of x-rays generated by electrons of different energy (voltage) on a tungsten target. The smooth curves depict what is called the Bremsstrahlen-spectrum generated by the stopping of the electrons; the little peaks are characteristic

---

*California Radiation Control Regulations, Title 17, Public Health, California Adminstrative Code, Chapter 5, Subchapter 4, Sections 30100 through 30397.

**Legal Exposure Limits are listed on page 6-17.

spectral lines of the tungsten. The shortest wavelength (greatest hardness) of the Bremsstrahlen-curve is given by $\lambda_{min} \sim 12.4/E_0$ Angstrom*) (for E_0 in kV). Fig. 6-6b shows how the spectrum from a 200 kV source is modified by a copper absorber of various thickness. Fig. 6-6c and d show how the spectrum and the total intensity of the x-rays are different for different observation angles with respect to the electron beam direction.

As for the effect which the x-rays have, for instance on man, it is not the energy flux in empty space that counts, but rather how much of it is absorbed. This absorbed part is call the "dose" and is measured in rads (symbol: rd), the dose per unit time is measured in rads per hour (or rd/h) etc. One rad is 100 ergs/g.

When correcting for differing effects on various materials of the human body by various types of ionizing radiation one replaces doses in rads with "dose equivalent" (DE) which is measured in rem. Government imposed limits on acceptable doses for workers are expressed in rem. For x-rays rad and rem are essentially equivalent. An additional simplification is that for purposes of shielding safety the dose rate in rem per hour can be taken to be numerically equal to the exposure rate in Roentgens per hour (R/hr) as measured by an x-ray exposure meter, as they are commercially available.

One must know the total x-ray energy flux (e.g. in Watt/m^2) and the spectral distribution to predict what the dose exposure rate in R/hr and ultimately the DE will be. The conversion factor α from W/m^2 to R/sec is given by the curve in Fig. 6-6e.

To assess a given situation with respect to the required precaution and necessary shielding, the most important quantity we need to know is the total x-ray energy flux (in all directions) generated by a given x-ray tube or electron beam target. This amounts to asking for the conversion efficiency from electron beam energy to x-ray

---

*) 1 Angstrom = 10^{-8}cm

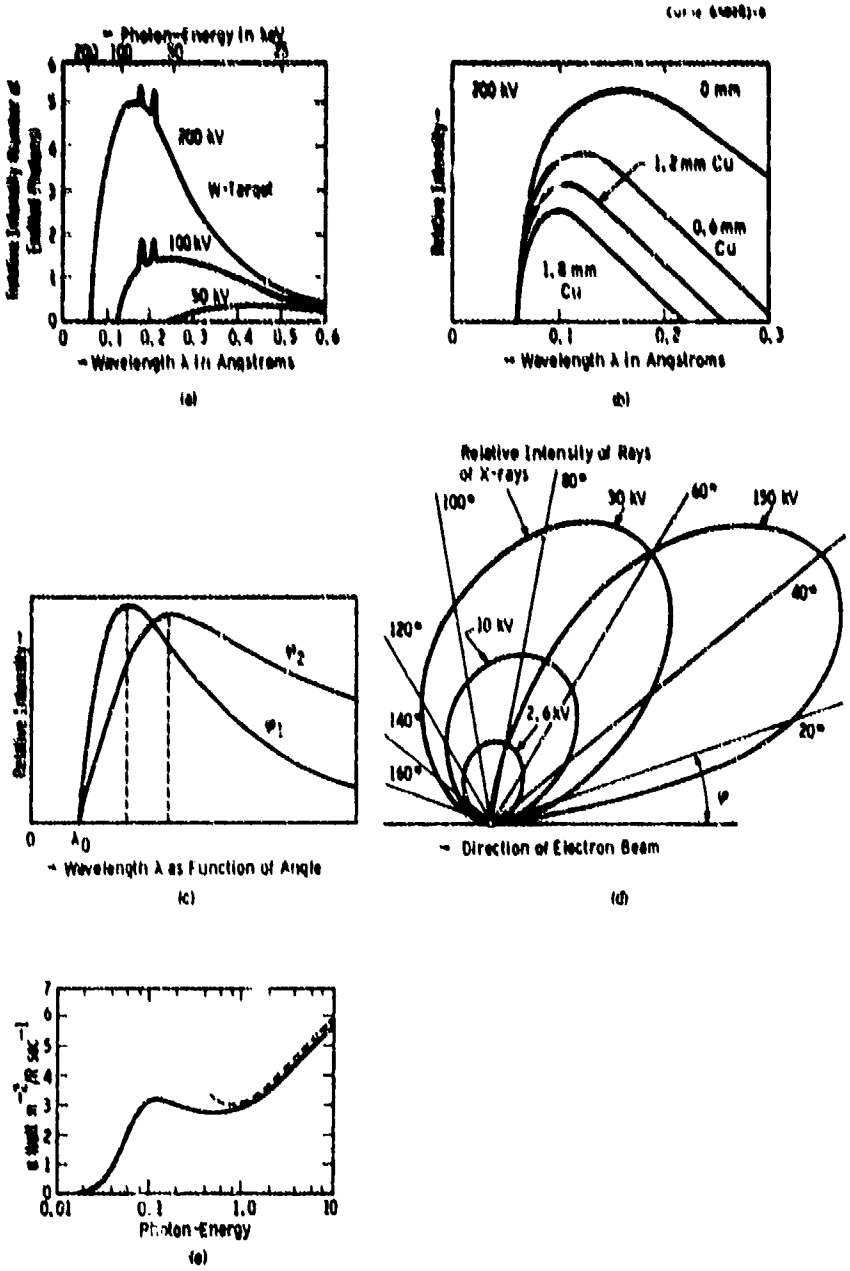

Fig. 6-6: Basic facts about x-ray generation. (a): Spectrum of the x-rays as function of the electron beam voltage. (b): Change of the spectrum due to filtering (or shielding) by copper sheets of various thickness. (c) and (d): Dependence of spectrum and intensity upon direction of observation. (e) Relationship of the energy flux density of the x-rays and the Röntgen-dosis measured in air. [(a) and (b) -- adapted from D. Nachtigall: "Dosimetry and Radiation Protection," Munich 1970; (c) and (d) adapted from F. Regler, "Phys. of x-rays and gamma-rays," Munich 1967, (e) adapted from R. Jaeger, in Landolt-Boernstein "Numerical Values and Functions," 6th Ed., Vol. IV/3, p. 992, 1957].

energy, which is given by equation (1) below. Fortunately, under our conditions the conversion efficiency is low, in the order of 1%.

After looking at the various aspects of x-ray generation depicted in Fig. 6-6 it will be appreciated that it is not an easy task to make an accurate prediction of the x-ray dose which one will find around on electron beam target, but a good enough estimate can be made as follows:

Efficiency of x-ray generation by an electron beam:

$$\eta = \frac{W_x}{W_o} = \frac{\text{Energy flux in the x-rays (total)}}{\text{Energy flux carried by the electron beam}} = \eta_o Z E_o \qquad (1)$$

Z = atomic number of target substance, for $E_o < 1$ MV one finds $\eta_o = (1 \pm .3) \times 10^{-6}$ hence:

$$\eta = Z \times E_o \times 10^{-6} \quad (E_o \text{ in kV}) \qquad (1')$$

At 1 m from the source the energy flux density F_x is $1/4\pi$ the total x-ray energy which is generated (assuming a uniform spherical distribution but see Fig. 6.3-1d, hence:

$$F_x = \frac{1}{4\pi} \eta W_o \qquad W\ m^{-2} \quad \text{(at 1 m from the source)}$$

(W_o is the electron beam power in watt).

This flux is inversely proportional to the square of the distance, considering the target area as a point source.

The absorbed energy per cm^3 per sec and the exposure rate R_x (R/sec) are not only functions of the energy flux F_x but of the quantum energy (or "hardness," or "voltage") of the x-rays. The approximate

relationship is given by the curve in Fig. 6.3-1e where $\alpha = F_x/R_x$ $W\ m^{-2}/R\ sec^{-1}$. Hence:

$$R_x = \frac{1}{\alpha} F_x = \frac{1}{4\pi\alpha} \eta W_o \qquad R/sec\ (at\ 1\ m) \qquad (3)$$

In the range of $70 < E_o < 200$ kV an average value of $\alpha = 3\ W\ m^{-2}/R\ sec^{-1}$ may be used. (The dimensions here may seem confusing, but the Roentgen implicitly contains the area already in its definition, just as the watt contains the time).

If we measure the electron beam current I_o in milliampere and E_o in kV, then $W_o = I_o E_o$; hence we may write for (3):

$$R_x/I_o = \frac{\eta_o}{4\pi\alpha} Z E_o^{\ 2} \qquad R\ mA^{-1}\ sec^{-1}\ (at\ 1\ m) \qquad (4)$$

with $\eta_o \simeq 1x10^{-6}$ and $\alpha = 3$ this gives

$$R_x/I_o = 2.7x10^{-8}\ Z E_o^{\ 2} \qquad R\ mA^{-1}\ sec^{-1}\ (at\ 1\ m) \qquad (4')$$

We can now calculate the expected x-ray dose for our situation from either (3) or (4). It will strongly depend upon the atomic number Z of the target material. Let us assume a "worst case" situation, namely a tungsten target with Z = 74. Then, with $E_o = 150$ kV we get from (4′):

$$R_x/I_o = .045\ R\ mA^{-1} sec^{-1} \quad (at\ 1\ m)$$

$$= 2.7\ R\ mA^{-1}\ min^{-1}\ (at\ 1m)$$

A 30 kW beam of 150 kV carries $I_o = 200$ mA, hence it produces an x-ray flux of

$$R_x = 540\ R/min \quad (at\ 1m)$$
$$= 32\ 400\ R/h \quad (at\ 1\ m)$$

This is the x-ray intensity against which we have to provide proper shielding.

6.3.3 X-ray tolerance levels and shielding

(a) Tolerance levels:

The x-ray dose which people may possibly receive from any such source as the e.b. rock cutter must stay below a certain tolerance level, which is established by law.

Confusion often exists because of the fact that the law says actually nothing over which period of time the tolerance dose may be accumulated, except that it is given as a 13-week average. Therefore the x-ray intensity in a normally unoccupied although accessible area can, without danger, be higher than, say, at the permanent operator's station of the machine.

The legal limits are listed in Table 6-1.

Note that if 1.25 Roentgen may be accumulated over a period of 13 weeks at 5 working days at 8 working hours, then the maximum permissible continuous dose rate is

$$R_x = 2.4 \text{ mR/hour}$$

The operator's station should not normally see a higher x-ray flux, but even a 100X increase for 1 minute once in a week is still harmless.

The instantaneous x-ray flux was, in all our tests, measured by proper instruments, for instance a Victoreen Type 440 survey meter. Each operator also had an audible sensor and alarm device and carried a film badge for the registration of the accumulated dose, and wore a low-energy sensitive dosimeter. (See also 6.3.5)

The x-ray intensity produced by the machine (See Section 6.3.2) must be attenuated by proper barriers or absorbers to a value of/or below the tolerance limit, whereby the hourse of use etc. can be taken into account.

Table 6-1 Legal x-ray exposure limits.

MAXIMUM PERMISSIBLE DOSE (MPD) VALUES OF THE NATIONAL COMMITTEE ON RADIATION PROTECTION (NCRP)

Organ of Reference	Annual MPD (rem)[1]	13-Week MPD (rem)[1]
Whole body	5	3
Head and trunk	5	3
Active blood-forming organs	5	3
Gonads	5	3
Lens of the eyes	5	3
Skin of whole body[2]	10	6
Hands and forearms	75	25
Feet and ankles	75	25

For each organ of reference listed, the NCRP states that the annual MPD may be exceeded at any time provided the 13-week MPD is not exceeded, and provided the MPD total, to the organ in question, accumulated at any age, shall not exceed the annual MPD multiplied by the number of years beyond 18.

The radiation levels to uncontrolled areas shall be such that it is improbable that any individual will receive a dose of more that 0.5 rem in any one year.

OCCUPATIONAL EXPOSURE LIMITATIONS OF 10 CFR PART 20[3]

Organ of Reference	13-Week Limit (rem)[4]
Whole body	1-1/4
Head and trunk	1-1/4
Active blood-forming organs	1-1/4
Gonads	1-1/4
Lens of the eyes	1-1/4
Skin of whole body	7-1/2
Hands and forearms	18-3/4
Feet and ankles	18-3/4

The annual limit in each case is simply four times the 13-week limit. An individual may be permitted to receive up to 3 rem in any 13-week period, and hence 12 rem per year to any or all of the first five organs of reference listed, provided the total accumulated occupational dose to the whole body shall not exceed 5 rem multiplied by the numbers of years beyond 18. In order to use this rule, an employer must first determine the individual lifetime occupational dose.

The radiation levels in unrestricted areas should be such that they are not likely to cause any individual to receive a dose to the whole body in any calendar year that is in excess of 0.5 rem.

[1] For X-rays the rem (roentgen-equivalent-man) is equal to the roentgen.

[2] This limit applies to radiation of low penetrating power such as electrons and low energy X-rays (under 50 kV)

[3] United States Atomic Energy Commission Code of Federal Register, Title 10, Part 20, "Standards for Protection against Radiation," November 1960.

[4] For X-rays the rem (roentgen-equivalent-man) is equal to the roentgen.

(b) Shielding of the primary beam

To what extent various materials will block or absorb x-rays is shown in Fig. 6-7 a and b. Practical considerations suggest using either lead sheet or concrete blocks for shielding, but earth, sand, gravel, granite boulders etc. may very well be used if locally readily available.

For shielding design we can assume that the operator is at least 2 m away from the source (see Fig. 4.2-6). The atomic number of the target is not 74 (tungsten) but lower, since the major constituent of rock is silicon with atomic number 14. The unshielded beam would then (following the calculation in Section 6.3.2) generate an exposure rate at the operator area of 3600 R/hour. This must be reduced to 2.4 mR/h by proper shielding. The required factor is obviously 1.5×10^6 which is equivalent to about a factor 2^{12}, or 12 "half-value layers" of shielding material. From Fig. 6-7a we see that for 200 kV x-rays the half-value thickness of lead is .050 cm; a lead barrier of .6 cm will therefore provide more than adequate shielding, since we are not even working with 200 kV but only with 150 kV x-rays. The shielding box for the beam catcher shown in Fig. 6-5 is made of 1/4" lead sheet, and was always proved adequate.

If we want to use concrete for the shielding, we see from Fig. 6-7a that its half-value thickness for 200 kV x-rays is 2.5 cm; again we need 12X this thickness or a total of 30 cm. The walls of the radiography room at Sunnyvale were much thicker (see 4.2-6).

As a cross check for the above calculation, or instead of it, the x-ray flux from a tube operated at a certain voltage and current, and attenuated by shielding of various thickness may also be obtained from graphs published in N.B.S. Safety Handbook #93. (Ref. 15), if extrapolated to our conditions.

HALF-VALUE THICKNESSES FOR VARIOUS MATERIALS

Gamma Energy (MeV)	0.1	0.2	0.5	1.0	2.0	5.0
Material	**Half-Value Thickness (cm)**					
Aluminum	1.60	2.14	3.05	4.17	5.92	9.11
Iron	0.26	0.64	1.07	1.49	2.09	2.84
Copper	0.18	0.53	0.95	1.33	1.86	2.47
Lead	0.012	0.068	0.42	0.90	1.34	1.44
Lead [a]	0.024	0.050	0.31	0.80	1.20	
Water	4.14	5.10	7.17	9.82	14.05	23.02
Air [b]	35.5	43.6	61.9	84.5	120.5	195.8
Concrete [c]	1.75	2.38	3.40	4.65	6.60	10.28
Concrete [a]	1.75	2.54	3.26	4.51	6.12	

[a] These are half-value layers for heavily filtered constant-potential X-rays.
[b] For air, distances are given in meters and inverse-square-distance effects are neglected.
[c] Average concrete density is 2.35 g/cm.[3]

Fig. 6-7a

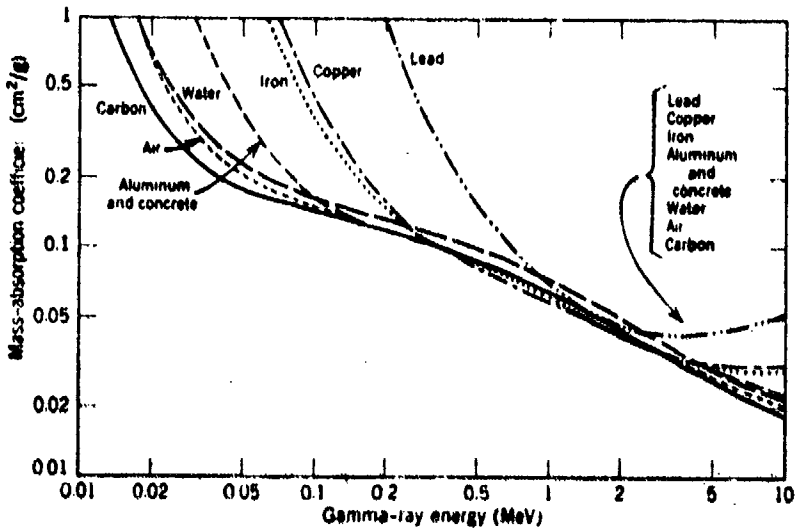

Mass-absorption coefficients. (From *Radiological Health Handbook*, pp. 144–150.)

Fig. 6-7b

(c) Shielding against stray radiations

It is not necessary, and in our rock cutting operation not always possible, to enclose the work area or x-ray source completely and hermetically with an x-ray shield of, say, 1/4" lead. On the other hand, it is not sufficient either to have only a barrier between the x-ray source and the operator. In this case, scattered x-rays may reach the operator's station over and around the barrier. The work area at Sunnyvale was open at the top. If any part of the primary x-ray beam would pass over the shielding walls then the back-scatter from the air alone would be enough to increase the x-ray intensity at the operator's station and in the surrounding area to above the tolerance level. While, as we have said, the x-ray shield must not be hermetically tight, it must nevertheless intercept the primary x-rays in all directions. Back-scattering from the air is sometimes called "sky-shine." Worse than this sky-shine is the back-scattering of the primary x-rays from any more solid object which lies in the range of the primary x-rays and at the same time in the field of view of the operator.

We had initially provided a horizontal sky-shine shield consisting of a 1/4" lead panel backed up by a plywood frame and suspended over the work area. This is shown in Fig. 6-8a. However, since the concrete walls of the work room were rather far from the test specimen, some of the primary x-ray radiation could pass below the sky-shine shield and yet get over the concrete walls. Consequently the scattered radiation in the surrounding of our work area became intolerably high at full beam power. We therefore had to provide additional side shields which also consisted of 1/4" lead bonded to a plywood frame. Fig. 6-8b shows how such shields against stray radiation must be set up properly. The essential point is to intercept the primary x-ray beam in every one direction.

The primary x-rays travelling towards the electron gun must also be intercepted. The gun itself does intercept part of these x-rays; however, for operation at full power we found it necessary to

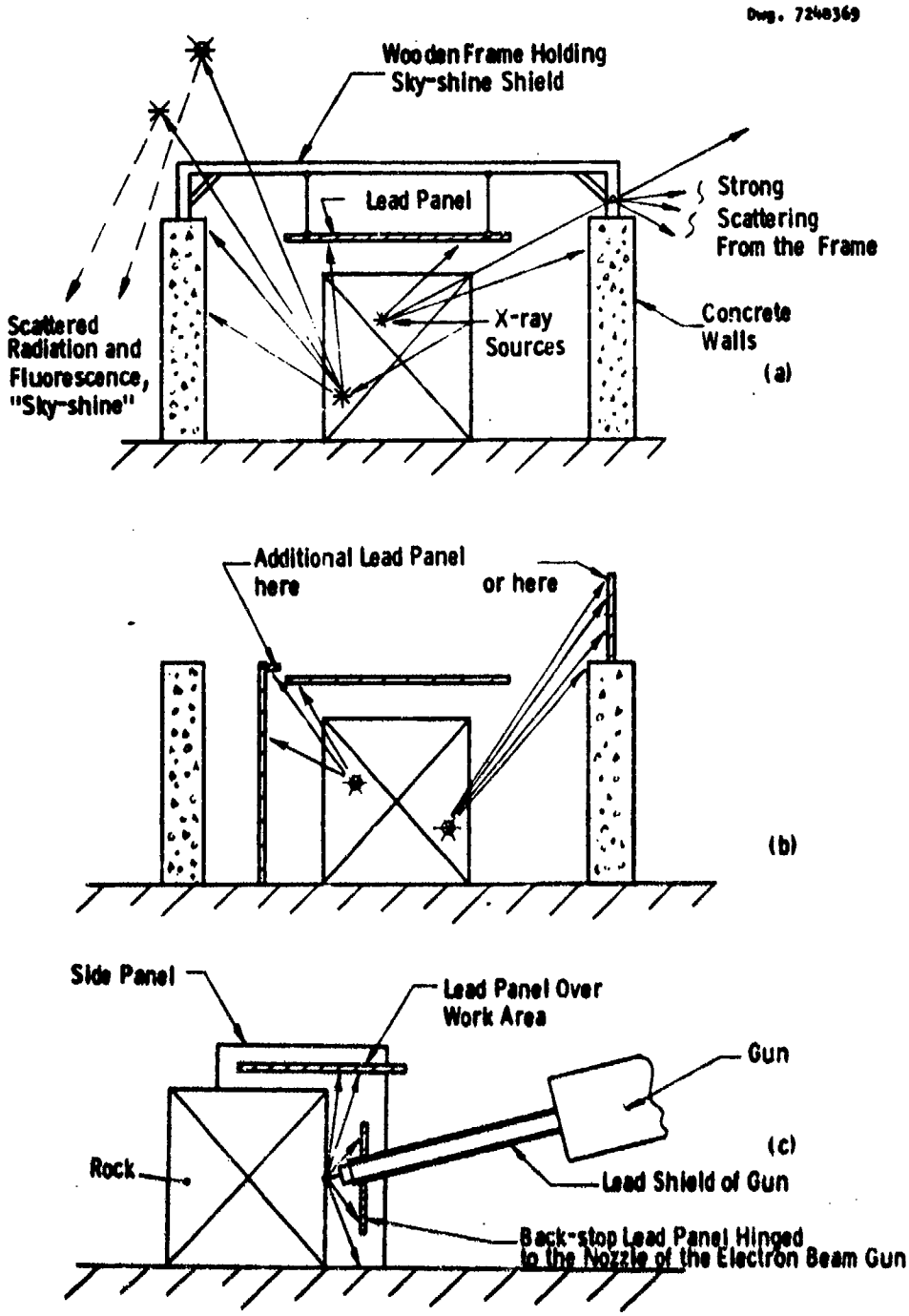

Fig 6-8 Proper placement of barriers for intercepting all of the primary x-rays. (a) Not all of the primaries are intercepted and some "sky-shine" is produced. (b) Proper placement of additional barriers. (c) Lead panel as back-stop suspended on the gun, "elephant ears."

attach a larger lead panel to the gun, as shown in Fig. 6-8 and also in Fig. 4.2-10. Such a shielding panel will not interfere with the movement of the gun because it can be hinged and therefore will swivel and keep itself parallel to the rock face when the gun is adjusted under an angle other than 90° to the rock face. There is nothing difficult about it once the principle which one has to follow is understood.

For work underground or in a tunnel the rock of the wall will provide complete shielding and only a back-stop on the gun would be needed plus some local shielding for the operator.

Secondary scattering of the already scattered radiation usually does not cause problems, because the intensity is low. Yet a final check must always be made in the form of a radiation survey using properly calibrated instrumentation.

6.3.4 Measurements in the primary beam

Considering the approximate nature of the x-ray flux calculations, as explained above, we felt some measurements should be made on our own machines, which differ from x-ray tubes in that they have no "window." Two series of such measurements were made, one at the e.b. welder installation in Pittsburgh, one at the installation in Sunnyvale. The latter survey was conducted in conjunction with Mr. K. Wong of the California State Dept. of Public Health, on October 26, 1972. Certain differences in the conditions existed, insofar as at Pittsburgh we measured the x-ray flux inside a small shielded room using electronic instruments; at Sunnyvale, we used film badges and the work area was rather spacious, hence back-scatter conditions were different.

The following is an account of both studies:

(a) Direct-X-ray intensities from non-vacuum e.b. gun (at Pittsburgh) June 1971.

Radiation rates from x-rays produced by the 9kW non-vacuum electron beam welding gun have been measured with the view in mind of specifying the amount of shielding required for the 36 kW rock cutting

machine. A Nuclear Chicago model 2588 Cutie Pie meter with a model 2520 ion chamber served as the x-ray detector and was used in the integration mode. The electron beam gun operated at 150 kV and produced a 1.5 mA beam, which was directed downwards at a target which was perpendicular to the beam and 0.8 in. below the gun muzzle. Two different target materials were used: tungsten and aluminum. In addition, measurements were made with no target in place, in which case the electron beam was dissipated in the atmosphere. The detector was positioned in a plane which was perpendicular to the beam and 14 cm above the target. The detector to target distance was 100.0 $\pm$ 0.5 cm.

The ion chamber of the detector had a thin window so as to permit detecting low energy photons. It was possible to cover the window with a plastic cap (beta shield), which substantially reduced the sensitivity to energies below about 20 keV. However, for energies greater than about 25 keV the sensitivity was independent of photon energy to within about $\pm$ 5 percent and was also independent of whether the beta shield was in place or not. (The calibrations, given by the manufacturer, were made with the axis of the ion chamber pointing toward the x-ray source when the shield was off and with the axis perpendicular to rays from the source when the shield was on. In our tests we used the appropriate orientation depending upon whether the shield was on or off.)

To simulate approximately the conditions described in the N.B.S. Safety Handbook[15], we took one measurement with a 1/8 in.-thick aluminum plate between the x-ray source and the detector. Thus we filtered out much of the very low energy radiation in a way which allowed us to compare our measurements with the handbook values.[16]

As a consistency check on our procedures, equipment, and theory, we made one measurement at a distance of 71.0 $\pm$ 0.5 cm, which is a factor $1/\sqrt{2}$ closer than 100 cm. As a result the radiation rate roughly doubled, as one would expect from the $1/r^2$ law. (This law is made use of the shielding specifications given in the N.B.S. Handbook.)

The following table summarizes the x-ray exposure rate measurements according to the various conditions. The rates have been scaled down by a factor of 2/3 to correspond to a beam current of 1 mA rather than the 1.5 mA actually used.

Note that installing the beta shield cuts the measured exposure roughly in half, a fact which indicates our x-ray spectrum is strongly peaked in the region below 20 keV. Note also that the proportionality between the x-ray exposure and atomic number of the target material, while approximately satisfied in comparing our data for aluminum and air, breaks down in the case of tungsten. Theoretically one might expect the rate for tungsten, based on that for aluminum, to be 2.07 x 74/13 = 11.8 R/mA min, rather than the 5.72 R/mA-min actually measured. This measured value is just 1/2 as great perhaps because of self absorption in the tungsten target (the mass absorption coefficient for tungsten is 30 to 120 times as large as for aluminum, whereas the electron range in g/cm^2 is comparable for the two materials).

X-Ray Exposure Rate Measurements; 9kW 150 kV electron beam gun operated with target in air.

Target Material	Measured Exposure Rate R/mA min			
	at 1 m distance			at .71 m
Tungsten (Atomic Number 74)	[9.85][1]	5.72	[1.46][2]	14.1
Aluminum (Atomic Number 13)	-	2.07	-	-
Air (Average Atomic Number 8)	[3.20][1]	1.60	-	-

1) Detector without Beta-Shield.

2) 1/8" Aluminum filter in the path of the x-rays

On the other hand the theoretical values according to eqn. (1) and (4) Section 6.3.1 are lower; they correspond to radiation filtered by, perhaps 1/16" aluminum. But such discrepancies concerning the soft end of the radiation spectrum are of little consequence for the shielding requirements.

With reference to the table the measured x-ray exposure produced with the tungsten target, when filtered through 1/8 in. of aluminum, is very close to the value (~1.4) given in the N.B.S. Handbook[16] for pulsed x-ray tube with a 3 mm aluminum filter but operated with a peak voltage of 200 kV. Shielding for 200 kVp is probably adequate for our case of 150 kV dc since the higher assumed peak voltage in the pulsed waveform case tends to compensate for the higher average voltage in the dc case. Using our measurement with the tungsten target (worst case situation) and the aluminum shield we calculate that the 36 kW gun, running at 240 mA, will produce 8×10^5 R during a 40 hour week at a distance of 1 m. Extrapolating the 200 kVp curve given in Fig. 17 of the N.B.S. Handbook we find that 10 mm Pb shielding reduces this radiation by a factor of 10^7, thus bringing the dose level for an operator, working as close as 1 m from the work area, to a value of 80 mr/week, which is below the standard accepted value of 100 mr/week. Actually, a 10 mm thickness of Pb gives much more than sufficient shielding and serves here mainly as an example, for in practice the operator will be more than 3 m away, observing the work area with a telescope. In addition, the x-ray intensities will be generally lower than what our measurements would seem to indicate since the beam penetration into the work piece during cutting and welding will result in significant self-shielding. The x-ray intensity when cutting rock will be reduced still further since it is composed of materials typically with atomic number between 8 and 20. Such radiation more nearly corresponds to that from the Aluminum target rather than the tungsten one.

(b) Direct beam measurements at Sunnyvale

The gun was operated at 150 kV 70 mA (10.5 kW), facing the granite block in the stationary piercing mode with an initial stand-off

distance of 1.5". (After a short time a piercing cavity developed, producing a self-shielding effect). Film badges were placed at various locations as identified in the following table.

Badge No.	Distance from Point of beam impingement (inch)/meter	Length of Exposure (min)	Total Dose (mR)	Unit Exposure Rate R $mA^{-1}min^{-1}$ (at 1 m)
759-009	24.8 (.63 m)	45	300000	0.038
-009	120*	45	420	-
-001	24.8 (.63 m)	3	35000	0.067
-015	78 (1.98 m)	3	1700	0.032
-019	78 (1.98 m)	45	12500	0.015
-020	156*	45	110	-

*Badge numbers 759-009 and 759-020 were shielded by the "elephant ears" on the gun column. All other badges were exposed to direct radiation for the time indicated.

Several points are obvious: (i) the badges from behind the lead panel on the gun (the "elephant ears") indicate a very low flux of scattered radiation; a man could safely stand behind such a single lead shield barrier for several minutes. (ii) The "Unit-Exposure-Rate" produced by the direct beam is 10 to 100 times <u>less</u> than predicted theoretically or based on the measurements at Pittsburgh. The reason is self-shielding of the beam, or rather the x-ray generating region, in and below the rock face (piercing process; not present during the measurements at Pittsubrgh using a low power beam). For both film badge locations the 3 min exposure produced twice as high a "Unit Exposure Rate" than the 45 min exposure, since the self-shielding effect increases with the depth of the cavity, i.e. with time. Regrettably, a 5 sec exposure was not made; its results would be really interesting. (iii) The $1/r^2$-law is not fulfilled; probably some scattered radiation contributed to the measurements or the self-shielding effect was different in the different directions where the film badges were placed.

In conclusion: There are no puzzles and no difficulties with respect to the x-ray generation by the rock cutter electron beam; self-shielding is clearly demonstrated, is effective, and reduces shielding requirement to some extent. But even without it, any radiation which is produced can be shielded and confined readily.

6.3.5 Shielding under field-test conditions

(a) Observations

Initially we had only a sky-shine shield as shown in Fig. 6-8a. Starting the gun at low power revealed immediately the presence of excessive stray radiation. Hence additional lead panels were placed to the right and left of the granite block and a swinging lead panel on the gun as shown already in Fig. 4.2-4 and others. Thus all the primary x-rays were intercepted as indicated in Fig. 6-8b and c.

Since we needed a beam catcher for quickly measuring the current by just moving the gun up to it we suspended a steel plate in front of the rock as shown in Fig. 6-9. Firing a beam at it from a large distance so that it would not melt revealed that we had lost so much self-shielding by the nearby gun that radiation levels became too high at full beam power; besides, the plate melted anyway. The simple remedy consisted in using a beam catcher with a deep hole into which the beam is fired, and with a wall so thick as to absorb all internally generated x-rays. A steel cylinder of 6" O.D., 2" I.D., 12" long was used; it is shown in Fig. 6-10.

(b) Final radiation survey

Before regular operations started a final radiation survey was taken. Fig. 6-11 shows how this was done. Radiation intensities measured at various locations are shown in the plan view of Fig. 6-12 and 6-13.

Radiation levels increased when the stand-off distance from the rock was increased, but not beyond the tolerance levels.

Steel plate at 6" stand-off distance will not stand up to full beam power; besides, this target configuration produces the strongest x-ray flux because self-shielding is at a minimum.

The steel plate is partly punctured; some electrons reach the rock behind it which begins to fluoresce and later to glow and spall.

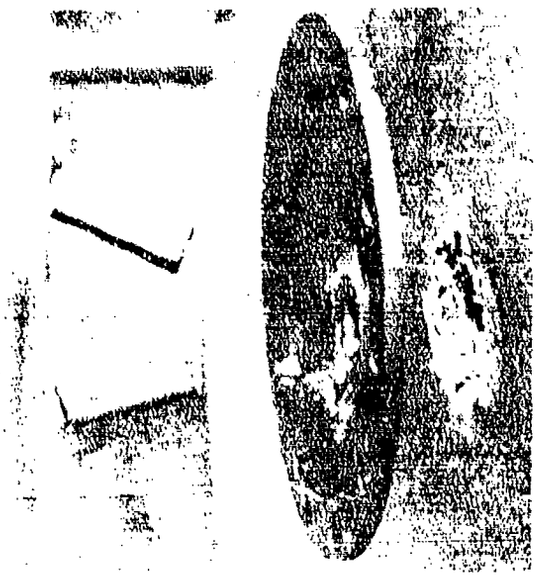

The end result is a hole in the steel plate, and a spallation crater in the rock.

Fig. 6-9

Hollow steel block, 6" O.D. with 2" dia. hole 10" deep, will get red hot but will not melt if beam is dissipated in the hole. The gun can be moved over to this beam catcher quickly for a tune-up of the transmission current and back to the work face. This catcher is self-shielding and x-ray flux is minimal.

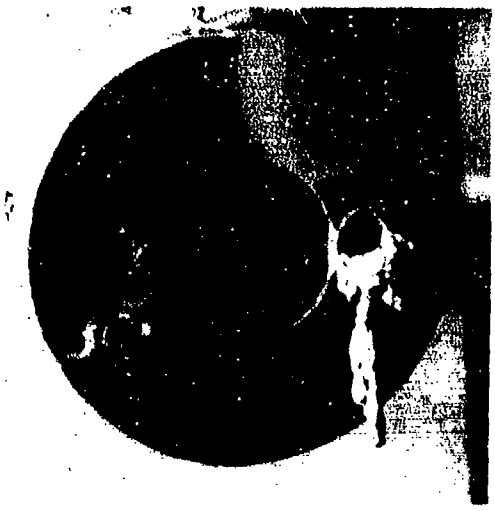

If the beam is misaligned the catcher will melt. The deep narrow melt trace in the right picture is another proof that the beam stays confined for a considerable distance, even in the atmosphere.

Fig. 6-10

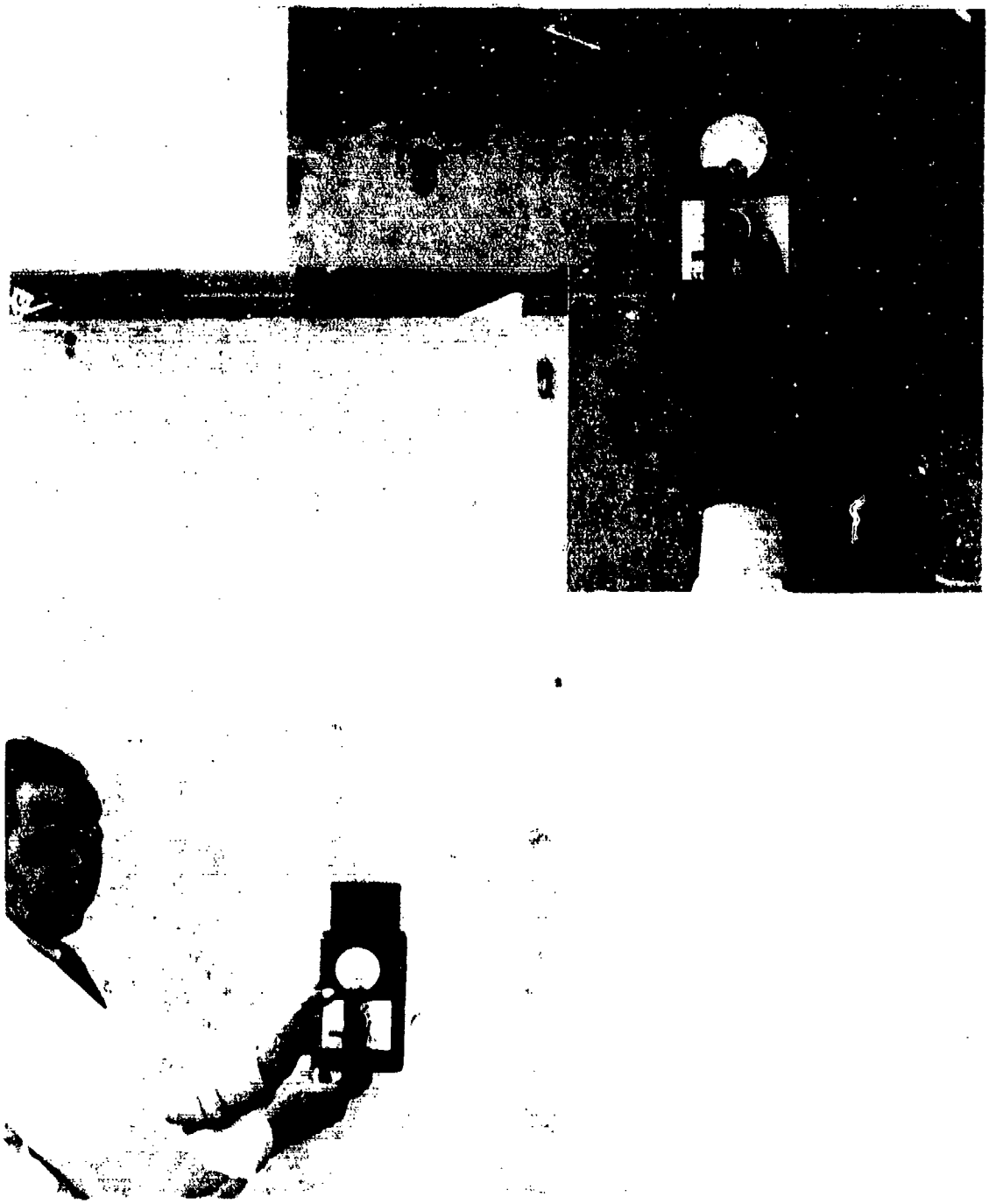

A radiation survey is taken; where people walk the radiation level is much less than the 7-hour per day 40-hour week permissible dose rate; the radiation intensity which comes over the wall is higher, but still not dangerous in case of a short exposure, because the direct beam is intercepted by local lead shields.

Fig. 6-11

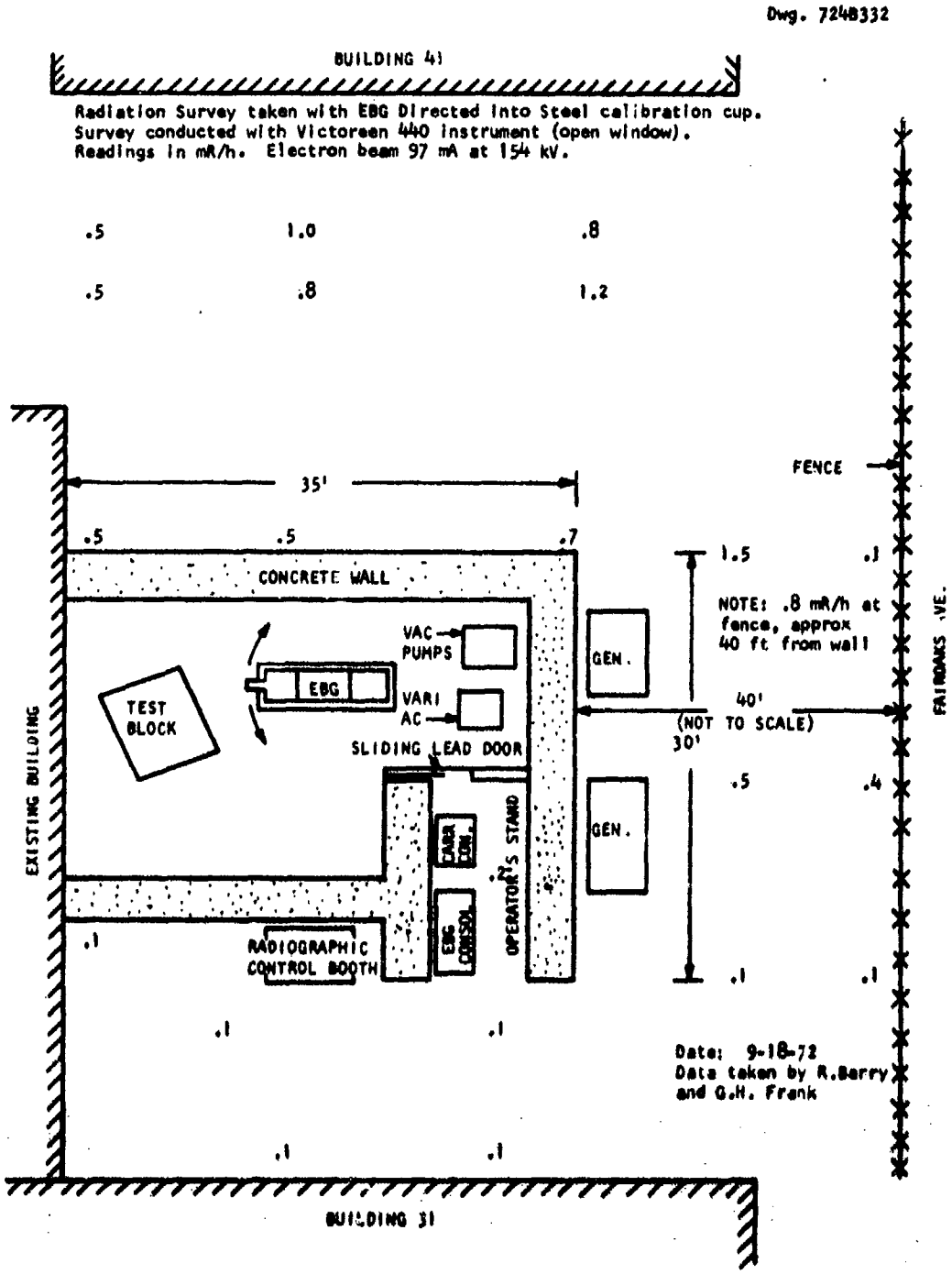

Fig. 6-12 Radiation survey results with electron beam directed into the steel beam catcher. Numbers give mR/h at various locations. Electron beam 97 mA at 154 kV.

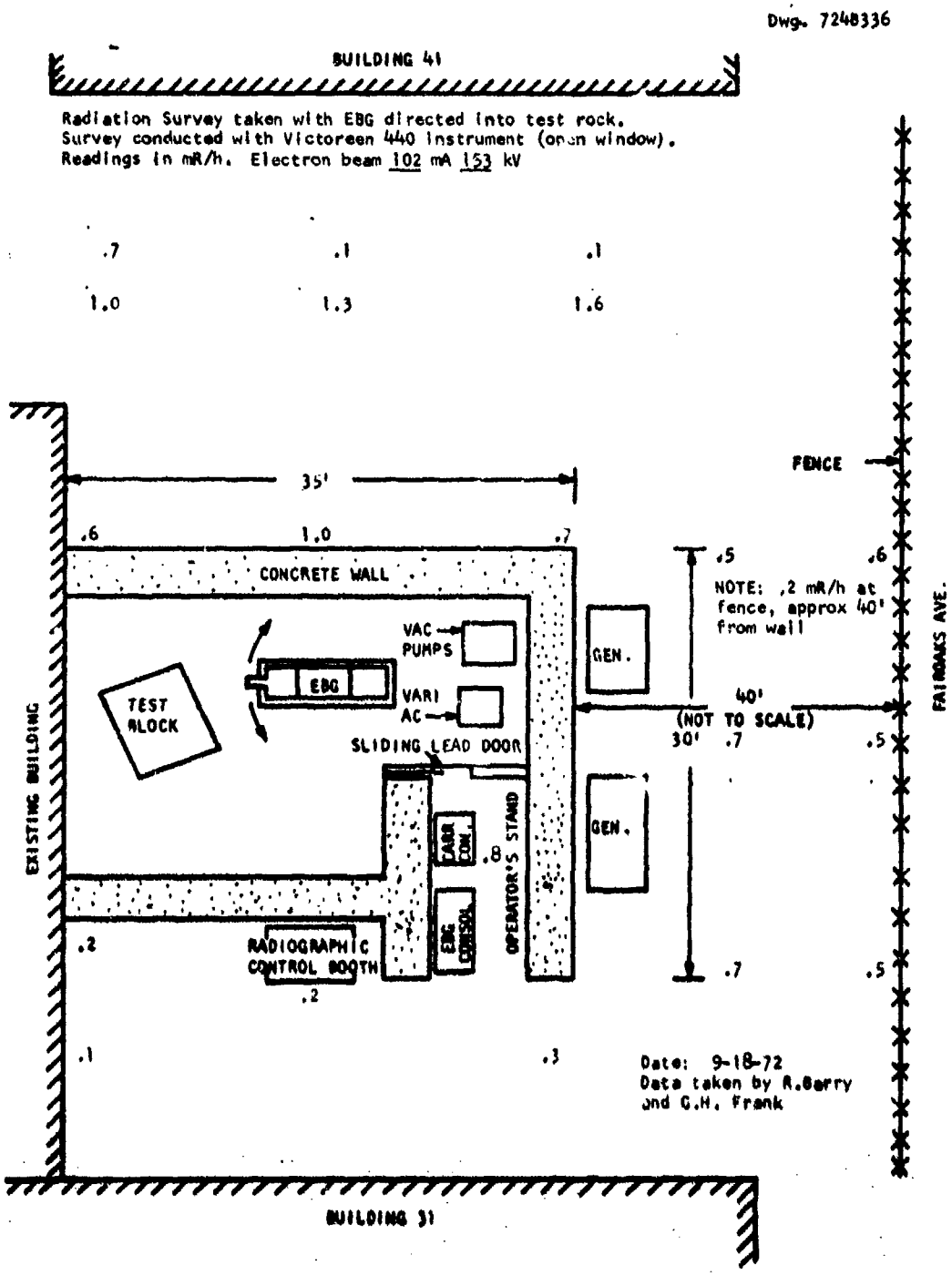

Fig. 6-13 Radiation survey results with electron beam directed into test rock. Numbers give mR/h at various locations. Electron beam 102 mA at 153 kV.

c) Measures to assure crew safety

1) At the rear of the operator's control for the gun a radiation meter/monitor was mounted (see Fig. A-9) which would trigger an interlock relay, shutting off the beam if radiation levels exceeded a pre-set limit.

2) The gun was started initially (each morning) at low power. During this start-up phase any anomalous situation would have been detected without encountering high radiation levels.

3) Each member of the crew working near the rock cutter had an audible alarm device which gave a chirping sound, the frequency of the chirps being the greater the higher the radiation intensity. At the 2 mR/h level at least several chirps per minute could be heard.*)

4) A calibrated survey meter, Victoreen Type 440, sensitive to even very soft x-rays was always operational and sitting on top of the operator's control console, clearly visible to anyone.

5) Everyone carried a registered film badge. During the complete series of tests reported here the accumulated doses for 5 persons were as follows: 15 mR, 10 mR, 10 mR, 25 mR, and 5 mR.

6) The access door to the work area (a sliding door with 1/4" lead on plywood) had an interlock switch. It could also be opened from the inside, should someone find himself in the work area and the gun come on. (Not likely in our two-man operation).

7) Whether or not the gun was running was evident at all times and everywhere from the singing noise of the high voltage transformers.

8) In a later field installation a warning signal could be installed inside the x-ray area, sounding an alarm before the beam is turned on, and also a cut-off button (or string) with which one can prevent it from coming on, should someone be trapped. A good viewing system for the operator would be part of the safety precautions.

---

*) Eberline Instrument Corp., Santa Fe, New Mexico, RAD-TAD Detector Model RT-1.

6.4 Performance Record of the Electron Gun

We had intended to conduct the field tests of electron beam rock cutting, as they are described in this report, with an electron gun capable of projecting a 36 kW beam into the air, and at the same time with a gun having a long-reach, long-barrel beam transfer column. The reasons for building such a long-barrel gun have been discussed elsewhere in this report.

Unfortunately, the initial layout of the magnetic lenses etc. for the long transfer column introduced certain limitations on the maximum beam current which could be transmitted through the beam exit nozzles, the sizes of which were determined by the size of the vacuum system.

Some delays in the original program occurred because time was spent trying to overcome these limits on the transmitted beam power, and indeed we found that the problem could be solved by reducing the distance between the exit nozzle and the second magnetic lens. The gun proper (cathode, grid, and anode) was capable, at all times, of delivering the expected higher beam current. More details on the electron optics are discussed in Section 8. Implementing the necessary changes in gun design would have delayed the test program still more; and it was considered more important to proceed with the tests, even at the lower power of the machine. No doubt existed then or now that guns with higher power can be built; at present a gun with 49 kW beam output (same exit nozzles as the rock cutter) at 165 kV is in operation in our laboratory.

Unfortunately and incorrectly, the delay in the test program because of the developmental work on the gun, was in some discussions attributed to reliability aspects of the gun. As a matter of fact, the electron gun and the beam transfer system to air, in its present form, when operated at or below the stated power level are absolutely reliable devices. In support of this statement we want in the following paragraphs

to summarize the service which the present rock cutting machine has seen, in connection with the development tests and cutting tests which have been described in other sections of this report.

(a) Operations started with about 100 hours of testing of the electron optical system and the long beam transfer column. In the initial start-up and these subsequent tests no trouble was encountered with the gun proper, which consists mainly of the high voltage insulator system, the cathode turret, and the auxiliary power supply (floating at the -150 kV dc potential level). One set of micarta insulators supporting the auxiliary power supply chassis (high voltage deck) showed arc tracking marks after some time; it was replaced by micalex insulators which did not deteriorate. All drives etc. going to the high voltage deck for controlling cathode power, bias voltage, and turret rotation have worked trouble-free. The main high voltage insulator did not require cleaning even once since it was installed; as a precautionary measure, it was cleaned prior to shipment of the gun to the Sunnyvale test site. The safe operating voltage exceeded 175 kV (the maximum no-load voltage which the power supplies could give).

(b) The beam transfer column, in connection with the early attempts at getting higher beam power transmitted, was badly abused in these tests. This abuse led to burn-up of the lower nozzles with an associated flow of metal vapors and other debris into the higher stages of the system. In spite of these conditions the gun proper kept firing a beam; no arc-out occurred; no dirt got into and accumulated in the high vacuum gun chamber or on the high voltage insulators.

Certain vacuum seals in the beam transfer column initially suffered heat damage, notably the seals of the ball valve. (It was not recognized that the valve-ball is essentially floating on the rubber sealing pads and has therefore no effective cooling by heat transfer to other metal parts; hence, even a weak but continuous current of stray electrons would heat this valve-ball to an excessive temperature.)

The problem was solved by incorporating a larger ball valve and shields against stray electrons.

(c) It was demonstrated that the cheap, 2" diameter oil diffusion pumps which we use on the electron gun chamber can tolerate an inclination of $\pm 30°$ to the vertical. It was therefore not necessary to suspend them on a fully flexible arm, which could, however, be done if a greater mobility of the rock cutter is desired than the one which we had needed for the present tests.

(d) Cathode life time (heater time with or without drawing beam current) was typically over 40 hours (more than a week). Cathode selection via turret rotation proved to be simple and reproducible. (The cathode can be seen, and positioned while hot, by looking into the beam transfer column from the front.)

During the tests at the Sunnyvale site four cathodes were "used up," not all from burn-out but because of dimensional changes in use and loss of optimum focusing conditions (see Section 8). After two cathodes had been lost, the gun was opened at a convenient time and the two cathodes replaced by new ones. Apart from this, there was no need to open up the gun during all these tests.

(e) While we were installing and experimenting with the optical beam position sensors, the gun and beam transfer column saw another 50 hours of service.

(f) The tests reported in Section 4.3.1 were made with this gun, adding about another 100 hours of beam time to its testing cycle. As long as the beam output is monitored (the beam going either into a catcher with meter, or its position being monitored by the optical sensors) so that slow drifts in position can be corrected, the gun can run indefinitely at its rated power level without overheating of any part of the system.

(g) Parallel operation of the power supplies, 3 modules of 12 kW rating each, posed no problems. It was also possible to switch on only one or two modules at a time.

On one occasion during the Sunnyvale tests a rectifier in one of the power supplies shorted out; tests were continued with only two power supply modules.

(h) As for the stability and regulation of the input voltage (220 volt, 400 Hz) we found the governor control on the commercial diesel-electric generator perfectly adequate. During all our rock cutting tests we used only manual high voltage settings and control, although we have available from the electron beam welders feedback controls for maintaining a preselected dc value of the high voltage regardless of beam current. (Welding requires programmed current changes, rock cutting does not.)

(i) During shipment of the gun from Pittsburgh to Sunnyvale the gun slipped off one of its supports and fell to the floor of the truck; apart from a few dents in a vacuum duct no damage occurred. When operations were resumed we found the filament was broken in the cathode which was in firing position, and which had seen about 10 hours of beam time at Pittsburgh prior to shipment. The second cathode in the turret, which had also been installed prior to shipment, was functional and provided a beam of 16 kW.

(j) In starting-up the machine after shipment we reached the high voltage level of 165 kV without any difficulty; there was no deterioration or contamination in the gun chamber or on the insulators due to shipment and nearly 4 months of "storage" time.

(k) The front end of the gun, in contact with the molten rock, can endure considerable abuse. Proof is shown in the many photographs in this report showing molten rock attached to the front end of the gun.

The shroud is more likely to suffer damage than the beam exit nozzle, because the latter are water cooled whereas the shroud is not. (Water cooling of the shroud could be installed readily.)

(l) Only once during the Sunnyvale tests did we have to exchange the beam exit nozzles, which had become enlarged due to beam drift. This required an excessive amount of over-pressure gas (helium) but did not impair the vacuum so as to stop the gun.

(m) Never once did the gun arc-over and shut-off. This is positive proof that no debris (or dust or vapor) is sucked into the gun chamber, in spite of the rough conditions in the work area, and in spite of burned out nozzles.

Beam drift (for instance due to unsettled thermal conditions in the first half hour of operation) led at times to an automatic shut-off by the temperature sensors at the nozzles; the response was enough so that no damage occurred.

(n) At one time unexpected overnight rain drenched our whole installation. It caused a few shorts, burnt-out resistors and fuses in the control cabinet, but the electron gun with its high voltage power supplies and other gear showed no adverse effect; it was, after all, built to function in the presence of ground water and water spray.

--- . --- . ---

The above comments referred to the reliability of the gun as examplified during our tests. The inherent simplicity of an electron gun (no moving parts, for instance) and other design aspects have been discussed elsewhere.

APPENDIX A

Carriage for the Electron Gun

Support equipment for the electron beam gun comprises a gun carriage. All other equipment existed as laboratory equipment prior to work on the field test program, so the principal task in this area was the design and manufacture of a carriage to support, position, and manipulate the gun during field test operations.

The carriage is designed to permit working on vertical rock face approximately 8 feet wide. It has the capability to move the gun in the horizontal (X-axis) and vertical (Y-axis) directions parallel to the rock face and in the horizontal direction perpendicular to the rock face (Z-axis) to compensate for irregularities in the rock surface. The attitude of the gun relative to the rock face is also variable as the carriage can rotate the gun in the horizontal (yaw) and vertical (pitch) planes. (A more complete description of the carriage is given in the carriage design specification, pages A-4 to A-18.

A-1. Design Description*

The initial design concept consisted of a two-wheeled trailer, which provides the basic carriage, and several movable structures mounted on the trailer, which permit the motions previously described. A rectangular frame is contained within the trailer frame and is supported by trolley wheels that ride on the longitudinal members of the trailer. This wheeled box frame provides 30 inches of Z-axis motion. A second rectangular frame (the X-axis frame) is contained within the Z-axis frame and is similarly supported by trolley wheels, which ride on the transverse members of the Z-axis frame. The X-axis frame permits up to 36 inches of

*See pages following A-18 for the carriage assembly drawings.

motion in the X-axis direction. A thrust bearing is mounted on the X-axis frame and supports the carriage superstructure. This superstructure/thrust bearing combination results in a turntable that permits rotation in the yaw mode. The superstructure is comprised of two vertical members, which support and guide the gun mount during motion in the Y-axis direction. The gun mount, itself, is a 2-inch-diameter shaft that rotates and thereby provides the pitch rotation capability. The ends of the pitch shaft are supported by bearings incorporated in the Y-axis guides, which move vertically in the aforementioned vertical members.

The initial concept used a roller chain drive system, powered by dc variable speed gearmotors. This system was selected because (1) the small power requirements would result in a relatively low cost drive system, (2) most components appeared to be available as "off-the-shelf" hardware, (3) the ability of roller chain systems to function at low speed in dirty environments with minimum of maintenance is a desirable feature, and (4) the speed control capability of a dc drive system was attractive. Initial design layout work was done using the foregoing dc motor/roller chain system.

At this stage in the design task, it became apparent that the power requirements for pitch rotation had been underestimated and that the low speeds required were beyond the reduction capability of most standard gearmotors. At this point, the low-cost advantage of this drive system ceased to exist as the estimated cost of the drive system was over $4000. Alternate systems were then explored with the final selection being the hydraulic system/roller chain combination. This system has hydraulic cylinders and rotary actuators for power transmission and roller chains as mechanical synchronizing devices. It sacrifices the remote speed control capability of the dc motor system but has other advantages, such as (1) lower cost (about $2500), (2) buffering provided by the cylinders (i.e., prevent free fall of components) in the event of a mechanical failure, and (3) good reliability. The speed control is retained through the use of variable flow control valves for all motions,

although speed changes must now be accomplished by changing valve settings on the carriage. The remote speed control feature could be regained through the use of servo valves, but Westinghouse engineers at Sunnyvale felt that a servo system is more sophisticated than is required for field test operations.

The following section A-2 contains the carriage specifications as prepared in March 1971 and presented with the First Quarterly Report of 4-30-71.

WESTINGHOUSE ELECTRIC CORPORATION
SUNNYVALE, CALIFORNIA

S-71-1

ELECTRON BEAM GUN EVALUATION PROGRAM

CARRIAGE DESIGN SPECIFICATION

No Revision

February 1971

Sponsored By
Advanced Research Projects Agency
ARPA Order Number: 1578
Program Code Number: 0F10

Monitored By Bureau of Mines
Under Contract Number: H0110377
Effective Date of Contract: 11 Dec. 1970
Amount of Contract: $240,000

Prepared By
Senior Engineer
Telephone 408/735-2508

Approved

Approved

A-2 ELECTRON BEAM GUN CARRIAGE DESIGN SPECIFICATION

1.0 SCOPE

This document defines the design parameters and characteristics for an electron beam gun carriage for use in a field test of the gun's rock cutting capabilities.

2.0 INTRODUCTION

2.1 Field Test Program

The field test program is intended to evaluate the electron beam gun as a prime mechanism of fragmentation in a rock excavation process. The test will be conducted in a hard rock field environment with objectives of establishing a correlation between laboratory test data and field results, and determining effects of variables such as standoff distance and cutting speed. A secondary objective of the field tests is to evaluate gun handling and support systems in the field environment.

2.2 Carriage Functions

The carriage and associated equipment are intended for use with the electron beam gun in the field test program. The carriage is the device which supports, manipulates and positions the gun during transport and cutting operations. The carriage also carries ancillary equipment such as vacuum systems or shielding required in close proximity during these operations.

3.0 GENERAL REQUIREMENTS

3.1 Field Test Site

3.1.1 Work Face

The field tests will be conducted on a large, relatively unfractured rock mass. The maximum size of the rock face to be worked from a single carriage location shall be eight feet high by eight feet wide. The base of the six foot square work face shall be at ground level, i.e., in the plane upon which the carriage rests. In order to permit excavation of a tunnel, the total projected frontal area of the gun and carriage assembly must be contained within the six foot square work face outline described above.

3.1.2 Test Site Environment

The field tests will be conducted in surface excavation (quarry) or an underground excavation site. The ground surface can be expected to be crushed rock or earthfill. The carriage shall be designed to withstand and operate under the following environmental conditions:

a) Ambient temperature: variable from 32°F to 120°F

b) Exposure to direct sunlight

c) Exposure to intermittent rainfall

d) Atmosphere containing abrasive dust or fine rock debris product in excavation process.

3.2 Portability

3.2.1 Site to Site Movement

The carriage shall be designed in such a manner as to facilitate transportation from one work site to another. The carriage may be trailer-mounted or mounted on a skid requiring transportation by truck. In either case the capabilities of a commercial carrier should not be exceeded.

3.2.2 On Site Mobility

The carriage shall have the capability of being moved from one work location to another at the same test site. To achieve this mobility the carriage may be mounted on wheels or equipped with skids for handling with a fork lift. When on location on a work face, the carriage shall be stabilized to prevent carriage movement during cutting operations.

3.2.3 Support System Hook-up

Carriage support systems such as electro-mechanical or electro-hydraulic power supplies, hydraulic reservoirs, etc. shall be designed with portability in mind to minimize field assembly problems.

3.2.4 On Site Assembly

The carriage may be disassembled for transportation from one work site to another, but on-site assembly labor required shall be kept at a minimum. No special tooling or equipment beyond that intended for use in the field test program shall be required. The carriage may require a small crane or light hoisting capability for field assembly.

3.3 Radiation

The electron beam gun produces non-residual X-ray radiation during its operation. Components and materials used in the carriage drive system should be selected with operation and X-ray field as a consideration, or shielded components may be used. Work site shielding and control station shielding is required as outlined in para. 7.1.

4.0 GUN/CARRIAGE/ANCILLARY EQUIPMENT INTERFACES

4.1 Electron Beam Gun Systems

A schematic diagram of the electron beam gun system with ancillary equipment appears in figure 1. Portions of the system mounted on the carriage are indicated in the diagram.

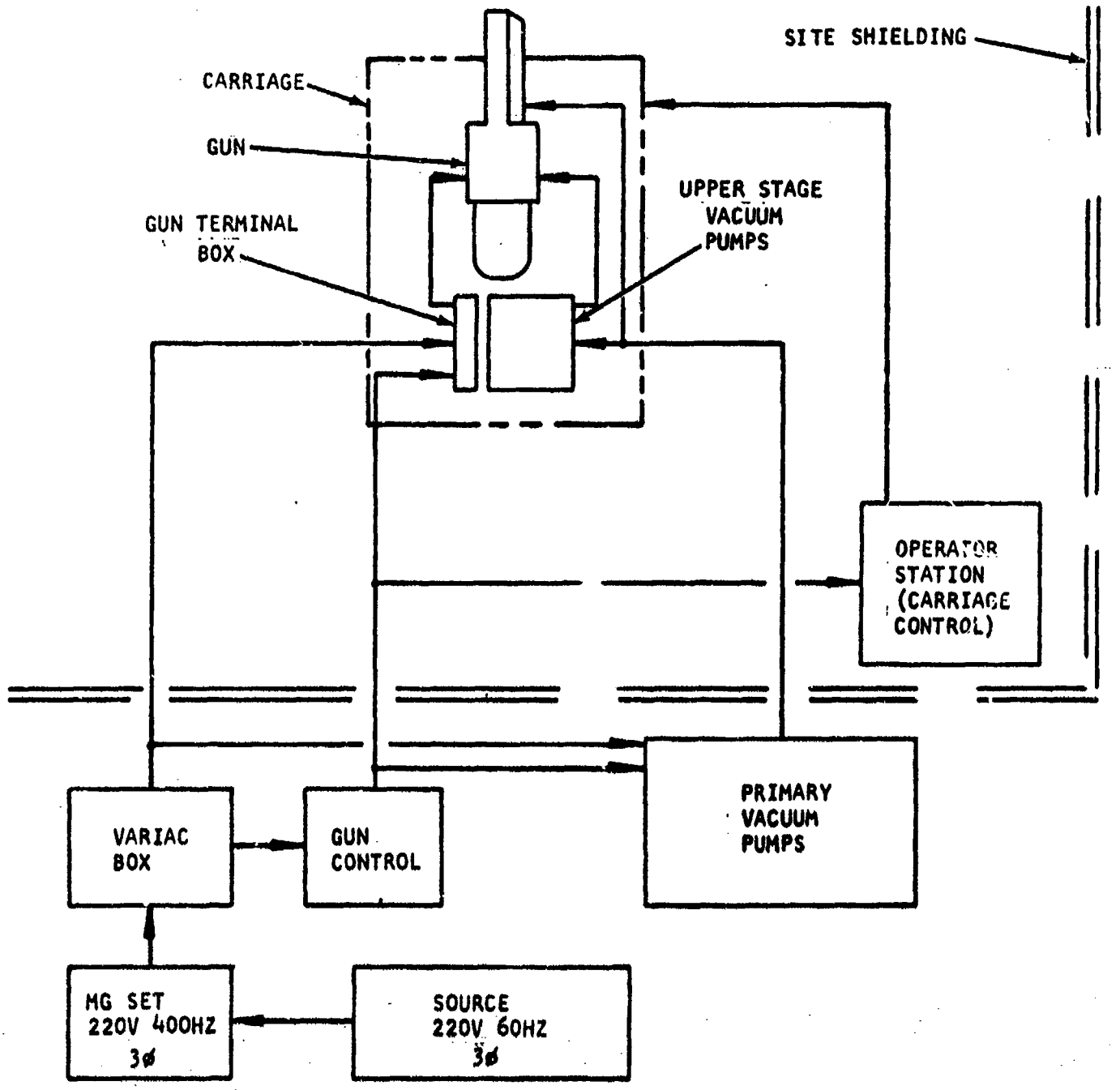

ELECTRON BEAM GUN
SYSTEM SCHEMATIC
FIG. A-1

4.2 Gun/Carriage Interface

4.2.1 EBG Space Envelope

The space envelope required by the electron beam gun is approximated by a rectangular solid 9 feet long by 4-1/2 feet high by 4 feet wide. The EBG electrical terminal box occupies a space 30 inches long by 32 inches high by 9 inches wide. The gun space envelope is shown in figure 2.

4.2.2 Gun Mounts

The mounting or attachmaent structure of the electron beam gun consists of two structural plates welded to each side of the power supply box in the location shown in figure 2. Each plate has ten drilled and tapped mounting holes as detailed in figure 3.

4.2.3 Weight

The weight of the electron beam gun assembly is approximately 1500 lbs.

4.3 Ancillary Equipment

4.3.1 Space Envelope

The space envelope required for the vacuum pump system for the upper pumping stages is a rectangular solid approximately 32 inches high by 29 inches long by 27 inches wide. This space envelope is illustrated in figure 4. Due to the vacuum system pump capability, the maximum allowable length of the flexible hose connecting the gun and the vacuum system is 6 feet, therefore the upper stage vacuum pump system must be located on or adjacent to the carriage.

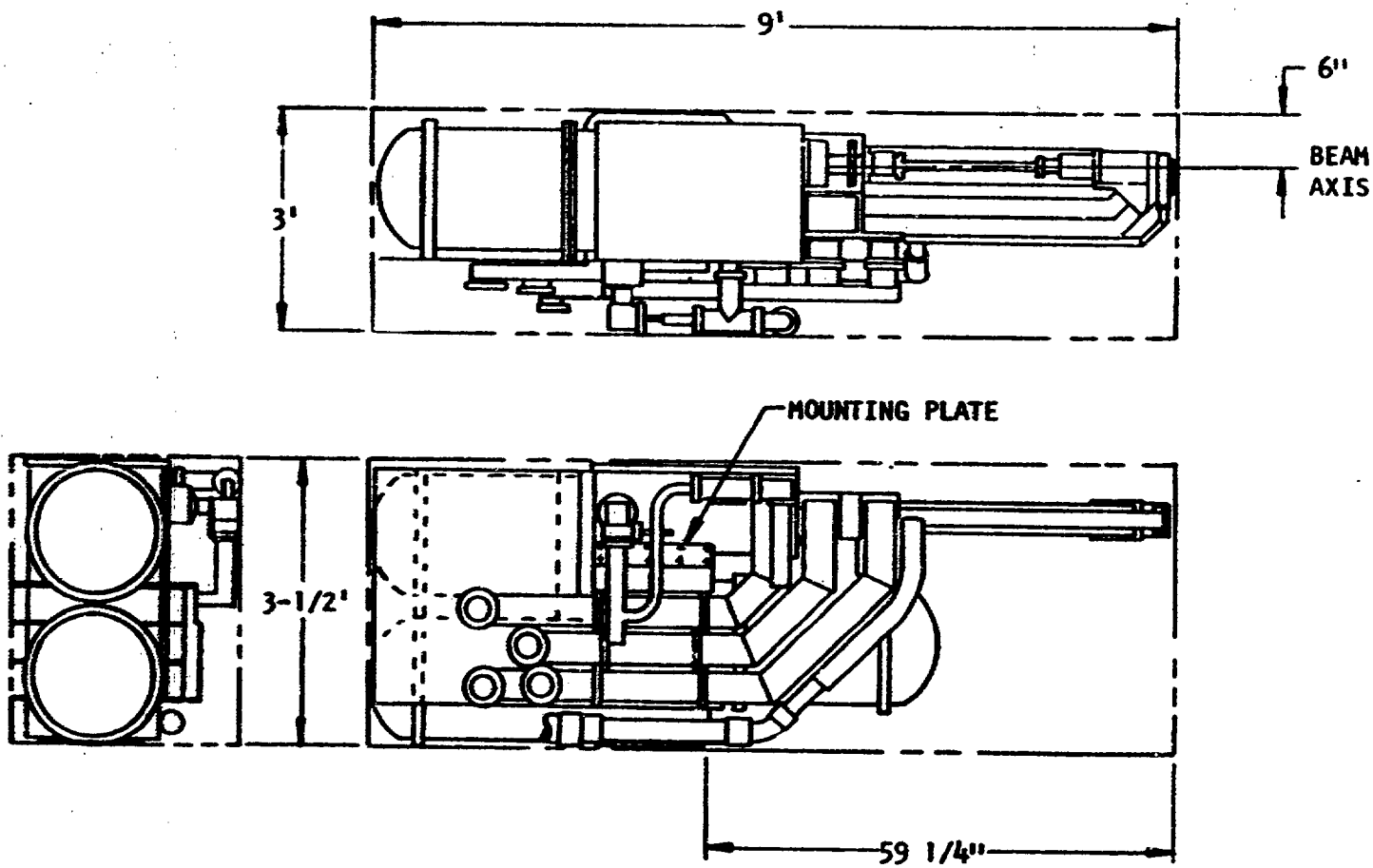

ELECTRON BEAM GUN
SPACE ENVELOPE
FIG. A-2

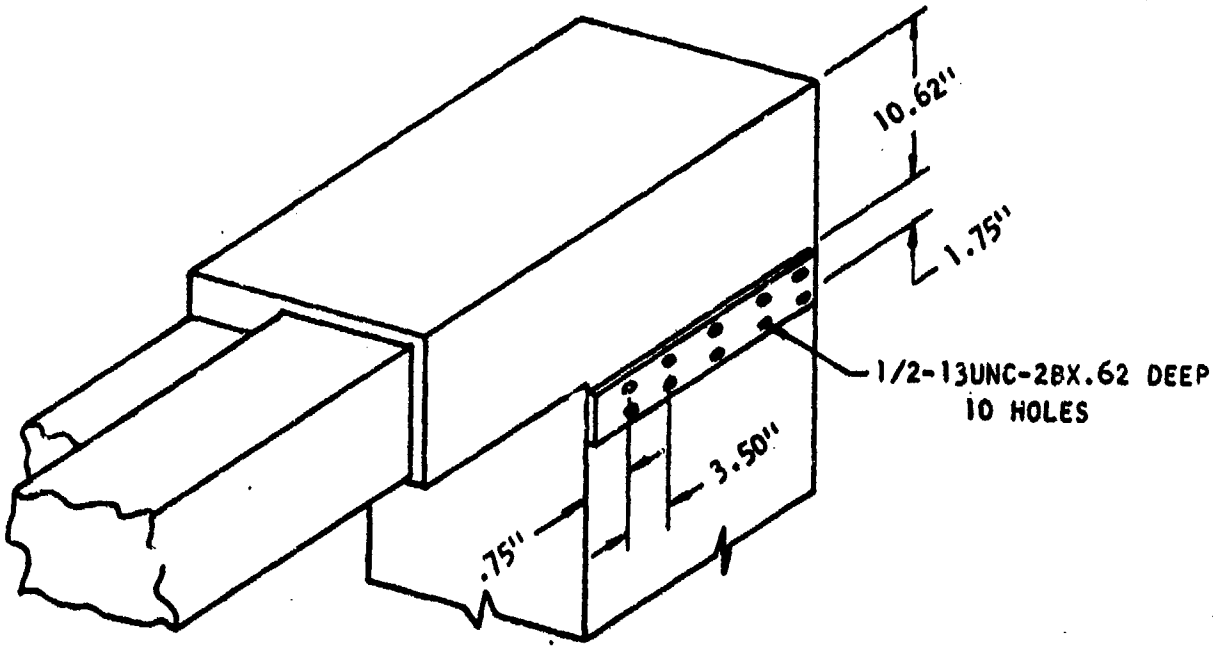

ELECTRON BEAM GUN
MOUNTING DETAILS
(LEFT SIDE SHOWN, RIGHT SIDF
SIMILAR TO OPPOSITE HAND)
FIG. A-3

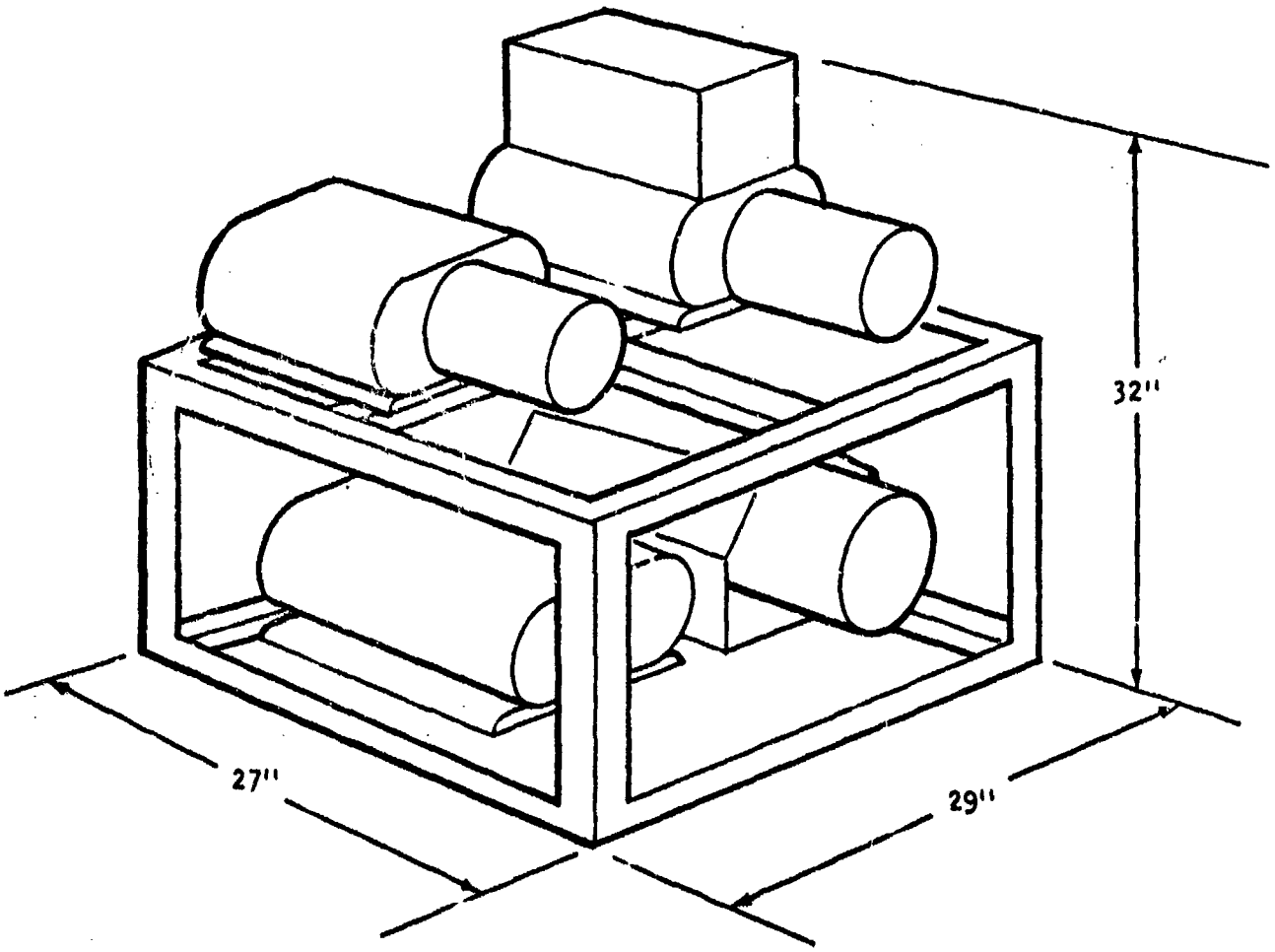

UPPER STAGE VACUUM PUMP SYSTEM SPACE ENVELOPE

FIG. A-4

4.3.2 Vacuum System Mounting

The vacuum system for the upper stages is mounted in a steel frame structure which may be bolted to the carriage or may be mounted on its own dolly within 6 feet of the gun.

4.3.3 Weight

The weight of uperstage vacuum pump system and its steel frame is approximately 675 lbs.

5.0 CARRIAGE PERFORMANCE

5.1 Gun Manipulation

5.1.1 Axis Orientation

For the purpose of describing gun motions the axes shown in figure 5 will be used. The X and Y axes define a vertical plane parallel to the rock face. The Z axis is perpendicular to the X-Y plane and the rock face and coincides with gun center line when the gun is centered on the carriage.

5.1.2 Gun Motions and Limitations

The amount of gun motion may be limited by the distance from the upper stage vacuum pump system as described in para. 4.3. Maximum hose length between this system and the gun is 6 feet. Another limitation is imposed by the oil diffusion pumping system used by the gun. The pumps used must be mounted so that their longitudinal axis does not deviate more than 15° from true vertical.

5.1.2.1 Rotation and Tilt

Rotation and tilt capabilities of the carriage shall be defined in terms of roll, pitch and yaw. Roll refers to rotation of about the Z

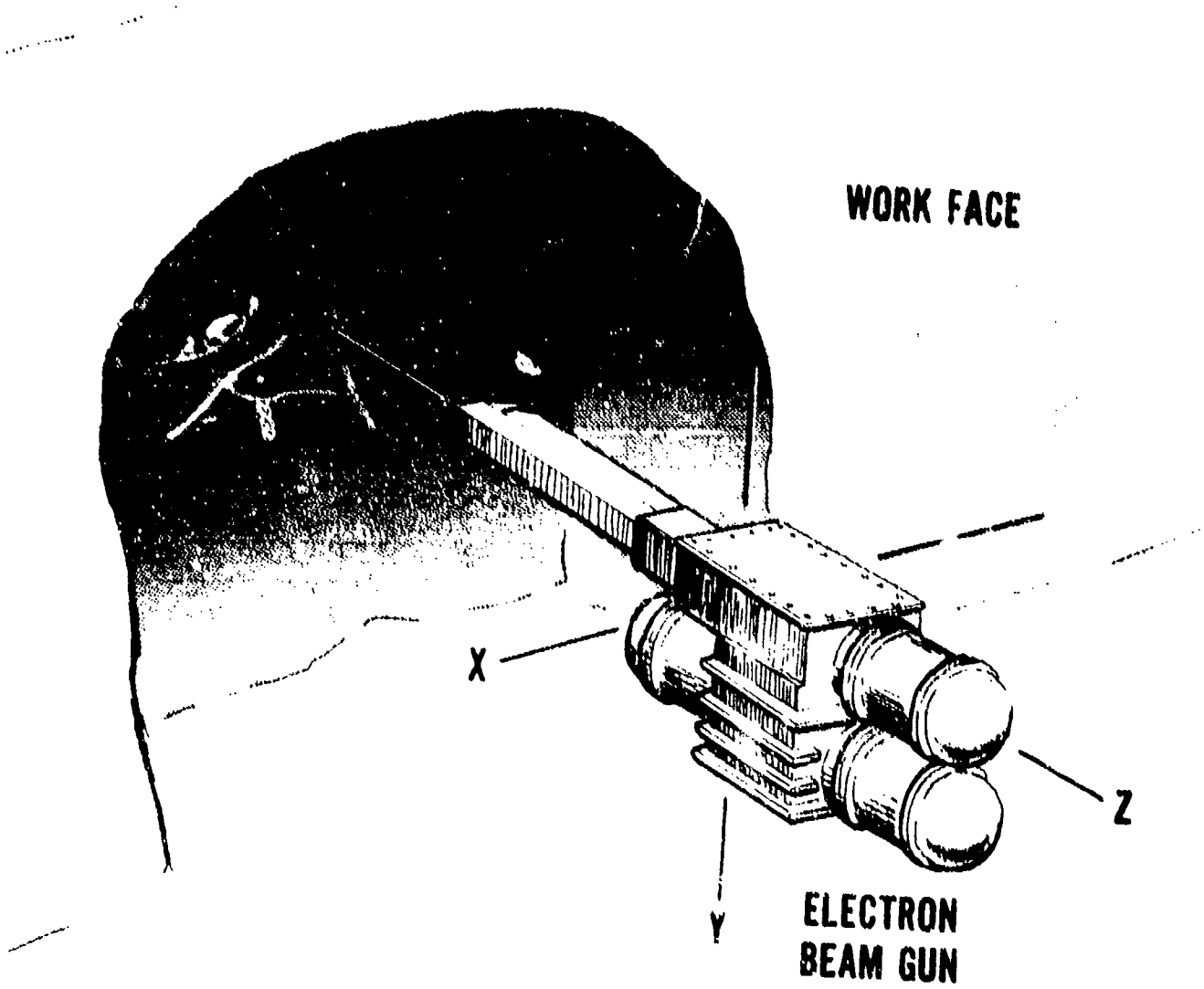

AXIS ORIENTATION
FIG. A-5

5.1.2.1 Rotation and Tilt (cont'd)

axis and shall be limited to within 15° of the vertical. Pitch is defined as rotation about the X axis, i.e., in the plane defined by the gun transfer column and the vertical, and the gun is limited to a maximum of ± 15° pitch. The carriage should, however, be designed with the capability for a total pitch angle of 90° such as from 15° above the horizontal axis to 75° below the horizontal axis to enable the gun to reach a work location at the excavation floor. Yaw is defined as rotation in a horizontal plane about the vertical or Y axis there are no limitations on the amount of yaw which can be tolerated. Design yaw capability shall be 45° minimum to either side of the line perpendicular to the work face.

5.1.2.2 X Axis Motion

X axis motion (horizontal traverse) shall be provided as required to enable the gun to work at 6 foot wide face. X-axis motion may be combined with yaw, (rotation about the Y axis,) to achieve the desired width. A minimum of 3 feet of horizontal traverse capability of X axis motion is desirable.

5.1.2.3 Y Axis Motion

Y axis motion (vertical traverse) shall be provided as required to enable the gun to work a 6 foot high rock face. Rotation about the X axis (pitch), may be combined with Y axis motion to achieve the desired work face height.

5.1.2.4 Z Axis Motion

Z axis motion shall be provided to permit some fore and aft movement of gun. The carriage shall be capable of Z axis motion regardless of gun attitude. A minimum of ± 6 inches motion from the nominal gun operating position is required.

5.1.2.5 Velocity of Motions

Motions in Z axis direction may be constant and shall not exceed 15 inches per minute. Velocity in all other modes of operation refers to the velocity of the gun exit nozzle relative to the work face. Velocities during cutting operations shall be variable from 1 inch per minute to 30 inches per minute and shall be controllable to within ± 10 percent.

5.2 Carriage Power System

The required carriage motions and gun manipulations are to be achieved through the use of electro-mechanical or electro-hydraulic power transmission systems. Any hydraulic fluids used should be fire resistant such as a phosphate-ester fluid. Electronic components used in drive systems must be shielded for use in an X-ray field.

6.0 CONTROLS

6.1 Gun Controls

All control stations shall contain master on-off controls for the electron beam gun. The gun control console shall be remote from the carriage and located up to 200 feet from the electron beam gun.

6.2 Carriage Control

6.2.1 Operator's Station

The operator's station shall be remote from the carriage and shall contain all controls necessary to perform gun manipulations during cutting operations. The station shall contain gun on-off controls, equipment for communication to the other stations, and a radiation level monitor interlocked with the gun.

6.2.2 Position Controls

The carriage and manipulation system shall be equipped with controls and drive systems designed to stop the gun in any attitude, in any of its motions, and hold it in that position.

6.2.3 Interlocks

6.2.3.1 Gun Auxiliary Systems

The control system shall be equipped with interlocks as necessary to prevent operation of the electron beam gun without required gun auxiliary systems such as vacuum, water and air.

6.2.3.2 Over-Travel

The carriage drive system shall be equipped with over-travel interlocks or limit systems to prevent two-blocking the drive mechanisms.

6.2.3.3 Interference

Limit switches or other sensors shall be located on the transfer column adjacent to the exit nozzle. These shall be interlocked to prevent driving the gun into the work face in any of the modes of the gun motion.

6.2.3.4 Radiation

Radiation interlocks shall be provided as follows:

a) The radiation level monitor in the operator's station shall be interlocked to stop gun operation in the event that the detected emission rate exceeds 20 milliroentgens per hour.

b) The work site shielding doors shall be interlocked to prevent gun operation with open doors.

7.0 SAFETY REQUIREMENTS

7.1 Radiation

Due to X-ray radiation produced by the gun during its operation shielding must be provided for the operator and other field test observers.

7.1.1 Operator's Station

The operator's station shall consist of a plywood booth sheathed with lead .25 inches thick and equipped with leaded glass windows. The control station (para. 6.2) shall be located within this booth. The control station shall be interlocked in accordance with para. 6.2.3.4(a).

7.1.2 Work Site Shielding

The entire work site shall also be shielded for observers' protection by surrounding it with .25 inch lead sheathed plywood fence or equivalent (e.g. 3 or 4 layers of dense concrete block), also equipped with leaded glass windows. Shielding doors shall be interlocked in accordance with para. 6.2.3.4(b).

7.2 Physical Protection

Physical protection is required to minimize the possibility of damage due to rock falling from the work face or from adjacent strata. Gun protection may be incorporated in the carriage or may be obtained from structure covering the work site.

8.0 UTILITIES

The following utilities are required for operation of the electron beam gun.

8.1 Electrical

a) 220 volt, 3 phase, 60 cycle electrical power at 30 KW continuous, 60 KW peak.

b) 220 volt, 3 phase, 400 cycle electrical power 60 KW and 75 KVA.

8.2 Air, Water & Helium

a) Air at 60 lb. per sq. inch and 200 standard cubic feet per minute (20 SCFM for gun and 180 for blast jet use).

b) Water at 15 gallons per minute and 50 lb. per sq. inch, (5 GPM for gun and pump cooling water, 10 GPM for blast jet use and rock face debris removal.

c) Helium, at rate of 300 standard cubic feet per hour while beam is on.

BILL OF MATERIAL

SYM	ITEM	DESCRIPTION		GROUP 1	2	3	4	5	6	7	8	9	10
	122	SCREW, CAP, HEX HD - 1/4-20UNC-2A X 3/4 LG	STL CD PL		19								
	123	SCREW, CAP, HEX HD - 5/16-18UNC-2A X 3/4 LG	STL CD PL		16								
	124	SCREW, CAP, HEX HD - 7/16-14UNC-2A X 1 1/4 LG	STL CD PL		1								
	125	SCREW, CAP, HEX HD - 1/2-13UNC-2A X 1 1/4 LG	STL CD PL		16								
	126	SCREW, CAP, HEX HD - 1/2-13UNC-2A X 1 3/4 LG	STL CD PL		8								
	127	SCREW, CAP, HEX HD - 5/8-16UNC-2A X 3/4 LG	STL CD PL		2								
	128	SCREW, CAP, HEX HD - 1/2-13UNC-2A X 1 1/2 LG	STL CD PL		16								
	129	SCREW, CAP, HEX HD - 5/8-16UNC-2A X 1 IN. LG	STL CD PL		20								
	130	SCREW, CAP, HEX HD - 1/2-13UNC-2A X 1 IN. LG	STL CD PL		36								
	131	SCREW, MACH FL HD - 1/4-20UNC-2A X 5/8 LG	STL CD PL		3								
	132	SCREW, CAP, SKT HD - 3/8-16UNC-3A X 1 1/2 LG	STL CD PL		4								
	133	SCREW, CAP, SKT HD - 3/8-16UNC-3A X 2 IN. LG	STL CD PL		8								
	134	SCREW, CAP, HEX HD - 3/8-16UNC-2A X 1 3/4 LG	STL CD PL		16								
	135	NUT, PLAIN HEX (JAM) - 5/8-16UNC-2B	STL CD PL		26								
	136	NUT, PLAIN HEX - 1/2-13 UNC-2B	STL CD PL		8								
	137	NUT, PLAIN HEX - 3/8-16UNC-2B	STL CD PL		2								
	138	WASHER, LOCK SPLIT - #10 NOM	STL CD PL		17								
	139	WASHER, LOCK SPLIT - 1/4 NOM	STL CD PL		27								
	140	WASHER, LOCK SPLIT - 3/8 NOM	STL CD PL		22								
	141	WASHER, LOCK SPLIT - 7/16 NOM	STL CD PL		3								
	142	WASHER, LOCK SPLIT - 1/2 NOM	STL CD PL		32								
	143	WASHER, LOCK SPLIT - 5/8 NOM	STL CD PL		16								
	144	WASHER, LOCK SPLIT - 5/16 NOM	STL CD PL		16								
	145	WASHER, FLAT - 3/4 NOM	STL CD PL		4								
	146	WASHER, FLAT - 1 IN. NOM	STL CD PL		2								
	147	WASHER, FLAT - 1 1/2 NOM	STL CD PL		8								
	148	PIN, COTTER - 1/4 DIA X 2 1/2 LG	STL CD PL		4								
	149	PIN, COTTER - 1/8 DIA X 2 LG	STL CD PL		2								
	150	PIN, SPRING - 1/8 DIA X 1 1/8 LG	STL CD PL		1								
	151	PIN, SPRING - 1/8 DIA X 1 1/2 LG	STL CD PL		2								
	152	PIN, SPRING - 1/4 DIA X 1 1/2 LG	STL CD PL		4								
H	153	COLLAR - 5/8 SHAFT DIA	BOSTON NO. SC62		2								
H	154	BEARING, FLANGED (OIL IMP) 5/8 I.D. X 7/8 O.D. X 1 IN. LG BRZ	BOSTON NO. FB 1014-8		2								
	155	PIN, SPRING - 1/2 DIA X 1 IN. LG	STL CD PL		4								
	156	SETSCREW, CUP POINT - 1/2-13UNC-2A X 1/2 LG	STL CD PL		2								
	157	WASHER, FLAT - 1/2 NOM	STL CD PL		6								
	158	PIN, SPRING - 1/4 DIA X 3/4 LG	STL CD PL		2								

BILL OF MATERIAL

SYM	ITEM	DESCRIPTION		GROUP 1	2	3	4	5	6	7	8	9	10
	62	ADAPTER	994 J 689-50		6								
	63	SHIM	944 J 689-51		6								
	64	KEY, SQUARE 1/2 X 2 IN. LG	STL		1								
	65	KEY, SQUARE 3/8 X 8 IN. LG	STL		1								
	66	KEY, SQUARE 1/2 X 1 1/2 LG	STL		2								
	67	KEY, SQUARE 1/2 X 1 IN. LG	STL		2								
	68	KEY, SQUARE 1/2 X 2 1/4 LG	STL		1								
	69	KEY, SQUARE 1/4 X 2 1/2 LG	STL		1								
	70	SHIM	944 J 689-52		2								
A	71	HYDRAULIC CYLINDER - UNIVERSAL MODEL NO. MPU3-L, 2 IN. BORE, 18 IN. STROKE, 1 IN. DIA ROD WITH STD MALE STYLE 2 ROD END. NO CUSHIONS			1								
A	72	HYDRAULIC CYLINDER - UNIVERSAL MODEL NO. MPU3-L, 1 1/2 IN. BORE, 26 IN. STROKE, 1 IN. ROD DIA WITH STD MALE STYLE 2 ROD END. CUSHIONED - CAP END ONLY.			2								
A	73	HYDRAULIC CYLINDER - UNIVERSAL MODEL NO. MPU3-L, 2 IN. BORE, 30 IN. STROKE, 1 IN. DIA ROD WITH STD MALE STYLE 2 ROD END. NO CUSHIONS			1								
A	74	FEMALE CLEVIS - 3/4-16	UNIVERSAL NO. N20-403		4								
A	75	PIVOT PIN (3/4 DIA X 2 29/32 LG)	UNIVERSAL NO. N20-404		4								
A	76	CLEVIS BRACKET	UNIVERSAL NO. N15-405		4								
A	77	PIVOT PIN (1/2 DIA X 1 7/8 LG)	UNIVERSAL NO. N15-407		4								
B	78	FLANGED CARTRIDGE BEARING - STD SERIES 1 15/16 DIA	FAFNER NO. RCJT 1 15/16		6								
B	79	FLANGED CARTRIDGE BEARING - STD SERIES 1 1/2 DIA	FAFNER NO. RCJT 1 1/2		1								
C	80	BEARING - ECONO-TRAK SERIES 2000	ROTEK NO. L6-17P12		1								
C	81	BEARING - ECONO-TRAK SERIES 1000	ROTEK NO. M4-26P42		1								
D	82	ROTARY ACTUATOR - 7,500 LB IN TORQUE 180° 2 RACK SOLID SHAFT	MODEL NO. SM 7,500		1								
D	83	ROTARY ACTUATOR - 30,000 LB IN TORQUE 360° 2 RACK HOLLOW SHAFT	MODEL NO. HS 30,000										
E	84	WHEEL - 12 IN. DIA X 4 IN. WIDE (4 1/4 HUB WIDTH) 1 1/2 BORE THRU BRG - 4800 LB CAPACITY	ALBION NO. PY-12701		4								
F	85	TROLLEY WHEEL (3 1/8 NOM DIA)	NICE NO. 4955-2		22								
F	86	TROLLEY WHEEL (2 1/8 NOM DIA)	NICE NO. 5646		6								
G	87	SPROCKET - 1/2 PITCH,25 TEETH,TYPE B HUB - STL, BORED TO 1 IN. DIA WITH KEY SEAT & TWO SET SCREWS (KEY SEAT MUST BE IN LINE WITH CENTER OF ONE TOOTH WITHIN .030)	ACME NO. 40B25		2								
G	88	SPROCKET - 1/2 PITCH,10 TEETH,TYPE B HUB - STL,STK 1/2 IN. BORE NO SETSCREW	ACME NO. 10B10		-								
G	89	SPROCKET - 5/8 PITCH,11 TEETH,TYPE B HUB - STL,STK 5/8 IN. BORE NO SETSCREW	ACME NO. 50B11		2								
G	90	SPROCKET - 5/8 PITCH,23 TEETH,TYPE B HUB - STL, BORED TO 2 IN. DIA WITH KEY SEAT & TWO SETSCREWS (KEY SEAT MUST BE IN LINE WITH CENTER OF ONE TOOTH WITHIN .030)	ACME NO. 50B23		2								
G	91	SPROCKET - 5/8 PITCH,19 TEETH,TYPE A PLATE STL,STK 5/8 BORE			2								
G	92	SPROCKET - 5/8 PITCH,28 TEETH,TYPE B HUB STL,BORED TO 2 IN. DIA WITH KEY SEAT & TWO SETSCREWS (KEY SEAT MUST BE IN LINE WITH CENTER OF ONE TOOTH WITHIN .030)	ACME NO. 50B28		2								
G	93	SPROCKET - 1 1/4 PITCH,11 TEETH,TYPE B HUB STL BORED TO 1 1/2 DIA WITH KEYSEAT & TWO SETSCREWS	ACME NO. 100B11		1								
G	94	SPROCKET - 1 1/4 PITCH,32 TEETH,TYPE B HUB STL BORED TO 2 IN. DIA WITH KEY SEAT & TWO SETSCREWS	ACME NO. 100B32		1								
G	96	ROLLER CHAIN - 1/2 PITCH ASA NO. 40 SINGLE WIDTH X 239 PITCHES			1								
G	97	ROLLER CHAIN - 1/2 PITCH ASA NO. 40 SINGLE WIDTH X 229 PITCHES			1								
G	98	ROLLER CHAIN - 1/2 PITCH ASA NO. 40 SINGLE WIDTH X 99 PITCHES			1								
G	99	ROLLER CHAIN - 1/2 PITCH ASA NO. 40 SINGLE WIDTH X 369 PITCHES			1								
G	100	ROLLER CHAIN - 5/8 PITCH ASA NO. 50 SINGLE WIDTH X 171 PITCHES			2								
G	101	ROLLER CHAIN - 5/8 PITCH ASA NO. 50 SINGLE WIDTH X 177 PITCHES											
G	102	ROLLER CHAIN - 1 1/4 PITCH ASA NO. 100 SINGLE WIDTH,RIVETED, 43 PITCHES			1								
G	103	CONNECTING LINK FOR ASA NO. 40 ROLLER CHAIN			8								
G	104	CONNECTING LINK FOR ASA NO. 50 ROLLER CHAIN			8								
G	105	CONNECTING LINK FOR ASA NO. 100 ROLLER CHAIN			1								
G	106	OFFSET LINK FOR ASA NO. 40 ROLLER CHAIN			4								
G	107	OFFSET LINK FOR ASA NO. 50 ROLLER CHAIN			4								
	108	OFFSET LINK FOR ASA NO. 100 ROLLER CHAIN			1								
H	109	COLLAR - 2 IN. SHAFT DIA	BOSTON NO. SC200		2								
H	110	BEARING, FLANGED (OIL IMP) 5/8 I.D. X 3/4 O.D X 3/4 LG BRZ.	BOSTON NO. FB-1012-6		4								
H	111	BEARING, FLANGED (OIL IMP) 1/2 I.D. X 5/8 O.D. X 3/4 LG BRZ	BOSTON NO. FB-810-6		6								
H	112	BEARING, FLANGED (OIL IMP) 1/2 I.D. X 5/8 O.D. X 1 IN. LG BRZ	BOSTON NO. FB-810-8		1								
H	113	BEARING, FLANGED (OIL IMP) 1/2 I.D. X 5/8 O.D. X 1 3/4 LG BRZ	BOSTON NO. FB-810 [illegible]		[illegible]								
H	114	BEARING, FLANGED (OIL IMP) 1 IN. I.D. X 1 1/4 O.D. X 3/4 LG BRZ	BOSTON NO. FB-1620-6		2								
	115	KEY, SQUARE - 5/16 X 1 1/2 LG	STL		1								
	116	SCREW, MACH FL HD - 1/2-13UNC-2A X 2 IN. LG	STL CD PL		22								
	117	SCREW, MACH FL HD - 1/2-13UNC-2A X 1 1/2 LG	STL CD PL		6								
	118	SCREW, MACH PAN HD - #10-24UNC-2A X 1/2 LG	STL CD PL		9								
	119	SCREW, CAP, HEX HD - #10-24UNC-2A X 1/2 LG	STL CD PL		8								
	120	SCREW, CAP, HEX HD 1/4-20UNC-2A X 1/2 LG	STL CD PL		4								
	121	SCREW, CAP, HEX HD - 1/4-20UNC-2A X 5/8 LG	STL CD PL		8								

B

SYM	ITEM	
	1	ELECTRON BEAM GUN CARR
	2	TRAILER FRAME
	3	BRACE, TRAILER FRAME
	4	CARRIAGE
	5	CARRIAGE
	6	CARRIAGE
	7	BEAM
	8	BEAM
	9	PIVOT BASE
	10	BEARING PLATE
	11	BOGIE
	12	CARRIAGE
	13	CARRIAGE
	14	SPROCKET HOUSING
	15	FLANGE
	16	BRACKET, GUN MOUNTING
	17	BRACKET, GUN MOUNTING
	18	SHAFT, PITCH
	19	SHAFT, TORSION
	20	SHAFT, TORSION
	21	PIN
	22	SPROCKET BRACKET
	23	BRACKET
	24	ANGLE
	25	CHAIN ADJUSTER
	26	CHAIN ADJUSTER
	27	CHAIN ADJUSTER
	28	PIN (1/2 DIA X 3.00)
	29	SPROCKET SHAFT
	30	PIN
	31	MOUNTING PLATE
	32	SHAFT, PITCH DRIVE
	33	SHAFT
	34	PIN (1/2 DIA X 2.62)
	35	PIN (1/2 DIA X 3.62)
	36	PIN (5/8 DIA X 3.00)
	37	WHEEL ADJUSTER
	38	BRIDGE
	39	BEARING BLOCK
	40	BEARING BLOCK
	41	SPROCKET SUB-ASSY
	42	CHAIN GUIDE
	43	CHAIN GUIDE
	44	SHIM
	45	CHAIN GUIDE
	46	CHAIN GUIDE
	47	CHAIN GUIDE
	48	CHAIN GUIDE
	49	CHAIN GUIDE
	50	CHAIN GUIDE
	51	CHAIN GUIDE
	52	CHAIN GUIDE
	53	CHAIN GUIDE
	54	SPROCKET BRACKET
	55	SPROCKET BRACKET
	56	SPROCKET BRACKET
	57	SPROCKET BRACKET
	58	SHIM
	59	SHIM
	60	CHAIN GUIDE
	61	WHEEL BRACKET

A. MAY BE PURCHASED FROM UNIVER
B. MAY BE PURCHASED FROM FAFNER
C. MAY BE PURCHASED FROM ROTEK
D. MAY BE PURCHASED FROM FLO-TO
E. MAY BE PURCHASED FROM ALBION
F. MAY BE PURCHASED FROM NICE B
G. MAY BE PURCHASED FROM ACME C
H. MAY BE PURCHASED FROM BOSTON

BILL OF MATERIAL

Description	Part No. / Source	1	2	3	4	5	6	7	8	9	10
ADAPTER	944 J 689-50		6								
SHIM	944 J 689-51		6								
KEY, SQUARE 1/2 X 2 IN. LG STL			1								
KEY, SQUARE 3/8 X 8 IN. LG STL			1								
KEY, SQUARE 1/2 X 1 1/2 LG STL			2								
KEY, SQUARE 1/2 X 1 IN. LG STL			2								
KEY, SQUARE 1/2 X 1 1/4 LG STL			1								
KEY, SQUARE 1/4 X 2 1/2 LG STL			1								
SHIM	944 J 689-52		2								
HYDRAULIC CYLINDER - UNIVERSAL MODEL NO. MPU3-L, 2 IN. BORE, 10 IN. STROKE, 1 IN. DIA ROD WITH STD MALE STYLE 2 ROD END. NO CUSHIONS			1								
HYDRAULIC CYLINDER - UNIVERSAL MODEL NO. MPU3-L, 1 1/2 IN. BORE, 26 IN. STROKE, 1 IN. ROD DIA WITH STD MALE STYLE 2 ROD END. CUSHIONED - CAP END ONLY.			2								
HYDRAULIC CYLINDER - UNIVERSAL MODEL NO. MPU3-L, 2 IN. BORE, 30 IN. STROKE, 1 IN. DIA ROD WITH STD MALE STYLE 2 ROD END. NO CUSHIONS			1								
FEMALE CLEVIS - 3/4-16	UNIVERSAL NO. N20-403		4								
PIVOT PIN (3/4 DIA X 2 23/32 LG)	UNIVERSAL NO. N20-404		4								
CLEVIS BRACKET	UNIVERSAL NO. N15-405		4								
PIVOT PIN (1/2 DIA X 1 7/8 LG)	UNIVERSAL NO. N15-407		4								
FLANGED CARTRIDGE BEARING - STD SERIES 1 15/16 DIA	FAFNER NO. RCJT 1 15/16		6								
FLANGED CARTRIDGE BEARING - STD SERIES 1 1/2 DIA	FAFNER NO. RCJT 1 1/2		1								
BEARING - ECONO-TRAK SERIES 2000	ROTEK NO. LK-17P12		1								
BEARING - ECONO-TRAK SERIES 1000	ROTEK NO. MA-26P4Z		1								
ROTARY ACTUATOR - 7,500 LB IN TORQUE 180° 2 RACK SOLID SHAFT	MODEL NO. SH 7,500		1								
ROTARY ACTUATOR - 30,000 LB IN TORQUE 360° 2 RACK HOLLOW SHAFT	MODEL NO. HS 30,000										
WHEEL - 12 IN. DIA X 4 IN. WIDE (4 1/4 HUB WIDTH) 1 1/2 BORE THRU BRG - 4800 LB CAPACITY	ALBION NO. PT-12701		4								
TROLLEY WHEEL (3 1/8 NOM DIA)	NICE NO. 4955-2		22								
TROLLEY WHEEL (2 1/8 NOM DIA)	NICE NO. 5646		6								
SPROCKET - 1/2 PITCH, 25 TEETH, TYPE B HUB - STL, BORED TO 1 IN. DIA WITH KEY SEAT & TWO SET SCREWS (KEY SEAT MUST BE IN LINE WITH CENTER OF ONE TOOTH WITHIN .030)	ACME NO. 40B25		2								
SPROCKET - 1/2 PITCH, 10 TEETH, TYPE B HUB - STL, STK 1/2 IN. BORE NO SETSCREW	ACME NO. 40B10										
SPROCKET - 5/8 PITCH, 11 TEETH, TYPE B HUB - STL, STK 5/8 IN. BORE NO SETSCREW	ACME NO. 50B11		2								
SPROCKET - 5/8 PITCH, 23 TEETH, TYPE B HUB - STL, BORED TO 2 IN. DIA WITH KEY SEAT & TWO SETSCREWS (KEY SEAT MUST BE IN LINE WITH CENTER OF ONE TOOTH WITHIN .030)	ACME NO. 50B23		2								
SPROCKET - 5/8 PITCH, 19 TEETH, TYPE A PLATE STL, STK 5/8 BORE			2								
SPROCKET - 5/8 PITCH, 20 TEETH, TYPE B HUB STL, BORED TO 2 IN. DIA WITH KEY SEAT & TWO SETSCREWS (KEY SEAT MUST BE IN LINE WITH CENTER OF ONE TOOTH WITHIN .030)	ACME NO. 50B20		2								
SPROCKET - 1 1/4 PITCH, 11 TEETH, TYPE B HUB STL BORED TO 1 1/2 DIA WITH KEYSEAT & TWO SETSCREWS	ACME NO. 100B11		1								
SPROCKET - 1 1/4 PITCH, 32 TEETH, TYPE B HUB STL BORED TO 2 IN. DIA WITH KEY SEAT & TWO SETSCREWS	ACME NO. 100B32		1								
ROLLER CHAIN - 1/2 PITCH ASA NO. 40 SINGLE WIDTH X 239 PITCHES			1								
ROLLER CHAIN - 1/2 PITCH ASA NO. 40 SINGLE WIDTH X 229 PITCHES			1								
ROLLER CHAIN - 1/2 PITCH ASA NO. 40 SINGLE WIDTH X 99 PITCHES			1								
ROLLER CHAIN - 1/2 PITCH ASA NO. 40 SINGLE WIDTH X 369 PITCHES			1								
ROLLER CHAIN - 5/8 PITCH ASA NO. 50 SINGLE WIDTH X 171 PITCHES			2								
ROLLER CHAIN - 5/8 PITCH ASA NO. 50 SINGLE WIDTH X 177 PITCHES			2								
ROLLER CHAIN - 1 1/4 PITCH ASA NO. 100 SINGLE WIDTH, RIVETED, 43 PITCHES			1								
CONNECTING LINK FOR ASA NO. 40 ROLLER CHAIN			8								
CONNECTING LINK FOR ASA NO. 50 ROLLER CHAIN			8								
CONNECTING LINK FOR ASA NO. 100 ROLLER CHAIN			1								
OFFSET LINK FOR ASA NO. 40 ROLLER CHAIN			4								
OFFSET LINK FOR ASA NO. 50 ROLLER CHAIN			4								
OFFSET LINK FOR ASA NO. 100 ROLLER CHAIN			1								
COLLAR - 2 IN. SHAFT DIA	BOSTON NO. SC200		2								
BEARING, FLANGED (OIL IMP) 5/8 I.D. X 3/4 O.D X 3/4 LG BRZ.	BOSTON NO. FB-1012-6		4								
BEARING, FLANGED (OIL IMP) 1/2 I.D. X 5/8 O.D. X 3/4 LG BRZ	BOSTON NO. FB-810-6		6								
BEARING, FLANGED (OIL IMP) 1/2 I.D. X 5/8 O.D. X 1 IN. LG BRZ	BOSTON NO. FB-810-8		1								
BEARING, FLANGED (OIL IMP) 1/2 I.D. X 5/8 O.D. X 1 3/4 LG BRZ	BOSTON NO. FB-810-4		1								
BEARING, FLANGED (OIL IMP) 1 IN. I.D. X 1 1/4 O.D. X 3/4 LG BRZ	BOSTON NO. FB-1620-6		2								
KEY, SQUARE - 5/16 X 1 1/2 LG STL			1								
SCREW, MACH FL HD - 1/2-13UNC-2A X 2 IN. LG STL CD PL			22								
SCREW, MACH FL HD - 1/2-13UNC-2A X 1 1/2 LG STL CD PL			6								
SCREW, MACH PAN HD - #10-24UNC-2A X 1/2 LG STL CD PL			9								
SCREW, CAP, HEX HD - #10-24UNC-2A X 1/2 LG STL CD PL			8								
SCREW, CAP, HEX HD 1/4-20UNC-2A X 1/2 LG STL CD PL			4								
SCREW, CAP, HEX HD - 1/4-20UNC-2A X 5/8 LG STL CD PL			8								

BILL OF MATERIAL

SYM	ITEM	Description	Part No.	1	2	3	4	5	6	7	8	9	10
	1	ELECTRON BEAM GUN CARRIAGE	GR 2 THIS DWG	1									
	2	TRAILER FRAME	944 J 689-16		1								
	3	BRACE, TRAILER FRAME	944 J 689-32		1								
	4	CARRIAGE	944 J 689-38		1								
	5	CARRIAGE	944 J 688-4		1								
	6	CARRIAGE	944 J 690-15		1								
	7	BEAM	944 J 688-43		1								
	8	BEAM	944 J 688-44		1								
	9	PIVOT BASE	944 J 688-33		1								
	10	BEARING PLATE	944-J-690-1		1								
	11	BOGIE	944 J 690-4		1								
	12	CARRIAGE	944 J 688-24		1								
	13	CARRIAGE	944 J 688-30		1								
	14	SPROCKET HOUSING	944 J 690-11		1								
	15	FLANGE	944 J 690-19		1								
	16	BRACKET, GUN MOUNTING	944 J 690-51		1								
	17	BRACKET, GUN MOUNTING	944 J 690-52		1								
	18	SHAFT, PITCH	944 J 690-45		1								
	19	SHAFT, TORSION	944 J 690-43		1								
	20	SHAFT, TORSION	944 J 690-44		1								
	21	PIN	944 J 690-56		1								
	22	SPROCKET BRACKET	944 J 690-47		2								
	23	BRACKET	944 J 690-39		1								
	24	ANGLE	944 J 690-42		2								
	25	CHAIN ADJUSTER	944 J 688-49		4								
	26	CHAIN ADJUSTER	944 J 688-50		4								
	27	CHAIN ADJUSTER	944 J 688-51		8								
	28	PIN (1/2 DIA X 3.00)	944 J 688-61		1								
	29	SPROCKET SHAFT	944 J 688-58		2								
	30	PIN	944 J 688-59		4								
	31	MOUNTING PLATE	944 J 688-60		1								
	32	SHAFT, PITCH DRIVE	944 J 690-46		1								
	33	SHAFT	944 J 688-57		1								
	34	PIN (1/2 DIA X 2.62)	944 J 688-53		3								
	35	PIN (1/2 DIA X 3.62)	944 J 688-55		1								
	36	PIN (5/8 DIA X 3.00)	944 J 688-56		2								
	37	WHEEL ADJUSTER	944 J 688-21		1								
	38	BRIDGE	944 J 688-1		1								
	39	BEARING BLOCK	944 J 688-2		1								
	40	BEARING BLOCK	944 J 688-3		1								
	41	SPROCKET SUB-ASSY	944 J 689-1		1								
	42	CHAIN GUIDE	944 J 689-5		1								
	43	CHAIN GUIDE	944 J 689-6		1								
	44	SHIM	944 J 690-55		2								
	45	CHAIN GUIDE	944 J 689-7		2								
	46	CHAIN GUIDE	944 J 689-8		2								
	47	CHAIN GUIDE	944 J 689-9		1								
	48	CHAIN GUIDE	944 J 689-10		1								
	49	CHAIN GUIDE	944 J 689-11		1								
	50	CHAIN GUIDE	944 J 689-12		1								
	51	CHAIN GUIDE	944 J 689-13		3								
	52	CHAIN GUIDE	944 J 689-14		1								
	53	CHAIN GUIDE	944 J 689-15		1								
	54	SPROCKET BRACKET	944 J 690-22		1								
	55	SPROCKET BRACKET	944 J 690-23		1								
	56	SPROCKET BRACKET	944 J 690-24		1								
	57	SPROCKET BRACKET	944 J 690-25		1								
	58	SHIM	944 J 690-9		14								
	59	SHIM	944 J 690-10		6								
	60.	CHAIN GUIDE	944 J 689-49		1								
	61	WHEEL BRACKET	944 J 690-42		6								

A. MAY BE PURCHASED FROM UNIVERSAL FLUID DYNAMICS CO., ALPENA, MICHIGAN.
B. MAY BE PURCHASED FROM FAFNER
C. MAY BE PURCHASED FROM ROTEK INC., RAVENNA, OHIO
D. MAY BE PURCHASED FROM FLO-TORK DIV., ALLEN ELECTRIC & EQUIPMENT CO., ORVILLE, OHIO.
E. MAY BE PURCHASED FROM ALBION INDUSTRIES INC., ALBION MICHIGAN.
F. MAY BE PURCHASED FROM NICE BALL BEARING CO., PHILADELPHIA, PENN.
G. MAY BE PURCHASED FROM ACME CHAIN CORP., HOLYOKE, MASS. OR EQUAL.
H. MAY BE PURCHASED FROM BOSTON GEAR, QUINCY, MASS.

REV	ZONE	DESCRIPTION	APP

DO NOT SCALE THIS DWG.

WESTINGHOUSE ELECTRIC CORPORATION

ELECTRON BEAM GUN CARRIAGE ASSY

944J6E7

A-18-41

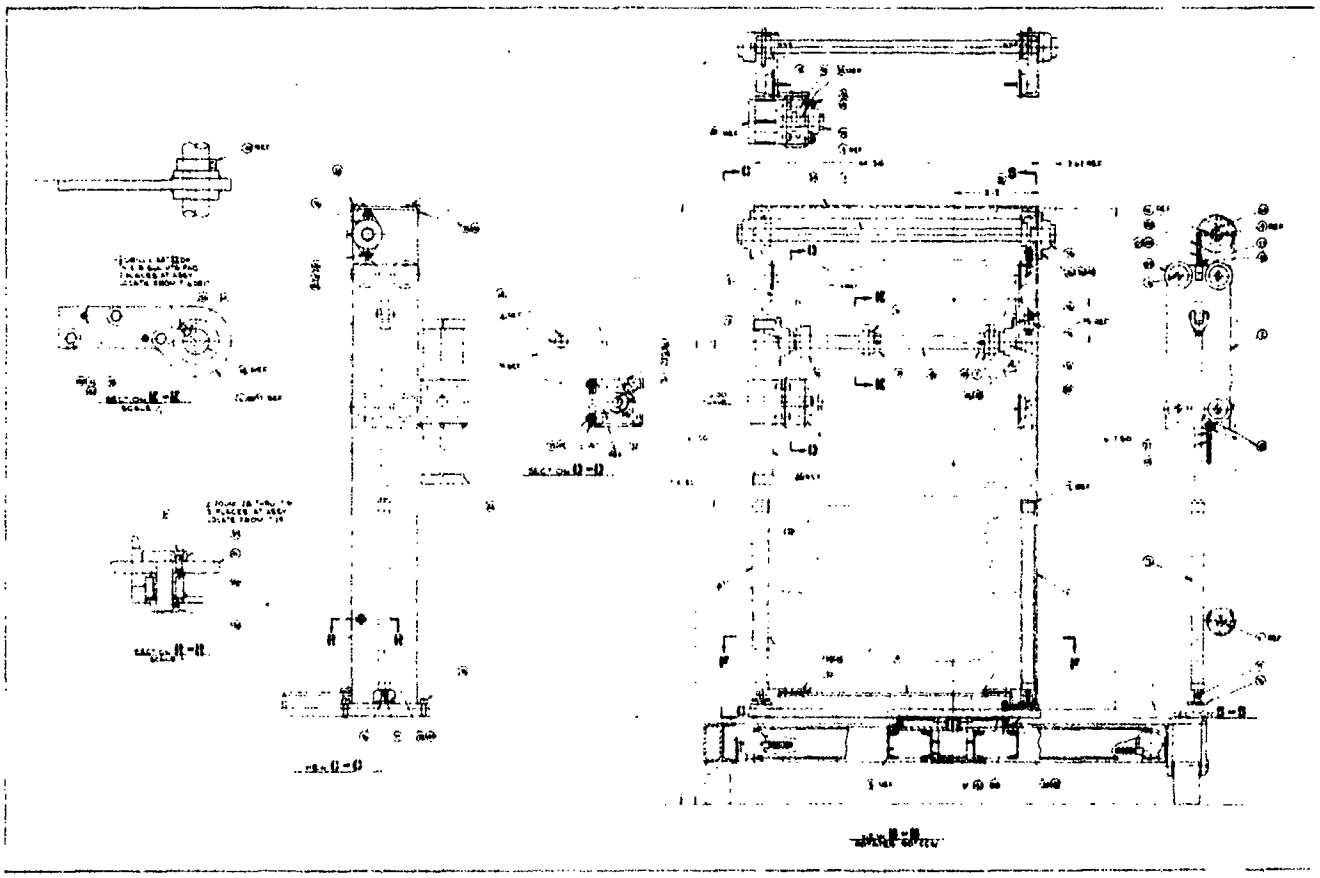

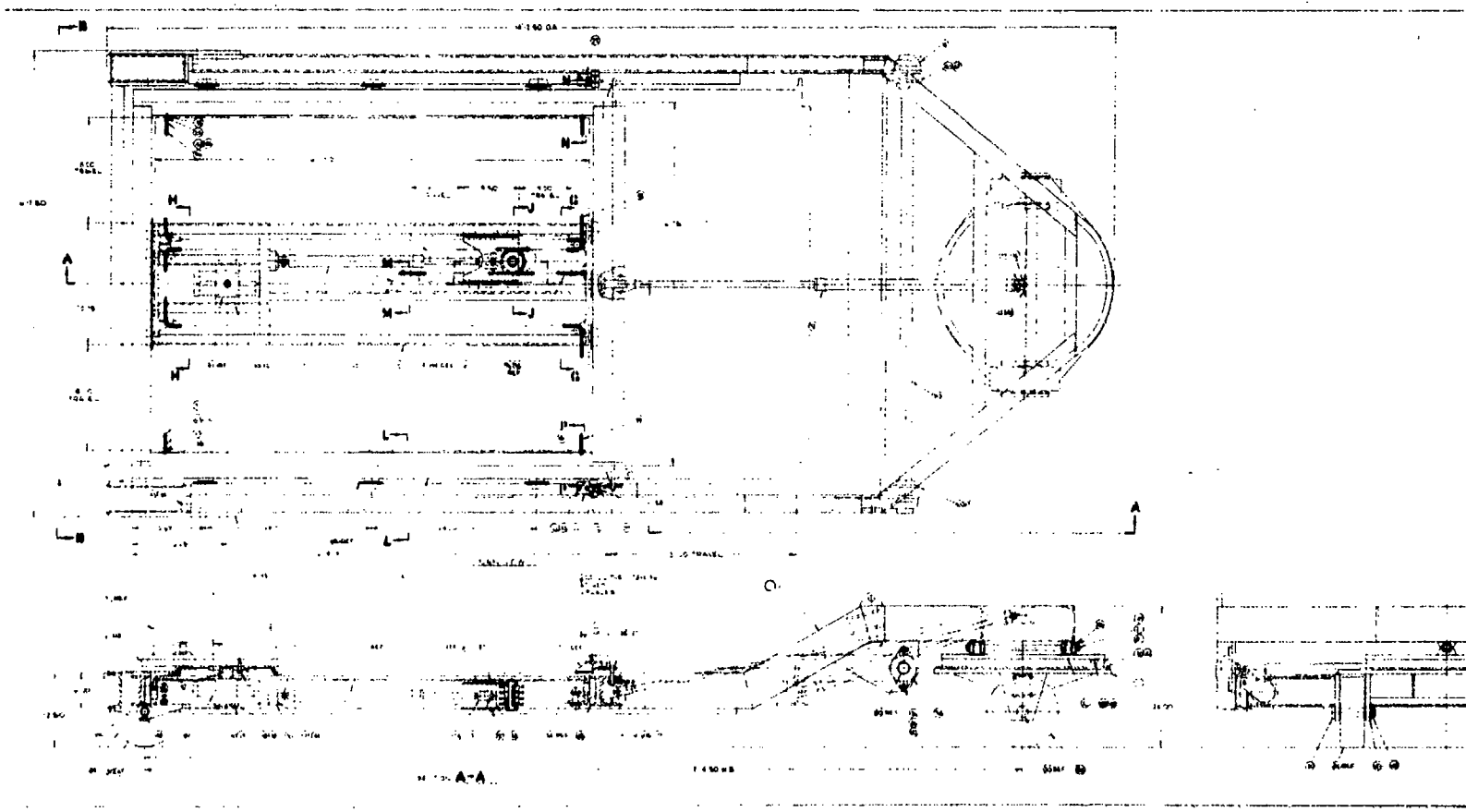
A-A

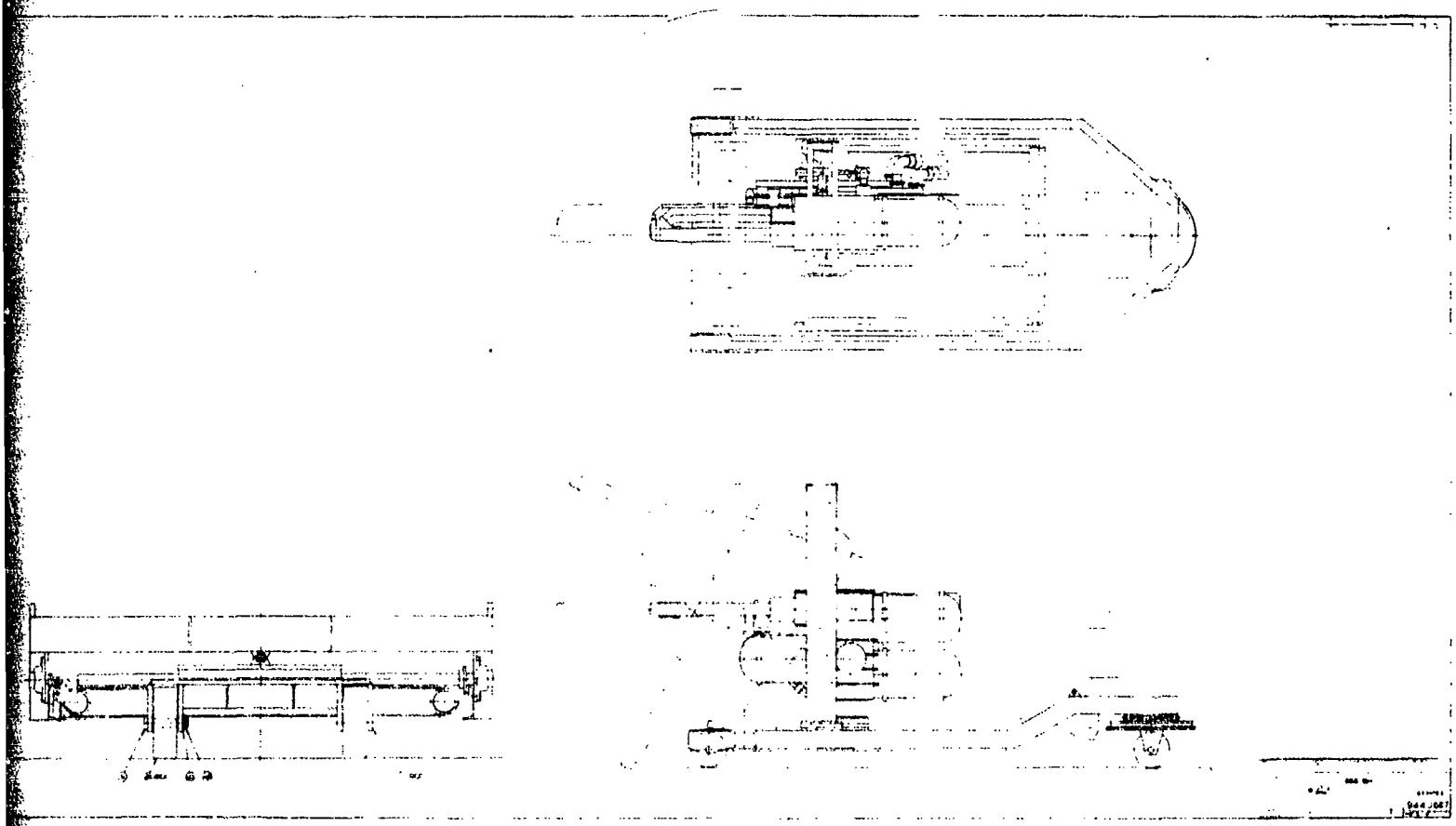

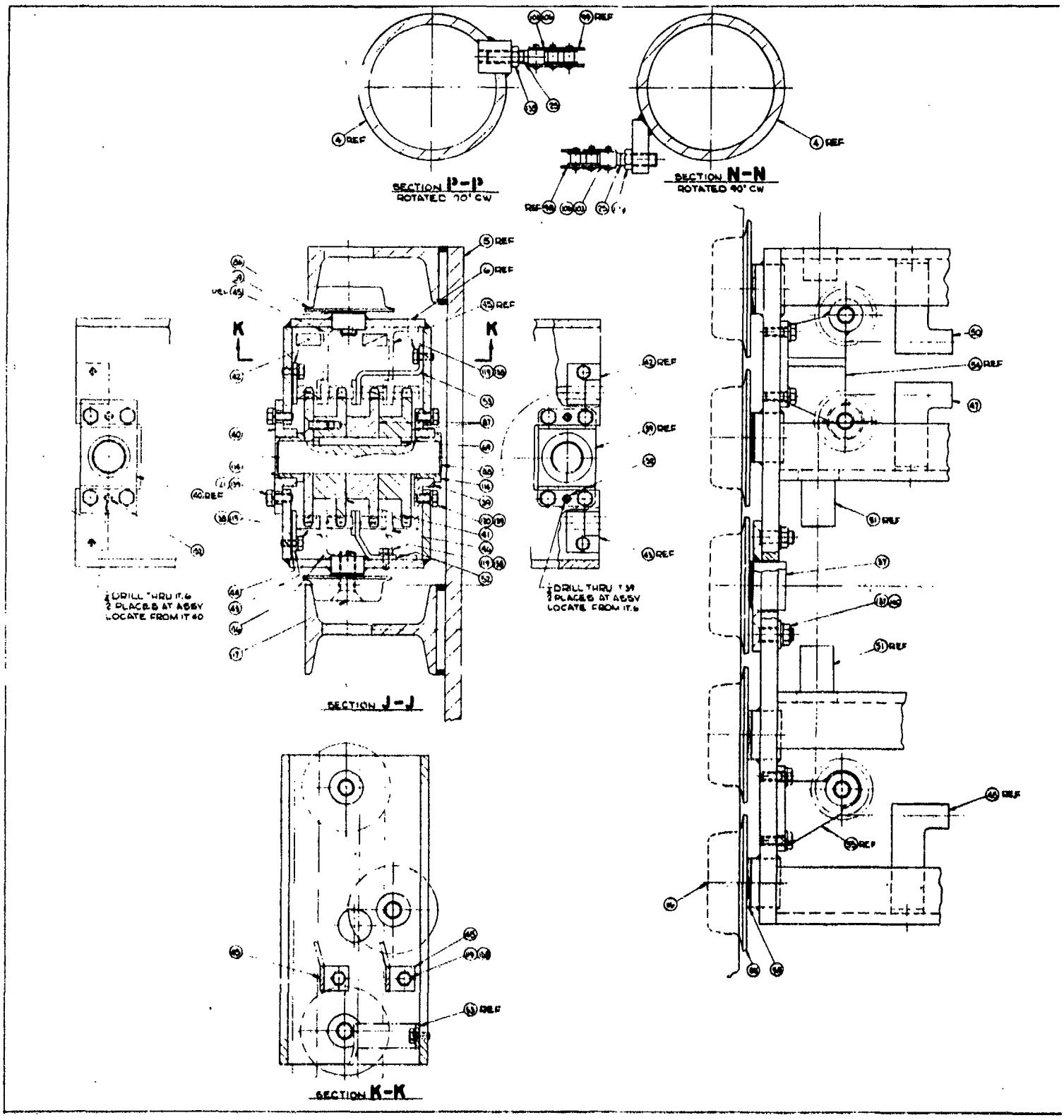
SECTION P-P
ROTATED 70° CW
SECTION N-N
ROTATED 40° CW
SECTION J-J
SECTION K-K
DRILL THRU IT.6
2 PLACES AT ASSY
LOCATE FROM IT 40
DRILL THRU IT 39
2 PLACES AT ASSY
LOCATE FROM IT.6
REF

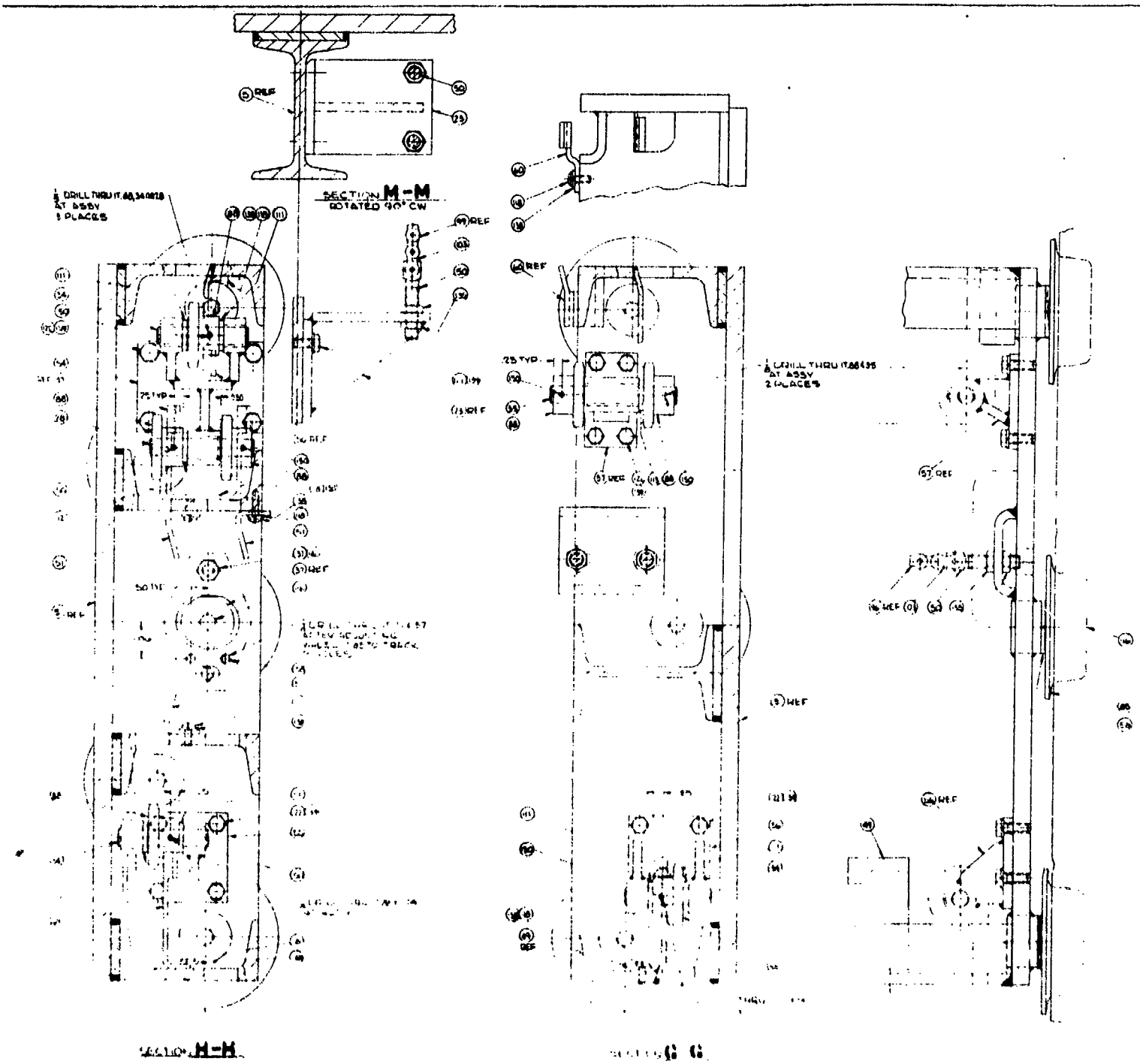
SECTION M-M
ROTATED 90° CW
SECTION H-H
SECTION G-G

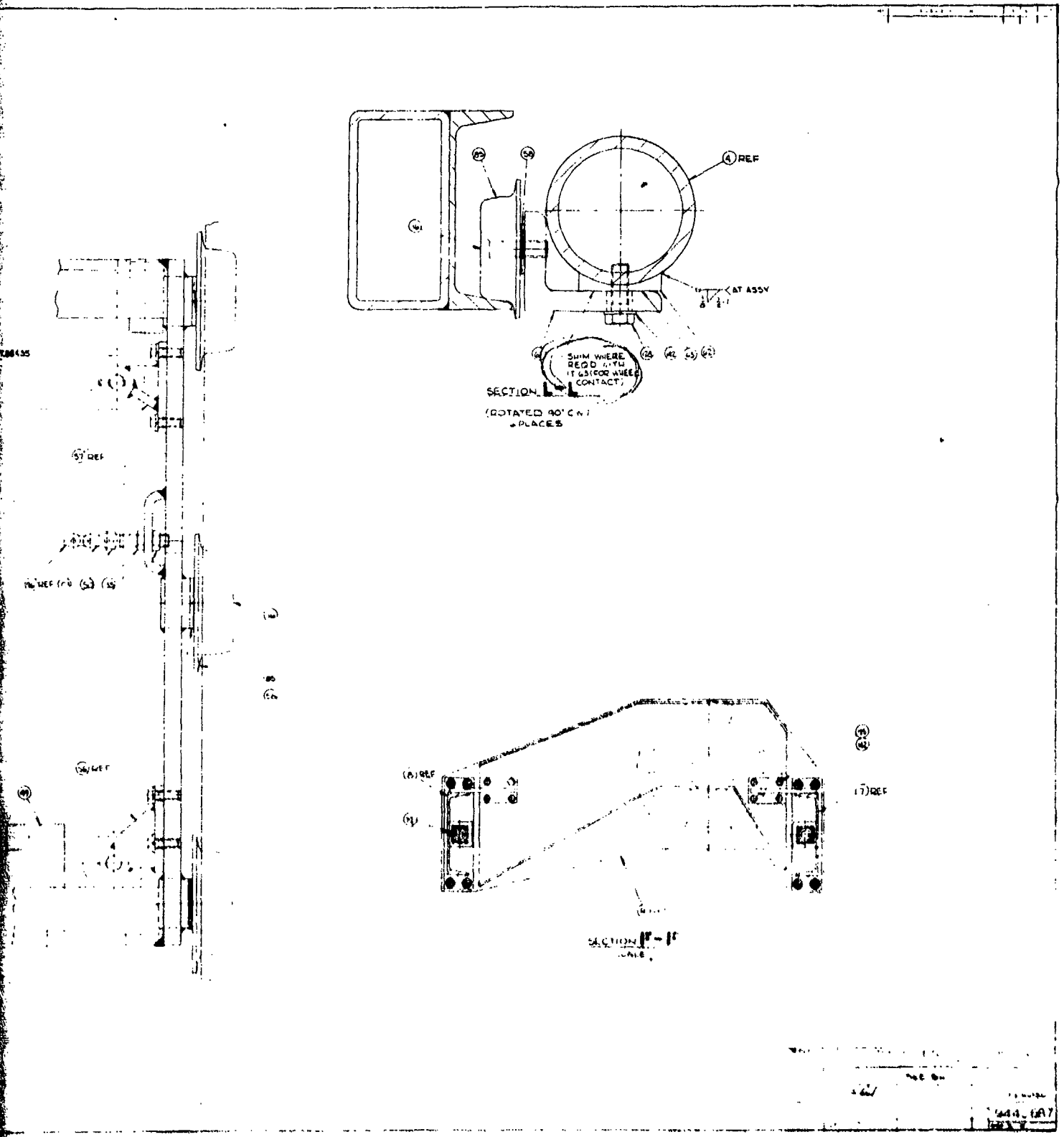

4 REF
AT ASSY
SHIM WHERE REQD WITH IT 65 (FOR WHEEL CONTACT)
SECTION L-L
(ROTATED 90° C.W.)
4 PLACES
57 REF
56 REF
(8) REF
(7) REF
SECTION F-F

A-3 CARRIAGE TESTING

Work on the carriage since delivery consisted of completing the electrical and control systems, conducting an operational test of the carriage, and making minor modifications as a result of deficiencies observed in the tests. In-plant testing of the EBG carriage is subdivided into two categories: (1) an initial phase using a mock-up of an EBG, and (2) a final phase to verify operation of the carriage in conjunction with the 36-kW EBG. The first results of the initial phase testing were reported in the Second Quarterly Report, as follows.

1. Initial Tests

The initial phase of the in-plant tests consists of several tests to verify operation of the carriage hydraulic system, to obtain calibration data for the system velocity controls, and to detect and measure any beam oscillations that might occur as a result of hydraulic transients or structural vibrations. Preliminary carriage tests were performed in a no-load condition to verify operation of all components. A concrete and steel pipe mock-up of the EBG was then constructed and mounted on the carriage for the remaining tests. The mock-up gun approximates the field test gun in space envelope, weight, and center-of-gravity location. The carriage, with the mock-up gun installed, appears in Figure A-6 through A-9. Figure A-8 is a time exposure taken during carriage translation with a light attached to the end of the transfer column to record the gun motion. Although all modes of operation are represented in Figure A-8, these motions do not extend to the limits of the gun manipulator. The control panel for the carriage is shown in Figure A-9.

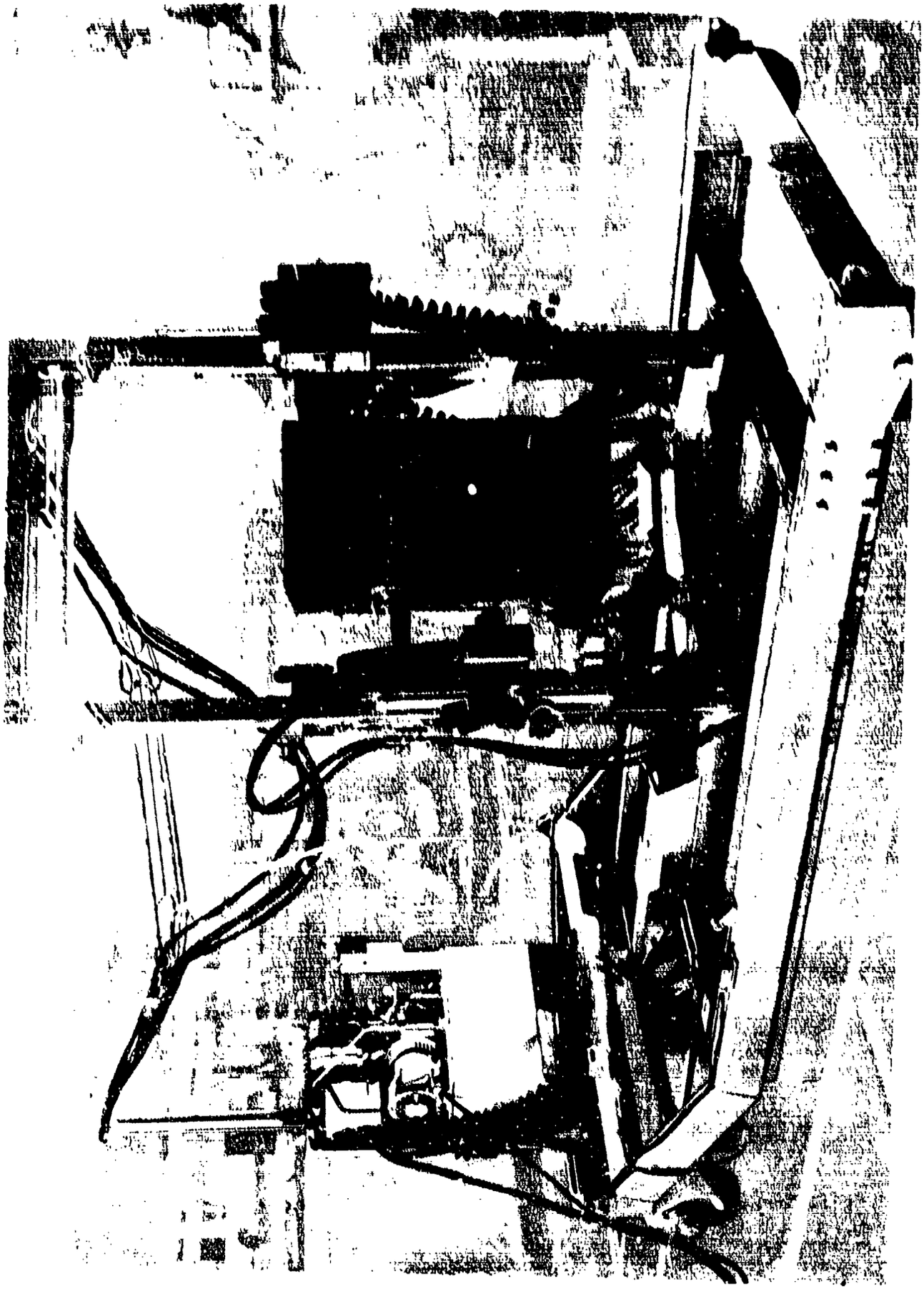

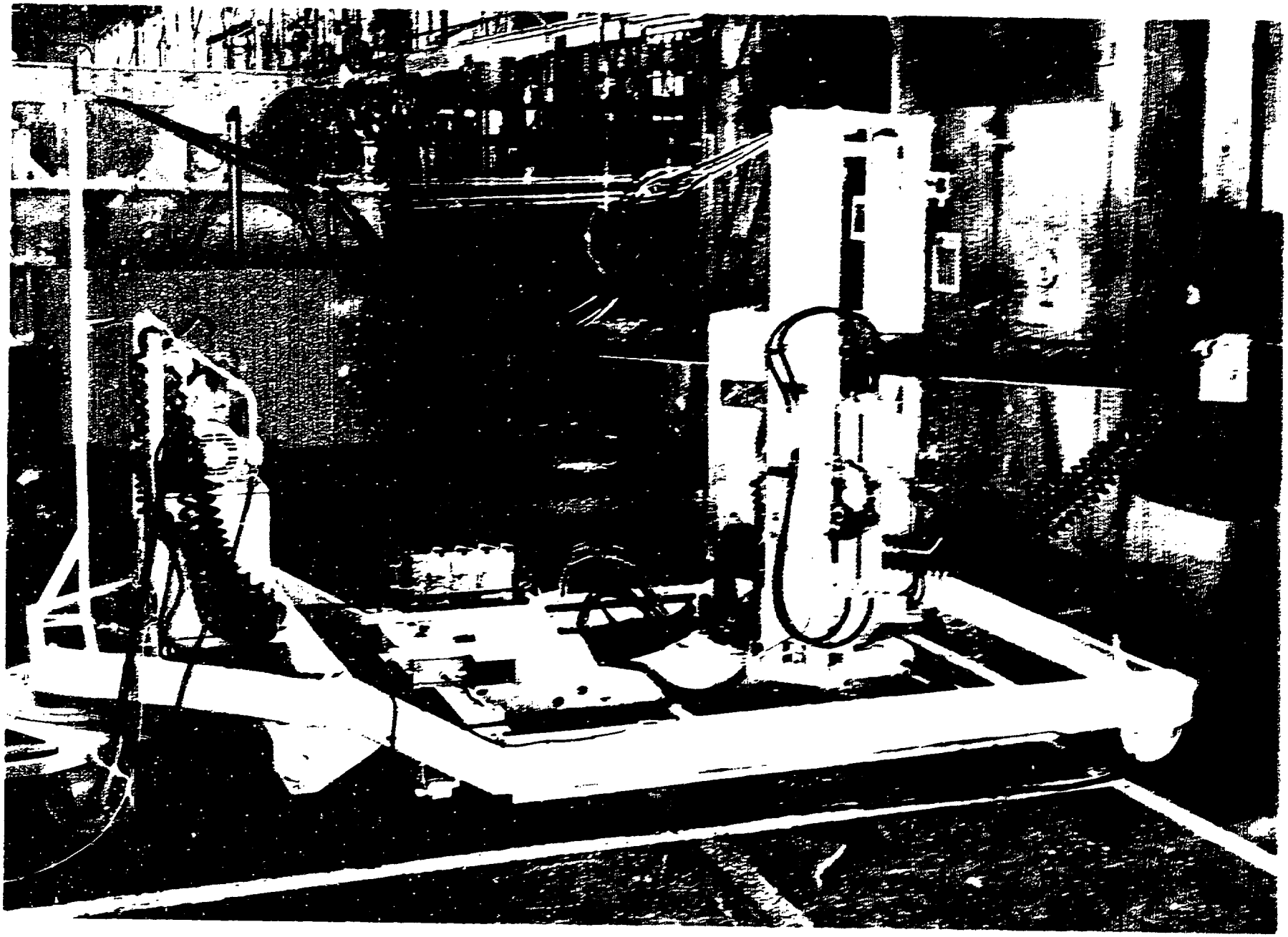

Figure A-7. Carriage with Mock-up of [illegible] from Beam Gun (Right [illegible])

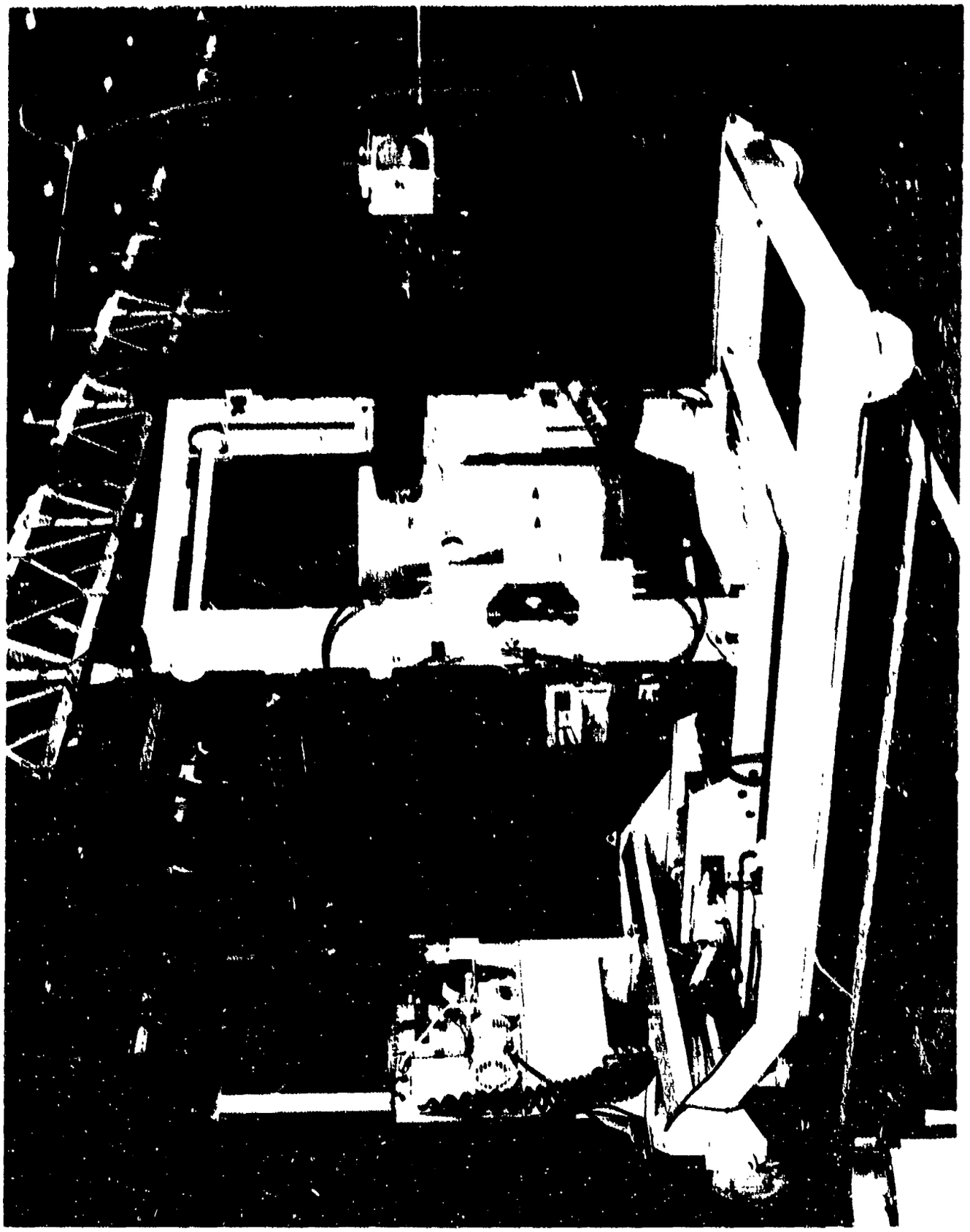

Figure A-8. Time Exposure with Light Attached to End of Simulated Transfer Column During Translation

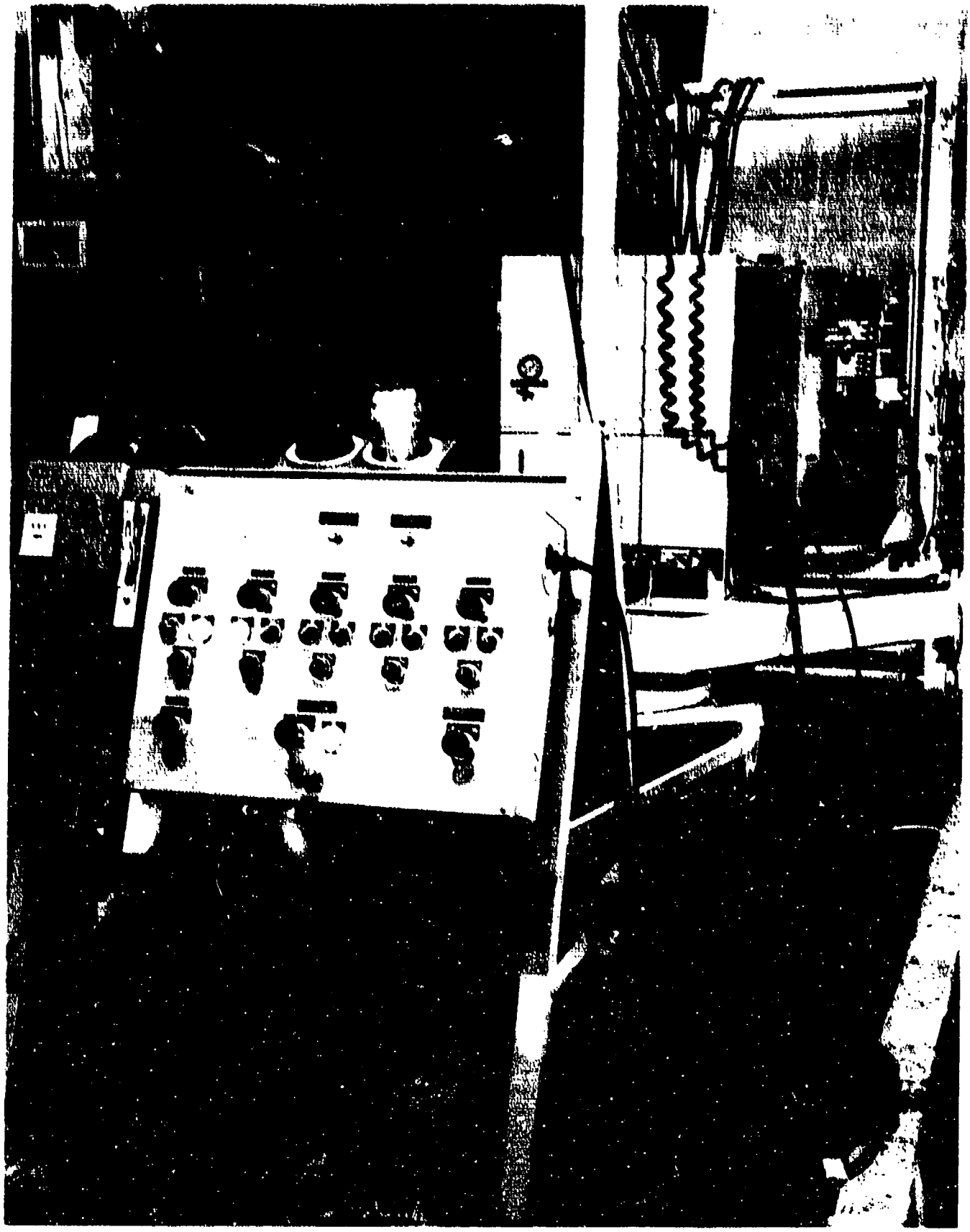

Figure A-9. Control Panel for Electron Beam Gun Carriage

After installation of the mock-up, a series of calibration tests was run to obtain the data required for velocity control. Each portion of the carriage hydraulic system is equipped with temperature- and pressure-compensated variable flow control valves. These valves will permit repeatable and constant velocity control for each mode of operation. The calibration consists of operating the various portions of the hydraulic circuit at several flow control settings. The actuation time for each operation is recorded and the results plotted as beam velocity vs. valve setting. These tests will be completed in early July.

The second phase of testing will begin when the 36-kW gun is installed on the carriage. This phase is comprised of a series of tests to recheck the previous valve calibration data, to identify any physical interference problems that may exist, and to verify operation of the EBG with the field configuration of vacuum pumps and motor-generator sets. The operational tests will include some preliminary cutting tests, to be performed using a 6 x 6 x 5-foot granite test block.

2. Modifications

In the preliminary testing, some discrepancies in carriage operation were noted. The clearances between the portions of the gun mount, which move in the Y-axis or vertical mode, were found to be excessive, and under certain loading conditions, the movable portions could be "derailed". A system of auxiliary guide rollers has been designed and installed to redistribute the loads, and thereby alleviate the problem. As mentioned in the First Quarterly Report, a flexible coupling was provided in the gear drive system to prevent any misalignment problems that might result from a redundant center condition. The rigid coupling appeared to function properly but was removed anyway and replaced with the flexible device. The flexible rubber insert in the new coupling resulted in soft or spongy response in the yaw drive with a considerable amount of over-shoot observed at the end of the actuator stroke and upon control valve closure. The rigid coupling will be

reinstalled to eliminate these undesirable characteristics. The results of the remaining initial phase tests are described below. (As in the 3rd Quarterly Report.)

3. Carriage Test, Continued

Tests were conducted to verify proper operation of the carriage hydraulic system and controls and to determine velocities of motion resulting from various hydraulic system adjustments. To simulate the operational configuration of the carriage with the EBG installed, an EBG mock-up was constructed and installed on the carriage for the preliminary tests. This mock-up, made of concrete and steel pipe, approximates the 36-kW EBG in weight, overall dimensions, and center of gravity location as indicated in Table A-1.

Table A-1

COMPARISON OF 36 KW EBG AND MOCK-UP EBG

	36 KW EBG	Mock-up
Weight	1500*	1474
Moment due to CG Location	18,000 in.-lb.	15,500 in.-lb.

The carriage is capable of moving the gun along the x, y, and z axes and in the rotational modes of pitch and yaw. Axis orientation and rotational modes are indicated in Figure 5. Motion in each of the five modes of operation is accomplished using linear or rotary hydraulic actuators with velocity control in all modes except the z axis achieved through the use of temperature and pressure compensated flow control valves. Velocity control in the z-axis mode is achieved using an uncompensated variable orifice flow control valve.

4. Carriage Test Results

Measurements of linear and rotary full stroke displacements were made for each mode of operation. Each of the actuators was then

*The 1500-pound weight was a very conservative early estimate of the gun weight. Actual weight is approximately 975 pounds.

cycled at several different flow control valve settings. The time required for actuation at each setting was measured and recorded.

An additional test was conducted to determine the amplitude and frequency of vibration or beam oscillation present at the end of the gun transfer column. No mention was made in the design requirements of vibration limits, but this was subsequently determined to be an area of concern. Horizontal and vertical vibrations were measured at several flow control valve settings for each mode of operation using MB velocity pickups in conjunction with an MB meter and an oscilloscope.

Actuation Velocities. Times required for full-stroke actuation for various valve settings were used to calculate velocities at the gun exit nozzle. Velocities for each mode of operation were plotted against valve opening (see Figures A-10 through A-13).

Temperatures. Hydraulic fluid temperatures were recorded throughout the test. The fluid temperature repeatedly reached the maximum allowable temperature of 150°F after about 4 to 6 hours of continuous operation; test operations had to be halted to permit the system to cool.

Vibration. Amplitude and frequency of horizontal and vertical exit nozzle vibration were measured and recorded during each mode of operation at various flow control valve settings. Both amplitude and frequency appear to be independent of actuation velocity. Frequencies were 3 to 4 cps in the horizontal direction and 8 to 10 cps in the vertical. Amplitudes (peak to peak) varied from 0.001 inch to 0.01 inch with averages from 0.0005 inch to 0.001 inch.

5. Conclusions and Recommendations

General Performance. The electron beam gun carriage performs as required by the design requirements specification except for the irregularities in velocity control and the problem of hydraulic system overheating. No

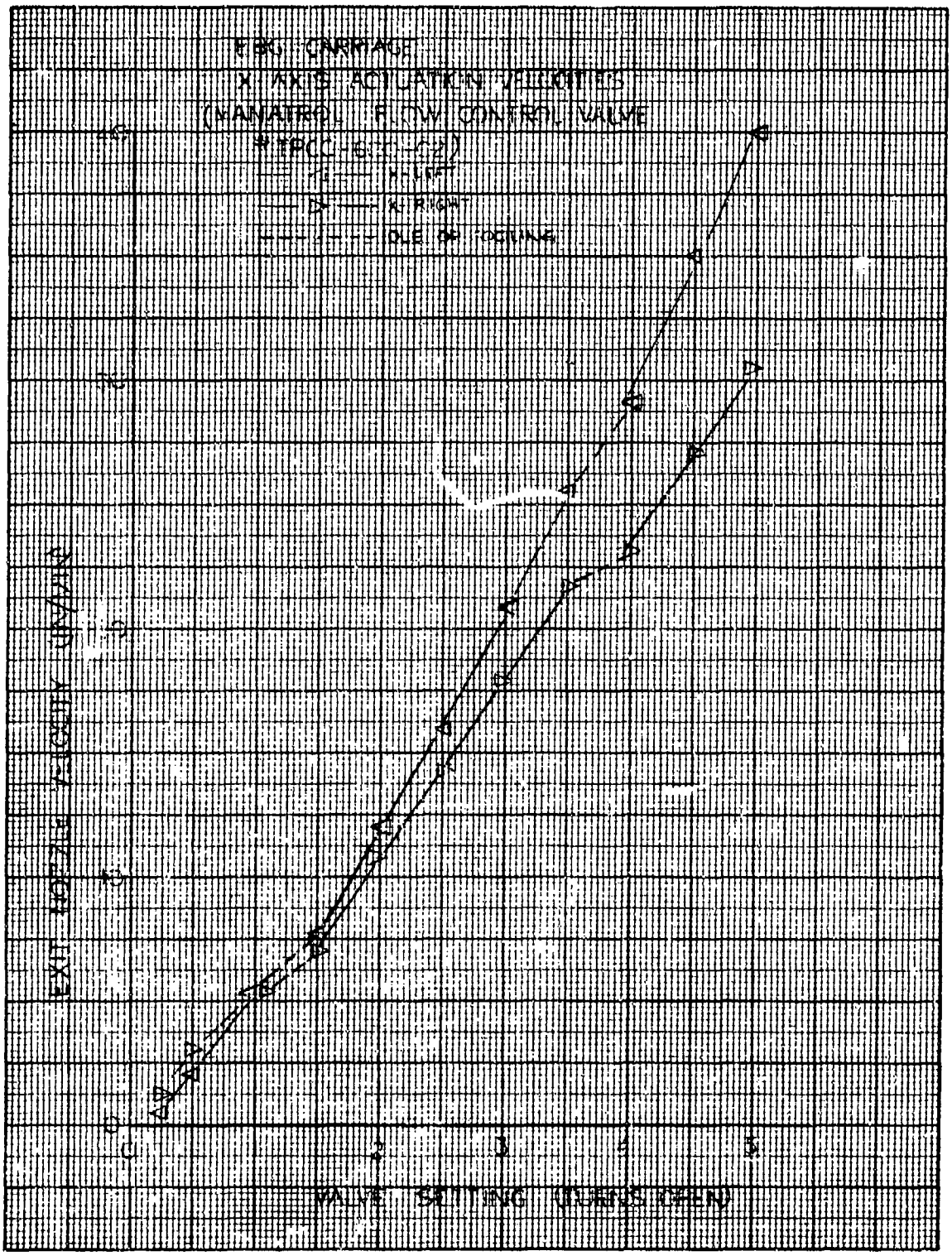

Figure A-10. EBG Carriage - X-Axis Actuation Velocities

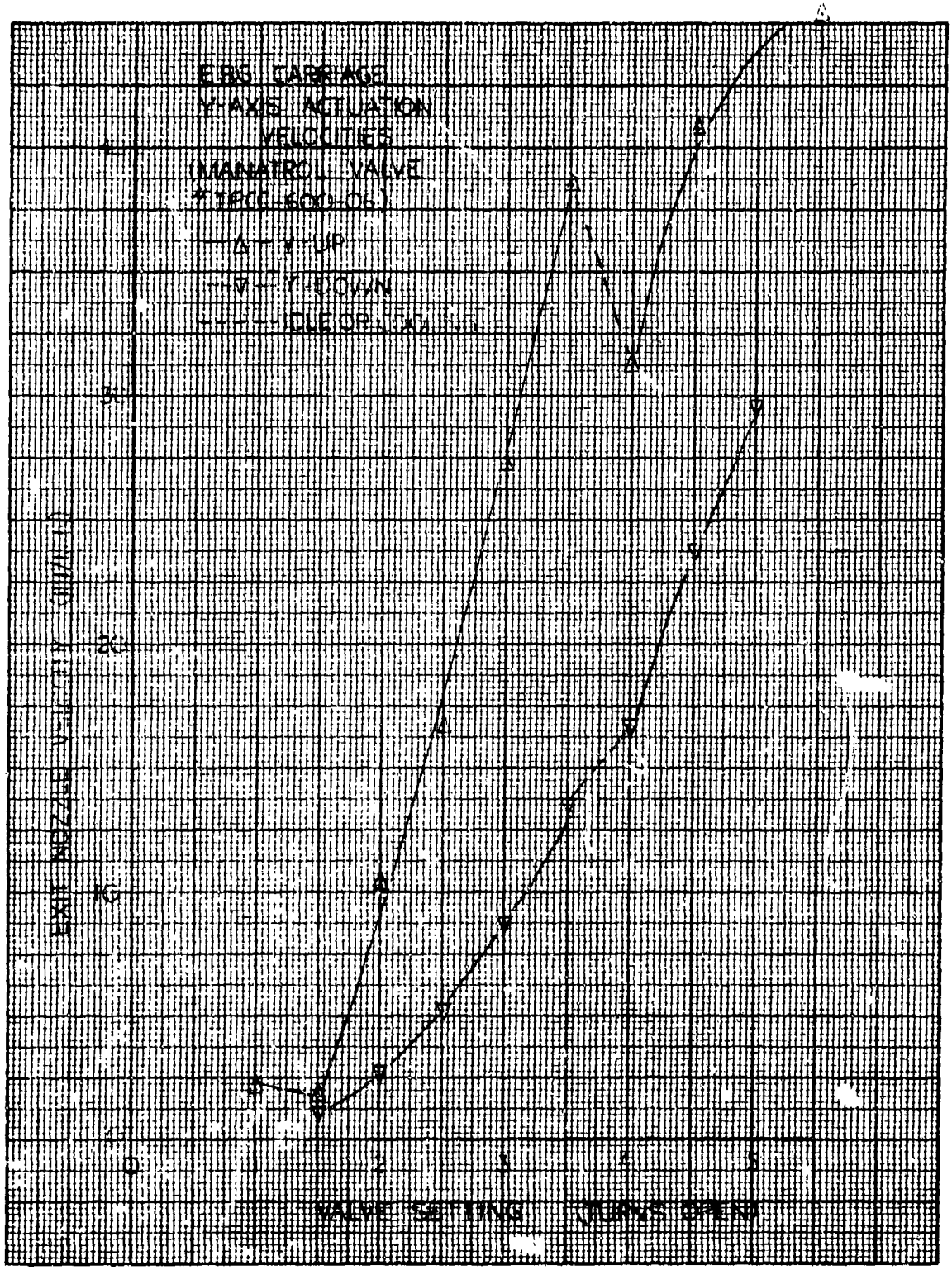

Figure A-11. EBG Carriage - Y-Axis Actuation Velocities

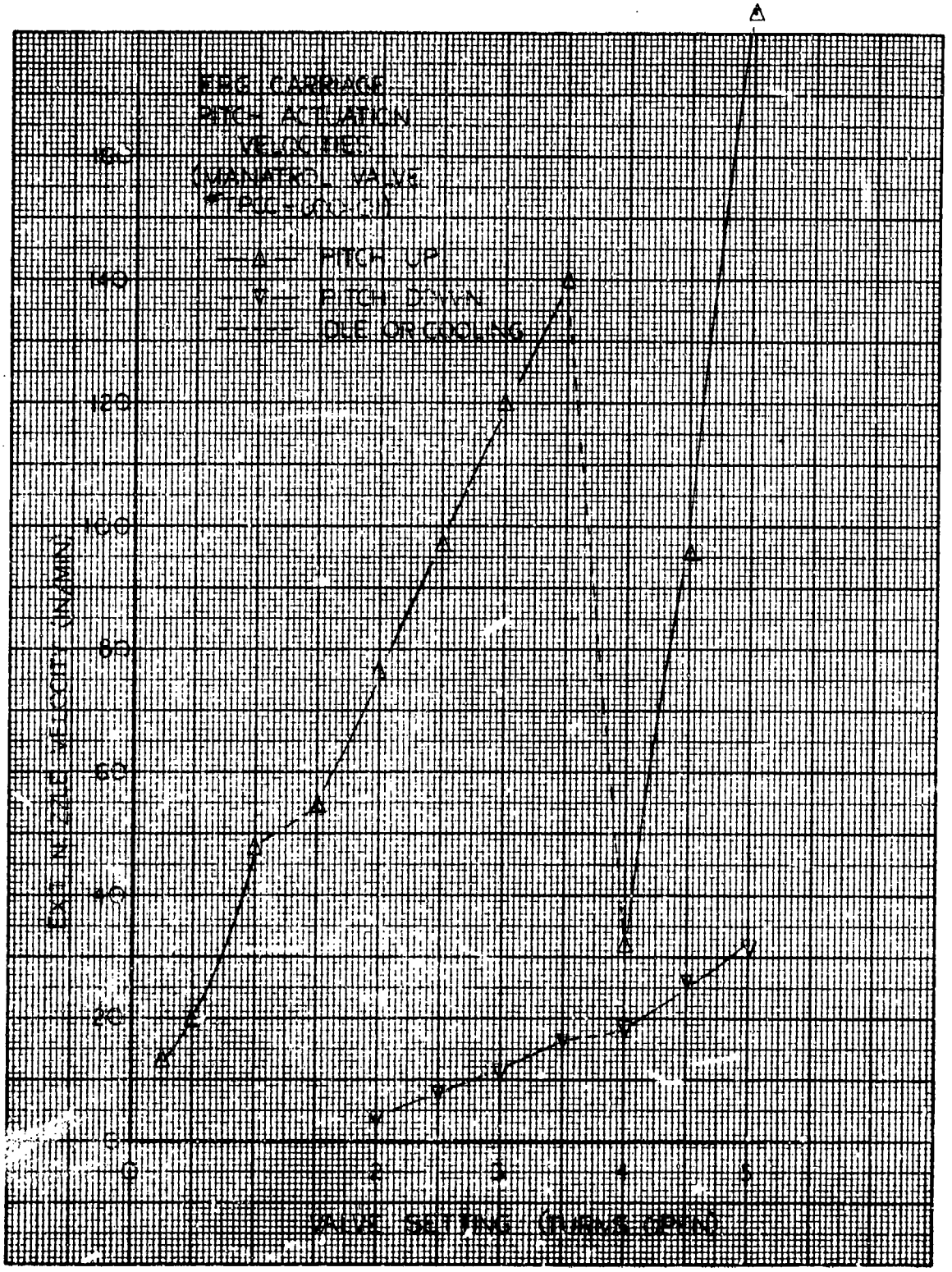

Figure A-12. EBG Carriage - Pitch Actuation Velocities

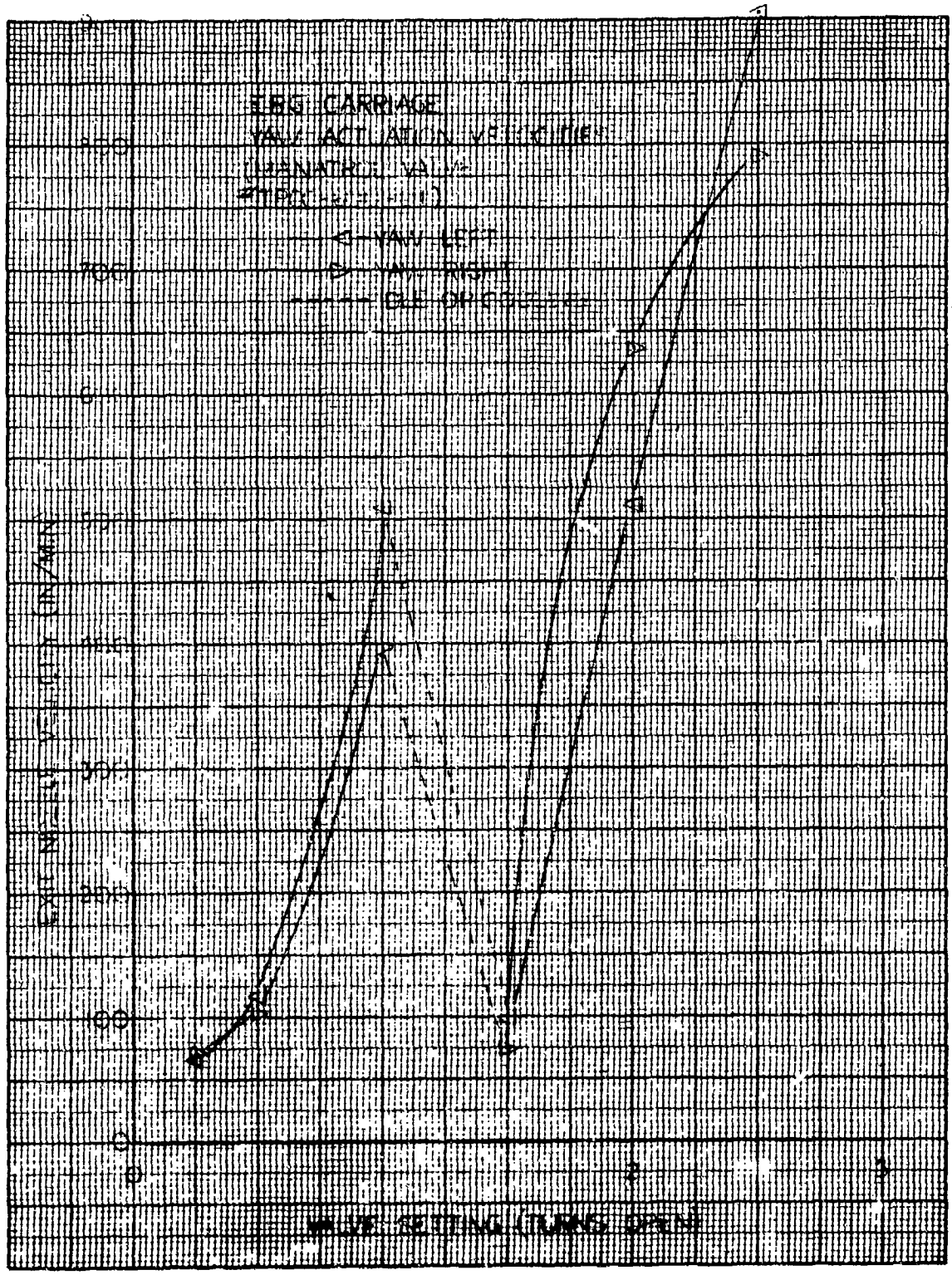

Figure A-13. EBG Carriage - Yaw Actuation Velocities

anomalies were noted during operation, and the only construction discrepancy noted was the use of fixed elbow hose connections in the hydraulic system when swivel elbows had been called for on the carriage procurement drawings. Replacement of the fixed elbows with swivel elbows is recommended.

Actuation Velocities. The specification requires actuation velocities in all modes to be variable within the range of 0 to 30 inches per minute. The X- and Y-axis control systems perform in accordance with the specification requirements except for some irregularities which appear on the velocity plots as apparent decreases in velocity resulting from an increase in valve opening. This behavior is attributed to changes in oil temperature and viscosity.

Actuation velocities and their control in the pitch and yaw mode are less satisfactory. In the yaw mode, performance was characterized by very high velocities, varying from 67 inches with the valve 0.25 turn open to 900 inches per minute at 2.5 turns open, and by large irregularities in flow resulting from temperature changes in the hydraulic fluid. The manufacturer's specification for performance of the yaw and pitch circuit flow control valves states that they will maintain constant flow over a pressure range of 70 to 3000 psi with a ± 1.0 percent variation in flow, and over a temperature differential of 60°F with ± 2.5 percent variation in flow, in the flow range from 0 to 25 cubic inches per minute. To achieve operation at the desired velocities, the flow controls must operate properly in the bottom 2 percent of the flow range, and they are apparently not capable of this performance. A possible remedy, which may be employed to achieve more precise control in the yaw circuit, would require replacement of the present direct coupling of the actuator to its driven mechanism with a chain or gear drive with at least a 2:1 reduction.

Pitch circuit performance is also characterized by high velocities in the "up" direction and by very low velocities in the "down" direction.

Velocities measured in the "up" direction varied from 13.8 inches per minute at a valve setting of 0.25 turn to 185 inches per minute at 5.0 turns open. These velocities correspond to flow rates of 7.7 cubic inches per minute and 104 cubic inches per minute, respectively. Since the maximum flow rate for this valve is 25 cubic inches per minute, the flow control valve is apparently defective. The pitch "down" circuit provides satisfactory velocity control, except that motion was extremely slow until the valve was opened 2.0 turns.

The flow control valve manufacturer has agreed to replace the defective valves. They will also test valves to find two that operate satisfactorily in the lower portions of their flow range. These will replace those presently in the yaw circuit.

Temperature. The maximum permissible operating temperature for the carriage hydraulic system is 150°F. This temperature was reached several times during the test, necessitating a halt in test operations to permit the system to cool to an allowable operating temperature. The temperature fluctuations also have a pronounced effect on flow control valve performance. For these reasons, installation of an air/oil or water/oil heat exchanger is recommended to maintain a maximum fluid temperature of approximately 100°F. Rough heat load calculations indicate that the required heat exchanger should have a maximum capacity of removing 60 btu/minute from the hydraulic fluid returning to the reservoir. The actuation velocity tests should be repeated after installation of a heat exchanger and replacement of defective valves.

Vibration. Amplitudes recorded during the vibration test remained constant at several valve settings and appeared to be affected only by background vibration, such as that caused by motion of heavy machinery in the adjacent area. These inputs, transmitted through the concrete floor of the test area, resulted in large response motion of the carriage and test weight. In field tests, this will not be a problem

and the 0.0005 inch to 0.001 inch amplitudes recorded as steady-state vibration may be considered negligible.

6. FINAL TESTS

No action was taken on the recommendations of the preceding paragraph. When the electron gun was delivered to Sunnyvale in April of 1972, it would not fit the carriage because the pitch-gear projected inside the space envelope of the gun. An extension bracket had to be made for the foot of the left upright rail to place the rails further apart. No stand for the small pumps (Fig. A-4) had been provided and no support brackets for the electrical junction box. By the end of July 1972 these parts became available and the electron gun was lifted from the laboratory carriage to the main carriage. Installing the small vacuum pumps required some changes on the stand to avoid interferences between the flexible hoses and the stand as well as the frame of the main carriage.

While these problems could be overcome, the above described shortcomings in the speed settings and the vibrational responses were not alleviated at the time, and they have to some extent hampered the tests, as discussed in Section 6.1. They must be corrected before the equipment is taken into the field.

Appendix B

Preparations for Field Tests

Expecting to be able to go into the field under the present contract, once the electron gun was put on its carriage and traversing mechanism, certain preparations for field tests have been made, as follows: (1) review and selection of test sites, (2) the development of site support equipment such as radiation shielding, and (3) registration of the electron beam gun with the California State Department of Public Health as a radiation producing machine. (See Section 6.5)

B-1 Test Site Selection

A meeting was held at the U. S. Bureau of Mines Twin Cities Research Center on 25 January 1971 to discuss various aspects of test sites. With this discussion in mind, Westinghouse began to review candidate test sites. Because of the complications that might be encountered in an underground mine site, such as limited access and space and the possibility of environmental problems (heat, gases, etc.), Westinghouse has concentrated on open quarry sites for the first field tests. Some of the aspects considered as desirable site features are the following:

1. Geologic considerations
   a. Relatively hard rock type
   b. Large, relatively unfractured, constrained rock mass
   c. Rock surface relatively unweathered
   d. Several feet of overburden above test location
2. Facility considerations
   a. Availability of utilities, communications, security
   b. Availability of acceptable security arrangements

c. Safety requirements: reasonable proximity to medical facilities and X-ray film badge service

d. Availability of large open work area around test site

e. Proximity to Westinghouse Sunnyvale, California

f. Availability of accommodations for site personnel

g. Climate: minimal chance for precipitation during the four- to six-week test period.

3. Site Support considerations

a. Availability of skilled and unskilled labor

b. Availability of support equipment such as cranes, welding equipment, earthmoving equipment, etc.

With the foregoing criteria in mind, Westinghouse has reviewed 12 quarry sites and 1 mine site. The mine, in Alburquerque, New Mexico, is unsuitable for our purposes because of its remote location, the limited access to test faces, and the lack of utilities at the mine site, as well as other reasons. The quarry sites visited range from granite quarries in the Rocklin, California area; granodiorite quarries in Madera, California; and granite, limestone, and sandstone quarries in the coast range from Monterey to Marin County (north of San Francisco). Most of the sites reviewed were deemed unsuitable for Westinghouse use for various reasons such as inaccessibility, lack of sufficient rock face and overburden, inadequate utilities available at the site, and high probility of interference with the owners' quarrying operations. However, one site had been located which fulfills most of the site requirements and was therefore tentatively selected as a field test site, but it was rejected later.

The first selected site was the Logan quartz gabbro quarry in Aromas, California, near Watsonville (see Figure B-1 and B-2). This quarry is owned and currently operated by the Granite Rock Company of Aromas, California and is available for electron beam gun test use. It is located about eight miles from Watsonville and is approximately one hour and 15 minutes travel time from the Westinghouse Sunnyvale

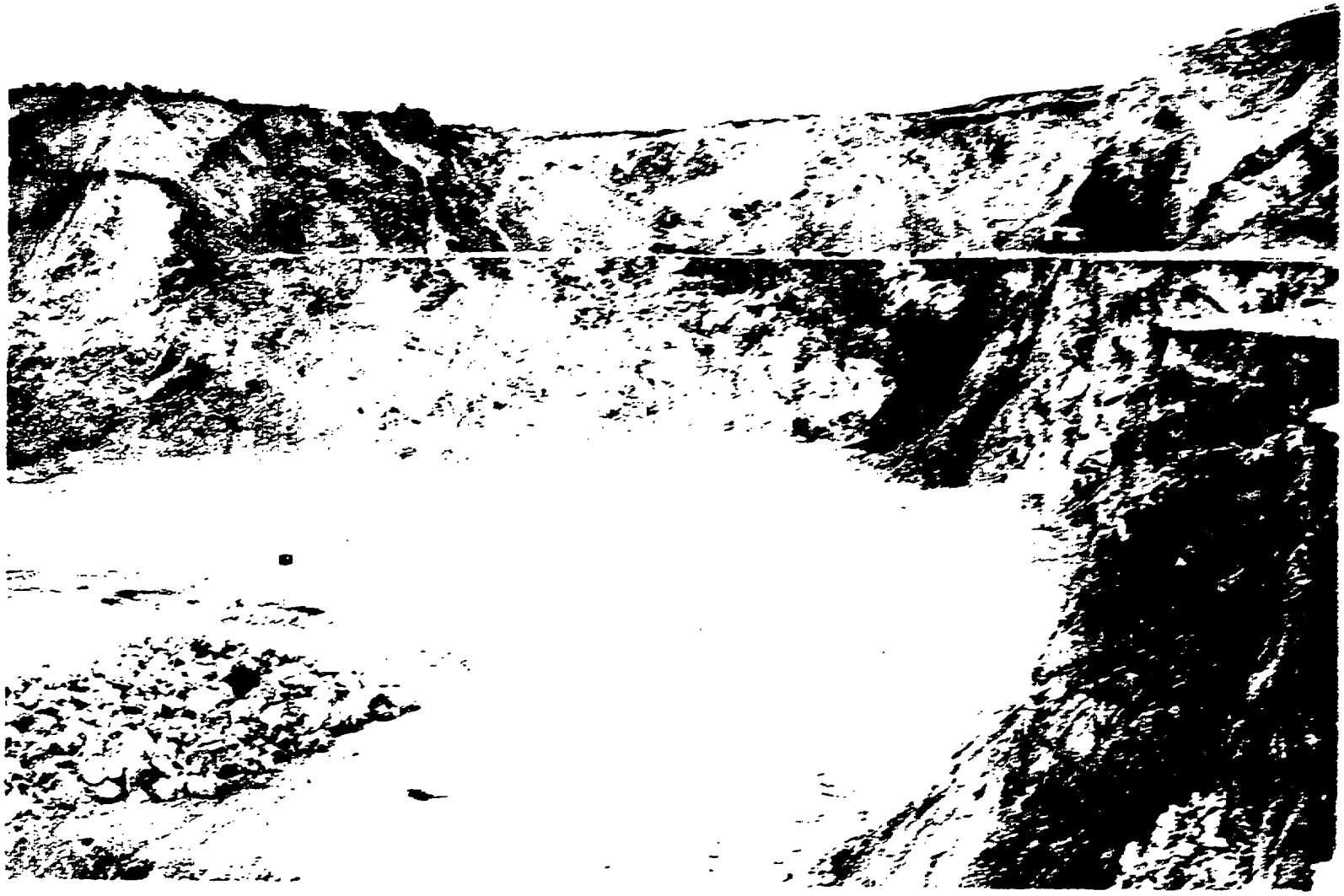

Figure B-1. View from West Rim of Logan Quartz Gabbro Quarry, Aromas, California, Looking Towards Fractured Rock Area (Arrow indicates proposed working face shown in Figure B-2.

Figure B-2. South End of Logan Quarry Showing Rock Face and 100-foot Wall

facility. While not far from Watsonville, the site is relatively isolated and has limited access; thus security should not be a large problem. Utilities are avilable at the site, and site support equipment and labor are available at cost from the quarry operator.

The quarry itself is approximately one-half mile across and has a flat floor of packed granite sand. The rock walls of the quarry vary from 80 to about 100 feet high and present excellent exposures of unweathered rock, both fractured and relatively unfractured (see Figure B-2). The rock itself is a hornblende quartz gabbro containing about 10 percent quartz and 35 to 48 percent green hornblende. The Logan formation is described in greater detail by Donald C. Ross in Reference 31.

A view of this site is presented in Fig. B-1 and B-2. Since it is located on the San Adreas Fault, the Logan rock is extensively fractured and faulted. After a second visit to the Logan site by Westinghouse and Bureau of Mines personnel in June 1971, this site was rejected as a prime test site, and another site was located that more completely fulfills the desired geologic requirements.

The approved test site, also visited by Westinghouse and Bureau of Mines personnel, is the Raymond Granite Company's "Sierra White"* granite quarry. The quarry is located in the Sierra Nevada foothills of California and 25 miles south-southwest of Yosemite National Park. A section of the USGS map for California gives an indication of geological formations in the Raymond area.**

The Raymond quarry is a producer of white granite dimension-stone products, which are excavated from an exposed face of an extensive mesozoic granitic formation. The rock is an even textured, fine grained moscovite-biotite granite, grayish white in color. The chemical composition of the rock and some of its physical properties were listed in Section 4.3.1 of the main text of this report.

---

*"Sierra White" is the producer's trade name for the rock from this quarry.

**See Mariposa Sheet of Olaf P. Jenkins' Edicition of Geologic Map of California Compilation by Rudolph G. Strand, U.S. Geological Survey, 1967.

Figure B-3. The granite block used in the tests came from this dimenstion stone quarry in Raymond, California

In their excavation of the quarry, the operators have refrained from the use of explosives whenever possible, and therefore, the rock mass is almost entirely fracture-free. Figure B-3 shows the location. The test block for the tests described in Section 4.3 came from this site.

While this site is ideal geologically, its use presents other difficulties, primarily because of its rather remote location. Utilities and telephone communications are available, but the closest living accommodations and medical facilities are in Madera. The support equipment and labor available from the quarry operator are rather limited. He will provide a part-time electrician to provide power to the test face, but all other labor must be provided by Westinghouse. A small machine shop and some welding equipment are available for Westinghouse use, but again, personnel must be provided by Westinghouse.

Other arguments which speak against the use of this test site have been advanced already in Sections 4.3 of this report.

B-2 Equipment

A set of shielding panels, consisting of 1/4" lead on plywood and backed by a frame of 2 x 4 lumber, have been bought. In addition some lead glass panes were bought to cover new windows which were cut into some of the lead panels. None of the above was used, except the panels for the "sky-shine" shield discussed in Section 4.2

The motor generator sets which were used at the Sunnyvale test site were rented units; they would have been used at the field site as well, but the lease on them was not extended after the Sunnyvale tests were completed.

APPENDIX C

Literature References

1. Maurer, William C., Novel Drilling Techniques, Pergamon Press, 1968.

2. The Staff, U.S. Bureau of Mines, Twin City Mining Research Center, Minneapolis, Minn. "USBM Examines Exotic Ways of Breaking Rock" Engineering & Mining Journal, April 1968, p. 85-92.

3. B. W. Schumacher, "Electron Beam Cutting of Rocks and Concrete," Electron and Ion Beam Science and Technology, Third International Conference, (R. A. Bakish, ed.); The Electrochemical Society Inc. New York, 1968, p. 447-468. Also E/MJ, June 1969, p. 116-119.

4. B. W. Schumacher and C. R. Taylor, "Rock Breakage by Means of Electron Beam Piercing (Laboratory Tests), "Record of 10th Symposium on Electron, Ion, and Laser Beam Technology (L. Marton, ed.); San Francisco Press, Inc., 1969, p. 271-284.

5. B. W. Schumacher, Electron Beams as Tools for Underwater Cutting and Welding--Laboratory Tests. Symposium Proceedings Underwater Welding and Hand Tools, Oct. 1967; published by Marine Technology Society 10501 15th St., N/W., Washington, D.C. 20005.

6. Klemens, Paul, G., 3rd Intern. Conf. Electron and Ion Beam Science and Technology, Boston, Mass. May 1968, R. Bakish, Ed., The Electrochemical Society, Inc., New York 1968, p. 291.

7. Schubert, D.C. and Schumacher, B.W., 3rd Intern. Conf. Electron and Ion Beam Science and Technology, Boston, Mass. May 1968, R. Bakish, Ed., The Electrochemical Society, Inc., New York 1968, p. 269.

8. Schubert, D.C. "Computation of Small-Angle Scattering and Its Importance for Electron Beam Welding," Record of 10th Symposium on Electron, Ion, and Laser Beam Technology (L. Marton, ed.); San Francisco Press, Inc., 1969, p. 271-284.

9. B. W. Schumacher, "Dynamic Pressure Stages for High-Pressure/High-Vacuum Systems," in: 1961 Transaction of the Eighth Vacuum Symposium and Second International Congress, p. 1192-1200, Pergamon Press, New York 1962. - Also OPTIK 10, p. 116-132, 1953.

10. I. B. Margiloff "Flame Working Minerals," U.S. Patent No. 3,245,721, April 1966.

11. R. Teale, "The Concept of Specific Energy in Rock Drilling," Int. J. Rock Mech. Mining Sci. 2, p. 57-73, 1965.

12. G. S. Reichenbach, "State of the Grinding Art," Science and Technology, Oct. 1965, p. 14-17.

13. M. Mellor "Normalization of specific energy values" Int. J. Rock Mech. Min. Sc. 9, 661-663, 1972.

14. K. Barron, "Detection of Fracture Initiation in Rock Specimens by the Use of a Simple Ultrasonic Listening Device, "Int. J. Rock Mech. Min. Sci., 8, 55-59 (1971).

15. Safety Standard for Non-Medical X-Ray and Sealed Gamma-Ray Sources. Part I. General, Handbook 93, U. S. Department of Commerce, National Bureau of Standards, April 1966.

16. Ibid., Fig. 17, p. 50.

17. J. D. Jackson, Classical Electrodynamics, John Wiley & Sons, New York 1962, Chap. 13.

18. B. W. Schumacher and F. D. Seaman, Studies of Factors Producing High Efficiency Welds with a Non-Vacuum Electron Beam Welder. 10th Symp. on Electron, Ion, & Laser Beam Technology May 21-23, 1969, Gaithersburg, Md. Proceedings, San Francisco Press 1970.

19. R. B. Sosman, The Properties of Silica, The Chemical Catalog Company, Inc., New York 1927.

20. K. Thirumalai, Potential of Internal Heating Method for Rock Fragmentation, U.S. Bureau of Mines, Twin Cities, Minn., 1970.

21. K. Thirumalai, Proceedings Eleventh Symposium on Rock Mechanics, June 16-19, 1969, The American Institute of Mining, Metallurgical and Petroleum Engineers, Inc., New York 1970.

22. J. C. Jaeger, Journal of Mathematics and Physi[illegible] p. 316.

23. W. M. Rahsonow and H. Choi, Heat, Mass and Momentum Transfer, Prentice-Hall, Englewood Cliffs, New Jersey, 1961, p. [illegible].

24. J. C. Jaeger and N.G.W. Cook, Fundamentals of Rock Mechanics, Methuen & Company, London, 1969.

25. W. Weibull, "A Statistical Theory of the Strength of Materials," Ingvetnsk. Akad. Handl. No. 151.

26. J. A. Hudson, Proceedings of the Eighth Symposium on Rock Mechanics, September 15-17, 1966, The American Institute of Mining, Metallurgical, and Petroleum Engineers, Inc., New York, 1967, p. 162.

27. Schumacher, B. W., 3rd Int. Conf. Electron and Ion Beam Science and Technology, Boston, Mass. May 1968, R. Bakish, Ed., The Electrochemical Society, Inc. New York 1968, pp.31-73.

28. F. Sauter, Differential Equations of Physics, Sammlung Göschen, Vol. 1070, p. 58.

29. R. E. Riecker and T. P. Rooney, "Water-induced weakening of Hornblende and Amphibolite" Nature 224, 1299, 1969.

30. E. Bas Z. angew. Phys. 7, 337, 1955.

31. Donald C. Ross, "Quartz Gabbro and Anorthositic Gabbro: Markers of Offset Along the San Andreas Fault in the California Coast Range," Bulletin of Geological Society of America, Vol. 81 (Dec. 1970), pp. 3647-3662.

- - - - - - - - - - - - - -

During the two years this contract was active three technical reports were issued, namely:

First Quarterly Technical Report	30 April 1971
Second " " "	30 July 1971
Third " " "	30 October 1971

The contents of these reports is included in full in the present Final Report and therefore no cross reference to these earlier reports appears herein.